Technical University of Denmark

Exploration, modelling and management of groundwater-dependent ecosystems in karst

– the Sian Ka'an case study, Yucatan, Mexico

Bibi R. N. Gondwe

DTU Environment
Department of Environmental Engineering

PhD Thesis
March 2010

Exploration, modelling and management of groundwater-dependent ecosystems in karst

– the Sian Ka'an case study, Yucatan, Mexico

Bibi R. N. Gondwe

PhD Thesis
March 2010

DTU Environment
Department of Environmental Engineering
Technical University of Denmark

Bibi R. N. Gondwe

Exploration, modelling and management of groundwater-dependent ecosystems in karst
– the Sian Ka'an case study, Yucatan, Mexico

PhD Thesis, March 2010

The thesis will be available as a pdf-file for downloading from the homepage of the department: www.env.dtu.dk

Address:	DTU Environment Department of Environmental Engineering Technical University of Denmark Miljoevej, building 113 DK-2800 Kgs. Lyngby Denmark
Phone reception:	+45 4525 1600
Phone library:	+45 4525 1610
Fax:	+45 4593 2850
Homepage:	http://www.env.dtu.dk
E-mail:	reception@env.dtu.dk

Printed by:	Vester Kopi Virum, March 2010
Cover:	Torben Dolin
ISBN:	978-87-91855-85-6

Preface

This PhD thesis is based on research undertaken from November 2006 to February 2010 at the Department of Environmental Engineering, Technical University of Denmark (DTU). The work was carried out under the supervision of Associate Professor Peter Bauer-Gottwein. Associate Professor Esben Auken, Department of Earth Sciences, Aarhus University, was co-supervisor. The work was primarily funded by DTU.

The research was primarily carried out at DTU, but included two field trips to the study area in Mexico (Feb–Apr 2007, Jan–Mar 2008), a short external stay at Geological Survey of Austria (Nov–Dec 2007) and a longer research stay at Rosenstiel School of Marine and Atmospheric Sciences, University of Miami, Florida, USA (Mar–Jun 2008).

The content of this thesis is based on five scientific journal papers. At the time of writing, two have been published:

I Gondwe, B.R.N., Hong, S.-H., Wdowinski, S., Bauer-Gottwein, P. (2010). Hydrologic dynamics of the ground-water-dependent Sian Ka'an wetlands, Mexico, derived from InSAR and SAR data. Wetlands 30 (1), 1–13. doi: 10.1007/s13157-009-0016-z.

II Supper, R., Motschka, K., Ahl, A., Bauer-Gottwein, P., Gondwe, B., Alonso, G.M., Romer, A., Ottowitz, D., Kinzelbach, W. (2009). Spatial mapping of submerged cave systems by means of airborne electromagnetics: an emerging technology to support protection of endangered karst aquifers. Near Surface Geophysics 7 (5–6), 613–327.

III Gondwe, B.R.N., Ottowitz, D., Supper, R., Motschka, K., Merediz-Alonso, G., Bauer-Gottwein, P. (submitted). Exploring regional-scale preferential flow paths in the karst aquifer of Southern Quintana Roo, Mexico. Manuscript submitted.

IV Gondwe, B.R.N., Lerer, S., Stisen, S., Marín, L., Rebolledo-Vieyra, M., Merediz-Alonso, G., Bauer-Gottwein, P. (in review). Hydrogeology of the south-eastern Yucatan Peninsula: New insights from water level measurements, geochemistry, geophysics and remote sensing. Manuscript submitted.

V Gondwe, B.R.N., Merediz-Alonso, G., Bauer-Gottwein, P. (submitted). The influence of conceptual model uncertainty on management decisions for a groundwater-dependent ecosystem in karst. Manuscript submitted.

In the thesis, these papers are referred to by author names and Roman numbers.

A technical note is included as an appendix, displaying maps and coordinates of field data points.

Additionally, the following publications, related to the topic of the thesis, have been co-authored during the PhD-study, but are not included in the thesis:

Bauer-Gottwein, P., Gondwe, B.N., Christiansen, L., Herckenrath, D., Kgotlhang, L., Zimmermann, S. (2010). Hydrogeophysical exploration of three-dimensional salinity anomalies with the time-domain electromagnetic method (TDEM). Journal of Hydrology 380 (3–4), 318–329. doi: 10.1016/j.jhydrol.2009.11.007.

Gondwe, B.N., Bauer-Gottwein, P., Merediz-Alonso, G., Fregoso, A., Supper, R. (2010). Groundwater resources management in Quintana Roo, Mexico: Problems, scientific tools and policy. In: Friedman, M.J. (Ed.): Global water issues. U.S. Department of State, Bureau of International Information Programs. In press.

Kgs. Lyngby, February 2010
Bibi Ruth Neuman Gondwe

Acknowledgements

First of all, I would like to extend a warm thank you to my supervisor, Peter Bauer-Gottwein. You have been an inspiring supervisor, always willing and ready to help, guide and discuss, and full of contagious enthusiasm and motivation.

I also owe a great thank you to Amigos de Sian Ka'an, for introducing me to this exciting topic and for a good cooperation throughout.

The field work could not have been possible without the extensive help, personnel- and equipment-wise, from Amigos de Sian Ka'an, especially Gonzalo, Miriam, Alejandra, Luis, Basilio, Valdemar and Albert; from Luis Marin and students from UNAM – Pépé, Gabriela, Alexander, José Antonio and Mario B. , and from Judith Morales. CICY-CEA staff, particularly Mario Rebolledo, is gratefully acknowledged for use of equipment and for chemical analyses. Global Vision International is kindly acknowledged for lodging in Tulum. I furthermore greatly appreciate the field work and project work carried out by the DTU M.Sc. students Chiara, Sara and Guillaume.

I thank Shimon Wdowinski and Sang-Hoon Hong from RSMAS/MGG, University of Miami, as well as Robert Supper, David Ottowitz and the rest of the staff from the Geophysics Department of Geological Survey of Austria for the cooperation on the work reported in three of the papers. I also thank Esben Auken and staff at Department of Earth Sciences, University of Aarhus, and Yusen Ley-Cooper, now Geoscience Australia, for help and discussions on ground-based and airborne EM data.

I am grateful to Jim Coke, Quintana Roo Speleological Survey, and Grupo de Exploracion Ox Bel Ha for permission to use cave maps. The principal explorers of the Ox Bel Ha system: B. Birnbach, S. Bogaerts, F. Devos, C. Le Maillot, S. Meacham, B. Philips, S. Richards, D. Riordan, S. Schnittger, G. Walten and K. Walten, and the principal explorers of the Sac Actun system: S. Bogaerts, K. Davidson, D. Jones, B. Phillips and R. Schmittner are gratefully acknowledged.

CONAGUA, especially Ing. José Luis Acosta, Ing. Iván Gamboa and Ing. Sergio Peña, are acknowledged for access to borehole and climate data. CAPA, especially Ing. Angel Huape and Ing. Dionné Rivas, are acknowledged for access to water supply wells and chemical data sets. I thank well operators, private ranch owners, subdelegados, commisariados ejidal, and private well owners for granting us access to sample water, measure water levels and log in wells. CONANP staff is acknowledged for reading surface water gauges inside Sian Ka'an.

I thank Sinh Hy Nguyen and Jens Schaarup Sørensen for lab analyses of water samples, and Centre for Ice and Climate, Niels Bohr Institute, University of Copenhagen, for oxygen isotope analyses. I appreciate the help with figures and printing of the thesis from Lisbet Brusendorff and Torben Dolin.

Funding from WWF Verdensnaturfonden/Aase & Ejnar Danielsens Fond 2006 and 2007, the COWIfoundation, Amigos de Sian Ka'an, the Austrian Science Fund (project L524-N10 'XPLORE'), The Nature Conservancy, UNESCO, Geological Survey of Austria, ETH Zürich, Otto Mønsted's foundation and the NASA Cooperative Agreement No. NNX08BA43A (WaterSCAPES: Science of Coupled Aquatic Processes in Ecosystems from Space) is gratefully acknowledged.

My family, both in Denmark, USA, Mexico, Botswana, Malawi and Israel, has been wonderful. A special thank you to my parents, Inger and Ouri, for your constant support, encouragement and love. Thanks to my colleagues at DTU and to my friends for fun times and good chats.

Most especially, a huge and warm thank you to my husband, Tiyezge. You turn difficult days in to fun ones, and make happy days even happier. Also thanks to our li'l "+" for kicks of encouragement.

Abstract

Sian Ka'an is a nature reserve of international importance, located on one of the world's largest and most spectacular karst aquifers – the Yucatan Peninsula in Mexico. The vast wetlands in Sian Ka'an are fed by groundwater from the aquifer through both submerged caves and diffuse flow from the rock matrix. Groundwater-dependent ecosystems (GDEs) are increasingly the focus of environmental protection efforts worldwide. GDEs in karst, such as Sian Ka'an, are particularly sensitive and susceptible to pollution, because of fast water flow and pollution transport in karst. Stress on the quality and quantity of groundwater resources is increasing on the Yucatan Peninsula, making Sian Ka'an's wetlands vulnerable. Ensuring water for both the wetlands and human use has attracted regional and international attention. The Sian Ka'an wetlands and their catchment serve as the case study of this PhD study. With the ultimate aim of improving the management of the groundwater resources feeding the wetlands the following objectives were outlined:

1. To physically characterize the data-scarce groundwater catchment area of the Sian Ka'an wetlands
2. To develop conceptual hydrogeological models for the study area, based on the collected data
3. To develop numerical hydrological models of the groundwater catchment. The models should produce results relevant for groundwater and ecosystem management in the region

A multi-disciplinary approach working on scales from local to regional was applied to address the objectives. The approach is applicable to other catchment-scale studies of data-scarce karst regions.

The dynamics of Sian Ka'an's surface water wetlands were investigated using the backscattered amplitude of remotely sensed synthetic aperture radar (SAR) data, and interferometric processing of the SAR data (InSAR). Wetland extent ranged from 1067 km^2 in the dry season to 2588 km^2 at the end of the wet season. The flooding extent variations correlated with a 3-month backward moving average of the catchment precipitation. This highlighted the connection of the

wetlands to a much larger groundwater catchment. InSAR was used for determination of surface water flow directions and surface water divides in the extensive and complex wetlands. The usefulness of SAR and InSAR techniques for multi-purpose hydrodynamic investigations of vast data-scarce wetlands was documented.

Recharge was estimated to be ~17% of mean annual precipitation in the conjectural groundwater catchment, using remotely sensed thermal infrared imagery and vegetation indices. Aquifer salinity stratification was investigated using the time-domain electromagnetic method. The regional freshwater lens was found to be well described at the regional scale using the Dupuit-Ghyben-Herzberg principle. Inland the freshwater lens was up to 100 m thick.

On a local scale karstic caves were mapped using airborne electromagnetic (EM) measurements, and verified using cave maps produced by scuba divers. For the regional-scale, potential high-permeability zones were outlined using visual inspection of optical and near-infrared satellite imagery. In one case, exploration of the outlined structures with airborne EM confirmed a higher electrical conductivity within the structure compared to outside it. The structure is therefore likely a zone of higher permeability. The nature of the remaining structures could not be characterized using airborne EM, because of a shallow, highly conductive geological layer preventing deep penetration of the EM signals. Using airborne and borehole EM this layer, 200–800 mS/m and 3–8 m thick, was found to be present relatively close to the ground surface within the hilly inland areas, but apparently absent in surface-near sediments of the flat areas nearer to the coast. The high-conductive layer may locally be responsible for perched aquifers, seasonally inundated areas and ephemeral surface water runoff.

The nature of the regional structures was further investigated using inverse hydrological modelling. Hydrological models based on seven different conceptual models were developed and automatically calibrated. Models showed that model fit improved when structures were assigned a different hydraulic conductivity (K) than the bulk matrix. $K_{structures}$ was calibrated to be 1–2 orders of magnitude larger than K_{matrix}. However, a model with a lower coastal resistance assigned to the coastline north of Sian Ka'an than to the remaining coastline, and with little difference between K_{matrix} and $K_{structures}$, gave an equally good fit to data, and could also be plausible.

Monte Carlo simulations based on the different plausible conceptual models illustrated the effect of model structure error on management decisions and gave first-order estimates of travel time zone distributions. The modelling highlighted that future research efforts should focus on determining the nature of the regional inland structures and on quantifying groundwater travel times within matrix and caves. The results of the case study are useful for land use zonation within the catchment of Sian Ka'an to protect groundwater resources. Restriction of polluting activities above highly permeable zones and critical recharge areas may be valuable tools in management. Vulnerability mapping, based on the results of this research, could provide a further way forward to ensure groundwater of good quality for both human beings and ecosystems in the region.

Sammenfatning

Sian Ka'an er et naturreservat af enestående international betydning, beliggende på en af verdens største og mest spektakulære karst-akviferer – Yucatan-halvøen i Mexico. Grundvand fra akviferen tilfører vand til Sian Ka'an's vidstrakte vådområder via både vandfyldte underjordiske huler og diffus tilstrømning fra akviferens bjergartsmatrix. Grundvandsafhængige økosystemer (GDE'er) er i stigende grad fokus for miljøbeskyttelsesindsatser verden over. GDE'er i karst, som f.eks. Sian Ka'an, er særligt følsomme og påvirkelige overfor forurening, fordi vand og forureninger transporteres hurtigt igennem karst-geologi. På Yucatan-halvøen er grundvandskvaliteten og -kvantiteten i stigende grad udsat for belastninger, hvilket gør Sian Ka'ans vådområder sårbare. At sikre vand både til vådområderne og til forbrug har fået regional og international bevågenhed. Sian Ka'ans vådområder og deres opland er valgt som case i nærværende PhD-studium. De følgende formål blev opstillet, med det ultimative mål for øje at forbedre forvaltningen af de grundvandsressourcer, der tilfører vand til vådområderne:

1. Fysisk at karakterisere Sian Ka'ans vådområders data-fattige grundvandsopland
2. At udvikle konceptuelle hydrogeologiske modeller for området, baseret på de indsamlede data
3. At udvikle numeriske hydrologiske modeller af grundvandsoplandet. Modellerne skal producere resultater, der er relevante for grundvands- og økosystemforvaltning i regionen

En multi-disciplinær tilgang, arbejdende på lokale til regionale skalaer, blev brugt til at adressere formålene. Denne tilgang er relevant også for andre studier på oplandsskala af data-fattige karst-regioner.

Dynamikken i Sian Ka'ans vådområder blev undersøgt vha. backscattered amplitude af satellit-bårne synthetic aperture radar (SAR) data samt interferometrisk processering af SAR-data (InSAR). Udstrækningen af vådområderne varierede fra 1067 km^2 i den tørre sæson til 2588 km^2 i slutningen af regnsæsonen. Variationerne i oversvømmelsernes udbredelse var korrelerede

med et 3-måneders bagud-rettet glidende gennemsnit af nedbøren i oplandet. Dette fremhævede forbindelsen mellem vådområderne, og et meget større grundvandsopland. InSAR blev brugt til at bestemme flow-retninger for overfladevand samt overfladevandsskel i de udstrakte og komplekse vådområder. Således blev nytteværdien af SAR- og InSAR-teknikker til hydrodynamiske undersøgelser af vidstrakte og data-fattige vådområder demonstreret.

Grundvandsdannelse blev estimeret til at være ~17% af gennemsnitlig årlig nedbør i det midlertidige grundvandsopland, ved brug af termisk infrarøde data fra satellit-bårne sensorer, samt vegetations-index fra samme. Salinitetslagdeling i akviferen blev undersøgt ved brug af den transiente elektromagnetiske geofysiske metode. Den regionale ferskvandslinse blev fundet godt beskrevet ved brug af Dupuit-Ghyben-Herzberg-princippet. Inde i landet var ferskvandslinsen op til 100 m tyk.

På lokal skala blev karst-hulerne kortlagt ved brug af luftbårne elektromagnetiske (EM) målinger, og blev verificeret ved brug af kort over huler produceret af dykkere. På regional skala blev potentielle høj-permeable zoner afgrænset via visuel inspektion af optiske og nær-infrarøde satellitbilleder. I et tilfælde bekræftede luftbårne EM-målinger, at der var en højere elektrisk ledningsevne over en af de afgrænsede strukturer, sammenlignet med udenfor strukturen. Strukturen er derfor sandsynligvis en zone med højere permeabilitet. De resterende strukturers karakter kunne ikke bestemmes vha. luftbåren EM, idet et overfladenært, højt-ledende geologisk lag forhindrede dybere indtrængning af EM-signalerne. Ved brug af luftbåren og borehuls-EM blev dette lag, 200–800 mS/m og 3–8 m tykt, fundet til stede i de bakkede områder inde i landet, relativt tæt på jordens overflade, men var tilsyneladende ikke til stede i overfladenære sedimenter i de kystnære flade områder. Det højt-ledende lag kan lokalt være årsagen til hængende grundvandsspejl, sæsonbetingede oversvømmede områder og efemeral afstrømning.

De regionale strukturers karakter blev yderligere undersøgt ved brug af invers hydrologisk modellering. Hydrologiske modeller baseret på syv forskellige konceptuelle modeller blev udviklet og automatisk kalibreret. Modellerne viste at model-fittet blev forbedret, når strukturerne blev tildelt en anden hydraulisk ledningsevne (K) end bulk matrix. $K_{strukturer}$ blev kalibreret til at være 1–2 størrelsesordner over K_{matrix}. En model med en lavere modstand mod outflow ved kysten nord for Sian Ka'an end langs resten af kysten, og med begrænset forskel mellem K_{matrix} og $K_{strukturer}$ kunne dog give et lige så godt fit til data, og var derfor også sandsynlig.

Monte Carlo-simuleringer baseret på de forskellige sandsynlige konceptuelle modeller illustrerede indflydelsen af strukturelle fejl i modellerne på forvaltningsbeslutninger, og gav førsteordensestimater for udbredelsen af zoner med forskellige grundvandstransporttider til Sian Ka'an. Modelleringen fremhævede, at en fremtidig forskningsindsats bør fokusere på at fastslå karakteren af de regionale strukturer inde i landet, og på at kvantificere grundvandstransporttider i matrix og huler. Resultaterne af case-studiet er anvendelige i forbindelse med zonering af land i Sian Ka'ans opland for at beskytte grundvandsressourcerne. Indskrænkning af forurenende aktiviteter oven over høj-permeable zoner og kritiske grundvandsdannende områder kan være vigtige forvaltningsmæssige værktøjer. Sårbarhedskortlægning, baseret på resultaterne af nærværende forskning, kan være en yderligere vej fremad for at sikre grundvand af god kvalitet for både mennesker og økosystemer i regionen.

Table of contents

1 Introduction

1.1 Background and motivation

Groundwater and surface water can be viewed as one continuous water resource, given the high degree of interaction most often observed between these two categories of water. Groundwater consequently provides water for many wetlands, which commonly have a rich biodiversity and a high productivity. Worldwide, protection of groundwater-dependent ecosystems (GDEs) is receiving increasing focus, in recognition of their global and regional value (Eamus and Froend, 2006; Münch and Conrad, 2007; Krause et al., 2007; Rodríguez-Rodríguez et al., 2008). The need to ensure water both for human use and for ecosystems is becoming a priority within water management (e.g. Young et al., 2000; Acreman and Dunbar, 2004; Powell et al., 2008; Hinsby et al., 2008).

GDEs in karst are highly vulnerable. Karst aquifers are characterized by caves, sinkholes and other geological heterogeneities created by dissolution of the parent carbonate or evaporitic rock. Worldwide an estimated 20–25% of the population largely depends on groundwater from karst aquifers (Ford and Williams, 2007). However, karst water resources are highly susceptible and sensitive to pollution. Groundwater and contaminants are transported fast through these aquifers, and little filtration or retention of contaminants takes place in karst. Caves account for the majority of karst groundwater flow. In a section of the aquifer in the Caribbean Yucatan 99.7% of all groundwater flow was found to take place in caves (Worthington et al., 2000). Knowledge about the location and properties of submerged caves is therefore essential to understand groundwater flow in karst. However, it is a challenge to obtain data on the location and properties of the underground caves, particularly at the catchment scale on which many water management initiatives must be carried out.

Karst wetlands exist in many regions of the world, including Australia, Bulgaria, Ireland, Mexico, Slovenia and USA. The catchment of the Sian Ka'an Biosphere Reserve on the Yucatan Peninsula in Mexico provides an excellent case for studying the regional scale water management problematic of protecting GDEs in karst. Fed by one of the world's largest karst aquifers, the wetlands of Sian Ka'an take up approximately ⅓ of the total 5280 km^2 area of the Reserve. They consist of a mosaic of freshwater sloughs, channels, floodplains, marshes and brackish tidally influenced areas (Fig. 1). Inflow of groundwater takes place through both underground cave systems and rock matrix, and is not directly observable. Sian Ka'an is one of Mexico's largest protected areas and is regionally and internationally valued. It hosts a rich biodiversity with both endemic and endangered species (Pozo de la Tijera and Escobedo Cabrera, 1999; Lopez-Ornat and Ramo, 1992). Besides the wetlands, tropical forests and part of the world's second largest coral reef system also constitute important ecosystem types within Sian Ka'an. Through the Ramsar Convention Sian Ka'an has been recognized as a 'Wetland of International Importance', and the Reserve has been designated a World Heritage site by UNESCO (www.ramsar.org; http://whc.unesco.org/en/list).

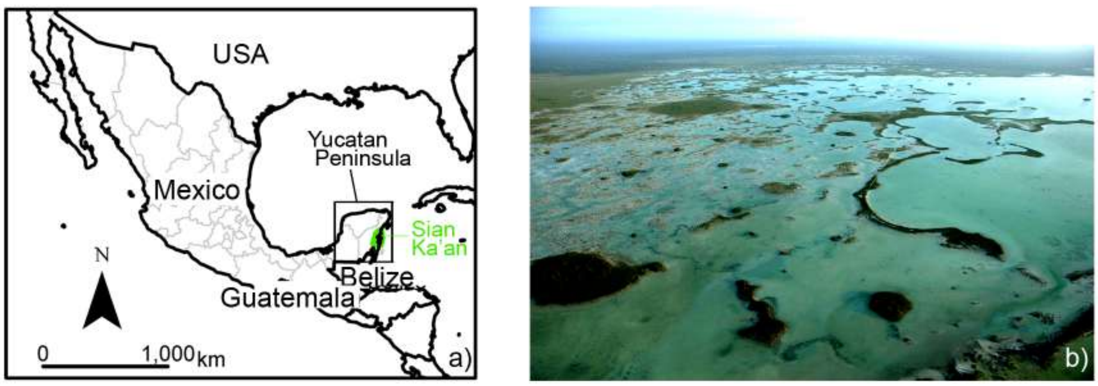

Fig. 1. a) Location of the Yucatan Peninsula and Sian Ka'an. In Fig. 10 an enlarged map of the Peninsula may be found. b) A brackish-water lagoon in Sian Ka'an with the vast vegetated wetlands stretching out behind it. Photo: Robert Supper.

Throughout the Peninsula, groundwater demands and groundwater pollution problems are growing. In northwestern Yucatan Peninsula and along the eastern coast, significant and rapid increases in population and water demands are taking place, partly due to an increasing tourism industry in the east (Escolero et al., 2000; Fideicomiso, 2006) (Fig. 2). Groundwater pollution in Yucatan State has been documented by Marin et al. (2000) and Pacheco et al. (2001). Wastewater on the Peninsula is often not treated, and is typically disposed into the Peninsular aquifer, e.g. through infiltration from septic tanks and direct injection into the saturated zone (ASK, 2003; Marin et al., 2000; Krekeler et al., 2007; Beddows, 2002; Beddows et al., 2007) (Fig. 3). Furthermore, agricultural activities are intensifying in the state of Quintana Roo (Mazzotti et al., 2005), potentially increasing the risk of groundwater contamination from agrichemicals. An illustration of the profound impact groundwater pollution may have in the region is seen in Merida, Yucatan State, where the upper 15 m of the 60 m thick freshwater lens have been rendered unfit for human consumption (Marin et al., 2000).

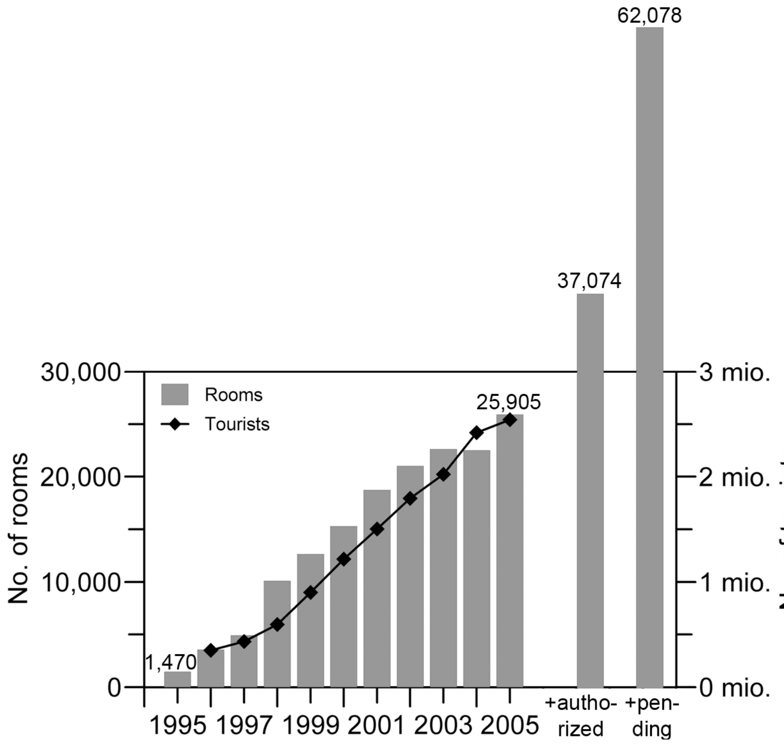

Fig. 2. Increase in number of hotel rooms and number of tourists from 1995 to 2005 in the Riviera Maya. Number of hotel rooms authorized, but not built, as well as number of rooms pending permission in 2003 is added to the last two columns. Sources: Fideicomiso (2006) and SEDUMA (2003).

Since 2003, regional stakeholders including non-governmental organizations (NGOs), research institutions, and governmental authorities for environment and water management have joined together in workshops and symposia to bring attention to and discuss how water management in the region can be improved (ASK, 2003; Holliday et al., 2007; Bautista et al., 2009). A basic prerequisite identified is the lack of knowledge on the area's hydrogeology and groundwater flow patterns (ASK, 2003). Previous research on the Peninsula hydrogeology has primarily concentrated on the Yucatan State (Back and Hanshaw, 1970; Lesser, 1976; Hanshaw and Back, 1980; Back and Lesser, 1981; Marin, 1990; Stoessell et al., 1993; Stoessell, 1995; Marin et al., 2000; 2004; Steinich and Marin, 1996;

1997; Perry et al., 1989; 1995; Escolero et al., 2000; 2002; Gonzalez-Herrera et al., 2002), whereas the eastern coast has received less attention. Primarily the regions north of Sian Ka'an have previously been studied (Back et al., 1986; Moore et al., 1992; Thomas, 1999; Beddows, 2003; 2004; Beddows et al. 2007; Stoessell et al., 1989; 2002). Perry et al. (2002; 2009) studied the Peninsula-wide hydrogeochemistry, but with relatively moderate contributions from the area west and south of Sian Ka'an. Thus, the need for scientific data to enable protection of the groundwater resources in the catchment of Sian Ka'an is clear (Merediz Alonso, 2007).

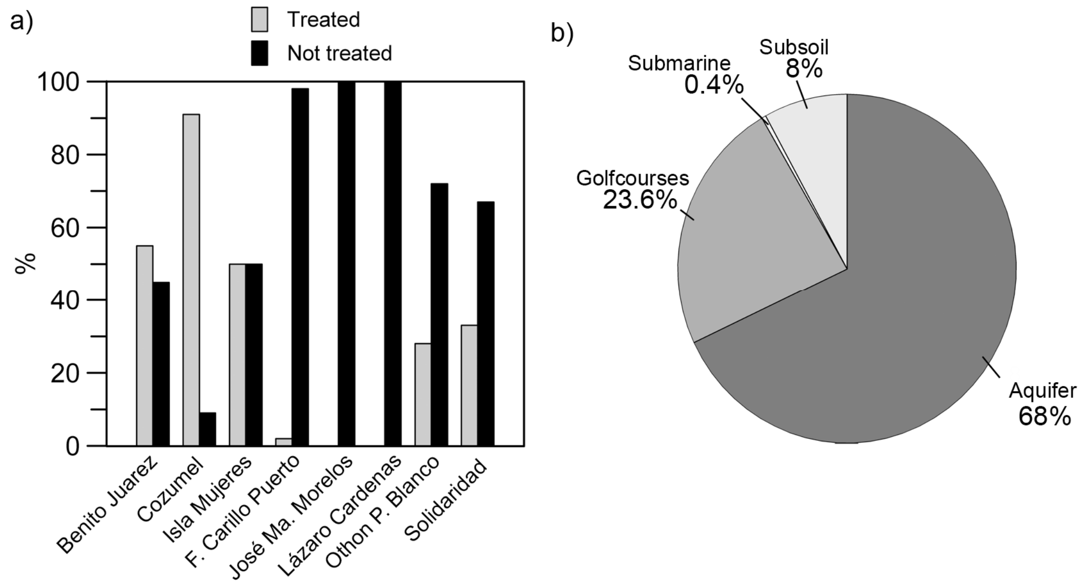

Fig. 3. a) Percentage of treated and untreated wastewater in the municipalities within the state of Quintana Roo. The municipalities Benito Juarez, Cozumel and Isla Mujeres lie outside the study area defined in Chapter 3. b) Recipient bodies of treated and untreated wastewater in Quintana Roo. In the municipalities of the study area 100% is lead into the aquifer. Source: Data from CONAGUA, distributed in ASK (2003).

1.2 Objectives and outline

To study the regional-scale hydrology of the study area, the following objectives were defined:

1. To physically characterize the conjectural groundwater catchment area of Sian Ka'an using data collected through field work and by remote sensors, on a local to regional scale – i.e. from individual cave systems, over the

whole wetland areas to the tentative groundwater catchment (Paper I, II, III, IV)

2. On the basis of the collected data to develop conceptual hydrogeological models for the study area (Paper IV, V)
3. To develop numerical hydrological models to describe the physical system with the aim of producing results relevant for groundwater and ecosystem management in the region (Paper V)

This thesis is based on the results from the five papers. First, a chapter is given on three main methodologies used in the research – synthetic aperture radar techniques, electromagnetic geophysics and numerical hydrological modelling. Subsequently an overall chapter on the study area follows. Main results from using each of the three main methodologies are then presented. The section on numerical hydrological modelling takes its point of departure in the findings from the previous sections. It utilizes the results from the site characterization in the model definition, calibration and validation. Thus, the hydrological modelling section, and Paper V, ties together the findings of the previous chapters, and elaborates upon them. In conclusion, perspectives for groundwater management are discussed based on the findings of the research, and possible future research directions are outlined.

2 Methodologies

2.1 Radar remote sensing for wetland hydrological monitoring

Remotely sensed data is increasingly being used to analyze the hydrology of the world's water bodies, including wetlands. Techniques yield direct or indirect information about water bodies and the hydrologic cycle. They utilize the visible, thermal or microwave bands of the electromagnetic spectrum, or gravity changes registered by remote sensors (Alsdorf et al., 2007a; Tang et al. 2009). Radars are active sensors that operate in the microwave spectrum (wavelengths (λ) = 0.1–100 cm). Their hydrological applications include measurement of rainfall (e.g. Grecu and Olson, 2006), soil moisture (e.g. Zribi et al., 2009), absolute water levels in rivers and lakes via radar altimetry (e.g. Berry et al., 2005), detection of flooded/non-flooded areas, and measurement of relative water level changes in wetlands via interferometry. The last two applications are described further in this section.

2.1.1 Synthetic Aperture Radar basics

As all electromagnetic radiation, the propagation of a radar pulse in the x-direction with time, t, can be described with the following expression, describing a planar harmonic wave in a plane perpendicular to the x-direction (e.g. Telford et al., 1990):

$$\psi(x,t) = A \cdot \cos\big(\kappa(x - V \cdot t)\big) = A \cdot \cos(\frac{2\pi}{\lambda} x - 2\pi \cdot ft) \tag{1}$$

where A is the amplitude [same dimensions as ψ, e.g. V/m for electric field strength or Tesla for magnetic induction], $\kappa/2\pi$ is the wave number i.e. number of wavelengths pr. unit length [1/m], V is the speed by which the wave travels (=speed of light for electromagnetic radiation) [m/s] and equals $V = f \cdot \lambda$, f is the frequency [1/s] and λ is the wavelength [m]. The term in the bracket of Eq.1 is known as the phase (φ), and describes the variation in angle of the wave with time and distance. The oscillations of the wave may be horizontally (H), vertically (V) (Fig. 4a) or circularly polarized. In radar detection, an antenna alternately transmits and receives electromagnetic pulses, thus imaging the target, in many cases while the sensor is moving. For a moving sensor, an object on the ground remains within the radar footprint at several consecutive data acquisitions, because the footprints of the different acquisition times overlap. Therefore, the same object will be imaged several times, albeit at different angles at different times. Because the sensor is moving while the waves are returned to it from objects on the ground, a shift in frequency will occur, known as the Doppler effect. Objects approaching the sensor will, from the sensors point of view, reflect a higher frequency than that sent out by the sensor, and objects receding from the sensor will reflect waves with a lower frequency than that sent out by the sensor. Synthetic Aperture Radar (SAR) is a signal processing technique that utilizes the knowledge on the Doppler frequency shift to improve imaging resolution in the direction of flight. Details on the SAR processing technique is given in e.g. Hanssen (2001). SAR processing enables the use of short antennas while obtaining high resolution in the flight direction in the order of tens of meters (Bürgmann et al., 2000). That is a practical advantage. In contrast, for real aperture radars, resolution in flight direction can only be improved by using longer antennas.

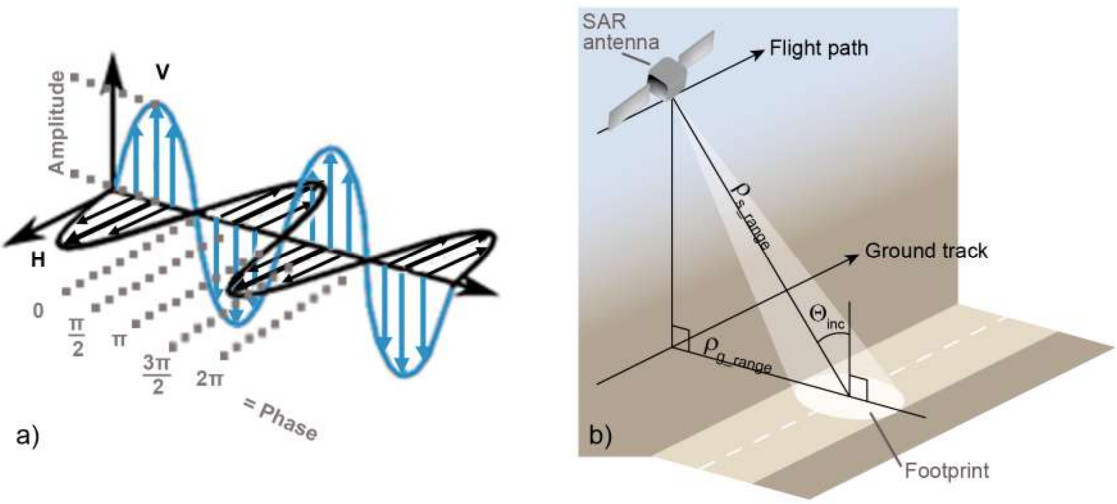

Fig. 4. a) V polarized and H polarized wave, shown in the same figure, with indications of amplitude and phase. b) Some definitions used within SAR.

SAR sensors measure the strength of the signal returned from the imaged object (amplitude, measured in decibels, dB) and the time it takes from a pulse is emitted till it is returned to the sensor (via the phase, measured in radians). Thereby, the distance from sensor to object in the sensor view direction, known as the slant range, ρ_{s_range}, can be determined, using the following general formula (Fig. 4b):

$$\rho_{s\_range} = \frac{time\_delay \cdot c}{2} = \frac{\lambda \cdot (no.\_of\_full\_waves + phase)}{2} \quad (2)$$

where c is the velocity of light (= 299,792,458 m/s).

2.1.2 Utilizing radar backscatter for flooding extent mapping

As the radar pulse encounters other media, the wave is scattered by reflection or refraction. Through scattering some of the emitted radiation is returned to the sensor. Because scattering is determined by the dielectric constant of the surface, its roughness and its local slope, the amplitude of the signal which is backscattered to the sensor can be used to map surface properties (Ulaby et al., 1982; Topp et al., 1980, Dalton et al., 1984). Two overall types of scattering exist: surface scattering and volume scattering. The latter consist of the cumulative effect of different point scatterers. Specular scattering and double-bounce scattering (two times specular reflection) (Fig. 5) are special cases of surface scattering, and only take place when the surface is smooth compared to the wavelength of the pulse (criteria for evaluating smoothness are given in e.g. Ulaby et al., 1982). Radar imaging is independent of cloud cover because radar wavelengths are much larger than the size of the cloud droplets. Scattering by clouds is therefore minimal. Over wetlands, the radar pulses interact with the vegetation canopies, trunks/stalks and the water surface (Fig. 5). The amplitude of the signal returned to the sensor depends, among other factors, on the degree of inundation, vegetation type, canopy closure, and leaf on/leaf of condition of the vegetation (Lu and Kwoun, 2008; Borgeau-Chavez et al., 2005). Therefore the backscattered amplitude may be used to discriminate between flooded and non-flooded conditions, as well as to map vegetation and wetland types (Henderson and Lewis, 2008 and references herein). For SAR wetland imaging, typically L-band (15–30 cm), C-band (3.75–7.5 cm) and X-band (2.5–3.75 cm) wavelengths are used. Due to their different penetration capabilities, L-band radar is used to investigate flooded forests, whereas C-band radar is used to investigate herbaceous wetlands (Kasischke et al., 1997, and references herein).

SAR backscatter amplitude has been used to map flooded and non-flooded areas for more than twenty years (Hess et al., 1990). Greater classification accuracies have been found when using SAR to map flooded/non-flooded areas rather than more differentiated wetland vegetation and landcover types (Henderson and

Lewis, 2008). Over the years numerous studies have investigated the effect on flood mapping of using different wavelengths, incidence angles and polarizations (e.g. Hess et al., 1995; Kasischke et al., 1997 and references herein; Pope et al., 2001; Lang and Kasischke, 2008), the effect of using different processing algorithms (e.g. Oberstadler et al., 1997; Solbø et al., 2003; Shen et al., 2008) or the fusing of results obtained using different algorithms (Schumann et al., 2009). Most studies have focused on few instances in time, whereas investigations of multi-temporal flooding dynamics using SAR data are presently relatively limited (Henderson and Lewis, 2008; Martinez and Le Toan, 2007; Lang et al., 2008; Sass and Creed, 2008). The study of flooding dynamics in Sian Ka'an (Gondwe et al., I) is therefore one of few multi-temporal SAR flooding studies (see Chapter 4.1).

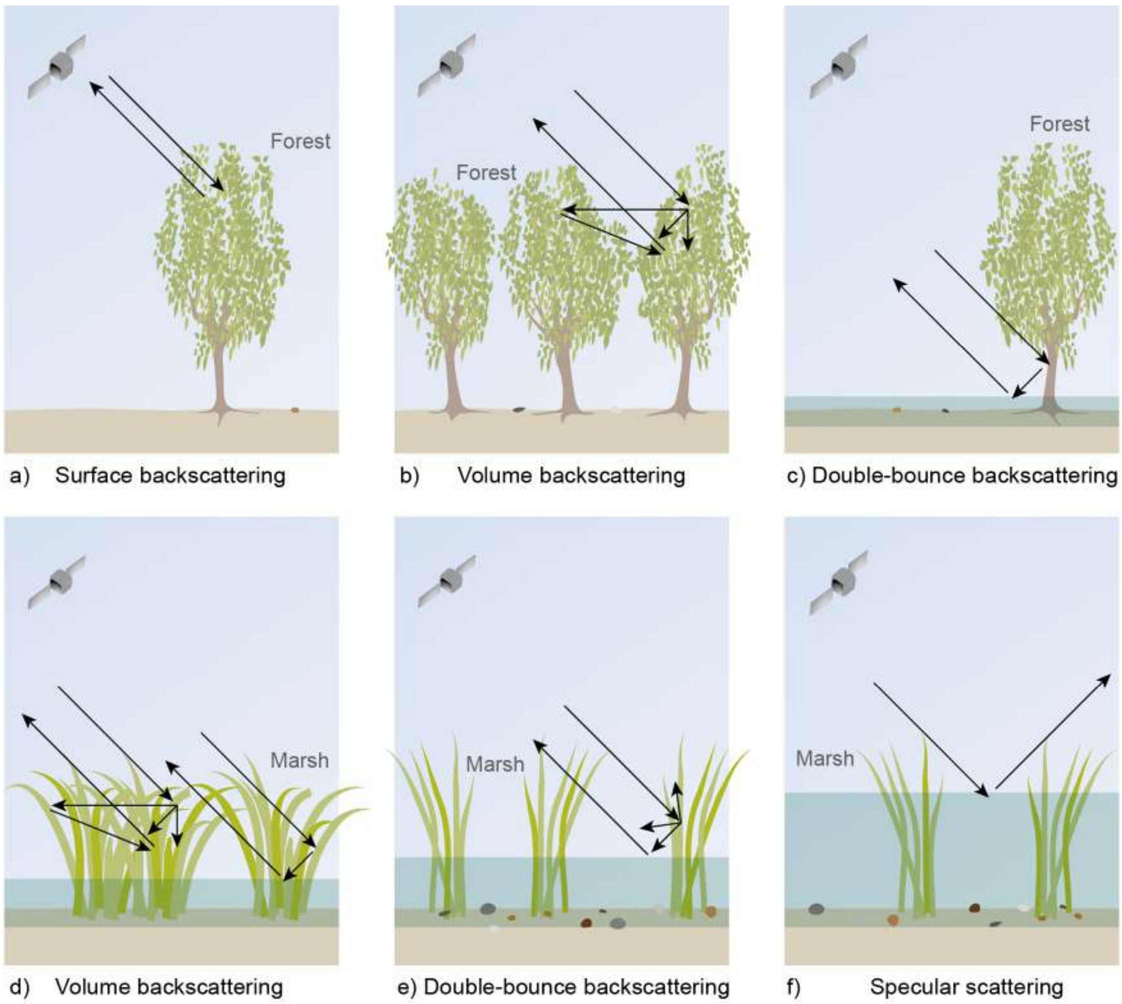

Fig. 5. Radar scattering mechanisms in different types of environments.

2.1.3 Utilizing InSAR for wetland hydrology

The measured distance from the sensor to an object is used in SAR interferometry (InSAR), through measurement of the phase of the returned signal. InSAR for derivation of glacial motion, topographic relief and topographic deformation is well established (e.g. Goldstein et al., 1993; Massonet et al., 1993; Amelung et al., 1999). In contrast, InSAR in wetlands is an emerging discipline. Primarily, wetland InSAR has been used to derive absolute water level changes. Wetland InSAR relies on double-bounce backscattering, and therefore is only useful in cases where double-bounce scattering dominates over surface- and volume scattering.

Interferometry uses measurement of the distance to an object from two (or more) different sensors at the same time or from one sensor located at approximately the same location at different instances in time (two-pass InSAR). The two (or more) images acquired are co-registered so they correspond exactly to each other, and the phases of the images (φ_1 and φ_2) are subtracted from on another, forming the so-called interferograms. An expression for the interferometric phase (ϕ_{int}) is found by first looking at the dependence of the phase on the distance travelled by the wave to the target and back again. This is expressed by $\varphi=-2\pi x/\lambda$, i.e. the distance-dependent term of the phase in Eq. 1, with a negative sign by convention (Rosen et al., 2000). The distance travelled by the wave can be expressed in terms of slant range as $x = 2\cdot\rho_{s\_range}$. An expression for the interferometric phase (ϕ_{int}) is then found by subtracting the two phases obtained at two different times (Rosen et al., 2000):

$$\phi_{\text{int}} = \varphi_1 - \varphi_2 = \frac{4\pi}{\lambda}(\rho_{s\_range,2} - \rho_{s\_range,1}) \tag{3}$$

This expression is valid for a system where each antenna alternately transmits and receives its own echoes, as in the case of two-pass InSAR. A different expression is valid for the interferometric phase obtained when one antenna transmits and two antennas receive the echoes (see Rosen et al., 2000).

The phase difference (or interferometric phase, ϕ_{int}) of a two-pass interferogram is influenced by topography, surface displacement, atmospheric effects and noise (e.g. Lu et al., 2009; Rosen et al., 2000; Massonnet and Feigl, 1998):

$$\phi_{int} = \phi_{topography} + \phi_{displacement} + \phi_{atmosphere} + \phi_{noise} \tag{4}$$

In order to obtain the surface displacement, the effect of topography is removed using a known digital elevation model. The effect of the approximately ellipsoidal shape of the Earth is also removed, along with the effect of the slightly different position of the sensor at the different acquisition times. Phase noise may occur if the dielectric properties of the surface changes significantly between the two acquisition times. Phase noise is evaluated via the term coherence. It is the cross-correlation of images estimated within windows of a few pixels' size. Large changes in surface properties may cause decorrelation, and then differential InSAR cannot be used. The Earth's atmosphere is also an important source of phase error. In the latitudes of Sian Ka'an, presence of large amounts of water vapor (clouds) can cause delays in the radar pulse propagation, resulting in errors in the estimated distances. Mitigation of atmospheric delay errors may be carried out by using dense GPS networks (e.g. Hanssen, 2001) or high-resolution weather models (Massonnet and Feigl, 1998, Lu and Kwoun, 2008) to estimate the delay. At present the latter is rarely carried out in practice (Foster et al., 2006).

Once the other effects have been removed from the interferometric phase, the surface displacement can be evaluated. A change in surface location between the two acquisition times will appear as phase changes in interferograms. One cycle of phase change (0–2π) is called a 'fringe'. The fringes in the interferogram may then be converted from these cycles of 0–2π to continuous changes in phase; a process which is called 'unwrapping' (Fig. 6) (e.g. Goldstein et al., 1988; Ghiglia and Pritt, 1998; Chen and Zebker, 2001). Unwrapping is the process of adding an integer multiple of 2π to the fringes, because the actual change in distance measured by the sensor via the phase is in fact equal to an unknown integer number (the ambiguity) plus the phase difference. Filtering of the interferograms is often carried out before unwrapping, but was minimized in the Sian Ka'an interferogram processing, because it was found that important small-scale fringes, characteristic for these wetlands, were smoothed out by this process.

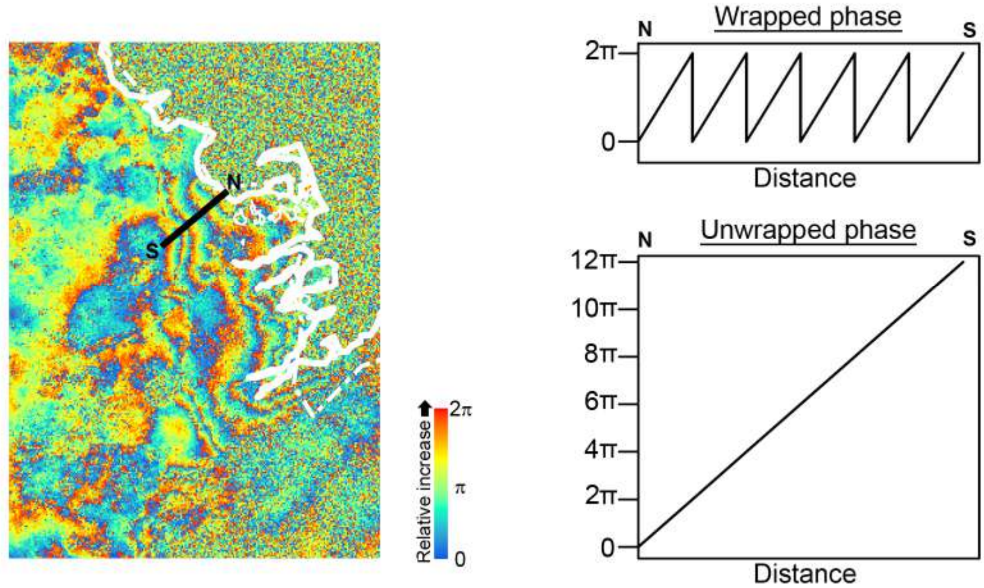

Fig. 6. Detail of interferogram over Sian Ka'an, showing principle of unwrapping.

If no other surface deformation (e.g. tectonic deformation) has taken place between acquisitions, and if only vertical movement between acquisition times is assumed, the phase change (ϕ_{int}) of the unwrapped interferograms can be recalculated to the water level change (Δh) using Eq. 3 together with the incidence angle (θ_{inc}, in radians, see Fig. 4b for definition) and the cosine relation:

$$\Delta h = \frac{\lambda \phi_{\text{int}}}{4\pi \cos(\theta_{inc})} \tag{5}$$

For the RADARSAT-1 SAR data used in the Sian Ka'an study, one phase cycle of 0–2π corresponded to 3.6 cm (FineBeam F1 data) and 3.9 cm (FineBeam F4 data) vertical displacement.

The number of previous studies using InSAR for wetlands is limited. Alsdorf et al. (2000; 2001) first described the utility of differential InSAR for mapping water level changes in wetlands, using the Amazon floodplains as a case study. Alsdorf et al. (2001) and Wdowinski et al. (2004; 2008) established that InSAR water level measurements using L-band data have an accuracy within centimeters. Lu et al. (2005) and Kim et al. (2005) were the first to show that also C-band data can be used for wetland InSAR. Previously C-band data were believed to bounce off the vegetation canopies in wetlands and therefore not provide the double-bounce backscatter necessary for the wetland InSAR measurements. However the high coherence obtained with C-band data by Lu et al. (2005), Kim et al. (2005) and the later studies of Lu and Kwoun (2008), Kim et al. (2009) and Gondwe et al. (I) using C-band data confirmed the usefulness of C-band data for wetland InSAR. Lu et al. (2005) stated that C-band data may give higher accuracy than L-band data, due to the shorter wavelength. Accuracies using C-band data in wetland InSAR appears to be less than or equal to about 2 cm (Lu and Kwoun, 2008; Gondwe et al., I). Lu et al. (2009) and Kim et al., (2009) used radar altimetry data to convert the relative water level changes from InSAR into absolute water level changes. This is convenient for areas where gauge data are not available. It could have been a useful approach for the Sian Ka'an wetlands as well, as the installed gauges were limited in space and time; however radar altimetry of the required quality were not sufficient over Sian Ka'an to be used (Gondwe et al., I). Lu and Kwoun (2008) found that HH polarization (horizontal receive, horizontal transmit) was preferable to VV polarization for wetland InSAR, and Kim et al. (2009) found HH polarization to also be better than HV polarization. In the Sian Ka'an study, RADARSAT-1 data with HH polarization was used.

Only Alsdorf et al. (2007b) has previously used wetland InSAR to deduce hydrological information other than relative water level changes. They studied an Amazon flood plain during the passing of a flood wave, and showed that fringe directions may be used to evaluate surface water flow directions. In the Sian Ka'an study the utility of InSAR for evaluating surface water flow directions was also demonstrated, and it was found that the technique can be applied to evaluate local-scale surface water divides (Gondwe et al., I) (see Chapter 4.1).

2.2 Electromagnetic methods for exploration of karst geology

Geophysical methods measure physical properties of the geology indirectly or directly. By measuring how geophysical signals, such as electric, magnetic and electromagnetic fields, seismic waves and radioactive radiation, behave in space and time information about the properties of the subsurface can be obtained, deduced or estimated. Geophysical methods have been used throughout the second half of the 20th century for examining aquifer properties. However, in recent years there has been a new focus on the use of geophysics for hydrogeological applications (e.g. Ferré et al., 2009; Rubin and Hubbard, 2005; Auken et al., 2009; Pellerin et al., 2009). Geophysical fields or earth properties explored in geophysical surveys may occur naturally in the subsurface (i.e. be inherent or emitted passively from the ground, such as the case of natural gamma radiation, gravity fields and natural magnetic fields) or may be emitted actively from sensors, after which the earth's response to the signal is recorded. The present section describes the use of active electromagnetic induction methods for hydrogeophysical characterization, because these were the main methods used to investigate the subsurface of the study area. However, other methods reported in the literature for investigating karst geology will be briefly mentioned as well.

2.2.1 Basic concepts of electromagnetic induction methods

Electromagnetic methods can only give indirect information about hydrogeologic properties of the subsurface, specifically the electrical conductivity (σ [S/m]) or resistivity ($\rho=1/\sigma$ [Ωm]) of the subsurface media. However, petrophysical relationships may be used to estimate the hydrologic properties from the geophysical parameters. An often used petrophysical relationship is Archie's Law (Archie, 1942), which relates measured formation conductivity or resistivity to formation porosity (φ_{por}[†]) and the pore fluid's conductivity or resistivity:

$$\rho=a\,\varphi_{por}^{-m}S^{-n}\,\rho_w \tag{6}$$

where a, m and n are empirical constants ($0.5 \leq a \leq 2.5$, $1.3 \leq m \leq 2.5$ and $n \approx 2$), S is the water-filled fraction of the pore space and ρ_w is the electrical resistivity of the pore-filling fluid (e.g. Telford et al., 1990). Archie's Law is valid for sediments and sedimentary rock, where the grains are non-conductive (e.g. do not contain clays or metals). When Archie's Law is valid, the electric conductivity of

[†] Subscript *por* used to differentiate this phi from that used to denote phase in the previous section.

the formation is dominated by the electrical conductivity of the pore-filling fluid. In other types of geologies the electrical conductivity of the formation may be dominated by ionic migration at the interface between soil grains and the pore fluid (details e.g. in review by Slater, 2007). Archie's Law may be used to estimate formation porosity from measured electrical conductivity or resistivity of the bulk formation. Other petrophysical relationships exist to recalculate porosity to an estimate of permeability (*k*) using grain size diameter (e.g. Berg, 1970; Revil and Cathles, 1999). *k* may then be recalculated to hydraulic conductivity (*K*) using the definition of *K* (e.g. Batu, 1998).

Maxwell's four equations govern electromagnetic phenomena. They describe the interaction between the vector functions of an electromagnetic field, namely **E**[‡]: the electrical field strength [V·s /m], **B**: the magnetic induction [Wb/m^2 or Tesla·s or V·s^2/m^2], **H**: the magnetic field intensity [A·s /m], **D**: the dielectric displacement [C·s /(m^2)] and **J**: the electric current density [A·s/m^2]. In the frequency-domain they are written as follows:

$$\nabla \times \mathbf{E} + i\omega\mathbf{B} = 0 \tag{7}$$

$$\nabla \times \mathbf{H} - i\omega\mathbf{D} = \mathbf{J} \tag{8}$$

$$\nabla \cdot \mathbf{B} = 0 \tag{9}$$

$$\nabla \cdot \mathbf{D} = \rho_{charge} \tag{10}$$

where i is the imaginary unit $\sqrt{-1}$, ω is the angular frequency [rad/s] (= $2\pi f$, where f is the frequency [1/s]). The angular frequency has the assumed time dependence $e^{-i\omega t}$. ρ_{charge} is the electric charge density [C·s /m^3][§].

The constitutive relations describe the relation between **J** and **E, D** and **E**, **B** and **H**:

$$\mathbf{J} = \sigma\mathbf{E} \tag{11}$$

$$\mathbf{D} = \varepsilon\mathbf{E} \tag{12}$$

$$\mathbf{B} = \mu_r \cdot \mu_0\mathbf{H} \tag{13}$$

[‡] Bold characters indicate that the parameter is a vector. Upper-case letters are used to represent the fields in frequency-domain; smaller-case letters to represent the fields in time-domain.
[§] Subscript *charge* used to distinguish this parameter from the ρ that indicates electrical resistivity in this section, and to distinguish this parameter from the the ρ_{s_range} used to indicate slant range in the previous section.

where ε is the dielectric permittivity [C/(Vm)], μ_0 is the magnetic permeability of free space, $\mu_0 = 4\pi \cdot 10^{-7}$ Vs/(A·m), and μ_r is the relative magnetic permeability [dimensionless]. σ, ε, and ($\mu_r \cdot \mu_0$) are actually tensors, but σ and ε can, for applications with earth materials, be regarded as complex numbers, which are functions of the angular frequency ω. For hydrogeological applications μ_r=1 is typically a reasonable approximation and ($\mu_r \cdot \mu_0$) is assumed a real number which is independent of frequency.

When applying the constitutive relations (Eq. 11, 12 and 13), Maxwell's inhomogeneous equations in frequency-domain can be written as (Ward and Hohmann, 1988):

$$\nabla \times \mathbf{E} + i\omega\mu_0 \cdot \mathbf{H} = -\mathbf{J}_m^S \tag{14}$$

$$\nabla \times \mathbf{H} - (\sigma + i\varepsilon\omega) \cdot \mathbf{E} = \mathbf{J}_e^S \tag{15}$$

where $\mathbf{J}_m{}^S$ and $\mathbf{J}_e{}^S$ are respectively the magnetic source current and the electric source current. In the absence of sources, the source terms are reduced to zero, and Eq. 14 and 15 become Maxwell's homogeneous equations.

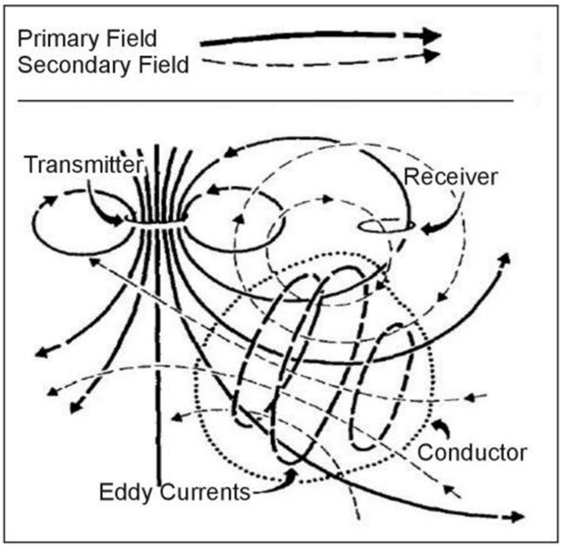

Fig. 7. Principle of EM induction methods, with generation of eddy currents in the subsurface. After Klein and Lajoie (1980), printed with permission from Northwest Mining Association.

The principle of induction is utilized in the electromagnetic methods. Ampere-Maxwell's Law (Eq. 8) explains that periodic variations in currents will generate periodically varying magnetic fields. Faraday's Law (Eq. 7) states that varying magnetic fields will generate varying electric fields, which then again (according to Ampere-Maxwell's Law) generate varying magnetic fields. In active geophysical electromagnetic methods a time-varying magnetic field is generated by either switching off an electric current in a loop abruptly (time-domain methods) or using an alternating current in a loop (frequency-domain methods). The time-varying magnetic field generated by this process induces eddy currents in the subsurface (Fig. 7). Depending on the conductivity of the earth, the eddy currents may be larger or smaller. The response from the earth is then measured by voltage induction in receiver coils within the measurement instrumentation. In time-domain methods the response of the earth is measured in the absence of the primary field generated by the instrument transmitter. The response measured at different times after current switch-off is used to obtain information about the conductivity of the subsurface at different depths (e.g. Christiansen et al., 2006). In contrast, frequency-domain methods measure the response of the subsurface while the primary field is on. In the methods considered here, a magnetic dipole source is used, generated by an electric current oscillating at a frequency *f*. Frequencies used in EM methods are radio frequencies (e.g. 0–100 MHz; the upper range however being ground penetrating radar methods); in the present study frequencies were all below 30 kHz. The secondary field induced in the subsurface is measured compared to the strength of the primary field (as a ratio, in the unit parts per million – ppm), since the secondary field is much lower than the primary field. The primary field is calculated at the location of the receiver and compensated for in order to measure the much smaller secondary field. Due to induction processes in the subsurface, a small phase shift exists between the secondary and the primary field. The secondary field is therefore a complex number, and both the inphase and quadrature ($\frac{\pi}{2}$ radians out-of-phase with the primary field) components are recorded (e.g. Siemon, 2006). The conductivity at different depths is for frequency-domain methods measured using different frequencies. The penetration depth is controlled by the resistivity of the subsurface and by the frequency, as described in the expression for skin depth (δ), which is the depth at which the amplitude of the electromagnetic wave within the subsurface has been reduced to $\frac{1}{e}$ of the amplitude of the electromagnetic wave at the surface (Kirsch, 2006):

$$\delta = \sqrt{\frac{2\rho}{\omega\mu}} \tag{16}$$

where μ is assumed equal to the free-space value μ_0 for the earth materials discussed here.

Solutions to the EM field response (Eq. 14 and 15) may be found when the current source can be described. The equations become easier to solve if Schelkunoff potentials are introduced. Schelkunoff potentials are defined so that their differentiation yields the fields **E** and **H**. The potential **A** [V·s²/m] is here defined as:

$$\mathbf{B} = \nabla \times \mathbf{A} \tag{17}$$

When an electric source type (denoted by subscript e) is assumed, the magnetic source current in Eq. 14 is assumed zero (Ward and Hohmann, 1988). Then, inserting Eq. 17, using the constitutive relationship of Eq. 13, and eliminating the curl operator on both sides of the equality sign, Eq. 14 becomes:

$$\mathbf{E}_e = -i\omega \cdot (\nabla \times \mathbf{A}) \tag{18}$$

Applying the quasi-static approximation that states that $\mu_0\varepsilon\omega^2 << \mu_0\sigma\omega$ for earth materials and frequencies less than 10 kHz (Ward and Hohmann, 1988), and inserting Eq. 18 into Eq. 15 yields:

$$\frac{1}{\mu_0}\nabla \times (\nabla \times \mathbf{A}) + i\sigma\omega \cdot \mathbf{A} = \mathbf{J}_e^S \tag{19}$$

which is the governing equation in frequency-domain for the propagation of EM fields expressed in terms of the vector potential **A**. In time-domain the solution is found by inverse Fourier transformation, yielding:

$$\frac{1}{\mu_0}\nabla \times (\nabla \times \mathbf{A}) + \sigma \cdot \frac{\partial \mathbf{A}}{\partial \mathrm{t}} = \mathbf{J}_e^S \tag{20}$$

These expressions are valid for heterogeneous as well as homogeneous subsurfaces. Likewise, expressions may be derived for magnetic source currents using the Schelkunoff potential **F**.

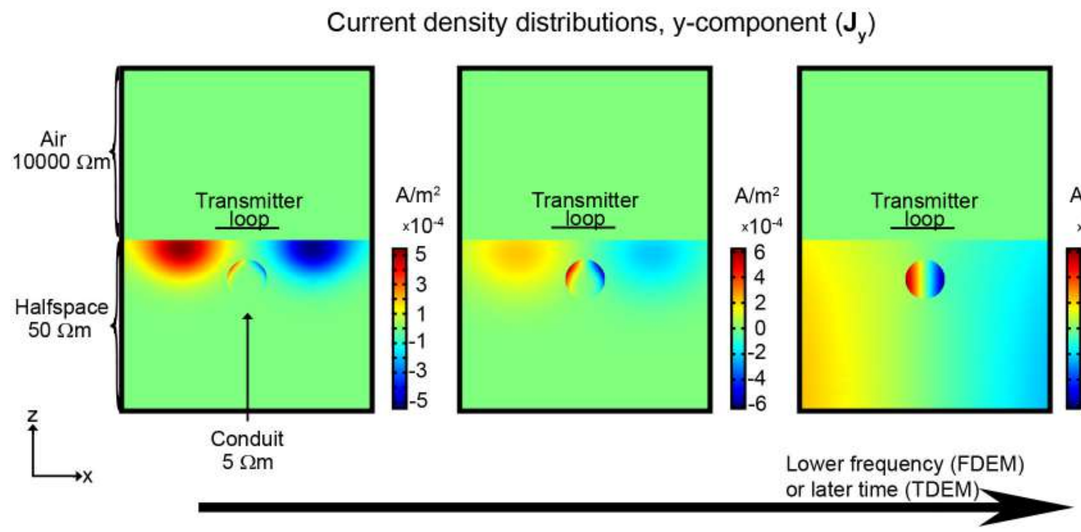

Fig. 8. Diffusion of current in halfspace with conduit, generated by simulation in COMSOL Multiphysics.

Solutions to the EM field response from the subsurface are given in Ward and Hohmann (1988) for homogeneous halfspace and layered earth (1D) configurations. Ward and Hohmann (1988) also present analytical solutions to simple geometries of anomalous 3D bodies in the ground. However, more advanced modelling of the propagation of the fields in the presence of 3D anomalous bodies requires numerical solutions. When an anomalous body exists in a layered halfspace both induction currents and galvanic currents form in the body. The latter is due to accumulation of charges at the interface between the body and the background medium. These processes are described further in West and Macnae (1991). Software exists for modelling the forward response of EM fields over a known 3D subsurface, e.g. EMIGMA (PetRos EiKon, 2003; Murray et al., 1999; Groom and Alvarez, 2002), AEM (Copyright © AKP Group 1994–1998; Pantrakov et al., 1997) and also general physical modelling software may be used to forward model EM fields in a 3D subsurface (e.g. Comsol Multiphysics; example in Bauer-Gottwein et al., 2010) (Fig. 8). Forward modelling codes are used in geophysical inversion routines, and although 1D inversion of frequency-domain EM is the most common way of interpretation (Siemon, 2006), 3D inversion methods are being developed and are the focus of recent research (for frequency-domain: e.g. Sasaki, 2001; Avdeev, 2005 and references herein; for time-domain: e.g. Newman and Commer, 2005).

Time-domain EM (TDEM) was in the present study used to map the depth to the freshwater-saltwater interface within the aquifer (Gondwe et al., IV and Chapter 3). Time-domain EM has been used for this purpose in many previous studies (e.g. Goldman et al., 1991; Kafri and Goldman, 2005; Nielsen et al., 2007). However, in the Yucatan Peninsula it had previously not been used at the regional-scale to examine the shape of the freshwater lens, as done by Gondwe et al. (IV). Christiansen et al. (2006) provide a detailed description of the technique.

Frequency-domain EM (FDEM) was in the present study used in the borehole logging carried out (Gondwe et al, IV and Chapter 3), and in the airborne EM exploration of caves and regional-scale structures described in Supper et al. (II), Gondwe et al. (III) and Chapter 4.2. Details on the technique are described in e.g. Siemon (2006) and Motschka (2001). Although the use of borehole logging as a method in this study is standard, borehole logging and airborne EM for mapping of a potential ejecta-layer (Gondwe et al., IV) had not previously been carried out at a regional scale. The successful use of the airborne frequency-domain EM technique for locating caves is unique to this study. To put the results into a context, previous work in this regard will be reviewed in detail in the following.

2.2.2 Geophysics and EM for karst cave exploration

Geophysical techniques have been applied to explore karst terrain for decades. However, detecting karst cavities (water- or air-filled) presents a particular challenge (e.g. Daniels, 1988), compared to detecting depths to karst bedrock, geological formations mapping and mapping of fault- and fracture zones with geophysical methods. Cavities in the subsurface may generate the following types of geophysical anomalies:

- Scattering of <u>seismic</u> and <u>ground-penetrating radar</u> (GPR) waves.
  For instance, acoustic velocity in water-filled cave is 1500 m/s, whereas it is 330 m/s in an air-filled cave, which is in both cases lower than what can generally be found in host rock (Daniels, 1988)
- <u>Gravity</u> anomalies, due to the lack of rock material at the cavity.
  For instance, a water-filled cave will have density 1 g/cm^3, an air-filled cave a density of ~0 g/cm^3, compared to the host rock density of e.g. 2.6 g/cm^3

- Nuclear magnetic resonance anomalies, caused by presence of a larger quantity of free (not surface-bound) water in a water-filled cave compared to in the surrounding aquifer matrix
- Conductivity or resistivity anomalies, caused by the fact that a water-filled cave will have a higher electrical conductivity (or lower electrical resistivity) than the surrounding aquifer matrix, due to absence of resistive rock material and presence of conductive fluid within the cave. There may thus be a significant resistivity contrast. In the case of an air-filled cave in e.g. limestone, the difference between the high resistivity of the host rock and the very high resistivity of the air may not be distinguishable, especially not with active EM methods

Seismics has a depth resolution which surpasses that of most other methods. Seismics has successfully been used to locate faulted and fractured zones in karst (e.g. Šumanovac and Weisser, 2001; Guérin et al., 2009). Combined with magnetic resonance soundings (MRS) Guérin et al. (2009) also succeeded in determining the exact location and width of karstic conduits from seismic data, with an accuracy of a few meters. They further used seismics and geoelectrics to determine that the limestone surrounding the caves was not homogeneous. However, the impact of a cave on the seismic signature may be highly variable, and efforts are undertaken to understand the effect of caves and voids on the seismic waves (e.g. Hackert and Parra, 2003). The scattering of the waves by the conduits is complex, and vugs[**] may cause a degree of attenuation that depends on the wave's frequency (Hackert and Parra, 2003). Seismics is therefore not always successful for locating karst caves. Water-filled conduits may be especially hard to detect using seismics (Guérin et al., 2009).

GPR has in many cases successfully located karst caves and been useful to determine also cave dimensions and geometry (Henson et al., 1997; Beres et al., 2001; Al-fares et al., 2002). Use of GPR requires absence of clayey layers atop the medium of interest, as the GPR signal cannot penetrate clays (Doolittle and Collins, 1998). GPR is mainly useful for detecting shallow (e.g. < 20 m below surface) air-filled caves (e.g. Beres et al., 2001; Al-fares et al., 2002) or caves filled with wet or dry sediments (e.g. Henson et al., 1997). In the Yucatan Peninsula GPR has also been carried out to detect caves. The results were ambiguous due to weak reflections which only sometimes correlated with known

[**] i.e. small cavities in the rock.

cave geometry. However, the study concluded that there was a potential for GPR to detect cave dimensions in Quintana Roo's geology (Schwaiger et al., 1997).

Microgravimetric measurements can often be used for reconnaissance of an area before applying other methods to characterize subsurface cavities (Ernstson and Kirsch, 2006). However, the method requires accurate determination of topographic elevations (accuracy < 1 cm), and therefore is not feasible on larger scales. Microgravimetry is often used in conjunction with other methods, which gives improved results. For instance, by using microgravimetric measurements, Beres et al. (2001) were able to accurately model a measured GPR signal above a cave. Mochales et al. (2008) used modelling of measured microgravimetric signals to determine the shape of a filled karstic depression, and determine its type of filling. A 3D model of a submerged cave system was constructed by McGrath et al. (2002) by modelling microgravimetric measurements, and constraining depth and position using geoelectric data and survey data from cave divers.

Magnetic resonance soundings (MRS) can be used to determine the volume of submerged caves, if the water quantity in the cave is sufficiently large to be detected, e.g. ≥ 6500 m^3 when using a 100x100 m^2 MRS loop (Legchenko et al., 2008). The cave must furthermore be relatively shallow, and EM noise in the surroundings must be low (Boucher et al., 2006). The lateral and vertical locations of water-filled conduits have successfully been located with MRS by e.g. Vouillamoz et al. (2003), Boucher et al. (2006) and Legchenko et al. (2008). The MRS signal may also be used to calculate transmissivities and permeabilities (Vouillamoz et al., 2003), and to determine the volume of the conduit with ±50% and ±75% error, depending on the size of the cave relative to the size of the MRS loop (Legchenko et al., 2008).

Geoelectrics (e.g. multielectrode resistivity tomography, DC-resistivity mapping etc.) has been used to locate both water-filled (e.g. Zhou et al., 2002; Supper et al., II) and air-filled caves (e.g. Nyquist et al., 2007). Several studies have found the dipole-dipole electrode array to be favorable for detecting caves (Zhou et al., 2002; Roth and Nyquist, 2003). The orientation of the survey line relative to the strike of the cave also influences whether the geoelectric method will detect the cave. The optimal orientation (parallel or perpendicular to strike) may depend on whether the cave or fracture is water- or air-filled (Roth et al., 2002; Roth and

Nyquist, 2003). The likelihood of detecting a cave therefore increases if multiple line orientations are used above the same target (Roth and Nyquist, 2003). The type of inversion used for data interpretation also affects the ability to resolve cave structures (Supper et al., II). Through inversion, geoelectrics may yield some information about cave depth and dimensions, but cannot with present techniques resolve these parameters in detail.

Ground-based EM methods may successfully detect the location of karst faults and caves, but have yielded little information about their depth and dimensions. With the passive EM Very Low Frequency (VLF) method, that utilizes signals from radio-transmitters worldwide, fractures have been delineated in karst (Bosch and Müller, 2005). Indirect mapping of the location of a cave has been carried out with VLF by mapping the boundary between a conductive and resistive rock unit, at which the conduit was located (Guérin and Benderitter, 1995). Coppo et al. (2006) successfully delineated an air-filled karstic cave with VLF, mainly because it was bounded by fractures.

With active ground-based FDEM methods Vogelsang (1987) successfully detected sediment- and water-filled karst faults and vertical karst pipes, believed to represent cross-sections above interconnected karst fissures. Robinson-Poteet (1989) used FDEM methods to successfully locate air-filled caves in limestone. Doolittle and Collins (1998) used FDEM methods to determine the depth to the karst bedrock, but could not detect cavities with the method in their survey environments. Shah et al. (2008) used FDEM methods in combination with geoelectrics to locate karst hydrostratigraphic contacts, faults zones and possible karst features. Supper et al. (II) used FDEM methods to detect the location of a known water-filled cave. No studies have been found in the literature of ground-based TDEM being used to locate karstic caves. This may be due to the low capabilities of the method for resolving the shallow parts of the geology (e.g. <15 m below surface). Also it may be due to the fact that the method samples a larger earth volume with time. The current in TDEM spreads outwards and downwards in time like a smoke-ring, always creating an angle of 30^{o} with horizontal (Christiansen et al., 2006). Therefore, if the current starts as an e.g. 40 m diameter ring near the surface, by the time it will be at 30 m depth, it will be a ring of ca. 100 m in diameter, thus sampling and averaging over a significantly larger earth volume. Common to the ground-based EM methods used for cave exploration are that they may indicate the location of a karst cave, but cannot provide unambiguous data that the anomaly actually represents a cave. Furthermore, depth and dimensions of the cave cannot be resolved with ground-based EM methods.

Airborne EM methods have been gaining increasing popularity for hydrogeophysical exploration in recent years. Airborne EM methods have the advantage that a much larger area can be explored in shorter time, compared to using ground-based EM methods. Furthermore, airborne EM exploration will be unaffected by obstacles on the ground, such as dense vegetation. Using airborne EM Doll et al. (2000) detected low resistivity anomalies in known karst areas, and other anomalies which might be related to fault and fracture zones. Gamey et al. (2001) used airborne EM to interpolate spatially between anomalies detected by ground geophysics, which coincided with lineaments. Smith et al. (2003) used airborne EM to map previously unknown and known linear features likely caused by karst structures, e.g. grabens. Smith et al. (2005a) also used airborne EM to map karst structures, revealing a structural complexity of the karst subsurface which was previously unknown. Although the literature thus shows the usefulness of airborne EM for karst structural exploration, specific and confirmed detection of caves had not been carried out with airborne EM (Smith et al., 2005b). Therefore, the correspondence of airborne EM anomalies with known caves, presented by Supper et al. (II), is a novel exploitation of the capability of airborne EM mapping. The dataset not only reveals the location of the caves, but may be used to obtain information on the depth of the caves. These results are summarized and briefly discussed in Chapter 4.2.

Magnetic anomalies may only in rare cases be used to distinguish caves and karst features (e.g. Rybakov et al., 2005), because the karst host rock is usually non-magnetic, making it impossible to distinguish the non-magnetic voids. Self-potential anomalies in karst have only in few cases been used to detect flowing water in the conduits (e.g. Zhou et al., 1999).

2.3 Hydrological modelling for karst groundwater management

Hydrological modelling is the discipline concerned with describing the land-phase processes of the hydrological cycle in a quantitative manner using coupled mathematical equations (e.g. Singh and Woolhiser, 2002) (Fig. 9). The water balance equation for the vadose zone is given by:

$$\frac{dV_{soil}}{dt} = P - ET_a - Q - R \tag{21}$$

For a 3D soil volume, V: volume of water stored in the soil zone [m^3/m^3, i.e. unitless], t: time [e.g. year], P: precipitation rate, ET_a: actual evapotranspiration rate, Q: rate of surface runoff, R: groundwater recharge rate [all e.g. 1/year]. Eq. 21 is valid under the assumption of zero lateral flows in the soil. All quantities in Eq. 21 may be a function of space and time. Models with a spatial discretization are called distributed models.

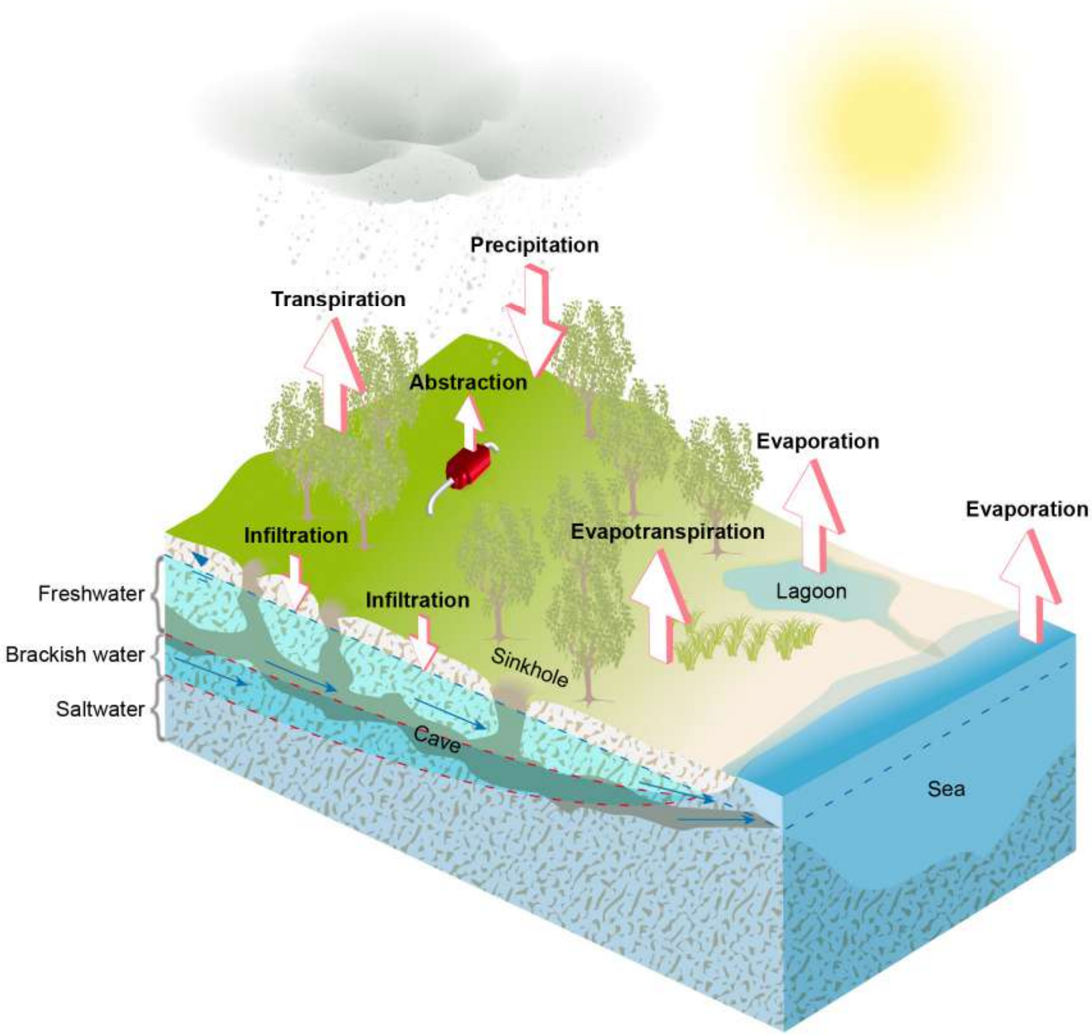

Fig. 9. Hydrological cycle.

Similarly, a water balance may be set up for the groundwater zone. This is done in the following, where also different types of distributed models for simulating karst aquifers are presented. Distributed models are now established tools used in water resources management, for instance to delineate groundwater catchments. Catchment delineation using stochastic methods will also be described in the following, along with the use of multiple conceptual models for evaluating model uncertainty.

2.3.1 Hydrological modelling of karst aquifers

Karst aquifers are triple porosity media, consisting of the rock matrix (intergranular porosity), the fractures and bedding planes and the karstic conduits (White, 1999). The majority of groundwater flow in karst takes place via the conduits, while the matrix is the major compartment for water storage (Atkinson, 1977; Worthington, 2003). For the matrix compartment, the groundwater flow can be described using Darcy's Law (e.g. Chow et al., 1988):

$$q = -K \cdot \frac{dh}{dl} \tag{22}$$

where q is the Darcy flux or specific discharge [e.g. m/s], K is the hydraulic conductivity [e.g. m/s], and dh/dl is hydraulic gradient (the change in head pr. unit length) [dimensionless]. Flow takes place in direction of negative hydraulic gradient as indicated by the negative sign.

Conservation of mass states that change in storage equals inflow minus outflow. For a 3D control volume in the groundwater matrix compartment, utilizing Eq. 22, this is for an incompressible (constant density) fluid written as:

$$S_s \frac{\partial h}{\partial t} = \frac{\partial}{\partial x}\left(K_x \frac{\partial h}{\partial x}\right) + \frac{\partial}{\partial y}\left(K_y \frac{\partial h}{\partial y}\right) + \frac{\partial}{\partial z}\left(K_z \frac{\partial h}{\partial z}\right) + W \tag{23}$$

where S_s is the specific storage [1/m], t is time [s], x, y and z are the three directions [m], and W represents sources and sinks [1/s]. S_s is only relevant for confined aquifers, since it is very small in the case of unconfined aquifers, and can then be neglected. Under steady state conditions, the term on the left hand side of Eq. 23 equals zero. Sources and sinks include groundwater recharge, which can be calculated using Eq. 21, evapotranspiration from the phreatic zone, pumping and/or injection via wells, and mass transfer to surface water bodies, if they interact with the groundwater.

Darcy's Law is applicable for laminar flow, such as that which often takes place in the rock matrix. Whether flow is laminar or turbulent can be evaluated by calculating the Reynold's number, R_e (e.g. Ford and Williams, 2007):

$$R_e = \frac{\rho_{dens} \cdot d_H \cdot v}{\mu_{vis}} \qquad (24)$$

where ρ_{dens} is the density of the fluid [kg/m^3], v is the mean velocity of the fluid [m/s], μ_{vis} is the dynamic viscosity of the fluid [kg/(m·s)], and d_H is the hydraulic diameter of the conduit, equal to four times the cross-sectional area divided by the wetted perimeter. d_H equals the diameter, D, for circular pipes. If Eq. 24 is applied to granular or fractured media instead of to a conduit, v is replaced by the macroscopic velocity u, and the hydraulic diameter d_H is replaced by a length which represents the interstitial pore voids or the width of the fractures. Flow is turbulent if R_e is relatively large, and laminar if R_e is relatively small. The boundary for turbulent flow is at approximately $R_e \geq 4000$, while laminar flow occurs when $R_e \leq 2000$ (Hornberger et al., 1998; Chow et al., 1988). In between laminar and turbulent flow regimes a transition zone exists, where the flow cannot strictly be classified into one of the two categories.

If the flow is turbulent, which is often the case in karst conduits, expressions such as the Darcy-Weisbach equation may describe the flow in a conduit (e.g. Chow et al., 1988):

$$q = \sqrt{\frac{2 \cdot d_H \cdot g}{f_f} \frac{dh}{dl}} \qquad (25)$$

where g is the acceleration due to gravity [≈9.82 m/s^2] and f_f is the Darcy-Weisbach friction factor [dimensionless]. The friction factor describes loss of energy due to friction with the conduit wall, increasing as the roughness increases. f_f depends on the Reynold's number. Friction factors for karst conduits are scarce, but have been reported to range from 0.12 to 340 for various cave systems (Springer, 2004 and references herein). Specifically for caves in Quintana Roo, friction factors of 1–45; 11–449 and 500–1000 have been estimated using dye tracing and various measured and estimated hydraulic gradients (Beddows, 2003; 2004).

For fully turbulent conditions, flow may also be described using Manning's equation (Chow et al., 1988):

$$q = \frac{R_H^{\ 2/3} \cdot \sqrt{\frac{dh}{dl}}}{n} \tag{26}$$

where R_H is the hydraulic radius of the conduit [m], defined as cross-sectional area divided by wetted perimeter, and equal to $d_H/4$ for circular conduits. n is Manning's roughness coefficient [s/m$^{1/3}$] and equal to the reciprocal of Manning's M, which is sometimes given instead. Manning's n does not depend on the value of Reynold's number. n may be estimated from f_f by combining Eq. 25 and 26:

$$n = \sqrt{\frac{f_f}{8g}} R_H^{\ 1/6} \tag{27}$$

It is seen that for laminar flow (e.g. matrix flow), flow is proportional to the hydraulic gradient, whereas for turbulent flow (e.g. conduit flow), flow is proportional to the square root of the hydraulic gradient, whether described by Darcy-Weisbach or Manning's equation (cp. Eq. 22, 25 and 26). Limited work from caves in Quintana Roo indicated high Reynold's numbers, i.e. clearly turbulent flow (Beddows, 2003; 2004). Other karst studies have shown the possibility of conduit flow being turbulent or laminar depending on season or location within the conduit system (Cheng and Chen, 2005; Barfield et al., 2004). Flow in fractures may be laminar or turbulent, but is mostly assumed laminar (Worthington, 2003).

Karst aquifers may thus be modelled by explicitly modelling each of the three compartments, and including exchange components between the three; however such triple-porosity modelling is only rarely carried out (Kaufmann, 2003; Cheng and Chen, 2005). More common is the conduit-matrix conceptualization, where conduit flow is modeled as turbulent (pipe) flow, whereas matrix flow is modeled using Darcy's Law. An exchange component (q_{ex}) is included between the two. This exchange is currently not well understood (Martin and Screaton, 2001; Bauer et al., 2003; Peterson and Wicks, 2005), but is often formulated as a linear exchange term that depends on the head difference between conduit (h_C) and matrix (h_M) (e.g. Cornaton and Perrochet, 2002; Birk et al., 2003; Arfib and de Marsily, 2004):

$$q_{ex} = \alpha_{ex} (h_M - h_C) \tag{28}$$

The exchange coefficient α_{ex} is thought to depend also on the hydraulic conductivity of the matrix component, the surface area of the conduits (area available for exchange), the geometry of the conduits, the slope of the regional groundwater table and conduits, and the relative elevation of groundwater table and conduits (Martin and Screaton, 2001; Bauer et al., 2003). Besides conduit-matrix model codes generated by individual research institutions (e.g. used in Birk et al., 2003; Bauer et al., 2003; Liedl et al., 2003; Arfib and de Marsily, 2004), commercial and open-source software exists for creating conduit-matrix models, e.g. MIKE SHE coupled with MOUSE (DHI Software), the MODFLOW variant MODFLOW-DCM (Painter et al., 2007) and the Conduit-Flow Process module for MODFLOW (Shoemaker et al., 2008) which builds upon software developed by research institutions (Clemens, 1998; Hückinghaus, 1998; Bauer, 2002; Birk, 2002). Conduit-matrix models are physically sound but also complex and computationally expensive. Problems occur, especially on large scales, in the parameterization of the highly variable caves (e.g. cave location, course, roughness, dimensions) and in quantifying the exchange. Slight changes in some cave parameterizations can change model output notably (Peterson and Wicks, 2006). Conduit-models without the matrix-component have also been used to model karst in some cases (e.g. Halihan and Wicks, 1998; Jeannin, 2001; Springer, 2004).

A third conceptualization used in distributed karst modelling is the equivalent porous medium. This is the simplest representation of karst aquifers. The assumption that the aquifer can be represented by an equivalent porous medium is reasonable if the numerical cell size is 'large enough', i.e. equals or exceeds a "representative elementary volume" (REV). The value of K assigned to a cell represents the combined effect of matrix, fractures and conduits within the cell. The use of only one value of K throughout the model domain (single-continuum models) has only been successful in few cases (e.g. Larocque et al., 1999; 2000; Scanlon et al., 2003), and is often criticized as too simplistic to represent karst flow (e.g. Kovacs et al., 2005). A modification is the dual-continuum equivalent porous medium model, where important conduits are represented as zones of higher K than the matrix. Both compartments are described using Darcy's Law, but some of the heterogeneity of karst aquifers is incorporated. Water can exchange between the zones of different K. Sometimes, the K assigned to conduits varies along the course of the conduit to reflect larger conduits or an increasing number of branches in the downstream direction (e.g. Lindgren et al., 2005). Dual-continuum approaches give a higher accuracy than single-continuum models, if zonation and assignment of values are reasonably reliable (Durlofsky, 1992). Dual-continuum models have been successfully used by e.g. Teutsch and

Sauter (1991), Knochenmus and Robinson (1996), Lindgren et al. (2005) and Kiraly (2003). The approach is especially applicable for regional-scale studies and was also used in Gondwe et al. (IV).

2.3.2 Multiple Model Simulation

When using models to guide management decisions, uncertainty assessment is important. Several authors have found that uncertainty in the conceptual model usually is far greater than the impact of any model parameter uncertainty, although conceptual model uncertainty may often be neglected (Neuman and Wierenga, 2003; Højberg and Refsgaard, 2005; Refsgaard et al., 2006). Conceptual model uncertainty can be addressed using Multiple Model Simulation (MMS). In MMS a number of different plausible conceptual models are formulated and calibrated. Based on validation tests, models are accepted or rejected. All accepted models are subsequently used for prediction and uncertainty assessment. The difference between the results obtained using the different accepted models thus gives a measure of the impact of conceptual model uncertainty on the model result uncertainty (Refsgaard et al., 2006). MMS increases the robustness of model predictions and yields explicit analyses of the consequences of using alternative models. The method was used in Gondwe et al. (V). The limitations of the MMS approach are that the selection of conceptual models is necessarily subjective and often incomplete. Important plausible conceptual models may be left out, and it is not possible to quantify the probability of each alternative model (Refsgaard et al., 2006; 2007). Methods do exist for combining the results from multiple conceptual models: Pooling (linear combination of the results with equal weights assigned to each model, Block et al., 2009, and references herein); linear regression weighting (linear combination of results, weights of each model determined from regression coefficient of observed vs. modelled conditions for each model, Block et al., 2009, and references herein), and Bayesian model averaging (e.g. Neuman, 2003; Rojas et al., 2008; 2009; Li and Tsai, 2009). For transient models the 'hierarchical mixture of experts' framework (Marshall et al., 2006) and kernel density estimators (Block et al., 2009) may be used to let the weight of each model in a linear combination vary in time. Moreover, non-linear weighting of conceptual models by means of artificial neural networks has been applied (Xiong et al., 2001). Combining different conceptual models typically provides more robust results compared to using one single conceptual model (e.g. Georgakakos et al., 2004; Rojas et al., 2008; Block et al., 2009). Combinations may however be sensitive to the assumptions used in the analysis. For instance, Rojas et al. (2009) showed that Bayesian averaging methods rely not only on the posterior probabilities of each model (i.e. the weights used) but also on the prior model probabilities, i.e. the assumed probability distributions of the model input parameters.

2.3.3 Monte Carlo catchment delineation

Catchment delineation is frequently carried out using particle tracking methods in hydrological models. However, because model parameters are often uncertain, it can be an advantage to carry out stochastic modeling of the catchments instead of relying on the result of one deterministic model (Vassolo et al., 1998). An often used group of stochastic modeling methods are the Monte Carlo methods, which use repeated random sampling of equally likely model inputs in order to generate the model results. In that way, errors in model inputs are propagated through the model, and uncertainties on model results arising from model input uncertainties can thus be quantified. Monte Carlo methods have been used to delineate the spatial probability distribution of groundwater catchments in several studies (e.g. Vassolo et al., 1998; Stauffer et al., 2002; 2005; Hendricks Franssen et al., 2004, Gondwe et al., V). In Gondwe et al. (V) multiple realizations of input parameter (*K*-value) combinations were generated using the Markov chain Monte Carlo method called the Metropolis-Hastings algorithm (Hastings, 1970), which is widely used. It requires drawing random numbers and specifying a probability density function and a proposal density function. The probability density function used in Gondwe et al. (V) was a multivariate normal distribution, and cross-correlation of the parameter values, obtained from inverse model calibration, was incorporated. In the Metropolis-Hastings algorithm the random values are then accepted or rejected using the probability density function and the proposal density function. Each new value to be tested is generated from the proposal density function as well, and depends on the previously generated value, which is where the 'Markov chain' term comes in. Further information on the Metropolis-Hastings algorithm may be found in e.g. Chib and Greenberg (1995). Following generation of the numerous realizations of the model input parameter combinations the hydrological models were run using each parameter combination, and particle tracking was carried out. Finally, the resulting spatially distributed catchment results were stacked to obtain probability maps of the catchment's spatial distribution.

3 Study area

The focus area of the PhD study is the conjectural groundwater catchment of Sian Ka'an, outlined based on topographic divides and a few known flow divides (Fig. 10). The groundwater heads available for the Peninsula are in agreement with these tentative catchment boundaries (Gondwe et al., IV), while geochemical results of Perry et al. (2002) support the water divide at Lake Chichankanab. The study area is 35000 km^2 large, and largely located within the state of Quintana Roo.

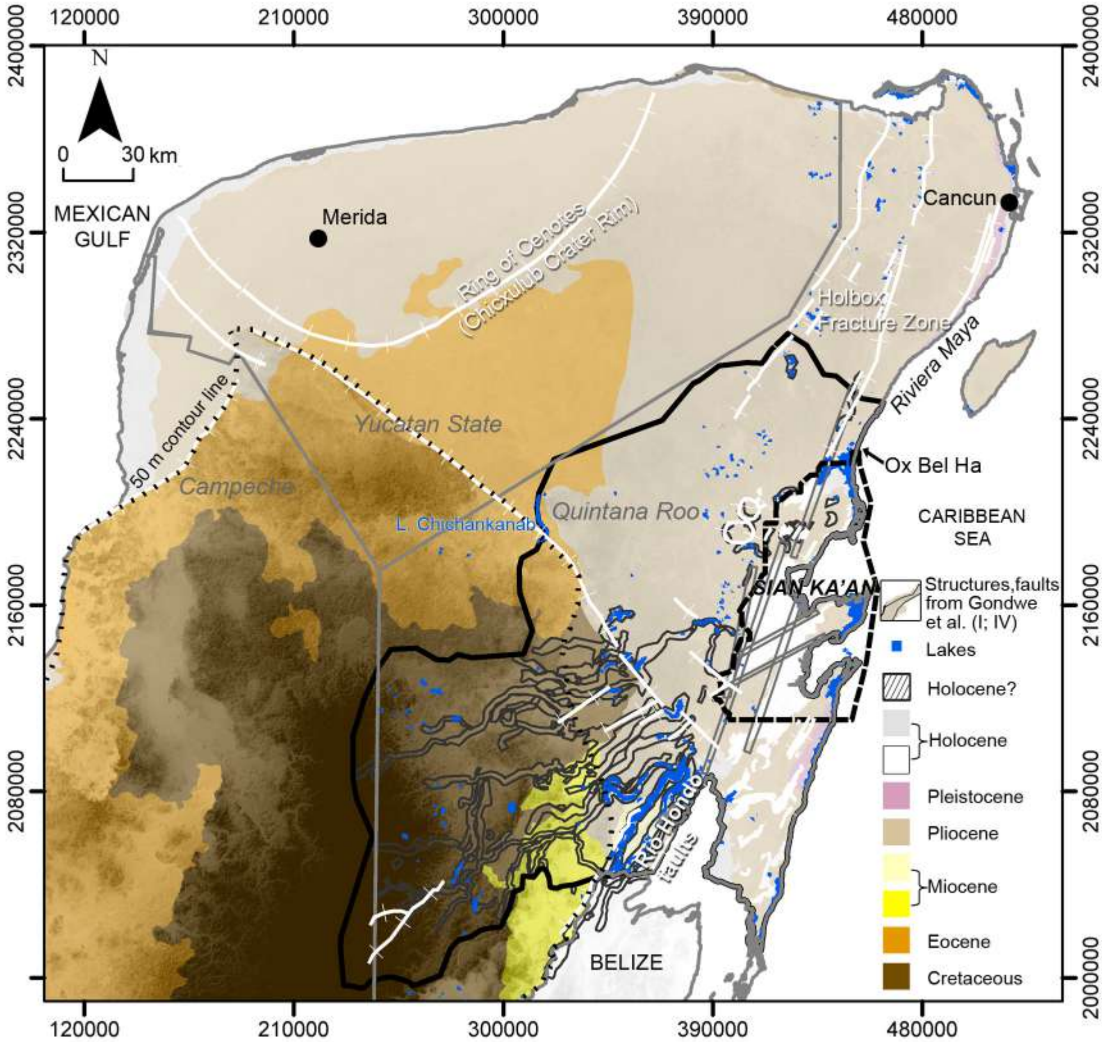

Fig. 10. Geology of the Yucatan Peninsula, modified from SGM (2007). Oldest sediments dated as Cretaceous instead of Paleocene based on Schönian (2005) and Lopez-Ramos (1975) (Ichaiche Formation). Topography from SRTM (USGS, 2006) overlain as grey-scaled transparent. Study area outlined with thick black polygon. Coordinates are UTM zone 16N, WGS84 datum and ellipsoid.

Average precipitation ranges from 840 to 1550 mm/year within the study area. Three quarters of the precipitation falls between May and October (unpubl. climate data from Comisión Nacional del Agua). Actual evapotranspiration was estimated using the 'triangle method' (e.g. Stisen et al., 2008) and MODIS data (Gondwe et al., IV). Subtracting this estimate from spatially distributed precipitation data from the Tropical Rainfall Measurement Mission yielded the average annual recharge distribution. Within the study area average recharge equals about 17% of mean annual precipitation – roughly 200 mm/year (Gondwe et al., IV). Average monthly temperatures range from 23 to 27°C. The area is subject to tropical storms.

The Yucatan Peninsula consists of limestones, dolomites and evaporites reaching thicknesses of >1500 m (Weidie, 1985). The surficial sediments span Upper Cretaceous to Holocene in age, and are generally nearly horizontally layered and off-lapping, with gradually younger carbonates deposited towards the Peninsula margins (Lopez-Ramos, 1975; SGM, 2007; Schönian et al., 2005) (Fig. 10). The Cretaceous age of the oldest surficial sediments is a recent interpretation (Schönian et al., 2005) but the possibility was already mentioned by Lesser (1976). In the southern and central Peninsula the geology is poorly constrained due to few exposures and difficulties in dating the sediments through biostratigraphy (Kenkmann and Schönian, 2006). Examples of Upper Cretaceous sediments wrongly dated to be younger were also mentioned in Pope et al., (2005). Ejecta associated with the Chicxulub meteorite impact, at the contact between Cretaceous and Paleogene sediments, has been found at the ground surface in southern Quintana Roo and neighboring Belize (Ocampo et al., 1996; Fouke et al., 2002; Pope et al., 2005; Schönian et al., 2005; Kenkmann and Schönian, 2006). The ejecta blanket's extent is not well known, but it has been proposed that it extends south and east of Lake Chichankanab (Perry et al., 2009). The ejecta is clay-rich and described to have a sealing or partially sealing effect (Ocampo et al., 1996; Grajales-Nishimura et al., 2000). Using borehole logging and airborne EM, Gondwe et al. (III; IV) found a shallow, high-conductive geological layer in the inland central and southern parts of the study area (thickness: 3–8 m, apparent conductivity 200–800 mS/m). The layer was also associated with high natural gamma radiation (about 80 counts pr. second) (Fig. 11). It was proposed that this layer might be the ejecta layer. Its location in the geological sequence appeared to correspond with being at the Cretaceous/Paleogene boundary, and the spatial occurrences of the layer partly corresponded with other findings of surface-near ejecta (Gondwe et al., III; Schönian et al., 2004; 2005). Geochemical results showing high Sr-concentrations in the region of the anomalous layer also supported the possibility of the layer being ejecta (Gondwe et al., III; Perry et al., 2002; 2009).

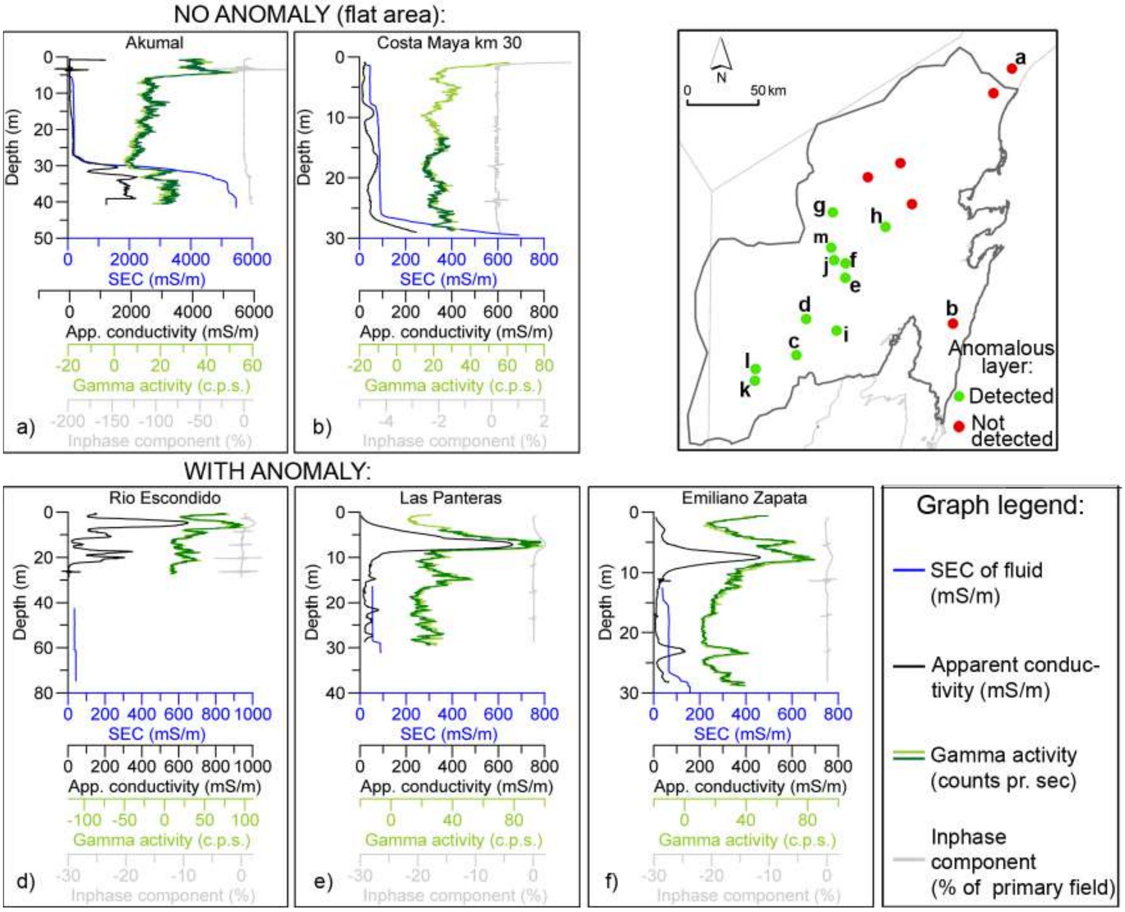

Fig. 11. Example results from the borehole logging. a) and b) show typical results from the flat area (no anomalous layer detected). d) through f) show logs with the anomalous layer detected. Lettering follows that used in Gondwe et al. (IV). SEC: specific electrical conductivity of the well fluid – its top indicates location of water table. Location map at top right. Modified from Gondwe et al. (IV).

Topographically the study area contains a notable contrast. Large parts of the Pliocene geology is rather flat, with elevations ranging 0–20 meters above mean sea level (mamsl). In the area of the oldest, Cretaceous, geology, cone karst hilly landforms dominate, and elevations range between 50 and 340 mamsl. In between a transition zone with moderately undulating relief exists (20–50 mamsl) (Fig. 10).

The Yucatan carbonates and evaporites are heavily karstified. Some of the world's longest underwater cave systems have been mapped along the Riviera Maya by cave divers (www.caves.org/project/qrss/qrlong.htm; www.caverbob.com/uwcave.htm). Mapped caves may be >30 m wide and up to 10 meters high. Maximum mapped cave depths are 22.3 ± 8.7 m for inland caves, and 11.8 ± 6.2 m for coastal caves. In the Riviera Maya the overall passage density is 1.8 km/km^2, but may locally be up to 4.3 km/km^2 (Beddows, 2004; Smart et al., 2006). Most parts of the study area have not been explored by cave divers and the location and properties of caves here are therefore unknown. Regional-scale zones of potential higher permeability were mapped and explored by Gondwe et al. (III); some of which were found to be associated with the two regional fault systems present in the study area – the Río Hondo faults and the Holbox fracture zone (Fig. 10). Additional faults located within the Sian Ka'an Biosphere Reserve and possibly connecting the Río Hondo and Holbox systems were proposed by Gondwe et al. (I), based on surface water flow patterns and the shape of wetland boundaries (Fig. 10). Further investigation of these zones and faults is elaborated upon in Chapter 4.2 and 4.3.

Groundwater in the Yucatan Peninsula is a 0–100 m thick freshwater lens floating on top of saline water (Gondwe et al., IV; Perry et al., 1989; Steinich and Marin, 1996; Marin et al., 2004). In the Pliocene geology the depth to the saltwater-freshwater interface was found to be described well, on a regional scale, by the Dupuit-Ghyben-Herzberg relationship, where depth to interface equals 40 times the height of the freshwater table (all with respect to mean sea level) (Gondwe et al., IV).

A notable contrast was found in the measured groundwater heads across the study area. Like the topographical contrast, the boundary between the contrasting areas appears coincident with geological boundaries. Within the Pliocene geology measured heads range from 0 to 3 mamsl, yielding low hydraulic gradients of 3–7 cm/km, and water level variations are relatively small (5–40 cm within a year) (Gondwe et al., IV) (Fig. 12). This indicates high transmissivity. Hydraulic gradients in the same range have been found in the Pliocene geology in the northwestern and northeastern parts of the Peninsula (Back and Hanshaw, 1970; Marin, 1990; Moore et al., 1992; Beddows, 2004). In the hilly area, mainly covered by the Cretaceous geology, measured water levels range from 4 to 92 mamsl, yielding hydraulic gradients of 10 to 190 cm/km (Gondwe et al., IV).

Geochemical results show that only in the hilly area, waters are close to saturation with gypsum and anhydrite (Gondwe et al., IV; Perry et al., 2002). Gypsum and anhydrite are known to have low primary porosity, with water flow mainly taking place through developed karst features, if any are present (Klimchouk, 1997; Mayr et al., 2008). Consequently, measured groundwater heads and water chemistry indicate a lower transmissivity of the geology in the hilly area, compared to that of the flat, Pliocene area. In addition, water level measurements in the study area revealed the presence of perched aquifers in the hilly area and transition zone (Fig. 12). These perched aquifers may be formed due to the shallow, likely clayey, layer detected in the borehole logs and airborne EM (Gondwe et al., III; IV).

From the measured groundwater heads in the study area, overall groundwater flow directions appear to be from SW to NE within the hilly area, and from W to E within the Pliocene geology (Gondwe et al., IV) (Fig. 12).

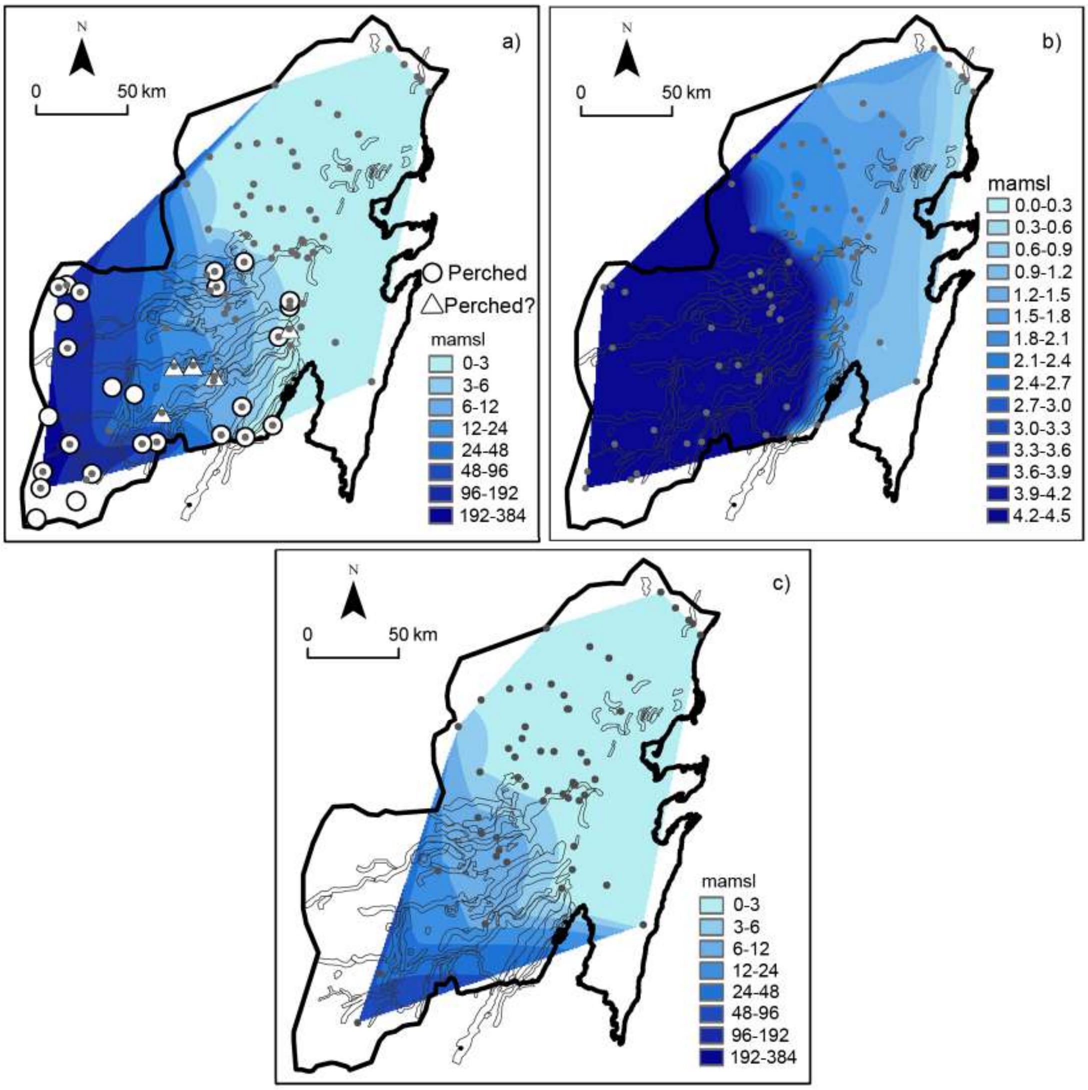

Fig. 12. Examples of water levels measured in the dry season, interpolated using Natural Neighbor algorithm. a+b) are including, c) is excluding points believed to be perched water. The "Perched?" label in a) indicates localities with possibly perched aquifers. a + b) show the same data, but with different legends to show the overall regional water level differences. Water levels refer to meters above mean sea level. Modified from Gondwe et al. (IV).

4 Results from radar remote sensing, EM exploration of geological structures and groundwater modelling

4.1 Wetland hydrodynamics derived from radar data

4.1.1 Mapping flooding extent from SAR backscatter data

For Sian Ka'an, the temporal dynamics of flooding extent in the period August 2006 to February 2008 was investigated using SAR backscatter data (Gondwe et al., I). The wetland extent varied between 1067 km^2 and 2588 km^2. The flooding extent was found to be correlated with a 3-month backward moving average of precipitation (Fig. 13), indicating the likely effect of a larger groundwater catchment on the wetland hydroperiod. The largest wetland extent during normal years was found to occur in December, two months after the end of the rainy season. However, when an extreme rainfall from a hurricane took place in September 2007, this month yielded the largest flooding extent that year. Lowest flooding extent occurred in May, at the end of the dry season. The flooding maps further indicated areas providing main water inflow to the wetlands. These were seen as the areas which were still flooded at the driest time of the year, and may be caused by water-carrying faults providing water to the wetlands (Gondwe et al., I).

The accuracy of the flooding map was evaluated by comparing with a flooding extent classification created using nearly cloud-free Landsat imagery. Landsat and other optical imagery is generally evaluated as optimal for flood extent mapping, but is limited by the cloud cover often present in the images, as well as the inability to penetrate through vegetation. Landsat imagery for flood extent mapping has been carried out by e.g. Pietroniro et al., (1999), Hudson and Colditz (2003), Wright and Gallant (2007) and Islam et al. (2008). Using SAR data the classification accuracies obtained in the Sian Ka'an study ranged between 63% and 75%, depending on class. These accuracies were in agreement with that of other studies (e.g. User's accuracies: 65–95% in Hess et al., 2003; 56–80% in Bourgeau-Chavez et al., 2005).

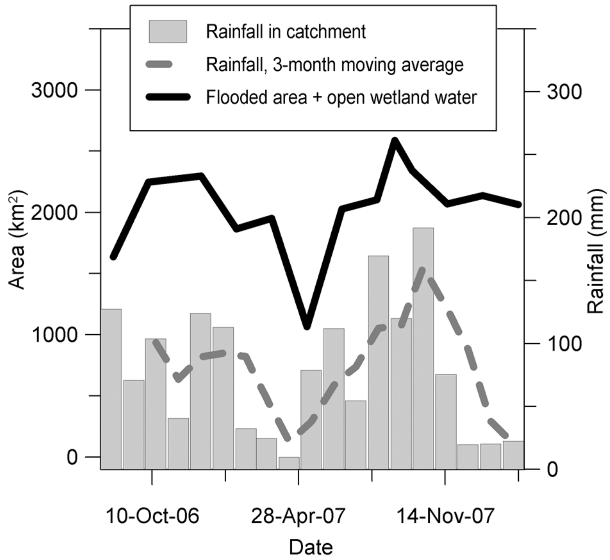

Fig. 13. Flooding extent variations with time, mapped by classification of SAR backscatter data. Precipitation data (histogram) from the Tropical Rainfall Measuring Mission (TRMM, NASDA/NASA, 2008), along with a 3-month backward moving average of this precipitation (thick dashed line). These data are a spatial average for the study area (conjectural catchment of Sian Ka'an). From Gondwe et al. (I).

4.1.2 Surface water flow directions and water level changes from InSAR

For the Sian Ka'an wetlands, interferogram fringe directions along with the shape of tree islands, which indicate up- and downstream directions of dominant water flows, were used to deduce the overall surface water flow directions within Sian Ka'an (Fig. 14) (Gondwe et al., I). The interferograms analyzed spanned the time period from July 2006 to March 2008. Fringe directions also revealed local-scale water divides. These may not necessarily be impenetrable to water, but the flooding regime differs on either side of the divide (Fig. 14). This information on the surface water flows and flooding regimes has not previously been known for Sian Ka'an. It is often difficult or impossible to obtain such data for vast wetlands, but these results illustrate how InSAR offers new possibilities for learning about the hydrodynamics of large and often inaccessible wetlands. The surface water flow directions and local-scale water divides of Sian Ka'an can be used to guide water quality monitoring programs with the aim of identifying pollution transport pathways. These results are also important for further studies on the interaction between ecology and hydrology in the wetlands.

The interferograms generated over Sian Ka'an showed that relative water level changes are generally small. The areas with the largest relative water level changes were the sloughs and four main coastal outlets of Sian Ka'an (Fig. 14, interferogram example in Fig. 6). Due to the lack of radar altimetry and gauge data, the results of water level change over Sian Ka'an focus on the relative changes rather than absolute changes. Detected relative water level changes were up to 28 cm within 24 or 48 days (Gondwe et al., I). The interferograms produced over Sian Ka'an were smooth at times with large water amounts in the wetlands (November and December). These were the same times when the flooding extent was largest, also indicating large water amounts. However, mostly Sian Ka'an interferograms showed irregular fringe patterns, with some areas of steep relative water level changes (the local-scale water divides, with several fringes over short distances). Irregular fringe patterns appear to characterize natural wetlands, because this was also found by Alsdorf et al. (2007b) and Wdowinski et al. (2008). The most irregular fringe patterns were in Sian Ka'an observed at the beginning and middle of the wet season, where surface water level changes were more localized (July–September). The fringe patterns may be compared with the results of hydrological models, to verify and/or constrain the models. This was partly done in Gondwe et al. (V).

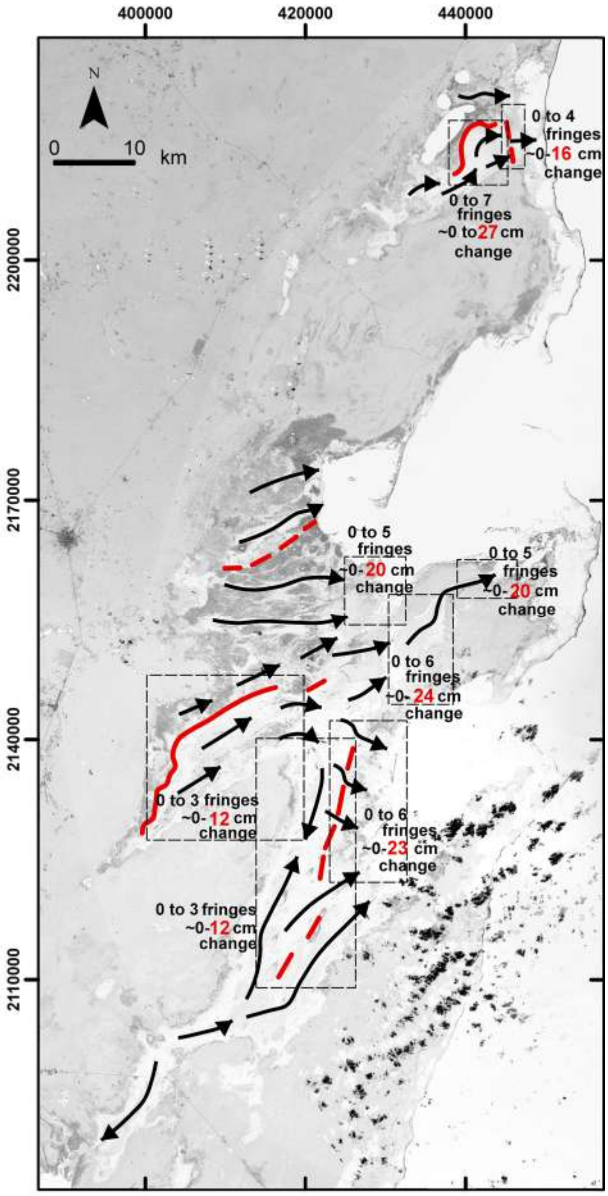

Fig. 14. Black arrows: Surface water flow directions, deduced from interferograms and visual inspection of Landsat imagery. Red lines: Semi- or impermeable water divides, deduced from abrupt phase changes and fringe lines. Dashed boxes: Areas with largest relative water level changes (most fringes). Background image: Grey-scaled Landsat TM Tri-Decadal mosaic, band 7. From Gondwe et al. (I).

4.2 Investigation of karst features using EM

4.2.1 Local-scale exploration of karst caves

Airborne EM measurements were carried out over the well-mapped Ox Bel Ha cave system, located just north of Sian Ka'an. The purpose was to determine the usefulness of airborne EM in detecting submerged caves in the geology of Quintana Roo. Finding out the location and properties of caves and highly permeable geological zones is crucial in order to determine the groundwater flow patterns in karst. The equipment used in the exploration was a modified Geotech Hummingbird of the Geological Survey of Austria, applying four frequencies (340 Hz, 3200 Hz, 7190 Hz and 28850 Hz) (Motschka, 2001). The cave system clearly appeared in the data set as anomalies of higher signal strength (Fig. 15). Most anomalies were correlated with the location of caves known from cave maps constructed by scuba divers. Others had not previously been mapped by divers, but some of them were verified at dive expeditions following the airborne EM campaign (Supper et al., II). The inphase components of the 3200 Hz and 7190 Hz frequencies responded most strongly to the presence of caves in this survey. That is likely because the main depths of the explored caves corresponded well with the exploration depth of these two frequencies in this geological configuration.

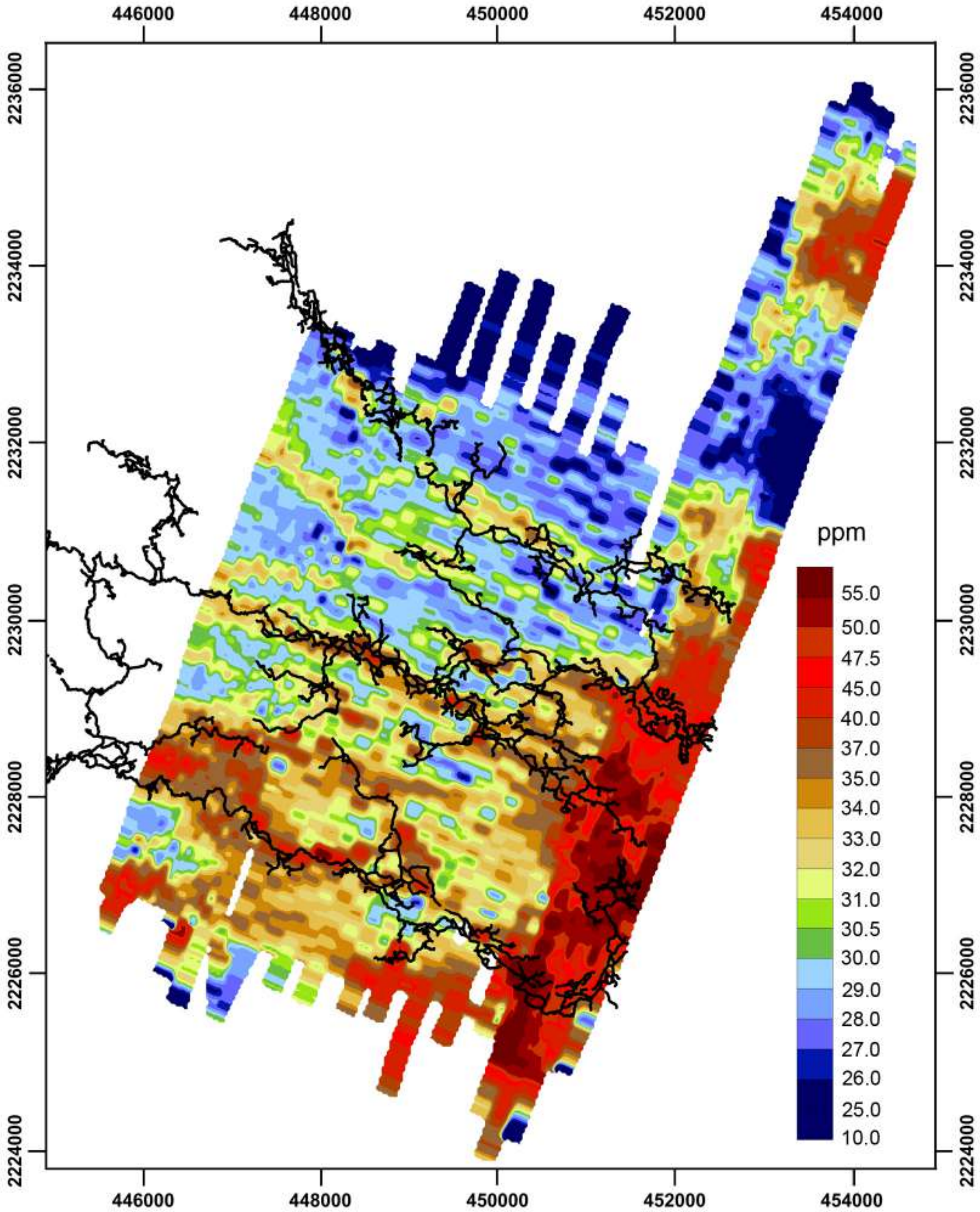

Fig. 15. Inphase component of the 7190 Hz frequency, measured over the Ox Bel Ha cave system, after rough empirical altitude correction and profile leveling. Known caves (black lines) are overlain. Ox Bel Ha cave line map kindly provided by Grupo de Exploracion Ox Bel Ha and Quintana Roo Speleological Survey 2006. Principal explorers of the Ox Bel Ha system: B. Birnbach, S. Bogaerts, F. Devos, C. Le Maillot, S. Meacham, B. Philips, S. Richards, D. Riordan, S. Schnittger, G. Walten and K. Walten. From Supper et al. (II).

Layered inversions of the Ox Bel Ha airborne EM dataset have shown that the EM data can not only be used to determine the lateral location of caves, but can also be used to obtain information on the depth of the caves. In fact the caves represent a 3D exploration problem, but interpretations using 1D multilayered inversions have shown to work well (Y. Ley-Cooper, Royal Melbourne Institute of Technology University, unpublished results) (Fig. 16). However, determining exact cave dimensions from the EM data does not appear possible with the present knowledge. One reason appears to be that the bulk rock matrix immediately surrounding the caves has a strong impact on the measured signal.

3D forward modelling of the Ox Bel Ha signal, using cave dimensions known from dive surveys, indicates that the modelled signal anomalies are smaller than the actual measured signal anomalies over the caves (Ottowitz, 2009). One explanation for this may be that the matrix surrounding the caves has an increased porosity, yielding a lower bulk matrix resistivity in the vicinity of caves, and increasing the signal magnitude (see Fig. 15 and Fig. 16). This topic has received little attention in the literature. A 'halo' effect is known to occur around man-made caves, resulting in a zone of increased fracturing surrounding the cavity. This makes the effective geophysical size of the cavity larger than the cavity itself. In natural caves, secondary effects on the surrounding rock may also be present (Daniels, 1988). The limestone medium surrounding karst conduits was in one case described as inhomogeneous, based on geophysical measurements (Guérin et al., 2009). A higher porosity surrounding karst caves may also correspond to the proposed "annex-to-drain" conceptualization, where storage in the karst aquifer is believed to take place in large karstic voids with a high head loss connected to conduits (Mangin, 1974; Bakalowitz, 2005). However, the nature of the medium surrounding caves in Quintana Roo remains to be determined, and therefore it is difficult to state exactly when airborne EM will be able to detect caves in this medium. However, besides the matrix surrounding the caves, the airborne EM signal is sensitive to the following factors: the proportion of saltwater in the cave (for instance, Ox Bel Ha caves are filled partly with fresh, partly with saline water); the size of the cave; the presence of several caves in the vicinity of each other; the shape and depth of the cave; the resistivity contrast in the geology, and the sensor height (Gondwe, unpubl. results of forward modelling experiments).

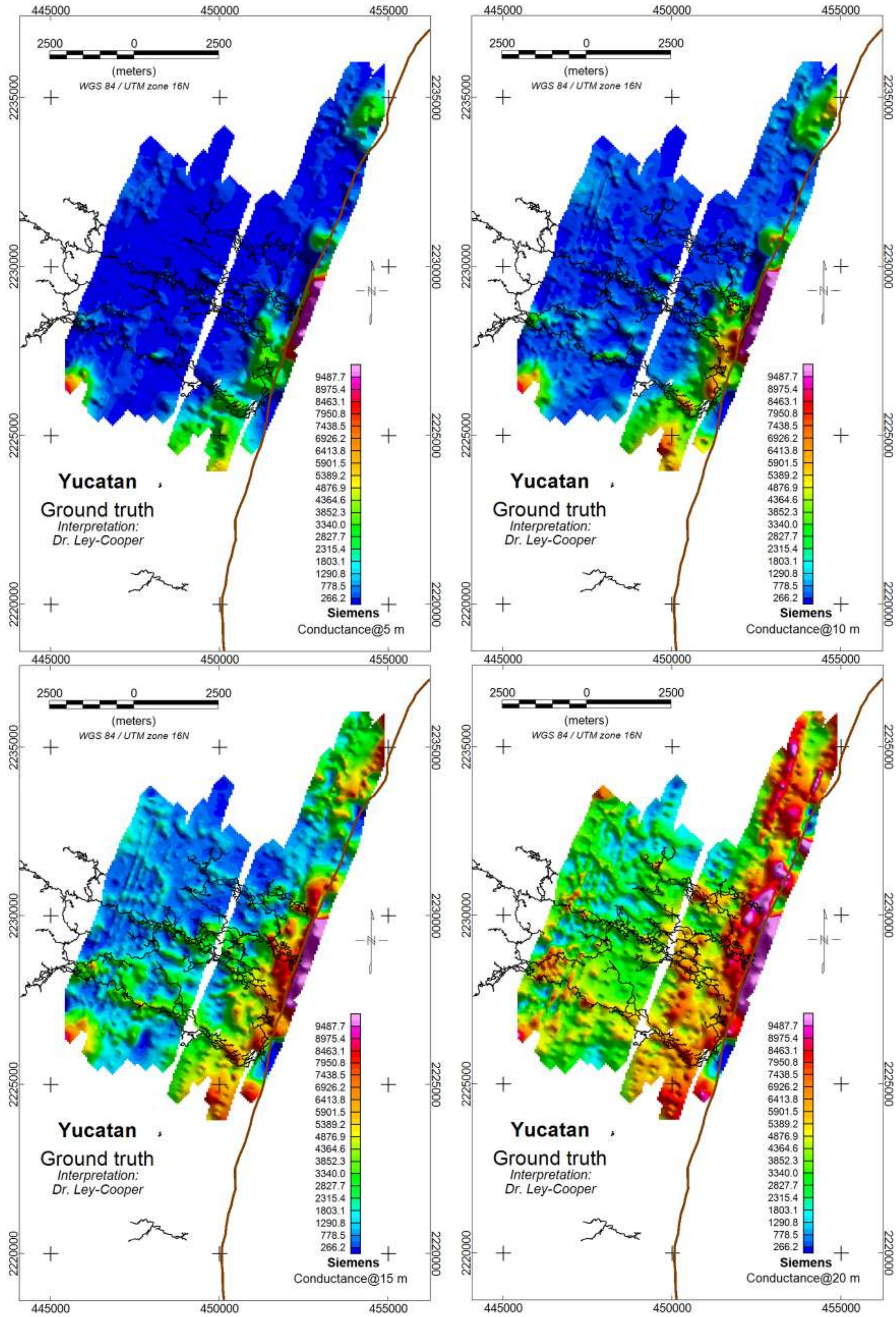

Fig. 16. Layered inversion results of the Ox Bel Ha survey. Inversion made by Dr. Yusen Ley-Cooper, RMIT Australia. Unit: Conductance (conductivity times thickness) in Siemens. Ox Bel Ha cave line map credits: Please see figure text below Fig. 15.

4.2.2 Regional-scale structure investigation

After showing that airborne EM *is* able to locate subsurface caves in Quintana Roo, the next step was to investigate parts of the study area, where the location and extent of caves and high permeable zones were unknown. The airborne EM measurements were focused on areas in which the likelihood of encountering high permeable zones was expected to be comparatively higher, by using the structures delineated from visual inspection of satellite imagery as a guide (Gondwe et al., III) (Fig. 10). Airborne EM results obtained over a structure which is part of the Holbox fracture zone showed higher signal strength over this zone, compared to over the bulk rock surrounding the zone. Layered inversions showed that the bulk resistivity in the freshwater part of the Holbox fracture zone was about 50 Ωm, whereas outside the zone it was >130 Ωm (Fig. 17). If applying Archie's Law (Eq. 6) and assuming freshwater resistivities (ρ_w) between 4 and 10 Ωm (i.e. 2.5 to 1 mS/cm, Beddows, 2004), and typical values for the constants in Archie's Law (a=1.5, m=n=2), then this resistivity difference across the Holbox zone corresponded to a higher porosity within the zone. With $\rho_w = 4$ Ωm, Holbox zone porosity would be ~0.35 while bulk matrix porosity would be <0.25. With $\rho_w = 10$ Ωm, Holbox zone porosity would be ~0.55 while bulk matrix porosity would be <0.4. By inference, this structure in the Holbox zone is therefore also likely to be a zone of higher permeability to water flow.

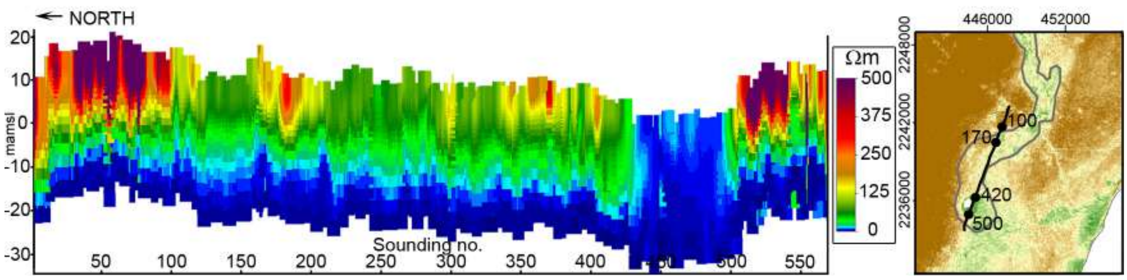

Fig. 17. Inversion results from profiles over the Holbox fracture zone. Soundings 170 to ~500 are within the delineated Holbox zone and appear as more conductive than surroundings. Sounding 420–500 is an open water body (Laguna La Union). Sounding 100–170 likely represents an irrigated field. Location map at right side. Modified from Gondwe et al. (III).

Airborne EM data on transects across structures in the inland areas also showed a higher signal strength above structures compared to the inter-structure areas (Fig. 18). However, forward modelling showed that these anomalous signals could not be explained by caves of realistic dimensions (Gondwe et al., III). Instead, the anomalous shallow conductive layer encountered in the inland borehole logs (Gondwe et al., IV) was useful to obtain a reasonable explanation of the signals measured across inland structures. The airborne EM signals across the inland structures could be modelled well if the high-conductive, shallow layer was simulated to be present along the full length of all transects. The reason for a stronger EM signal over the structures was then simply that in these areas, which also corresponded to topographic depressions, the layer was exposed relatively closer to the surface. Likely erosion by surface water runoff within the structures, would have removed relatively larger portions of the strata above the anomalous layer over structures, compared to the inter-structure areas.

Due to the presence of the high-conductive, shallow layer, little information could be obtained about the subsurface beneath it, using the airborne EM. Higher-strength anomalies over structures in the 340 Hz part of the signal could be matched well when a low-resistivity zone of ~5 Ωm was included at depth. This could suggest higher bulk porosity beneath the anomalous layer at the structure locations. However, this possibility is highly uncertain because of equivalences and the low sensitivity to the geology beneath the conductive, shallow anomalous layer. The 340 Hz signal was furthermore more affected by data noise and drift than the more reliable 3200 Hz and 7190 Hz parts of the signal. Forward calculations showed that signal perturbations due to high-permeable freshwater zones beneath the conductive, shallow anomalous layer would only be observable in the most reliable 3200 Hz and 7190 Hz signal components if the sensor height was relatively low (≤ 30 m) – a sensor height difficult to obtain in the study area due to tall vegetation. In addition, such signal perturbations would not be distinguishable from changes caused by slight variation in the resistivity and/or thickness of the low-resistive layer. Such changes do characterize the anomalous layer encountered in the borehole logs, and therefore, the airborne EM system used would not be capable of detecting high-permeable zones in the inland areas throughout which the shallow, conductive layer appears to be present.

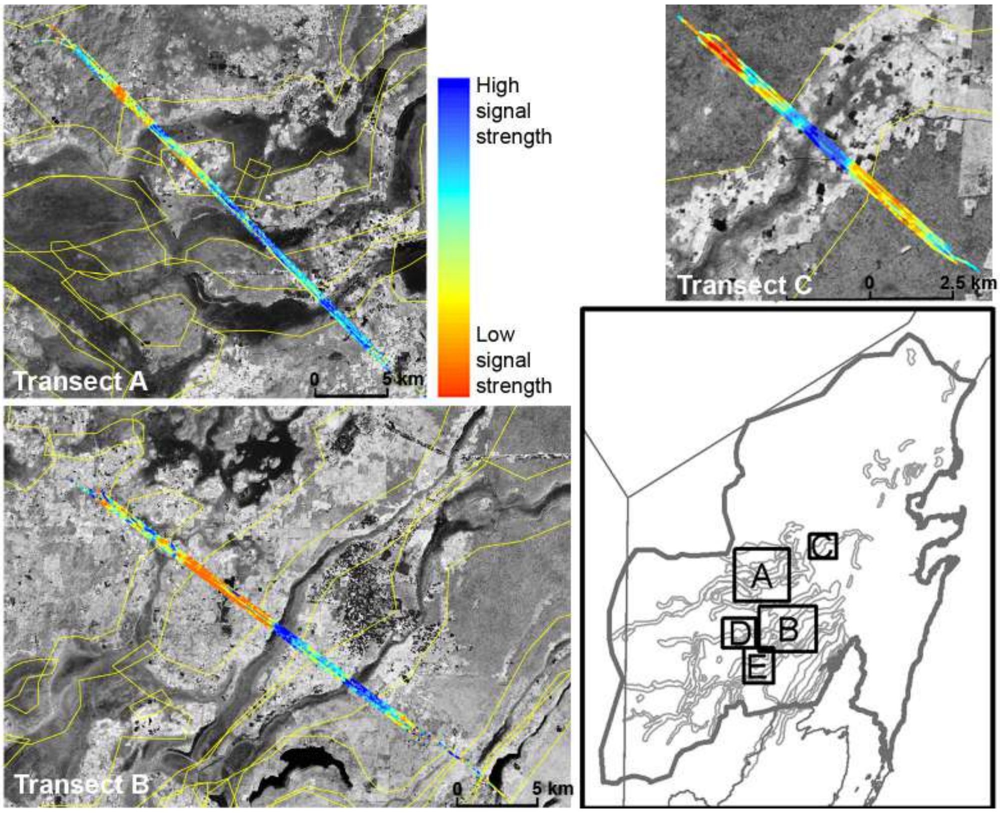

Fig. 18. Examples of HEM signals measured over inland structures, transformed with Eq. 1 in Gondwe et al. (III). Thin yellow lines outline structures. Background: Landsat Tri-Decadal TM band 4. Location map also shows the structures delineated, and the location of Transects D and E (not shown). Modified from Gondwe et al. (III).

4.3 Hydrological modelling of the Sian Ka'an catchment

4.3.1 Multiple Model Simulation of the Sian Ka'an catchment

Distributed hydrological modelling of the Sian Ka'an catchment was carried out to investigate central management questions such as the extent of the groundwater catchment for Sian Ka'an's wetlands, and the extent of travel time zones of groundwater flow from the catchment to the Reserve. However, the hydrogeological role of the structures outlined with satellite imagery could not be determined from the field data sets. Therefore, inverse hydrological modelling and Multiple Model Simulation was chosen as methods to investigate the possible role of the structures for the groundwater flow patterns in the catchment.

Seven different conceptual models were set up for the conjectural catchment of Sian Ka'an's wetlands (Gondwe et al., V) (Fig. 19). The equivalent porous medium modelling approach was used. Only the flat area was discretized; the hilly region was modelled as a lumped inflow boundary, due to lack of sufficient data to represent this area with a discretized model. The conceptual models differed with respect to whether the structures were assigned a different hydraulic conductivity ($K_{structures}$) than the rest of the domain (K_{matrix}) (single- or dual-continuum equivalent porous medium models), and with respect to the magnitude of the lumped inflow from the hilly area. Finally, the coastal resistance to flow was differentiated at the coast north of Sian Ka'an in one conceptual model (Model 7), to accommodate the theoretical possibility of caves not being distributed evenly in the Tertiary sediments but only being present in the Pleistocene sediments along Riviera Maya (Gondwe et al., V, and references herein).

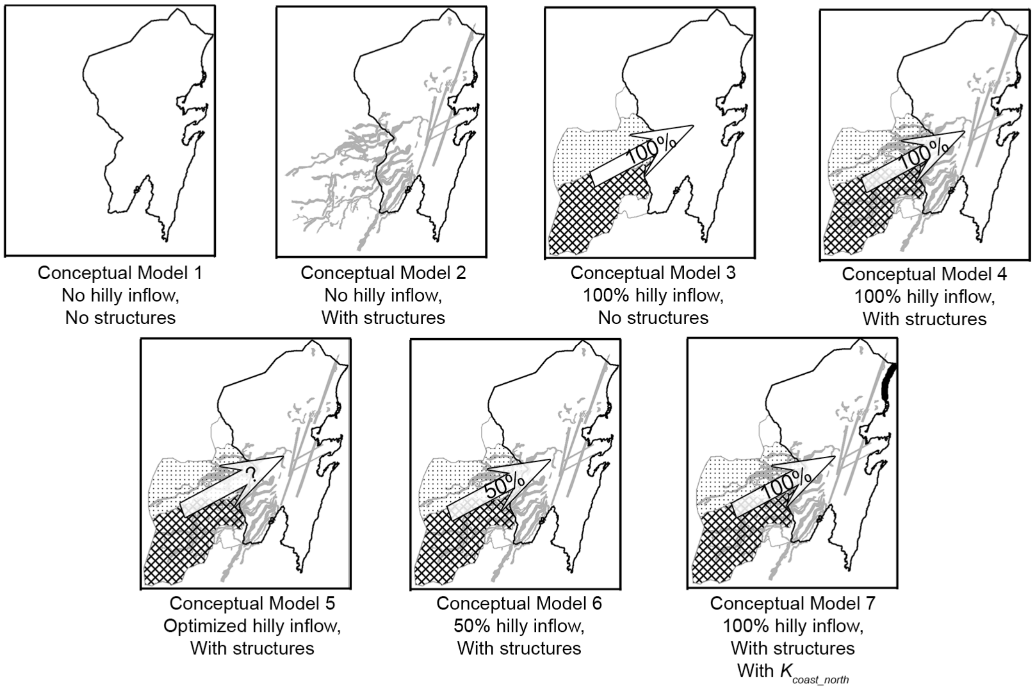

Fig. 19. The different conceptual models used in the Multiple Model Simulation.

In the cases where coastal resistance to outflow was assumed homogeneous along the whole coastal boundary, the six conceptual models showed an improvement in model fit to measured groundwater heads when structures were assigned a different hydraulic conductivity than the rest of the domain (dual-continuum approach). Model fit also improved when inflow from the hilly area was included. In these six cases $K_{structures}$ was always calibrated to be 1–2 orders of magnitude larger than K_{matrix}, indicating that the structures would be zones of higher permeability. However the seventh conceptual model, which differentiated the coastal resistance across the domain, gave an equally good fit to data. In this model, coastal resistance north of Sian Ka'an was calibrated to be lower than the coastal resistance of the remaining coastline. In this model, there was little difference between K_{matrix} and $K_{structures}$. By comparing output from all models with data published in the literature on e.g. coastal discharge and maximum flows in high permeable zones, both Model 7 and three of the conceptual models which had a constant coastal resistance, were found to be plausible. Only two conceptual models could be rejected based on comparison with system data from the literature. Model 5 was largely similar to Model 4, because the automatically optimized hilly inflow in Model 5 became close to the magnitude of the hilly inflow in Model 4. Model 5 was therefore not included in the further analysis (Gondwe et al., V).

Stochastic modelling of the steady state catchment was carried out with the four accepted models. The results illustrated the effect of model structure uncertainty on the management decisions. It was seen that if structures in reality do have a different hydraulic conductivity than the rest of the domain, then areas in the south-central part of the study area would also contribute with water to Sian Ka'an (Gondwe et al., V) (Fig. 20). Finding out whether these areas are part of the catchment is critical because these are the areas where agricultural activities are expanding, possibly leading to increased use of pesticides and fertilizers.

Travel time zones delineated with transient versions of two of the hydrological models illustrate the significant influence that the choice of conceptual model and effective porosity has on management decisions (Fig. 21). Again the influence of the structures on the areas that need to be protected is clear. The effective porosity controls the travel times, and is an uncertain parameter. In Gondwe et al. (V), scenarios were modelled by calibrating effective porosities so that modelled groundwater velocities would match values reported in the literature.

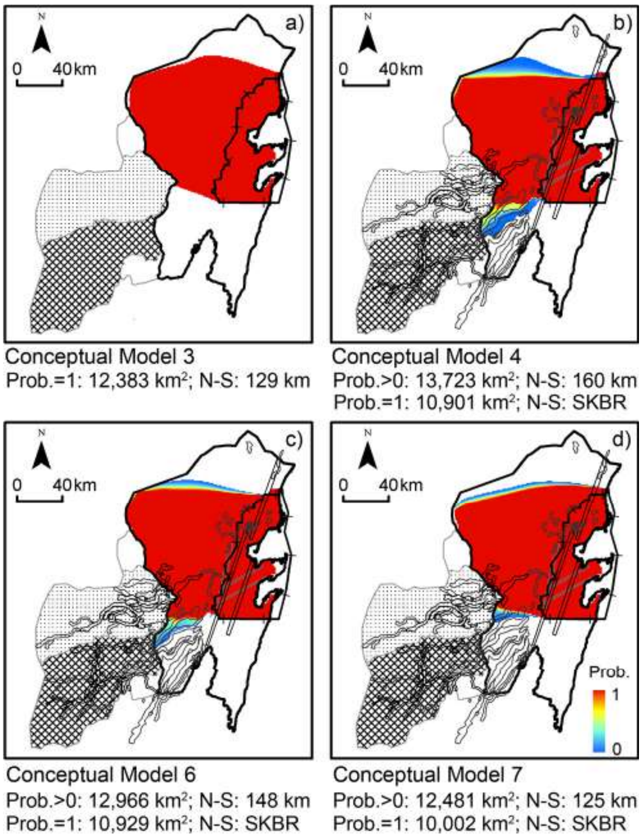

Fig. 20. Probability (Prob.) of a cell belonging to Sian Ka'an's steady state catchment, for Conceptual Models 3, 4, 6 and 7.

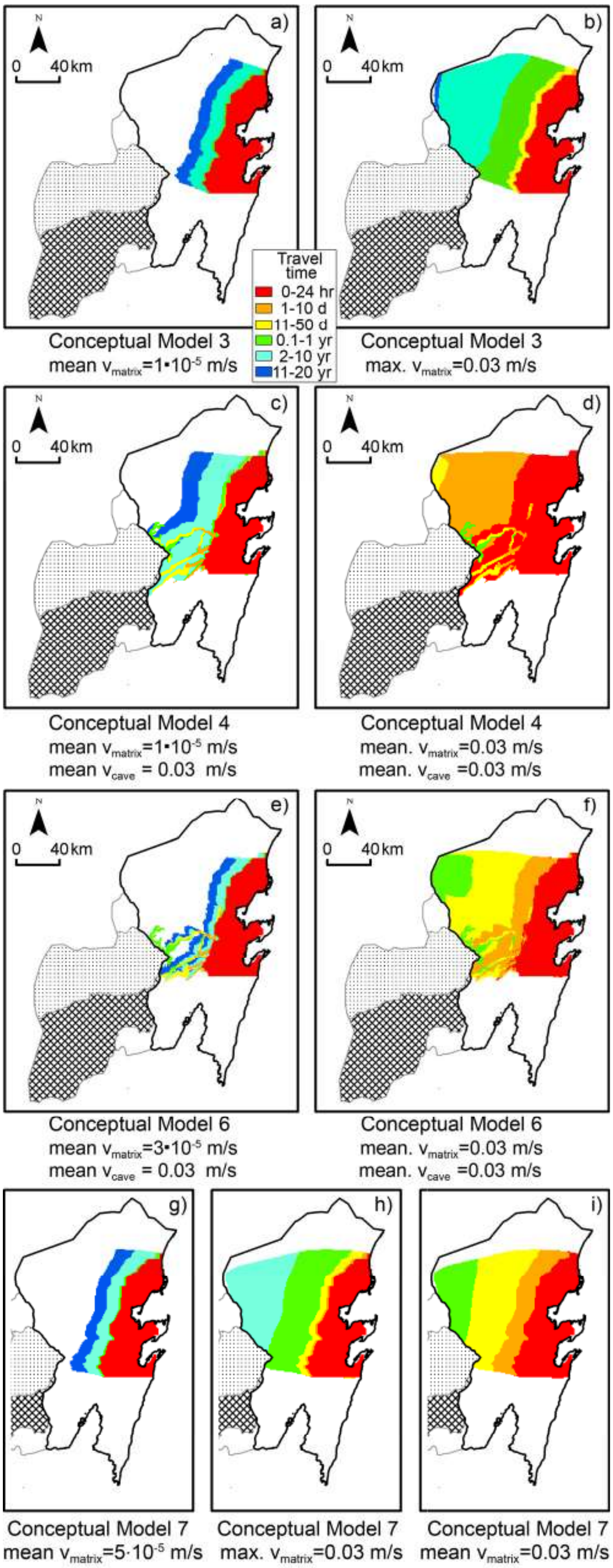

Fig. 21. Modelled travel time zones for different conceptual models and different values of effective porosity, adjusted to give the indicated modelled water travel times (v).

4.3.2 Robust modelling results independent of conceptual model choice

All the plausible hydrological models show that Sian Ka'an's wetlands only exist due to recharge from the catchment. Recharge over Sian Ka'an itself only constitutes on average about 41 mio. m^3/year. In comparison, the total outflow from Sian Ka'an according to the models is ~2700–2900 mio. m^3/year, of which ~280–540 mio. m^3/year exits via the wetlands (overland flow) (Gondwe et al., V).

Recharge to the aquifer in the model domain constitutes 17% ± 3% of the mean annual precipitation (4400 mio. m^3/year ± 700 mio. m^3/year). Results from the automatic calibration indicate that boundary inflows from the hilly area to the model domain may be of similar magnitude. Water exits the domain through overland flow (4–12%) and groundwater flow (88–96%). The latter is distributed between coastal outflow to the sea, and groundwater outflow towards the north via the Holbox fracture zone. Outflow from the domain via the Holbox zone towards the north is in agreement with dye tracing results of Beddows and Hendrickson (2008). However, the magnitude of this Holbox outflow can not be determined with the present range of plausible hydrological models (Gondwe et al., V).

Groundwater outflow through Sian Ka'an's coastal boundary is 68–90 m^3/s. The groundwater that passes through Sian Ka'an is therefore a significant contribution to the marine environment. Hence, if the groundwater that flows into Sian Ka'an is protected, a high water quality for the marine environment, which hosts one of the most productive coral reef systems in the world, can also be ensured (Gondwe et al., V).

The modelled flooding dynamics of Sian Ka'an's wetlands generally corresponds well with the flooding dynamics observed using SAR data. Both show that the timing of Sian Ka'an's flooding peak is different from the timing of the yearly rainfall maximum (Gondwe et al., I; V). This is a further indication that Sian Ka'an's wetland dynamics is controlled by the catchment. The months April to August are the times with least water in the wetlands, and therefore are likely the most vulnerable times of the wetlands, since any water-borne pollutants may be less diluted at these times, and low water amounts may create increased vulnerability to reduction in water quantity. The remaining months of high and medium flows are however also important to maintain the natural cycle of the wetlands (Gondwe et al., V).

5 Conclusions and perspectives

The previous two chapters have summarized the results that answer to the objectives stated with bullet points in Chapter 1. Those results will not be repeated here. Instead this chapter focuses on the general advantages of the presented multi-disciplinary approach applied to study groundwater-dependent ecosystems in karst, as well as on how the results of the research can be applied.

5.1 Advantages of the multi-disciplinary multi-scale approach

When studying data-scarce regional-scale areas as the one investigated in this thesis, it is inconvenient to rely solely on ground-based field data, because they are limited in number and have a limited spatial support scale. Combining ground-based field data with data from remote sensors (aircrafts and satellites) allows the coverage of a greater area, and the investigation of the study area with a wide variety of data types. The methods complement each other, both in information types and in scale. To tackle problems such as the management of Sian Ka'an, a multi-disciplinary and multi-scale approach is needed.

The remotely sensed SAR data used in this study provided information on wetland hydrodynamics. Such data is otherwise difficult to obtain, because wetlands are often vast and largely inaccessible. The remotely sensed data used for recharge estimation enabled spatial estimates of this parameter to be generated. Actual evapotranspiration is generally difficult to estimate, and obtaining estimates for a regional scale requires remote sensing data (e.g. Stisen et al., 2008). The use of remotely sensed precipitation estimates ensures data coverage even over areas not monitored by gauges. A spatial estimate of recharge is more suitable for distributed modelling than point-based estimates, especially when ground-based point density is limited as it often is in real cases (e.g. Brunner et al., 2007). Remotely sensed estimates can sometimes circumvent scaling issues, because the estimates may be provided on the same scale as the regional-scale hydrological model is formulated on (e.g. Grayson et al., 2002).

Ground-based methods are needed to obtain calibration data for groundwater flow models. Groundwater level data can presently only be collected in situ. Likewise, water chemistry data can only be collected as point samples from ground-based field work, but provides useful information about the geology of the subsurface. In the Sian Ka'an case such indirect data were valuable because borehole lithological logs are extremely scarce.

The airborne geophysical measurements gave important information on geological structures and caves on a local to regional scale. The advantage of airborne geophysical measurements is the dense sampling, the ability to access vast areas during short times, and the ability to measure in areas which may otherwise be difficult to access. The approach used in the present study of letting the airborne EM measurements be guided by satellite-derived maps of potential high-permeable zones improved data-collection efficiency, because areas likely to be highly permeable could be targeted. In the case of airborne geophysical measurements used for investigating regional-scale catchments this is important, because the high cost of airborne EM and the large size of the study area means that it will be practically impossible to cover the whole study area completely by airborne EM measurements.

The map of remotely sensed structures also provided an opportunity to upscale airborne EM measurements from transects to the catchment scale. However, in the present case the EM data interpretation was more complex, because the shallow, high-conductive geological layer obstructed the airborne EM sensors from obtaining geological information at depth in the inland areas.

The ground-based geophysical measurements enabled a better interpretation of the airborne EM data. Data from the geoelectric, time-domain EM and borehole logging induction measurements could be used to constrain the inversions. The borehole logging method was able to look beyond the shallow, high-conductive layer in the inland regions. Other ground-based EM methods would not have been able to do so, because the induced current would have been confined to the shallow, high-conductive layer without penetrating further down into the subsurface. Geoelectrics could also have been used to look beyond the shallow anomalous layer in the inland regions, but the method is tedious to apply in the study area, due to difficulties in inserting the electrodes into the hard carbonates that often outcrop beneath a thin or inexistent soil layer. This geology also makes it difficult to maintain electrical contact between the electrodes and the geology. Applying borehole logging in private wells belonging to ranches gave a relatively good spatial distribution of data, which enabled the distinction of regional geological differences across the study area. Likewise, a relatively good spatial distribution across the study area could be obtained with the ground-based time-domain EM method, so that the regional shape of the freshwater lens could be delineated. As an additional advantage, carrying out ground-based field measurements gave an insight into the functioning of the study area which cannot always be obtained from desktop studies, because ground-based field work enables direct observation as well as discussions with local inhabitants.

Applying hydrological modelling as a method enables the estimation of a water balance. By comparing modelled water fluxes with values estimated in the literature, hydrological modelling of the Sian Ka'an catchment enabled the distinction between plausible and unlikely conceptualizations of the aquifer. Hydrological models are useful tools for delineating catchment areas and travel time zones. Such results are valuable within groundwater management. The use of the results for management is further discussed in the following Chapter 5.2. Moreover, the data collection and the hydrological modelling work have pointed to areas which should be given highest priority in future research efforts. These are discussed in Chapter 5.3.

5.2 Perspectives for management

5.2.1 Management setup for water resources

In Mexico, water is national property according to the Constitution, and is managed by the federal agency Comisión Nacional del Agua (aka. CONAGUA – the National Water Commission), as stipulated in the National Water Act ("Ley de Aguas Nacionales") from 1992, and its revision from 2004. CONAGUA is a relatively new institution. It was formed in 1989, and only in 2004 regional and state offices of CONAGUA were created (Sánchez Meza, 2006). In addition, three different types of decentralized management bodies exist, whose roles are to support CONAGUA: Water Basin Councils, Water Basin Commissions and Technical Committees. Not all types exist in all regions (Escolero et al., 2002). The Yucatan Peninsula, which is one hydrological-administrative region within CONAGUA, has a Water Basin Council. It is comprised of the CONAGUA director, representatives of different users (irrigation users, water abstraction companies etc.), representatives of federal, state and municipal agencies and societal organizations. The aim of the Water Basin Councils is to develop and implement programs and activities to improve water management and preserve the water resources in the basin (Sánchez Meza, 2006). Although CONAGUA bases some decisions on recommendations from the Basin Council in the Yucatan Peninsula (Merediz Alonso, 2007) the Basin Council itself has no executing power, and agreements made within the Council are not binding (Sánchez Meza, 2006; Vaux, 2007a). Water management is therefore solely the responsibility of CONAGUA at present, although several authors argue for the transfer of power from CONAGUA to decentralized bodies with multiple stakeholder participation, such as the Basin Councils (Sánchez Meza, 2006; Asad and Garduño, 2005; Vaux, 2007a). The responsibility to in practice carry out water abstraction and provide wastewater infrastructure, is authorized to state and sub-state institutions. In the study area this organization is Comisión de Agua Potable y Alcantarillado (CAPA). However, CONAGUA maintains the regulatory power and the overall responsibility for aquifer protection (Sánchez Meza, 2006).

As indicated by the relatively recent institutional development, groundwater management and use of hydrological sciences on a catchment scale is a relatively new field within Mexico. For example a register of the nationwide concessions to extract water was completed as recently as 2002 (Asad and Garduño, 2005) and the first water balance of a river basin in Mexico was made in 2003 (Arreguín-Cortés and López-Pérez, 2007). In Quintana Roo, only about 35 groundwater monitoring stations exist, and are solely located in the part of the state stretching from Tulum northward to Cancun (unpublished data from CONAGUA). The institutional capacity of CONAGUA is presently described as weak with respect to enforcement of the laws (Asad and Garduño, 2005). The water management setup is thus in a developing state. However, although there may be a difference between the aims and objectives of the water management institution, and what is in practice being carried out by it, it is clear that stakeholders and CONAGUA agree on that there is a need for groundwater monitoring (quality and quantity), maintaining a database on water-related datasets and sustainably developing the groundwater resources in the Yucatan Peninsula (Arreguín-Cortés and López-Pérez, 2007; Vaux, 2007a).

5.2.2 Use of the thesis results within water management on short time-scale

An important result of mapping the aquifer thickness, the estimation of recharge and the hydrological modelling of the study area (Gondwe et al. IV; V) is that the available water resources have been assessed for the first time in the region. From this it is clear that groundwater quantity does not appear to be a problem in relation to abstraction rates, except possibly in coastal areas where the freshwater lens is thin and hotel and urban demands may be high. The hydrological modelling results show that in the study area, focus in water management should first and foremost be on protecting groundwater quality. Water, and any associated pollutions, may travel far in a short time – e.g. 6.5 km/day, possibly even tens of kilometers pr. day (Beddows, 2003; Gondwe et al., V). The probability maps of the steady state groundwater catchment of Sian Ka'an and the travel time zones delineated in Gondwe et al. (V) are directly useful for protecting the groundwater quality. In a short-term perspective, these results could be taken into use immediately to guide management initiatives. Within a short time-scale, better information is unlikely to be attained, so although the results show a wide range of uncertainty depending on conceptual model and effective porosity used, authorities should act on these presently available working estimates. In spite of the uncertainty, they represent science-based knowledge on groundwater flow patterns previously unavailable for the area.

Typical tools for managing groundwater in karst are (Kacaroglu, 1999; Escolero et al., 2002; Merediz Alonso, 2007): land use zonation; pollution risk assessment and management; groundwater monitoring; increased public awareness of the value and vulnerability of the aquifer; and a Code of Practice reviewed in detail by Drew and Höltz (1999) and including e.g. highways design, solid wastes and toxic substances management, disposal of municipal sewage, control of seawater intrusion, spring protection and codes dealing with agricultural practices. A first step of implementing groundwater management in karst is the delineation of catchment areas of wells and wetlands. Such results outline the areas on which groundwater protection efforts should in general be focused, and therefore, the catchment probability maps in Gondwe et al. (V) are useful. In Europe, delineating catchments is required by the Water Framework Directive and is also done for karst wetlands, although it is often difficult (Kilroy et al., 2005). The difficulty of obtaining a precise catchment for a karst aquifer is illustrated in the case of Mammoth Cave in USA, where it took hundreds of dye tracing experiments and >20 years of investigations to ascertain the drainage network (Watson et al., 1997). Uncertainty in catchment delineation is therefore expected within karst, and should not be a justification for lack of action. Rather, being open with regard to the uncertainties of the model results may increase confidence in hydrological models, rather than keeping uncertainties secret, which may raise suspicion and skepticism. Model uncertainty does complicate decision- and policy making, but models without uncertainties are unrealistic. Instead, scenario testing is advocated (Ivanović and Freer, 2009). The results from using different conceptual models are a form of extended scenario testing. When uncertain estimates are involved, using the precautionary principle (e.g. Ivanović and Freer, 2009) or adaptive management (Vaux, 2007b) may be advocated.

Currently there is no legislation on groundwater protection zones in Mexico, neither for ecosystem nor for well protection. Milanović (2004) has suggested criteria which could be used (Table 1), primarily based on travel time zones. Thus, the travel time results could be used to guide land use zonation. With regard to travel times it is also worth noting that bacteria have a 50 day survival rate, while viruses may survive for 1 year (Kacaroglu, 1999).

In addition to Table 1, a new official standard in Mexico (Norma Oficial Mexicana NOM-014-CONAGUA-2003, available on http://dof.gob.mx/nota_detalle.php?codigo=5105753&fecha=18/08/2009), adopted in September 2009, regulates artificial infiltration of wastewater in Mexico. For the first time in Mexico, the travel time zone concept is used. The standard states that travel time from the recharge point of the wastewater to the extraction point should be at least 1 year for the type of infiltration allowed in karst. Although technically this applies only to groundwater abstraction points, it may provide a useful perspective for ecosystem protection in Mexico as well, supporting the use of travel times for protection of resources. The standard could provide the legal framework for the beginning of land use zonation. From modelled depths to groundwater, and actual evapotranspiration rates compared to potential evapotranspiration rates, Gondwe et al., (V) generated maps that showed ecosystems likely to be groundwater-dependent. These maps should also be used in the land use zonation.

Within the zones of importance, active and potential pollution activities should be mapped and possibly relocated, as suggested in Escolero et al. (2000; 2002). Compared to other catchments, the study area is not extensively developed yet. Therefore, if land use regulation is implemented now, it will be easier to enforce strict protection. An example of an activity which should be highly considered within the perspectives outlined in Table 1 is the location of a proposed airport near Tulum. Proposals have included sites atop the Holbox fracture zone. However, airports are known to yield high risks of pollution by leakage of fuels. Gondwe et al. (III) showed that the Holbox zone is likely to be a zone of high permeability. Therefore, locating the airport on this zone would be highly disadvantageous.

Table 1. Criteria for groundwater protection zonation in karst, proposed by Milanović (2004). The importance of regular groundwater monitoring in combination with implementation of the zones was emphasized in Milanović (2004).

		Delineation	Restrictions
Zone I	Protection area of spring/well	Min. 50 m from well/spring	Only water supply activities. Protect all karst openings. Prohibited: - public traffic, traffic infrastructure on conduits leading to Zone I - agriculture
Zone II	Very severe protection and restriction	24 hr travel time zone + any sinkholes connected with the well/spring + any sinkholes (and 20–30 m zone around them) located in Zone III but which communicate with the well/spring within 24 hrs	Strict control of all caves, sinkholes, shafts. No use of them for dumping of waste. All houses must have safe and water-tight septic tank. Prohibited: - transport and storage of dangerous materials, esp. low-degradable chemicals and oil tanks - industry - use of pesticides - waste disposal - settlements - roads - railroads - farms - quarries
Zone III	Protection area	E.g. 1–50 days travel time zone + all sinkholes outside Zone II in direct contact with the well/spring + all conduits in contact with the well/spring	All roads and settlements need effective drainage systems. Pesticide use should be strictly controlled. Prohibited: - use of sinkholes for waste dumping - chemical industry - oil tanks
Zone IV	External protection area	Rest of the catchment, with travel times > 50 days Areas with groundwater velocities <1 cm/s	Prohibited: - storage of radioactive material - storage of chemical wastes

5.2.3 Use of the thesis results within water management on long time-scale

On a longer time-scale, vulnerability mapping should be carried out. The use of travel-times for land use zonation is known to give very large areas of maximum protection in karst compared to in other types of aquifers. Protecting such large areas may not be practically possible. Instead, vulnerability mapping is a way to prioritize areas for protection in a science-based way, balancing groundwater protection and socioeconomic considerations (Kacaroglu, 1999; Milanović, 2004; Goldscheider, 2005).

A number of methods for vulnerability mapping of aquifers exist. For porous and fractured media they include DRASTIC (Aller et al., 1987); GOD (Foster, 1987); AVI (Van Stempoort et al., 1993); and the GLA method (aka. the "The German concept") (Hölting et al., 1995). Specifically for karst and carbonate aquifers, the methods include: EPIK (Doerfliger, 1996); SINTACS (Civita and De Maio, 1997); the Irish groundwater protection scheme (Daly and Drew, 1999); REKS (Malik and Svasta, 1999); the PI method (Goldscheider et al., 2000); VULK (Jeannin et al., 2001); the Time-Input-Method (Kralik, 2001); COP (Vías et al., 2004); COP+K (Andreo et al., 2009); LEA (Dunne, 2003); VURAAS (Laimer, 2005); and the Transit Time Method (Brosig et al., 2008). Numerous studies compare the different methods (e.g. Vías et al., 2005; Morales López, 2007). The overall principles of vulnerability mapping are to assess the resource vulnerability spatially by obtaining spatially distributed indexes for the degree of protection by overlying geologic and soil layers, the degree of concentrated inflow and the degree of precipitation intensity and quantity. These indexes may in karst be combined with a spatial assessment of the horizontal flow paths' effect on vulnerability. In the case of the study area, it would be most reasonable to use one of the vulnerability mapping techniques developed for karst. Which one to use should be decided upon by the decision-makers, since they should trust in the method in order to be able to have confidence in and use the results. The modelling results of the present study, which are directly applicable within vulnerability mapping, are depth to groundwater table and the geological structure maps. Vulnerability mapping was carried out in a sub-set of the study area around Tulum in a study by Morales López (2007). The study contains an exhaustive review of the approach step by step. This example could be imitated for the rest of the catchment area delineated by the hydrological modelling results. In the Tulum area, the aquifer was found to be 'extremely vulnerable' in a belt 0–10 km from the coast and 'highly vulnerable' further inland (Morales López, 2007).

Vulnerability mapping should be integrated into a groundwater protection scheme, and may be validated e.g. by tracer tests (Goldscheider, 2001; Goldscheider, 2005). Vulnerability maps can be coupled with hazard maps (detailed mapping of possible polluting activities) to generate risk maps. An elaborate example of how this may be done is found in e.g. Mimi and Assi (2009). Land use zonation could then be based on the risk map. Another form of risk assessment in karst has been carried out using quantitative groundwater tracing, as detailed in Field and Nash (1997).

A long term groundwater management solution, which is not directly related to the modelling results, is implementation of cleaner technology. For instance, artificial wetlands and composting toilets have been advocated for in order to deal with Quintana Roo's wastewater (Beddows, 2002; Morales López, 2007; Krekeler, 2007). City-wide sewage and wastewater treatment have elsewhere in the Peninsula been stated to be unlikely due to high economic costs (Marin et al., 2000). Cleaner technology could also be implemented with respect to e.g. design of highways (Drew and Höltz, 1999) and landfills (Morales López, 2007 and references herein). Technological advances may also be applied to solve the groundwater *quantity* problems which may exist or develop along the coasts, through the implementation of water-saving initiatives and technologies. Improved water distribution infrastructure may also be required. In an example from Yucatan State, the distribution system was pointed out to be reason for loss of as much as 50% of the water abstracted from the aquifer (Marin et al., 2000).

Finally, compensation schemes have been suggested on a long-term, as part of a land use zonation program, in order to protect critical recharge areas in the catchments (Gondwe et al., 2010). The idea is to create a fund with money from water fees collected from the large tourist resorts. This money should then be used to compensate landowners in the critical recharge areas, in order to provide incentive to preserve the land in a pristine state and prevent polluting activities.

The above-mentioned actions deal with threats to the groundwater which are created by local human activity. Another threat, which has not been dealt with in the research of the thesis, is the threat from global climate changes. Central

America is a climate change hotspot. A regional climate model has predicted a 40% reduction in rainy season precipitation (May–Oct) using the Intergovernmental Panel for Climate Change's A2 scenario for the year 2100, that represents a heterogeneous world with substantial population growth (Karmalkar et al., 2009). Other climate change scenarios used in other climate models also predict a reduction in precipitation over the study area (e.g. Neelin et al., 2006; Christensen et al., 2007). A reduction in precipitation will likely mean a reduction of recharge to the aquifer. In a long-term perspective this would mean a decrease in the volumes of freshwater in the aquifer and a thinner freshwater lens. The latter could give a higher susceptibility to up-coning of saltwater during water abstraction, mainly near the coasts. Less rainfall could also give higher concentrations of groundwater pollutants, due to reduced dilution. For Sian Ka'an's wetlands, reduction in the precipitation amounts could change the length of the hydroperiod, which could have consequences for the ecosystems. Likewise a change in the precipitation patterns could affect the hydroperiod distribution patterns, which are also important for wetland ecosystem functioning. Potential sea level changes, caused by climate changes, would also affect Sian Ka'an's ecosystems, as they are low-lying and coastal. The impact depends on the magnitude of sea level change, and can best be predicted if better micro-topographic maps of Sian Ka'an become available. Possible sea level rises of 19 cm to 1 m by year 2100 have been mentioned (Meehl et al., 2007; Painter, 2009). A higher sea level would likely flood parts of Sian Ka'an's wetlands with saltwater, which could give changes in the ecosystem distribution.

5.3 Future research directions

Future research directions within the catchment of Sian Ka'an should mainly focus on obtaining more data on the catchment, and feeding it into the existing models. It is still required to mainly work on a large scale. The Multiple Model Simulation and scenarios to investigate the impact of input parameter uncertainty (Gondwe et al., V) showed that the present hydrological models developed are not yet robust. However, their results indicate the way forward. With more data improved models can be built or extracted from the conceptual models presented. The modelling results indicated where it would be worthwhile to focus future efforts for characterization and management of Sian Ka'an's catchment. The main points are: characterizing the nature of the structures; determining better the travel times and effective porosities within the catchment; investigating the flow within the Holbox fracture zone; determining coastal leakage; and further investigating the role of the hilly area for Sian Ka'an's catchment.

The differences between the conceptual models showed that it is important to further investigate the properties of the structures – specifically whether or not they conduct water flow more easily than the surrounding matrix. The properties of the structures could be investigated through geophysical measurements, direct drillings into the structures and flow measurements within and outside structures.

Dye tracing and/or testing with other tracers could be carried out in the zones likely to be part of the short groundwater travel-time zones, in order to better determine the value of the effective porosity, and the extent of the travel time zones. Dye tracing can yield useful results, such as mean residence time, mean flow velocities, dispersivity data and conduit geometric parameters useful for further detailed groundwater transport modelling (Field and Nash, 1997).

Quantification and characterization (e.g. temporally) of the flow through the Holbox fracture zone would be useful in order to determine whether the high flows simulated in Conceptual Model 3, 4 and 6 are realistic, or the outflows from Model 7 appear more reasonable (see Gondwe et al., V). Besides determining which conceptual model is more plausible, such a quantification might also be able to narrow down the uncertainty on the recharge estimate, as it was seen that the Holbox outflow was sensitive to variations in the recharge estimate (and, to a smaller degree, sensitive to the variations in the Holbox fixed head boundary level). Investigations of the Holbox flow could for instance be carried out using flow-meters inserted into some of the many sinkholes atop the Holbox zone, and possibly through dye tracing.

If it would be possible to measure or estimate total groundwater outflow along the coast of Sian Ka'an the uncertainty on the recharge input could be minimized, since this outflow is of the same magnitude in spite of which conceptual model is used. Identification of submarine springs along Sian Ka'an's coast and measurements of their outflow could be a first-order approach to this, although it is expected to be a tedious and costly affair, as the submarine springs are likely to be numerous. Furthermore, the results would be highly uncertain, since a large part of the outflow is expected to also take place through the aquifer matrix. If it could be determined whether leakage appears larger at the northern part of the coast around Tulum than in the remaining coastline of the domain, such investigation could – together with the structure properties analysis – enable determination of whether Conceptual Model 4 or 7 is more likely.

The present plausible hydrological models indicate that inflow from the Cretaceous area to the Pliocene geology may be important. However the extent of the catchment in the hilly, Cretaceous region has not been explored. The similarity between Conceptual Model 4 and 5 indicates that the surface water catchments delineated in the hilly area may indeed be related to groundwater catchments in this area (Gondwe et al., V). These surface water catchments may be an acceptable first order approach to determine where the water in the hilly area comes from. However, further studies of the hilly area's hydrogeology are warranted. A better conceptualization could enable the inclusion of this area into a distributed hydrological model which could give an improved spatial understanding and zonation of the catchment. In addition, the extent of the model domain, especially along the western boundary, should be checked, to ensure that areas further west do not influence the hydrology of Sian Ka'an.

Finally, although not a research direction per se, an important measure to implement in the future is a dense monitoring network of groundwater heads, flows and quality. Monitoring data with a representative spatial and temporal resolution are absolutely essential both for the understanding and modelling of the water resources of the area, and for the management of these resources. CONAGUA, as the responsible agency, should ensure that an effective monitoring system is implemented in the region as soon as possible.

6 References

Acreman, M., Dunbar, M.J., 2004. Defining environmental river flow requirements – a review. Hydrol. and Earth Syst. Sci. 8 (5), 861–876.

Al-fares, W., Bakalowicz, M., Guérin, R., Dukhan, M., 2002. Analysis of the karst aquifer structure of the Lamalou area (Hérault, France) with ground penetrating radar. J. Applied Geophysics 51, 97–106.

Aller, L., Bennet, T., Lehr, J.H., Petty, R.J., 1987. DRASTIC: a standardized system for evaluating ground water pollution potential using hydrogeological settings. U.S. Environmental Protection Agency Report EPA-600/2-87-035. 622 pp.

Alsdorf , D.E., Melack, J.M., Dunne, T., Mertes, L.A.K., Hess, L.L., Smith, L.C., 2000. Interferometric radar measurements of water level changes on the Amazon floodplain. Nature 404, 174–177.

Alsdorf, D.E., Smith, L.C., Melack, J.M., 2001. Amazon floodplain water level changes measured with interferometric SIR-C radar. IEEE Transactions on Geoscience and Remote Sensing 39, 423–431.

Alsdorf, D.E., Rodríguez, E., Lettenmaier, D.P., 2007a. Measuring surface water from space. Reviews of Geophysics 45, RG2002. 24 pp.

Alsdorf, D., Bates, P., Melack, J., Wilson, M., Dunne, T., 2007b. Spatial and temporal complexity of the Amazon flood measured from space. Geophysical Research Letters 34, L08402. doi:10.1029/2007GL029447.

Andreo, B., Ravbar, N., Vías, J.M., 2009. Source vulnerability mapping in carbonate (karst) aquifers by extension of the COP method: application to pilot sites. Hydrogeol. J. 17, 749–758. doi: 10.1007/s10040-008-0391-1.

Amelung, F., Galloway, D.L., Bell, J.W., Zebker, H.A., Laczniak, R.J., 1999. Sensing the ups and downs of Las Vegas: InSAR reveals structural control of land subsidence and aquifer-system deformation. Geology 27, 483–486.

Archie, G.E., 1942. The electrical resistivity log as an aid in determining some reservoir characteristics. T. Am. Inst. Mineral. Metall. Petrol. Eng. 146, 54–62.

Arfib, B., de Marsily, G., 2004. Modeling the salinity of an inland coastal brackish karstic spring with a conduit-matrix model. Water Resour. Res. 40 (11), W115061–W1150610.

Arreguín-Cortés, F., López-Pérez, M., 2007. An overview of Mexico's water regime and the role of groundwater. p. 13–26 in: Holliday, L., Marin, L., Vaux, H. (Eds.). Sustainable management of groundwater in Mexico: Proceedings of a Workshop (Series: Strengthening science-based decision making in developing countries). National Research Council. The National Academies Press, Washington D.C., USA. ISBN: 0-309-10583-8.

Asad, M., Garduño, H., Water resources management in Mexico: The role of the Water Rights Adjustment Program (WRAP). Sustainable Development Working Paper No. 24. 34636. The World Bank, Latin America and the Caribbean Region, Environmentally and Socially Sustainable Development Department. 73 pp.

ASK, 2003. Tratamiento de Aguas Residuales. Report prepared by Amigos de Sian Ka'an A. C. (ASK). Available on the cd-rom of the workshop: Construyendo las Bases Para la Conservación del Agua y su Biodiversidad Asociada en la Península de Yucatan". 10 y 11 de noviembre 2003, Cancún Quintana Roo, Organizado por Amigos de Sian Ka'an, The Nature Conservancy y la Comisión de Áreas Naturales Protegidas.

Atkinson, T.C., 1977. Diffuse flow and conduit flow in limestone terrain in the Mendip Hills, Somerset (Great Britain). J. Hydrol. 35, 93–110.

Auken, E., Guerin, R., de Marsily, G., Sailhac, P., 2009. Hydrophysics foreword. Comptes Rendus Geoscience 341 (10–11), 795–799. doi: 10.1016/j.crte.2009.09.003.

Avdeev, D.B., 2005. Three-dimensional electromagnetic modelling and inversion from theory to application. Surveys in Geophysics 26, 767–799.

Back, W., Hanshaw, B.B., 1970. Comparison of chemical hydrogeology of the carbonate peninsulas of Florida and Yucatan. J. Hydrol. 10, 330–368.

Back, W., Lesser, J.M., 1981. Chemical constraints of groundwater management in the Yucatan Peninsula, Mexico. J. Hydrol. 51, 119–130.

Back, W., Hanshaw, B., Herman, J.S., Van Driel, J.N., 1986. Differential dissolution of a Pleistocene reef in the ground-water mixing zone of coastal Yucatan, Mexico. Geol. 14, 137–140.

Bakalowicz, M., 2005. Karst groundwater: a challenge for new resources. Hydrogeol. J. 13, 148–160. doi: 10.1007/s10040-004-0402-9.

Barfield, B.J., Felton, G.K., Stevens, E.W., McCann, M., 2004. A simple model of karst spring flow using modified NRCS procedures. J. Hydrol. 287, 34–48.

Batu, V., 1998. Aquifer hydraulics: a comprehensive guide to hydrogeologic data analysis. Wiley-IEEE. 727 pp. ISBN: 0-471-18502-7.

Bauer, S., 2002. Simulation of the genesis of karst aquifers in carbonate rocks. Tübinger Geowissenshaftliche Arbeiten, Vol. 62. Reihe C. Institut und Museum für Geologie und Paäontologie der Universität Tübingen. Tübingen, Germany. 143 pp.

Bauer, S., Liedl, R., Sauter, M., 2003. Modeling of karst aquifer genesis: influence of exchange flow. Water Resour. Res. 39 (10), SBH61–SBH612.

Bauer-Gottwein, P., Gondwe, B.N., Christiansen, L., Herckenrath, D., Kgotlhang, L., Zimmermann, S., 2010. Hydrogeophysical exploration of three-dimensional salinity anomalies with the time-domain electromagnetic method (TDEM). J. Hydrol. 380 (3–4), 318–329. doi: 10.1016/j.jhydrol.2009.11.007.

Bautista, F., Quintana, P., Aguilar Duarte, Y., Pacheco, J., Cabañas, D., 2009. Programa General. Seminario: Análisis de la vulnerabilidad y riesgo de contaminación de las aguas subterráneas en la Península de Yucatán. Mérida, Yucatán, 10–11 December 2009.

Beddows, P.A., 2002. Where does the sewage go? The karst groundwater system of Municipalidad Solidaridad, Quintana Roo. Assoc. for Mex. Cave Stud. Activities Newsl. 25, 47–52.

Beddows, P.A., 2003. Cave hydrology of the Caribbean Yucatan coast. Assoc. for Mex. Cave Stud.. Bull. 11. Austin, TX, USA.

Beddows, P.A., 2004. Groundwater hydrology of a coastal conduit carbonate aquifer: Caribbean coast of the Yucatán Peninsula, México. PhD thesis. Sch. of Geogr. Sci.. Univ. of Bristol, UK.

Beddows, P.A., Smart, P.L., Whitaker, F.F., Smith, S.L., 2007. Decoupled fresh-saline groundwater circulation of a coastal carbonate aquifer: Spatial patterns of temperature and specific electrical conductivity. J. Hydrol. 346, 18–32.

Beddows, P.A., Hendrickson, M.R., 2008. When the survey is not enough: temperature, salinity and dye tracing reveal flow paths. p. 198–203 in: Elliott, W.R. (Ed.). Proceedings of the 18th National Cave and Karst Management Symposium, St. Louis, USA.

Beres, M., Luetscher, M., Olivier, R., 2001. Integration of ground-penetrating radar and microgravimetric methods to map shallow caves. J. Applied Geophysics 46, 249–262.

Berg, R.R., 1970. Method for determining permeability form reservoir rock properties. T. Gulf Coast Assoc. Geol. Soc. 20, 303–317.

Berry, P.A.M., Garlick, J.D., Freeman, J.A., Mathers, E.L., 2005. Global inland water monitoring from multi-mission altimetry. Geophysical Research Letters 32, L16401. doi: 10.1029/2005GL022814.

Birk, S., 2002. Characterization of karst systems by simulating aquifer genesis and spring responses: model development and application to gypsum karst. Tübinger Geowissenshaftliche Arbeiten, Vol. 60. Reihe C. Institut und Museum für Geologie und Paäontologie der Universität Tübingen. Tübingen, Germany. 122 pp. ISSN: 1610-4706. Accessed at http://tobias-lib.uni-tuebingen.de/volltexte/2002/558/pdf/tga_c60.pdf in Jan 2010.

Birk, S., Liedl, R., Sauter, M., Teutsch, G., 2003. Hydraulic boundary conditions as a controlling factor in karst genesis: a numerical modeling study on artesian conduit development in gypsum. Water Resour. Res. 39 (1), SBH21–SBH214.

Block, P., Souza Filho, F.A., Sun, L., Kwon, H.-H., 2009. A streamflow forecasting framework using multiple climate and hydrological models. J. Am. Water Res. Assoc. 45 (4), 828–843. doi: 10.111/j.1752-1688.2009.00327.x.

Bosch, F., Müller, I., 2005. Improved karst exploration by VLF-EM gradient surveys: comparison with other geophysical methods. Near Surf. Geophys. 3, 299–310.

Boucher, M., Girard, J.-F., Legchenko, A., Baltassat, J.-M., Dörfliger, N., Chalikakis, K., 2006. Using 2D inversion of magnetic resonance soundings to locate a water-filled karst conduit. J. Hydrol. 330, 413–421.doi: 10.1016/j.jhydrol.2006.03.034.

Bourgeau-Chavez, L.L., Smith, K.B., Brunzell, S.M., Kasischke, E.S., Romanowicz, E.A., Richardson, C.J., 2005. Remote monitoring of regional inundation patterns and hydroperiod in the Greater Everglades using synthetic aperture radar. Wetlands 25, 176–191.

Brosig, K., Geyer, T., Subah, A., Sauter, M., 2008. Travel time based approach for the assessment of vulnerability of karst groundwater: the Transit Time Method. Environ. Geol. 54, 905–911. doi: 10.1007/s00254-007-0898-0.

Brunner, P., Hendricks Franssen, H.-J., Kgotlhang, L., Bauer-Gottwein, P., Kinzelbach, W., 2007. How can remote sensing contribute in groundwater modeling? Hydrogeol. J. 15, 5–18. doi: 10.1007/s10040-006-0127-z.

Bürgmann, R., Rosen, P.A., Fielding, E.J., 2000. Synthetic aperture radar interferometry to measure Earth’s surface topography and its deformation. Annu. Rev. Earth Planet. Sci. 28, 169–209.

Chen, C.W., Zebker, H.A., 2001. Two-dimensional phase unwrapping with use of statistical models for coast functions in nonlinear optimization. J. Opt. Soc. Amer. A 18, 338–351.

Cheng, J.M, Chen, C.X., 2005. An integrated linear/non-linear flow model fort he conduit-fissure-pore media in the karst triple void aquifer system. Environ. Geol., 47, 163–174. doi: 10.1007/s00254-004-1128-7.

Chib, S., Greenberg, E., 1995. Understanding the Metropolis-Hastings algorithm. The American Statistician 49 (4), 327–335.

Chow, V.T. Maidment, D.R., Mays, L.W., 1988. Applied hydrology. McGraw-Hill Series in Water Resources and Environmental Engineering. Singapore. 1988. ISBN 0-07-100174-3. 572 pp.

Christensen, J.H., Hewitson, B., Busuioc, A., Chen, A., Gao, X., Held, I., Jones, R., Kolli, R.K., Kwon, W.-T., Laprise, R., Magaña Rueda, V., Mearns, L., Menéndez, C.G., Räisänen, J., Rinke, A., Sarr, A., Whetton, P., 2007. Regional climate projections. In: Solomon, S., Qin, D., Manning, M., Chen, Z., Marquis, M., Averyt, K.B., Tignor, M., Miller, H.L. (Eds.). Climate Change 2007: The Physical Science Basis. Contribution of Working Group I to the Fourth Assessment Report of the Intergovernmental Panel on Climate Change. Cambridge University Press, Cambridge, United Kingdom and New York, NY, USA.

Christiansen, A.V., Auken, E., Sørensen, K., 2006. The transient electromagnetic method. Chapter 6 in: Kirsch, R. (Ed.), Groundwater geophysics – A tool for hydrogeology. Springer. ISBN: 3-540-29383-3.

Civita, M., De Maio, M., 1997. SINTACS – Un sistema parametric per la valtazione e la cartografia della vulnerabilitá degli acquiferi all' inquinamento. Metodologia & automatizzazione (SINTACS – a parametrical system for assessment and vulnerability mapping of aquifer pollution). Collana "Quaderni di Techniche di Protezione Ambientale" 60, 208 pp.

Clemens, T., 1998. Simulation der Entwicklung von Karstaquiferen. PhD dissertation submitted to Eberhard-Karls Universtät Tübingen, Germany.

Coppo, N., Schnegg, P.-A., Défago, M., GSCB, 2006. Mapping a shallow large cave using a high-resolution Very Low Frequency electromagnetic method. p. 71–74 in Goldscheider, N., Mudry, J., Savoy, L., Zwahlen, F. (Eds.). Proceeding of the 8th conference on limestone hydrogeology, 2006, Neuchätel, Switzerland. ISBN 2-87867-143-2.

Cornaton, F., Perrochet, P., 2002. Analytical 1D Dual-Porosity Equivalent Solutions to 3D Discrete Single-Continuum Models. Application to Karstic Spring Hydrgraph Modelling. J. Hydrol. 262, 165–176.

Dalton, F.N., Herkelrath, W.N., Rawlins, D.S., Rhoades, J.D., 1984. Time-domain reflectometry – simultaneous measurement of soil-water content and electrical-conductivity with a single probe. Science 224, 989–990.

Daly, D., Drew, D., 1999. Irish methodologies for karst aquifer protection. p. 267–272 in: Beck, B.F., Pettit, A.J. and Herring, J.G. (Eds.). Hydrogeology and Engineering geology of sinkholes in karst. Balkema, Rotterdam, The Netherlands. ISBN: 9-0580-9046-9.

Daniels, J., 1988. Locating caves, tunnels and mines. Geophysics: The Leading Edge of Exploration. 32–52.

Doerfliger, N., 1996. Advances in karst groundwater protection strategy using artificial tracer tests analysis and multiattribute vulnerability mapping (EPIK Method). PhD thesis. University Neuchâtel. 308 pp.

Doll, W.E., Nyquist, J.E., Beard, L.P., Gamey, T.J., 2000. Airborne geophysical surveying for hazardous wast site characterization on the Oak Ridge Reservation, Tennessee. Geophys. 65 (5), 1372–1387.

Doolittle, J., Collins, M., 1998. A comparison of EM and GPR methods in areas of karst. Geoderma 85, 83–102.

Drew, D.P., Höltz, H., 1999. The management of karst environments. pp. 259–273 in : Drew, D.P., Höltz, H. (Eds.). Karst hydrogeology and human activities. Impacts, consequences and implications. IAH International Contributions to Hydrogeology 20. A.A. Balkema, Rotterdam, The Netherlands. ISBN: 9-0541-0464-3.

Dunne, S., 2003. Vulnerability mapping for the protection of UK karst aquifers. PhD thesis. Geography Department, Trinity College Dublin, Ireland.

Durlofsky, L.J., 1992. Representation of grid block permeability in course scale models of randomly heterogeneous porous media. Water Resour. Res. 28 (7), 1791–1800.

Eamus, D., Froend, R., 2006. Groundwater-dependent ecosystems: the where, what and why of GDEs. Aust. J. of Bot. 54, 91–96.

Ernstson, K., Kirsch, R., 2006. Aquifer structures: fracture zones and caves. Chapter 13 in in: Kirsch, R. (Ed.), Groundwater geophysics – A tool for hydrogeology. Springer. ISBN: 3-540-29383-3.

Escolero, O.A., Marin, L.E., Steinich, B., Pacheco, J., 2000. Delimitation of a hydrogeological reserve for a city within a karstic aquifer: the Merida, Yucatan example. Landsc. and Urban Plan. 51, 53–62.

Escolero, O.A., Marin, L.E., Steinich, B., Pacheco, J., 2002. Development of a protection strategy of karst limestone aquifers: The Merida Yucatan, Mexico case study. Water Resour. Manage. 16, 351–367.

Ferré, T., Bentley, L., Binley, A., Linde, N., Kemna, A., Singha, K., Holliger, K., Huisman, J.A., Minsley, B., 2009. Critical steps for the continuing advancement of hydrogeophysics. EOS Trans. AGU 90 (23). doi: 10.1029/2009EO230004.

Fideicomiso para la Promoción Turística de la Rivera Maya, 2006. Resumen de la actividad turistica 2005. Power Point presentation obtained from the Fideicomiso.

Field, M.S., Nash, S.G., 1997. Risk assessment methodology for karst aquifers: (1) Estimating karst conduit flow parameters. Environ. Monitoring and Assessment 47, 1–21.

Ford, D.C., Williams, P., 2007. Karst hydrogeology and geomorphology. Chichester, Wiley. ISBN: 978-0-470-84997-2. 576 pp.

Foster, S., 1987. Fundamental concepts in aquifer vulnerability, pollution risk and protection strategy. In: Van Duijvenbooden, W., Van Waegeningh, H.G. (Eds.). Vulnerability of soil and groundwater to pollutants. Proc. Inf. TNO Comm. Hydrol. Res., The Hague, The Netherlands 68, 69–86.

Foster, J., Brooks, B., Cherubini, T., Chacat, C., Businger, S., Werner, C.L., 2006. Mitigating atmospheric noise for InSAR using a high resolution weather model. Geophysical Research Letters 33, L16304. doi: 10.1029/2006GL026781.

Fouke, B.W., Zerkle, A.L., Alvarez, W., Pope, K.O., Ocampo, A.C., Wachtman, R.J., Grajales Nishimura, J.M., Claeys, P., Fischer, A.G.., 2002. Cathodoluminescence petrography and isotope geochemistry of KT impact ejecta deposited 360 km from the Chicxulub crater, at Albion Island, Belize. Sedimentol. 49, 117–138.

Gamey, T. J., Thompson, M., Mandell, W., Frano, G., 2001. Karst pathway delineation using combined spatial and geophysical analysis at Camp Crowder, Missouri. In Abstracts with Programs, Geol. Soc. Am. 33 (6), 132.

Georgakakos, K., Seo, D.-J., Gupta, H., Shaake, J., Butts, M.B., 2004. Towards the characterization of streamflow simulation uncertainty through multimodel ensembles. J. Hydrol. 298, 222–241. doi: 10.1016/j.jhydrol.204.03.037.

Ghiglia, D.C., Pritt, M.D., 1998. Two-dimensional phase unwrapping: theory, algorithms and software. Wiley Interscience. 493 pp.

Goldman, M., Gilad, D., Ronen, A., Melloul, A., 1991. Mapping of seawater intrusion into the coastal aquifer of Israel by the time domain electromagnetic method. Geoexplor. 28 (2), 153–174. doi: 10.1016/0016-7142(91)90046-F.

Goldscheider, N., Klute, M., Sturm, S., Hötzl, H., 2000. The PI method: a GIS-based approach to mapping groundwater vulnerability with special consideration of karst aquifers. Z. Angew. Geol. 463, 157–166.

Goldscheider, N., Hötzl, H., Fries, W., Jordan, P., 2001. Validation of a vulnerability map (EPIK) with tracer tests. 7th Conference on Limestone Hydrology and Fissured Media. Besancon, France, 20–22 Sept. 2001. Sci. Tech. Environ. Mém. 13, 167–170.

Goldscheider, N., 2005. Karst groundwater vulnerability mapping: application of a new method in the Swabian Alb, Germany. Hydrogeol. J. 13 (4), 555–564.

Goldstein, R.M., Zebker, H.A., Werner, C.L., 1988. Satellite radar interferometry - two-dimensional phase unwrapping. Radio Science 23, 713–720.

Goldstein, R.M., Engelhardt, H., Kamb, B., Frolich, R.M., 1993. Satellite radar interferometry for monitoring ice-sheet motion - Application to an Antarctic ice stream. Science 262, 1525−1530.

Gondwe, B.N., Bauer-Gottwein, P., Merediz-Alonso, G., Fregoso, A., Supper, R., 2010. Groundwater resources management in Quintana Roo, Mexico: Problems, scientific tools and policy. In: Friedman, M.J. (Ed.): Global water issues. U.S. Department of State, Bureau of International Information Programs. In press.

González-Herrera, R, Sánchez-y-Pinto, I., Gamboa-Vargas, J., 2002. Groundwater-flow modeling in the Yucatan karstic aquifer, Mexico. Hydrogeol. J. 10, 539–552.

Grajales-Nishimura, J.M., Cedillo-Pardo, E., Rosales-Domínguez, C., Morán-Zenteno, D.J., Alvarez, W., Claeys, P., Ruíz-Morales, J., García-Hernández, J., Padilla-Avila, P., Sánchez-Ríos, A., 2000. Chicxulub impact: the origin of reservoir and seal facies in the southeastern Mexico oil fields. Geol. 28 (4), 307–310.

Grayson, R.B., Blöschl, G., Western, A.W., McMahon, T.A., 2002. Advances in the use of observed spatial patterns of catchment hydrological response. Advances in Water Resources 25, 1313–1334.

Grecu, M., Olson, W.S., 2006. Bayesian estimation of precipitation from satellite passive microwave observations using combined radar-radiometer retrievals. J. of Applied Meteorology and Climatology 45, 416–433.

Groom, R., Alvarez, C., 2002. 3D EM modelling application of the localized non-linear approximator to near surface applications. Abstract, SAGEEP 2002. Accessed from URL: www.petroseikon.com in December 2007.

Guérin, R., Benderitter, Y., 1995. Shallow karst exploration using MT-VLF and DC resistivity methods. Geophys. Prospect. 43, 635–653.

Guérin, R., Baltassat, J.-M., Boucher, M., Chalikakis, K., Galibert, P.-Y., Girard, J.-F., Plagnes, V., Valois, R., 2009. Geophysical characterization of karstic networks - Application to the Ouysse system (Poumeyssen, France). Comptes Rendous Géoscience. doi: 10.1016/j.crte.2009.08.005.

Hackert, C.L., Parra, J.O., 2003. Estimating scattering attenuation from vugs or karsts. Geophysics 68 (4), 1182–1188.

Halihan, T., Wicks, C. M., 1998. Modeling of Storm Responses in Conduit Flow Aquifers with Reservoirs. J. Hydrol. 208, 82–91.

Hanshaw, B.B., Back, W.,1980. Chemical mass-wasting of the northern Yucatan Peninsula by groundwater dissolution. Geol., 8, 222–224.

Hanssen, R. F., 2001. Radar interferometry – data interpretation and error analysis. Remote Sensing and Digital Image Processing Series. Kluwer Academic Publishers, Dordrecht, The Netherlands. ISBN: 0-7923-6945-9.

Hastings, W.K., 1970. Monte Carlo sampling methods using Markov chains and their applications. Biometrika 57 (1), 97–109.

Henderson, F.M., Lewis, A.J., 2008. Radar detection of wetland ecosystems: a review. International Journal of Remote Sensing 29 (20), 5809–5835. doi: 10.1080/01431160801958405.

Hendricks Franssen. H.-J., Stauffer, F., Kinzelbach, W., 2004. Joint estimation of transmissivities adn recharges – application: stochastic characterization of well capture zones. J. Hydrol. 294, 87–102. doi: 10.1016/j.jhydrol.2003.10.021.

Henson, H., Sexton, J., Henson, M., Jones, P., 1997. Georadar investigation of karst in a limestone quarry near Anna. 67th Ann. Internat. Meet. SEG, 763–767.

Hess, L.L., Melack, J.M., Simonette, D.S., 1990. Radar detection of flooding beneath the forest canopy: a review. Int. J. Remote Sens. 5, 1313–1325.

Hess, L.L., Melack, J.M., Filoso, S., Wang, Y., 1995. Delineation of inundated area and vegetation along the Amazon floodplain with the SIR-C synthetic aperture radar. IEEE Transactions on Geoscience and Remote Sensing 33 (4), 896–904.

Hess, L.L., Melack, J.M., Novo, E.M.L.M., Barbosa, C.C.F., Gastil, M., 2003. Dual-season mapping of wetland inundation and vegetation for the central Amazon basin. Remote Sensing of Environment 87, 404–428. doi:10.1016/j.rse.2003.04.001.

Hinsby, K., Condesso de Melo, M.T., Dahl, M., 2008. European case studies supporting the derivation of natural background levels and groundwater threshold values for the protection of dependent ecosystems and human health. Sci. Total Environ. 401, 1–20. doi: 10.1016/j.scitotenv.2008.03.018.

Holliday, L., Marin, L., Vaux, H. (Eds.), 2007. Sustainable management of groundwater in Mexioc: Proceedings of a Workshop (Series: Strengthening science-based decision making in developing countries). National Research Council. The National Academies Press, Washington D.C., USA. 126 pp. ISBN: 0-309-10583-8.

Hölting, B., Haertle, T., Hohberger, K.H., Nachtigall, K.H., Villinger, E., Weinzierl, W., Wrobel, J.P., 1995. Konzept zur Ermittlung der Schutzfunktion der Grundwasserüberdeckung (Concept of protection assessment of the groundwater ocver). Geologisches Jahrbuch C63, Hannover, Germany. 5–24.

Hornberger, G.M., Raffensperger, J.P., Wiberg, P.L., Eshleman, K.N., 1998. Elements of physical hydrology. The Johns Hopkins University Press. Baltimore and London. ISBN: 0-8018-5856-9. 302 pp.

Hückinghaus, D., 1998. Simulation der Aquifergenese und des Wärmetransports in Karstaquiferen. Tübinger Geowissenshaftliche Arbeiten, Vol. 42. Reihe C. Institut und Museum für Geologie und Paäontologie der Universität Tübingen. Tübingen, Germany. 124 pp. ISSN: 1610-4706. Accessed at http://tobias-lib.uni-tuebingen.de/volltexte/2005/2030/pdf/42.pdf in Jan 2010.

Hudson, P.F., Colditz, R.R., 2003. Flood delineation in a large and complex alluvial valley, lower Pánuco basin, Mexico. J. Hydrol. 280, 229–245. doi: 10.1016/S0022-1694(03)00227-0.

Højberg, A.L., Refsgaard, J.C., 2005. Model uncertainty – parameter uncertainty versus conceptual models. Water Sci. and Technol. 52 (6), 177–186.

Islam, M.A., Thenkabail, P.S., Kulawardhana, R.W., Alankara, R., Gunasinghe, S., Edussriya, C., Gunawardana, A., 2008. Semi-automated methods for mapping wetlands using Landsat ETM+ and SRTM data. Int. J. Remote Sens. 29 (24), 7077–7106. doi: 10.1080/01431160802235878.

Ivanović, R.F., Freer, J.E., 2009. Science versus politics: truth and uncertainty in predictive modelling. Hydrological Processes 23, 2549–2554. doi: 10.1002/hyp.7406.

Jeannin, P.-Y., 2001. Modeling Flow in Phreatic and Epiphreatic Karst Conduits in the Hölloch Cave (Muotatal,Switzerland). Water Resour. Res. 37 (2), 191–200.

Jeannin, P.Y., Cornaton, F., Zwahlen, F., Perrochet, P., 2001. VULK: a tool for intrinsic vulnerability assessment and validation. 7th Conference on Limestone Hydrology and Fissured Media. Besancon, France, 20–22 Sept. 2001. Sci. Tech. Environ. Mém. 13, 185–190.

Kacaroglu, F., 1999. Review of groundwater pollution and protection in karst areas. Water, Air and Soil Pollution 113, 337–356.

Kafri, U., Goldman, M., 2005. The use of the time domain electromagnetic method to delineate saline groundwater in granular and carbonate aquifers and to evaluate their porosity. J. Applied Geophys. 57, 167–178. doi: 10.1016/j.jappgeo.2004.09.001.

Karmalkar, A.V., Bradley, R.S., Diaz, H.F., 2009. Regional hydrological response to climate change in Mexico and Central America. AGU Fall Meeting 2009, San Francisco, USA, 14–18 Dec. 2009. Abstract A33A-0219.

Kasischke, E.S., Melack, J.M., Dobson, M.C., 1997. The use of imaging radars of ecological applications – a review. Remote Sens. Environ. 59, 141–156.

Kaufmann, G., 2003. A model comparison of karst aquifer evolution for different matrix-flow formulations. J. Hydrol. 283 (1–4), 281–289. doi: 10.1016/S0022-1694(03)00270-1.

Kenkmann, T., Schönian, F., 2006. Ries and Chicxulub: Impact craters on Earth provide insights for Martian ejecta blankets. Meteorics and Planet. Sci. 41 (10), 1587–1603.

Kilroy, G., Coxon, C., Ryan, J., O'Connor, Á, Daly, D., 2005. Groundwater and wetland management in the Shannon river basin (Ireland). Environ. Sci. and Policy 8, 219–225. doi: 10.1016/j.envsci.2005.03.001.

Kim, S.-W., Wdowinski, S., Amelung, F., Dixon, T.H., 2005. C-band interferometric SAR measurements of water level change in the wetlands: examples from Florida and Louisiana. Geoscience and Remote Sensing Symposium. IGARSS '05. IEEE International 4, 2708−2710.

Kim, J.-W., Lu, Z., Lee, H., Shum, C.K., Swarzenski, C.M., Doyle, T.W., Baek, S.-H., 2009. Integrated analysis of PALSAR/Radarsat-1 InSAR and ENVISAT altimeter data for mapping of absolute water level changes in Louisiana wetlands. Remote Sensing of Environment 113, 2356–2365. doi: 10.1016/j.rse.2009.06.014.

Kiraly, L., 2003. Karstification and groundwater flow. Speleogenesis and Evolut. of Karst Aquifers 1 (3). 26 pp.

Kirsch, R., 2006. Electromagnetic methods – frequency domain. Ground based techniques. Chapter 5.2 in: Kirsch, R. (Ed.), Groundwater geophysics – A tool for hydrogeology. Springer. ISBN: 3-540-29383-3.

Klein, J., Lajoie, J., 1980. Electromagnetic prospecting for minerals. Practical Geophysics for the Exploration Geologist. Northwest Mining Association, Spokane, WA, USA, pp. 239–290.

Klimchouk, A.B., 1997. The role of karst in the genesis of sulfur deposits, Pre-Carpathian region, Ukraine. Environ. Geol. 31 (1–2), 1–20.

Knochenmus, L.A., Robinson, J.L., 1996. Descriptions of anisotropy and heterogeneity and their effect on ground-water flow and areas of contribution to public supply wells in a karst carbonate aquifer system. U.S. Geol. Surv. Water-Supply Pap. 2475. 46 pp. ISBN 0-607-86216-5.

Kovacs, A., Perrochet, P., Király, L., Jeannin, P.-Y., 2005. A quantitative method for the characterisation of karst aquifers base don spring hydrograph analysis. J. Hydrol. 303, 152–164. doi: 10.1016/j.jhydrol.2004.08.023.

Kralik, M., 2001. Spring dynamics as a tool to evaluate groundwater vulnerability. 7th Conference on Limestone Hydrology and Fissured Media. Besancon, France, 20–22 Sept. 2001. Sci. Tech. Environ. Mém. 13, 215–218.

Krause, S., Heathwaite, A.L., Miller, F., Hulme, P., Crowe, A., 2007. Groundwater-dependent wetlands in the UK and Ireland: controls, functioning and assessing the likelihood of damage from human activities. Water Resour. Manage. 21, 2015–2025. doi: 10.1007/s11269-007-9192-x.

Krekeler, M.P.S., Probst, P., Samsonov, M., Tselepis, C.M., Bates, W., Kearns, L.E., Barry Maynard, J., 2007. Investigations of subsurface flow constructed wetlands and associated geomaterial resources in the Akumal and Reforma regions, Quintana Roo, Mexico. Environ. Geol. 53, 709–726. doi: 10.1007/s00254-007-0684-z.

Laimer, H.J., 2005. Die Erfassung der Karstgrundwasser-Vulnerabilität mit der Metode "VURAAS" (Karst groundwater vulnerability assessment with the "VURAAS" method). Springer, Grundwasser, 167–176.

Lang, M.W., Kasischke, E.S., 2008. Using C-band synthetic aperture radar data to monitor forested wetland hydrology in Maryland's coastal plain, USA. IEEE Transactions on Geoscience and Remote Sensing 46, 535–546. doi: 10.1109/TGRS.2007.909950.

Lang, M.W., Kasischke, E.S., Prince, S.D., Pittman, K.W., 2008. Assessment of C-band synthetic aperture radar data for mapping and monitoring Coastal Plain forested wetlands in the Mid-Atlantic Region, USA. Remote Sensing of Environment 112, 4120–4130. doi: 10.1016/j.rse.2007.08.026.

Larocque, M., Banton, O., Ackerer, P., Razack, M., 1999. Determining karst transmissivities with inverse modeling and an equivalent porous media. Ground Water 37 (6), 897–903.

Larocque, M., Banton, O., Razack, M., 2000. Transient-state history matching of a karst aquifer ground water flow model. Ground Water 38 (6), 939–946.

Legchenko, A., Ezersky, M., Camerlynck, C., Al-Zoubi, A., Chalikakis, K., Girard, J.-F., 2008. Locating water-filled karst caverns and estimating their volume using magnetic resonance soundings. Geophysics 73 (5), G51–G61. doi: 10.1190/1.2958007.

Lesser, J. M., 1976. Estudio hidrogeologico e hidrogeoquimico de la Peninsual de Yucatan. Proyecto Conacyt-NSF 704, Secretaria de Recursos Hidraulicos, Direccion de Geohidrologia y Zonas Aridas, Mexico. 64 p.

Li, X., Tsai, F. T.-C., 2009. Bayesian model averaging for groundwater head prediction and uncertainty analysis using multimodel and multimethod. Water Resour. Res. 45, W09403. doi: 10.1029/2008WR007488.

Liedl, R., Sauter, M., Hückinghaus, D., Clemens, T., Teutsch, G., 2003. Simulation of the development of karst aquifers using a coupled continuum pipe flow model. Water Resour. Res. 39 (3), SBH61-SBH611.

Lindgren, R.J., Dutton, A.R., Hovorka, S.D., Worthington, S.R.H., Painter, S., 2005. Conceptualization and simulation of the Edwards Aquifer, San Antonio Region, Texas. In: Kuniansky, E. (Ed.). Sci. Investig. Rep. 2005-5160, 48–57.

Lopez-Ornat A., Ramo C., 1992. Colonial waterbird populations in the Sian Ka'an Biosphere Reserve (Quintana Roo, Mexico). Wilson Bull. 104, 501–515.

Lopez-Ramos, E., 1975. Geological summary of the Yucatan Peninsula. Chap. 7. In: Nairn, A.E.M., Stehli, F.G. (Eds.) The ocean basins and margins. Vol. 3 The Gulf of Mexico and the Caribbean. Plenum Press, NY, USA.

Lu, Z., Crane, M., Kwoun, O., Wells, C., Swarzenski, C., Rykhus, R., 2005. C-band radar observes water level change in swamp forests. EOS Transactions, AGU 86, 141–144.

Lu, Z., Kwoun, O., 2008. Radarsat-1 and ERS InSAR analysis over southeastern coastal Louisiana: Implications for mapping water-level changes beneath swamp forests. IEEE Transactions on Geoscience and Remote Sensing 46, 2167–2184. doi: 10.1109/TGRS.2008.917271.

Lu, Z., Kim, J.-W., Lee, H., Shum, C.,K., Duan, J., Ibaraki, M., Akyilmaz, O., Read, C.-H., 2009. Helmand river hydrologic studies using ALOS PALSAR InSAR and ENVISAT altimetry. Marine Geodesy 32 (3), 320–333. doi: 10.1080/01490410903094833.

Malik, P., Svasta, J., 1999. REKS – an alternative method of karst groundwater vulnerability estimation. Hydrogeology and Land Use Management, Proceedings of the XXIX Congress of the International Association of Hydrogeologists, Bratislava, September 1999, 79–85.

Mangin, A., 1974. Contribution à l'étude hydrodynamique des aquifers karstiques (Contribution the hydrodynamics of karst aquifers). Ann. de Spéléol. 29 (3), 283–332; 29 (4), 495–601; 30 (1), 21–124.

Marin, L.E., 1990. Field investigations and numerical simulation of ground-water flow in the karstic aquifer of northwestern Yucatan, Mexico. PhD thesis. Dept. of Geol., North. Ill. Univ., USA.

Marin, L.E., Steinich, B., Pacheco, J. Escolero, O.A., 2000. Hydrogeology of a contaminated sole-source karst aquifer, Mérida, Yucatán, Mexico. Geofís. Int. 49 (4), 359–365.

Marin, L.E., Perry, E.C., Essaid, H.I., Steinich, B., 2004. Hydrogeological investigations and numerical simulation of groundwater flow in the karstic aquifer of northwestern Yucatan, Mexico. p. 257–278. In: Cheng, A., H.-D., Ouazar, D., 2004. Coastal aquifer management: monitoring, modeling and case studies. CRC Press LLC. ISBN 1-56670-605-X.

Marshall, L., Sharma, A., Nott, D., 2006. Modeling the catchment via mixtures: Issues of model specification and validation. Water Resour. Res. 42, W11409. doi: 10.1029/2005WR004613.

Martin, J.B., Screaton, E.J., 2001. Exchange of matrix and conduit water with examples from the Floridan aquifer. In : Kuniansky, E. (Ed.). Water-Resources Investigations Report 01-4011, U.S. Geological Survey. 38–44

Martinez, J.-M., Le Toan, T., 2007. Mapping of flood dynamics and spatial distribution of vegetation in the Amazon floodplain using multitemporal SAR data. Remote Sensing of Environment 108, 209–223.

Massonnet, D., Rossi, M., Carmona, C., Adragna, F., Peltzer, G., Feigl, K., Rabaute, T., 1993. The displacement field of the Landers earthquake mapped by radar interferometry. Nature 364, 138–142.

Massonnet, D., Feigl, K.L., 1998. Radar interferometry and its application to changes in the Earth's surface. Reviews of Geophysics 36, 441–500.

Mayr, S.I., Burkhardt, H., Popov, Y., Wittmann, A., 2008. Estimation of hydraulic permeability considering the micro morphology of rocks of the borehole YAXCOPOIL-1 (Impact crater Chicxulub, Mexico). Int. J. Earth Sci. (Geol. Rundsch.) 97, 385–399.

Mazzotti, F.J., Fling, H.E., Merediz, G., Lazcano, M., Lasch, C., Barnes, T., 2005. Conceptual ecological model of the Sian Ka'an Biosphere Reserve, Quintana Roo, Mexico. Wetl. 25 (4), 980–997.

McGrath, R.J., Styles, P., Thomas, E., Neale, S., 2002. Integrated high-resolution geophysical investigations as potential tools for water resource investigations in karst terrain. Environ. Geol. 42: 552–557. doi: 10.1007/s00254-001-0519-2.

Meehl, G.A., Stocker, T.F., Collins, W.D., Friedlingstein, P., Gaye, A.T., Gregory, J.M., Kitoh, A., Knutti, R., Murphy, J.M., Noda, A., Raper, S.C.B., Watterson, I.G., Weaver, A.J., Zhao, Z.-C., 2007. Global Climate Projections. In: Solomon, S., Qin, D., Manning, M., Chen, Z., Marquis, M., Averyt, K.B., Tignor, M., Miller, H.L. (Eds.)Climate Change 2007: The Physical Science Basis. Contribution of Working Group I to the Fourth Assessment Report of the Intergovernmental Panel on Climate Change. Cambridge University Press, Cambridge, United Kingdom and New York, NY, USA.

Merediz Alonso, G., 2007. Science and NGO's: Collaboration for the conservation of groundwater resources in the Yucatan Peninsula. p. 97–103 in: Holliday, L., Marin, L., Vaux, H. (Eds.), 2007. Sustainable management of groundwater in Mexioc: Proceedings of a Workshop (Series: Strengthening science-based decision making in developing countries). National Research Council. The National Academies Press, Washington D.C., USA. ISBN: 0-309-10583-8.

Milanović, P.T., 2004, Water resources engineering in karst. CRC Press, Florida, USA. 312 pp. ISBN 1-56670-671-8.

Mimi, Z.A., Assi, A., 2009. Intrinsic vulnerability, hazard and risk mapping for karst aquifers: a case study. J. Hydrol. 364, 298–310. doi: 10.1016/j.jhydrol.2008.11.008.

Mochales, T., Casas A.M., Pueyo, E.L., Pueyo, O., Román, M.T., Pocoví, A., Soriano, M.A., Ansón, D., 2008. Detection of underground cavities by combining gravity, magnetic and ground penetrating radar surveys: a case study from the Zaragoza area, NE Spain. Environ. Geol. 53, 1067–1077. doi: 10.1007/s00254-007-0733-7.

Moore, Y.H., Stoessell, R.K., Easley, D.H., 1992. Fresh-water/sea-water relationship within a ground-water flow system, northeastern coast of the Yucatan Peninsula. Ground Water 30 (3), 343–350.

Morales López, J.A., 2007. Estrategia de manejo y conservación de recursos hídricos para la zona de influencia norte de Sian Ka'an. M.Sc. thesis. Universidad Autónoma de Querétaro. Querétaro, Mexico.

Motschka, K., 2001. Aerogeophysics in Austria. Bull. of Geol. Surv. of Jpn. 52 (2–3), 83–88.

Münch, Z., Conrad, J., 2007. Remote sensing and GIS based determination of groundwater dependent ecosystems in the Western Cape, South Africa. Hydrogeol. J. 15, 19–28. doi: 10.1007/s10040-006-0125-1.

Murray, I.R., Alvarez, C., Groom, R.W., 1999. Modelling of complex electromagnetic targets using advanced non-linear approximator techniques. Extended Abstracts, 69th SEG Conference, Houston, Texas.

NASDA/NASA, 2008. Tropical Rainfall Measuring Mission (TRMM), data product 3B43. TRMM algorithms were developed by the TRMM Science Team. TRMM data were processed by the TRMM Science Data and Information System (TSDIS) and the TRMM Office; archived and distributed by the Goddard Distributed Active Archive Center. TRMM is an international project jointly sponsored by the Japan National Space Development Agency (NASDA) and the U.S. National Aeronautics and Space Administration (NASA) Office of Earth Sciences.

Neelin, J.D., Münnich, M., Su, H., Meyerson, J.E., Holloway, C.E., 2006. Tropical drying trends in global warming models and observations. PNAS 103 (16), 6110–6115. doi: 10.1073/pnas.0601798103.

Neuman, S.P., 2003. Maximum likelihood Bayesian averaging of uncertain model predictions. Stoch. Environ. Res. and Risk Assess. 17, 291–305. doi:10.1007/s00477-003-0151-7.

Neuman, S.P., Wierenga, P.J., 2003. A comprehensive strategy of hydrogeologic modeling and uncertainty analysis for nuclear facilities and sites. Univ. of Ariz., Rep. NUREG/CR-6805.

Newman, G.A., Commer, M., 2005. New advances in three dimensional transient electromagnetic inversion. Geophysical Journal Internaitonal 160 (1), 5–32.

Nielsen, L., Jørgensen, N.O., Gelting, P., 2007. Mapping of the freshwater lens in a coastal aquifer on the Keta Barrier (Ghana) by transient electromagnetic soundings. J. Applied Geophys. 62, 1–15. doi: 10.1016/j.jappgeo.2006.07.002.

Nyquist, J.E., Peake, J.S., Roth, M.J.S., 2007. Comparison of an optimized resistivity array with dipole-dipole soundings in karst terrain. Geophys. 72, F139.

Oberstadler, R., Hönsch, H., Huth, D., 1997. Assessment of the mapping capabilities of ERS-1 SAR data for flood mapping: a case study in Germany. Hydrological Processes 11, 1415–1425.

Ocampo, A.C., Pope, K.O., Fischer, A.G., 1996. Ejecta blanket deposits of the Chicxulub crater from Albion Island, Belize. p. 75–88. In: Ryder, G., Fastovsky, D., Gartner, S. (Eds.) The Createaceous-Tertiary event and other catastrophes in Earth history. Geol. Soc. Am. Spec. Pap. 307.

Ottowitz, D., 2009. 3-D Modellrechnung der Karststrukturen des Ox Bel Ha Höhlensystems zur Methodenevaluierung - Aeroelektromagnetic. M.Sc. Thesis, Univ. of Vienna, Austria.

Pacheco, J., Marín, L., Cabrera, A., Steinich, B., Escolero, O., 2001. Nitrate temporal and spatial Patterns in 12 water-supply wells, Yucatan, Mexico. Environ. Geology 40 (6), 708–715.

Pankratov, O.V., Kuvshinov, A.V., Avdeev, D.B., 1997. High performance three-dimensional three-dimensional electromagnetic modelling using modified Neumann series. Anisotropic Earth. J. Geomag. Geoelectr. 49, 1541–1547.

Painter, S.L., Sun, A., Green, R.T., 2007. Enhanced characterization and representation of flow through karst aquifers. Am. Water Works Assoc. ISBN 1-8532-1489-5. 83 pp.

Painter, J., 2009. Americas on alert for sea level rise. BBC news article, accessed on URL: http://news.bbc.co.uk/2/hi/americas/7977263.stm in January 2010.

Pellerin, L., Holliger, K., Slater, L., Yaramanci, U., 2009. Special issue on Hydrogeophysics – Methods and processes foreword. Near Surface Geophysics 7 (5–6), 303–305.

Perry, E., Swift, J., Gamboa, J., Reeve, A., Sanborn, R., Marín, L, Villasuso, M., 1989. Geologic and environmental aspects of surface cementation, north coast, Yucatan, Mexico. Geol. 17, 818–821.

Perry, E.C., Marín, L.E., McClain, J., Velazquez, G., 1995. The Ring of Cenotes (sinkholes) northwest Yucatan, Mexico: Its hydrogeologic characteristics and association with the Chicxulub Impact Crater. Geol. 23, 17–20.

Perry, E., Velazquez-Oliman, G., Marin, L., 2002. The hydrogeochemistry of the karst aquifer system of the northern Yucatan Peninsula, Mexico. Int. Geol. Rev. 44, 191–221.

Perry, E., Paytan, A., Pedersen, B., Velazquez-Oliman, G., 2009. Groundwater geochemistry of the Yucatan Peninsula, Mexico: constraints on stratigraphy and hydrogeology. J. Hydrol. 367 (1–2), 27–40. doi: 10.1016/j.jhydrol.2008.12.026.

Peterson, E.W., Wicks, C.M., 2005. Fluid and solute transport from a conduit to the matrix in a carbonate aquifer system. Mathematical Geology 37 (8), 851–867. doi: 10.1007/s11004-005-9211-5.

Peterson, E.W., Wicks, C.M., 2006. Asessing the importance of conduit geometry and physical parameters in karst systems using the storm water management model (SWMM). J. Hydrol. 329, 294–305. doi: 10.1016/j.jhydrol.2006.02.017.

PetRos EiKon, 2003. EMIGMA Version 7.5. Software. Copyright © PetRos EiKon. Ontario, Canada.

Pietroniro, A., Prowse, T., Peters, D.L., 1999. Hydrologic assessment of an inland freshwater delta using multi-temporal satellite remote sensing. Hydrol. Process. 13, 2483–2498.

Pope, K.O., Rejmankova, E., Paris, J.F., 2001. Spaceborne imaging radar-C (SIR-C) observations of groundwater discharge and wetlands associated with the Chicxulub impact crater, northwestern Yucatan Peninsula, Mexico. Geol. Soc. America Bull. 113 (3), 403–416.

Pope, K.O., Ocampo, A.C., Fischer, A.G., Vega, F.J., Ames, D.E., King Jr., D.T., Fouke, B.W., Wachtman, R.J., Kletetschka, G., 2005. Chicxulub impact ejecta deposits in southern Quintana Roo, México, and central Belize. p. 171–190. In: Kenkmann, T., Hörz, F., Deutsch, A. (Eds.) Large meteorite impacts III. Geol. Soc. Am. Spec. Pap. 384.

Powell, S.J., Letcher, R.A., Croke, B.F.W., 2008. Modelling floodplain inundation for environmental flows: Gwydir wetlands, Australia. Ecol. Modelling 211, 350–362.

Pozo de la Tijera, C., Escobedo Cabrera, J.E., 1999. Mamíferos terrestres de la Reserva de la Biosfera de Sian Ka'an, Quintana Roo, México. Revista de Biología Tropical 47, 251–262.

Refsgaard, J.C., van der Sluijs, J.P., Brown, J., van der Keur, P., 2006. A framework for dealing with uncertainty due to model structure error. Adv. in Water Resour. 29, 1586–1597.

Refsgaard, J. C., van der Sluijs, J.P., Højberg, A.L., Vanrolleghem, P.A., 2007. Environ. Modelling & Softw. 22, 1543–1556. doi: 10.1016/j.envsoft.22007.02.004.

Revil, A., Cathles, L.M.I., 1999. Permeability of shaly sands. Water Resour. Res. 35 (3), 651–662.

Robinson-Poteet, D., 1989. Using terrain conductivity to detect subsurface voids and caves in a limestone formation. pp. 271–280 in: Beck, B.F., (Ed.). Engineering and environmental impacts of sinkholes and karst: proceedings of the third Multidisciplinary Conference on Sinkholes and the Engineering and Environmental Impacts of Karst, St. Petersburg Beach, FL, USA. ISBN: 90-6191-987-8.

Rodríguez-Rodríguez, M., Moral, F., Benavente, J., 2008. Hydrogeological characteristics of a groundwater-dependent ecosystem (La Lantejuela, Spain)., Water and Environ. J. 22, 137–147. doi: 10.1111/j.1747-6593.2007.00092.x.

Rojas, R., Feyen, L., Dassargues, A., 2008. Conceptual model uncertainty in groundwater modeling: Combining generalized likelihood uncertainty estimation and Bayesian model averaging. Water Resour. Res. 44, W12418. doi: 10.1029/2008WR006908.

Rojas, R., Feyen, L., Dassargues, A., 2009. Sensitivity analysis of prior model probabilities and the value of prior knowledge in the assessment of conceptual model uncertainty in groundwater modelling. Hydrol. Process. 23, 1131–1146. doi: 10.1002/hyp.7231.

Rosen, P.A., Hensley, S., Joughin, I.R., Li, F.K., Madsen, S.N., Rodríguez, E., Goldstein, R.M., 2000. Synthetic aperture radar interferometry. Proceedings of the IEEE 88 (3), 333–381.

Roth, M.J.S., Mackey, J.R., Mackey, C., Nyquist, J.E., 2002. A case study of the reliability of multielectrode earth resistivity testing for geotechnical investigations in karst terrains. Eng. Geol. 65 (2–3), 225–232.

Roth, M.J.S., Nyquist, J.E., 2003. Evaluation of multi-electrode earth resistivity testing in karst. Geotechnical Testing J. 26 (2), 1–12.

Rubin, Y., Hubbard, S.S., 2005. Introduction to hydrogeophysics. Chapter 1 in: Rubin, Y., Hubbard, S.S. (Eds.). Hydrogephysics. Springer, Dordrecht, The Netherlands, 3–21.

Rybakov, M., Rotstein, Y., Shirman, Al-Zoubi, A., 2005. Cave detection near the Dead Sea – a micromagnetic feasibility study. The Leading Edge 585–590.

Sánchez Meza, J.J., 2006. Se ha descentralizado la gestión del agua en México? Reporte de investigación. Comisión Estatal del Agua, Gobierno del Estado de Sonora. Centro del Tercer Mundo para Manejo de Agua A.C. www.thirdworldcentre.org. 24 pp.

Sasaki, Y., 2001. Full 3-D inversion of electromagnetic data on PC. J. Applied Geophys 46 (1), 45–54.

Sass,G.Z., Creed, I.F., 2008. Characterizing hydrodynamics on boreal landscapes using archived synthetic aperture radar imagery. Hydrological Processes 22, 1687–1699. doi: 10.1002/hyp.6736.

Scanlon, B.R., Mace, R.E., Barrett, M.E., Smith, B., 2003. Can we simulate regional groundwater flow in a karst system using equivalent porous media models? Case study, Barton Springs Edwards Aquifer, USA. J. Hydrol. 276, 137–158. doi: 10.1016/S0022-1694(03)00064-7.

Schumann, G., Di Baldassarre, G., Bates, P.D., 2009. The utility of spaceborne radar to render flood inundation maps based on multialgorithm ensembles. IEEE Transactions on Geoscience and Remote Sensing 47 (8), 2801–2807.

Schönian, F., Stöffler, D., Kenkmann, T., Wittmann, A., 2004. The fluidized Chicxulub ejecta blanket, Mexico: Implications for Mars. Poster, 35th Annu. Lunar and Planet. Sci. Conf., Leag. City, TX, USA.

Schönian, F., Tagle, R., Stöffler, D., Kenkmann, T., 2005. Geology of southern Quintana Roo (Mexico) and the Chicxulub ejecta blanket. Abstract #2389. 36th Annu. Lunar and Planet. Sci. Conf., Leag. City, TX, USA.

Schwaiger, H.F., Murray, C., Brown, L., 1997. Effectiveness of ground penetrating radar in detecting caves in karst limestone of the Yucatan Peninsula, Mexico. Proceedings of the Symposium on the Application of Geophysics to Engineering and Environmental Problems, Reno, NV, USA. 588–586.

SEDUMA, 2003. Programa subregional de desarrollo urbano de la Región Caribe Norte. Secretaria de Desarrollo Urbano y Medio Ambiente, Quintana Roo. Accessed on URL: http://seduma.qroo.gob.mx/PDUs/2.-%20PDU%20SUBREGIONAL%20CARIBE%20NORTE%20(30%20MAYO%202003)/PDU%20SUBREGIONAL.pdf

SGM, 2007. Carta geológica de México. Escala 1:2,000,000. 6a edición. Servicio Geológico Mexicano (SGM).

Shah, S.D., Smith, B.D., Clark, A.K., Kress, W.H., 2008. A multi-tool geophysical and hydrogeological investigation of a karst aquifer system, Cibolo Canyon Deveopment Area, Bexar County, Texas. In: Kuniansky, E. (Ed.). U. S. Geol. Surv. Karst Interest Group Proc., Bowling Green, Kentucky, USA. p. 107–116.

Shen, G., Guo, H., Liao, J., 2008. Object oriented method for detection of inundation extent using multi-polarized synthetic aperture radar image. J. Applied Remote Sens. 2, 023512. doi: 10.1117/1.2911669.

Shoemaker, W.B., Kuniansky, E.L., Birk, S., Bauer, S., Swain, E.D., 2008. Documentation of a Conduit Flow Process (CFP) for MODFLOW-2005. U. S. Geol. Surv. Techniques and Methods, Book 6, Chapter A24, 50 pp.

Siemon, B., 2006. Electromagnetic methods – frequency domain. Airborne techniques. Chapter 5.1 in: Kirsch, R. (Ed.), Groundwater geophysics – A tool for hydrogeology. Springer. ISBN: 3-540-29383-3.

Singh, V.P., Woolhiser, D.A., 2002. Mathematical modelling of watershed hydrology. J. Hydrol. Engineering 7 (4), 270–292.

Slater, L., 2007. Near surface electrical characterization of hydraulic conductivity: from petrophysical properties to aquifer geometries – a review. Surv. Geophys. 28, 169–197. doi: 10.1007/s10712-007-9022-y.

Smart, P.L., Beddows, P.A., Coke, J., Doerr, S., Smith, S., Whitaker, F.F., 2006. Cave development on the Caribbean coast of the Yucatan Peninsula, Quintana Roo, Mexico. In: Harmon, R.S., Wicks, C. (Eds.) Perspectives on karst geomorphology, hydrology and geochemistry – A tribute volume to Derek C. Ford and William B. White. Geol. Soc. Am.. Spec. Pap. 404, 105–128.

Smith, B.D., Smith, D.V., Hill, P.L., Labson, V.F., 2003. Helicopter electromagnetic and magnetic survey data and maps, Seco Creek Area, Medina and Uvalde Counties, Texas. U. S. Geol. Surv. Open-File report 03-226. 60 pp.

Smith, B.D., Cain. M.J., Clark, A.K., Moore, D.W., Faith, J.R., Hill, P.L., 2005a. Helicopter electromagnetic and magnetic survey data and maps, Northern Bexar County, Texas. U. S. Geol. Surv. Open-File report 05-1158. 122 pp.

Smith, B.D., Gamey, J.T., Hodges, G., 2005b. Review of airborne electromagnetic geophysical surveys over karst terrains. In: Kuniansky, E. (Ed.). U. S. Geol. Surv. Karst Interest Group Proc., Rapid City, South Dakota, USA. p. 17–19.

Solbø, S., Malnes, E., Guneriussen, T., Solheim, I., Eltoft, T., 2003. Mapping surface-water with Radarsat at arbitrary incidence angles. Geoscience and Remote Sensing Symposium, 2003, IGARSS '03. Proceedings IEEE International. 4, 2517–2519. doi: 10.1109/IGARSS.203.1294494.

Springer, G.S., 2004. A Pipe-Based, First Approach to Modeling Closed Conduit Flow in Caves. J. Hydrol. 289, 178–189.

Stauffer, F., Attinger, S., Zimmermann, S., Kinzelbach, W., 2002. Uncertainty estimation of well catchments in heterogeneous aquifers. Water Resour. Res. 38 (11), 1238. doi: 10.1029/2001WR000819.

Stauffer, F., Guadagnini, A., Butler, A., Hendricks Franssen, H.-J., Van de Wiel, N., Bakr, M., Riva, M., Guadagnini, L., 2005. Delineation of source protection zones using statistical methods. Water Resour. Manage. 19, 163–185. doi: 10.1007/s11269-005-3482-7.

Steinich, B., Marin, L.E., 1996. Hydrogeological investigations in northwestern Yucatan, Mexico, using resistivity surveys. Ground Water 34 (4), 640–646.

Steinich, B., Marin, L.E., 1997. Determination of flow characteristics in the aquifer of the Northwestern Peninsula of Yucatan, Mexico. J. Hydrol. 191, 315–331.

Stisen, S., Sandholt, I., Nørgaard, A., Fensholt, R., Høegh Jensen, K., 2008. Combining the triangle method with thermal intertia to estimate regional evapotranspiration – Applied to MSG-SEVIRI data in the Senegal River basin. Remote Sens. Environ. 112, 1242–1255.

Stoessell, R.K., Ward, W.C., Ford, B.H., Schuffert, J.D., 1989. Water chemistry and $CaCO_3$ dissolution in the saline part of an open-flow mixing zone, coastal Yucatan Peninsula, Mexico. Geol. Soc. of America Bull. 101 (2), 159–169.

Stoessell, R.K., Moore, Y.H., Coke, J.G., 1993. The occurrence and effect of sulfate reduction and sulfide oxidation on coastal limestone dissolution in Yucatan cenotes. Ground Water 31 (4), 566–575.

Stoessell, R.K., 1995. Dampening of tranverse dispersion in the halocline in karst limestone in the Northeastern Yucatan Peninsula. Ground Water 33 (3), 366–371.

Stoessell, R.K., Coke, J.G., Easley, D.H., 2002. Localized thermal anomalies in haloclines of coastal Yucatan sinkholes. Ground Water 40 (4), 416–424.

Šumanovac, F., Weisser, M., 2001. Evaluation of resistivity and seismic methods for hydrogeological mapping in karst terrains. J. Applied Geophysics 47, 13–28.

Tang, Q., Gao, H., Lu, H., Lettenmaier, D.P., 2009. Remote sensing: hydrology. Progress in Physical Geography 33 (4), 490–509. doi: 10.1177/0309133309346650.

Telford., W. M., Geldart, L. P., Sheriff, R. E., 1990. Applied Geophysics. Second Edition, Cambridge University Press, 770 pp. ISBN 0-521—33938-3.

Teutsch, G., Sauter, M., 1991. Groundwater modeling in karst terranes: Scale effects, data acquisition and field validation. Proc. 3rd conf. on hydrogeology, ecology, monitoring and management of groundwater in karst terranes. Nashv., Tenn., USA. Natl. Ground Water Assoc., Dublin, Ohio, USA, 17–34.

Thomas, C., 1999. Aspects hydrogéologiques du Yucatan (Mexique). Karstologia 34 (2), 9–22.

Topp, G.C., Davis, J.L., Annan, A.P., 1980. Electromagnetic determination of soil water content: measurements in coaxial transmission lines. Water Resources Res. 16 (3), 574–582.

Ulaby, F.T., Moore, R. K., Fung, A.K., 1982. Microwave Remote Sensing: Active and Passive, Vol. II – Radar Remote Sensing and Surface Scattering and Emission Theory. Addison-Wesley, Advanced Book Program, Reading, Massachusetts, USA. 609 pp.

USGS, 2006. Shuttle Radar Topography Mission, 3 Arc Second, Finished 2.0. Global Land Cover Facility, University of Maryland, College Park, MD, USA. Accessed 15 June 2006.

Van Stempoort, D., Ewert, L., Wassenaar, L., 1993. Aquifer Vulnerability Index (AVI): a GIS compatible method for groundwater vulnerability mapping. Can. Water Res. J. 18, 25–37.

Vassolo, S., Kinzelbach, W., Schäfer, W., 1998. Determination of a well head protection zone by stochastic inverse modelling. J. Hydrol. 206, 268–280.

Vaux Jr., H., 2007a. Chairman's summary. p. 1–5 in: Holliday, L., Marin, L., Vaux, H. (Eds.). Sustainable management of groundwater in Mexico: Proceedings of a Workshop (Series: Strengthening science-based decision making in developing countries). National Research Council. The National Academies Press, Washington D.C., USA. ISBN: 0-309-10583-8.

Vaux Jr., H., 2007b. The elements of scientific advice. p. 36–43 in: Holliday, L., Marin, L., Vaux, H. (Eds.). Sustainable management of groundwater in Mexico: Proceedings of a Workshop (Series: Strengthening science-based decision making in developing countries). National Research Council. The National Academies Press, Washington D.C., USA. ISBN: 0-309-10583-8.

Vías, J.M., Andreo, B., Perles, M.J, Carrasco, F., Vadillo, I., Jiménez, P., 2004. The COP method. pp. 163–171 in: Zwahlen, F. (Ed.). Vulnerability and risk mapping for the protection of carbonate (karst) aquifers. Final report of COST Action 620, European Commission, Directorate-General XII Science, Research and Development, Brussels, Belgium.

Vías, J.M., Andreo, B., Perles, M.J., Carrasco, F., 2005. A comparative study of four schemes for groundwater vulnerability mapping in a diffuse flow carbonate aquifer under Meditarranean climatic conditions. Environ. Geol. 47, 586–595. doi: 10.1007/s00254-004-1185-y.

Vogelsang, D., 1987. Examples of electromagnetic prospecting for karst and fault systems. Geophys. Prospect. 35, 604–617.

Vouillamoz, J.M., Legchenko, A., Albouy, Y., Bakalowicz, M., Baltassat, J.M., Al-Fares, W., 2003. Location of saturated karst aquifer with magnetic resonance sounding and resistivity imagery. Ground Water 41 (5), 578–586.

Ward, S. H., Hohmann, G.W., 1988. Electromagnetic theory for geophysical applications. Chapter 4 (p. 131-312) in: Nabaighian, M.N. (Ed.), Electromagnetic methods in applied geophysics – Volume 1, Theory. Tulsa. Society of Exploration Geophysicists.

Watson, J., Hamilton-Smith, E., Gillieson, D., Kiernan, K. (Eds.), 1997. Guidelines for cave and karst protection. IUCN, Gland, Switzerland and Cambridge, UK. 63 pp.

Wdowinski, S., Amelung, F., Miralles-Wilhelm, F., Dixon, T.H., Carande, R., 2004. Space-based measurements of sheet-flow characteristics in the Everglades wetland, Florida. Geophysical Research Letters 31, L15503. doi: 10.1029/2004GL020383.

Wdowinski, S., Kim, S.-W., Amelung, F., Dixon, T., Miralles-Wilhelm, F., Sonenshein, R., 2008. Space-based detection of wetlands' surface water level changes from L-band SAR interferometry. Remote Sensing of Environment 112, 681–696. doi: 10.1016/j.rse.2007.06.008.

Weidie, A.E., 1985. Geology of Yucatan Platform. p. 1–12 in: Ward, W.C., Weidie, A.E., Back, W. (Eds.). Geology and hydrogeology of the Yucatan and Quaternary geology of northeastern Yucatan Peninsula. New Orleans Geol. Soc. Publ., New Orleans, LA, USA.

West, G. F., Macnae, J.C., 1991. Physics of the electromagnetic induction exploration method. p. 5–45 in Nabighian, M.N. (Ed.). Electromagnetic methods in applied geophysics - Volume 2 - Applications, part A and part B. Tulsa. Society of Exploration Geophysicists.

White, W.B., 1999. Conceptual models for karstic aquifers. p. 11–16 in: Palmer, A.N., Palmer, M.V., Sasowsky, I.D. (Eds.). Karst modeling. Spec. Publ. 5, The Karst Waters Institute, Charles Town, West Virginia, USA.

Worthington, S.R.H., Ford, D.C., Beddows, P.A., 2000. Porosity and permeability enhancement in unconfined carbonate aquifers as a result of solution. p. 463–471 in: Klimchouk, A., Ford, D., Palmer, A., Dreybrodt, W. (Eds.). Speleogenesis: Evolution of karst aquifers. Cave Books, St. Louis, USA. ISBN: 978-1-57958-399-6.

Worthington, S.R.H., 2003. A comprehensive strategy for understanding flow in carbonate aquifer. Speleogenesis and Evol. of Karst Aquifers 1 (1), 1–8.

Wright, C., Gallant, A., 2007. Improved wetland remote sensing in Yellowstone National Park using classification trees to combine TM imagery and ancillary environmental data. Remote Sens. Environment 107, 582–605.

Xiong, L., Shamseldin, A.Y., O'Connor, K.M., 2001. A non-linear combination of the forecasts of rainfall-runoff models by the first-order Takagi-Sugeno fuzzy system. J. Hydrol. 245, 196–217.

Young, W.J., Lam, D.C.L., Ressel., V., Wong, I.W., 2000. Development of an environmental flows decision support system. Environ. Modelling & Softw. 15, 257–265.

Zhou, W., Beck, B.F., Stephenson, J.B., 1999. Investigation of groundwater flow in karst areas using component separation of natural potential measurements. Environmental Geol. 37 (1–2), 19–25.

Zhou, W., Beck, B.F., Adams, A.L., 2002. Effective electrode array in mapping karst hazards in electrical resistivity tomography. Environmental Geol. 42, 922–928. doi: 10.1007/s00254-002-0594-z.

Zribi, M., Pardé, M., De Rosnay, P., Baup, F., Boulain, N., Descroix, L., Pellarin, T., Mougin, E., Ottlé, C., Decharme, B., 2009. ERS scatterometer surface soil moisture analysis of two sites in the south and north of the Sahel region of West Africa. J. of Hydrol. 375, 253–261. doi: 10.1016/j-jhydrol.2008.11.046.

7 Appendices

I Gondwe, B.R.N., Hong, S.-H., Wdowinski, S., Bauer-Gottwein, P. (2010). Hydrologic dynamics of the ground-water-dependent Sian Ka'an wetlands, Mexico, derived from InSAR and SAR data. Wetlands 30 (1), 1–13. doi: 10.1007/s13157-009-0016-z.

II Supper, R., Motschka, K., Ahl, A., Bauer-Gottwein, P., Gondwe, B., Alonso, G.M., Romer, A., Ottowitz, D., Kinzelbach, W. (2009). Spatial mapping of submerged cave systems by means of airborne electromagnetics: an emerging technology to support protection of endangered karst aquifers. Near Surface Geophysics 7 (5–6), 613–327.

III Gondwe, B.R.N., Ottowitz, D., Supper, R., Motschka, K., Merediz-Alonso, G., Bauer-Gottwein, P. (submitted). Exploring regional-scale preferential flow paths in the karst aquifer of Southern Quintana Roo, Mexico. Manuscript submitted.

IV Gondwe, B.R.N., Lerer, S., Stisen, S., Marín, L., Rebolledo-Vieyra, M., Merediz-Alonso, G., Bauer-Gottwein, P. (in review). Hydrogeology of the south-eastern Yucatan Peninsula: New insights from water level measurements, geochemistry, geophysics and remote sensing. Manuscript submitted.

V Gondwe, B.R.N., Merediz-Alonso, G., Bauer-Gottwein, P. (submitted). The influence of conceptual model uncertainty on management decisions for a groundwater-dependent ecosystem in karst. Manuscript submitted.

VI Technical Note. Maps and coordinates of field data points.

I

Hydrologic dynamics of the ground-water-dependent Sian Ka'an wetlands, Mexico, derived from InSAR and SAR data

Gondwe, B.R.N., Hong, S.-H., Wdowinski, S., Bauer-Gottwein, P.

Wetlands 2010, 30 (1), 1–13. doi: 10.1007/s13157-009-0016-z

Wetlands (2010) 30:1–13
DOI 10.1007/s13157-009-0016-z

ORIGINAL PAPER

Hydrologic Dynamics of the Ground-Water-Dependent Sian Ka'an Wetlands, Mexico, Derived from InSAR and SAR Data

Bibi R. N. Gondwe · Sang-Hoon Hong · Shimon Wdowinski · Peter Bauer-Gottwein

Received: 1 January 2009 / Accepted: 20 July 2009 / Published online: 8 January 2010

Abstract The 5,280 km^2 Sian Ka'an Biosphere Reserve includes pristine wetlands fed by ground water from the karst aquifer of the Yucatan Peninsula, Mexico. The inflow through underground karst structures is hard to observe making it difficult to understand, quantify, and predict the wetland dynamics. Remotely sensed Synthetic Aperture Radar (SAR) amplitude and phase observations offer new opportunities to obtain information on hydrologic dynamics useful for wetland management. Backscatter amplitude of SAR data can be used to map flooding extent. Interferometric processing of the backscattered SAR phase data (InSAR) produces temporal phase-changes that can be related to relative water level changes in vegetated wetlands. We used 56 RADARSAT-1 SAR acquisitions to calculate 38 interferograms and 13 flooding maps with 24 day and 48 day time intervals covering July 2006 to March 2008. Flooding extent varied between 1,067 km^2 and 2,588 km^2 during the study period, and main water input was seen to take place in sloughs during October–December. We propose that main water input areas are associated with water-filled faults that transport ground water from the catchment to the wetlands. InSAR and Landsat data revealed local-scale water divides and surface water flow directions within the wetlands.

B. R. N. Gondwe (✉) · P. Bauer-Gottwein
Department of Environmental Engineering,
Technical University of Denmark,
Miljoevej, Building 113,
DK-2800 Kgs. Lyngby, Denmark
e-mail: bng@env.dtu.dk

S.-H. Hong · S. Wdowinski
Division of Marine Geology and Geophysics,
University of Miami,
4600 Rickenbacker Causeway,
Miami, FL 33149, USA

Keywords Hydrology · Remote sensing · Surface water · Synthetic aperture radar interferometry · Yucatan Peninsula

Introduction

The 5,280 km^2 Sian Ka'an Biosphere Reserve (RBSK) is both a UNESCO World Heritage and Ramsar site, thus recognized to be internationally important. Located on Mexico's Caribbean coast (Fig. 1) it is one of the largest protected areas in Mexico. The area supports tropical forests, coral reefs, coastal savannahs, swamps, marshes, and mangroves, with a rich biodiversity and both endemic and endangered species (Pozo de la Tijera and Escobedo Cabrera 1999; Lopez-Ornat and Ramo 1992). Approximately one third of the area consists of wetlands in a mosaic of freshwater sloughs, channels, floodplains, and brackish tidally influenced areas. The Sian Ka'an wetlands provide protection from the impact of hurricanes and storms to the inland areas. In addition, their recreational value is increasingly being recognized by the tourism industry in the surrounding areas.

Ground water from the karst aquifer of the Yucatan Peninsula feeds the Sian Ka'an wetlands. The inflow through underground cave systems and karst structures is not directly observable making it difficult to understand, quantify, and predict the wetland dynamics. Yet, understanding the hydrology of the wetland is important for management of its water resources and for protecting the aquatic ecosystems. This is crucial as the wetland's catchment is under pressure from rapidly developing tourism activities, and intensifying agricultural and urban development (Mazzotti et al. 2005).

Space-based synthetic aperture radar (SAR) data offer possibilities for monitoring and analyzing the hydrologic

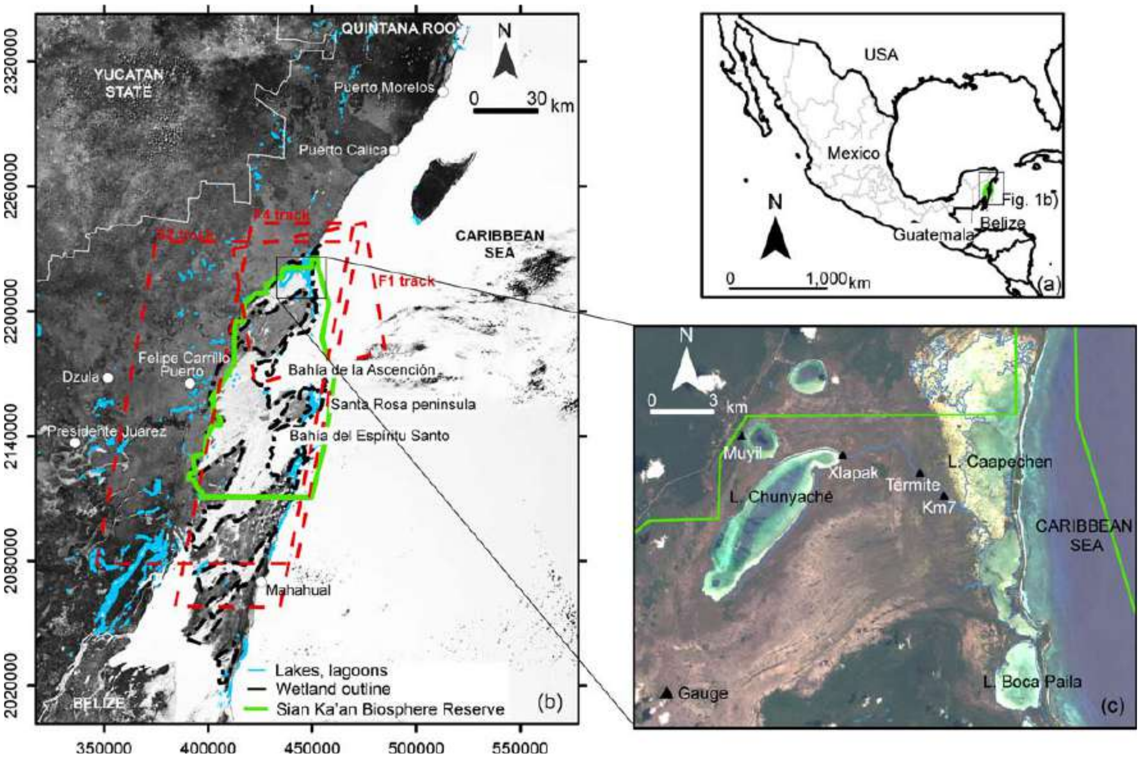

Fig. 1 Location of the study area and sites mentioned in the text. Background of **b** is Landsat TM Tri-Decadal mosaic, band 4 (near-infrared), with reversed color axis so that high absorbance is indicated by *bright colors* and vice versa. Water bodies, having high absorbance of near-infrared wavelengths, are therefore bright in this image. State and country boundaries are shown with a *thin white line*. Background of **c** is Landsat imagery true color composite (RGB: band 3, 2, 1)

dynamics of wetlands from space. SAR is an active microwave sensor, unaffected by cloud-cover and daylight conditions. It measures two observables of the backscattered signal: amplitude and phase. Both observables are sensitive to wetland hydrologic conditions. Pope et al. (1997) showed that the SAR backscatter from both L-band (wavelength, $\lambda=24.0$ cm) and C-band ($\lambda=5.7$ cm) data in a marshy wetland changed in amplitude and phase as the degree of flooding increased. In inundated areas with vegetation protruding through the water surface the radar signal will double-bounce on the water surface and the plants' stems, and thus it is backscattered to the satellite (Richards et al. 1987). The amplitude of radar backscatter depends on the degree of inundation, canopy closure, and canopy height, as these elements modify the dielectric constant of the surface and surface roughness (Ulaby et al. 1996; Bourgeau-Chavez et al. 2005). Temporal changes in the amplitude can thus indicate a change in flooding conditions. The backscatter amplitude's standard deviation also provides information on the degree of flooding in vegetated wetlands. Phase change of radar backscatter can, on the other hand, be related to changes in the surface water levels of vegetated wetlands using interferometric techniques. If water levels have changed between two image acquisitions, the travel time of the backscattered radar signal will also change (range change), yielding a phase change in an interferogram. The interferometric phase depends on the length of the baseline connecting the position of the satellite antenna at the two different image acquisitions, the topographical relief, the degree of cross-correlation between images for each pixel location (coherence), and the topographic displacement, which can be water level change for a wetland (Alsdorf et al. 2000). Since the first two can be determined with a certain accuracy, the degree of relative displacement may be obtained through SAR interferometry (InSAR) when there is a significant degree of image coherence.

Amplitude of SAR backscatter has previously been used to map flooding extent of wetlands (e.g., Hess et al. 2003; Bourgeau-Chavez et al. 2005; Lang and Kasischke 2008; Sass and Creed 2008). InSAR has been used to analyze hydrodynamics and map centimeter-level changes in Amazon floodplains (Alsdorf et al. 2000, 2001, 2007), Everglades wetlands (Wdowinski et al. 2004, 2008; Kim et al. 2005), and Louisiana marshes (Lu et al. 2005; Kim et al. 2005; Lu and Kwoun 2008). InSAR estimates of water level change over wetlands have been found to be accurate within centimeters (Alsdorf et al. 2001, 2007; Wdowinski et al. 2008).

In this paper we use SAR and InSAR data to detect spatio-temporal changes in flooding in Sian Ka'an and analyze flow directions and relative water level changes in the wetlands. We identify locations of main water sources to the wetlands and show in which season main inflow occurs.

Methods

Study Area and Ancillary Data

Sian Ka'an is located in a tropical climate, with distinct wet/dry periods. The rainy season is from May to October, and average precipitation in the catchment ranges from 840 mm/year to 1,550 mm/year (Comisión Nacional del Agua 2008). Most precipitation occurs near the Caribbean coast and in the southern part of Quintana Roo. The area is prone to hurricanes, and Hurricane Dean made landfall in Sian Ka'an on 21 August 2007. Actual evapotranspiration rates are poorly known; estimates range from 40% to 85% of mean annual precipitation (Lesser 1976; Beddows 2004). Recent estimates using remotely sensed data indicate rates in the higher end of this interval (Lerer 2008). Terrain elevations range from 0 m to 20 m above mean sea level (USGS 2006). Because the topographic gradient is very low, small elevation differences determine whether areas are dry land forests, seasonally inundated areas, or permanent wetlands. Vegetation in the Sian Ka'an wetlands consists mainly of perennial sedges and grasses, with mangroves being present in the near-coastal areas (Morales Barbosa 1992).

We installed surface water gauges in Sian Ka'an in early 2007 to obtain in situ data to verify and calibrate InSAR water level change measurements. Gauges were referenced to mean sea level using carrier-phase GPS and manually read. Estimated uncertainty with respect to mean sea level was 1–7 cm based on reoccupation with GPS antennas. Successive readings at the same location had an estimated accuracy of 1 cm on temporal water level variation. Limited accessibility to the wetlands constrained the number of gauges installed to four. All were located in a 1–2 m wide natural channel in the northern part of the reserve, thus representing a limited part of the wetlands (Fig. 1c). Within the monitored time interval, the water level changes in the natural channel were uniform throughout its west-east direction, and the water level sloped 100–120 cm towards the coastal lagoons over a 10 km stretch, giving a hydraulic gradient of 100–120 ppm here.

Approach

SAR Amplitude Data and Analysis

To map spatio-temporal changes in the degree of flooding we used a single-date parallelepiped image classification approach based on quantitative analysis of pixel backscatter amplitude. Data for this analysis consisted of 13 RADARSAT-1 (C-band, $\lambda = 5.6$ cm) SAR images, Standard Beam track S2 (descending), covering 18 August 2006 to 21 February 2008 (Fig. 2). The generally open and simple vegetation canopies in the Sian Ka'an wetlands enable C-band SAR to penetrate the vegetation. The RADARSAT-1 orbit repeat cycle is 24 days. We chose to use every other of the images available, yielding time steps of 48 days. However, just after Hurricane Dean (September 2007) we used 24 day time steps to resolve the effect of this event in detail. Scenes were cut to display the main wetlands of Sian Ka'an outlined in Fig. 1. Amplitude (σ_0) images were created from Single Look Complex (SLC) β_0 images using look-up tables of each pixel's incidence angle. Due to the flat topography of the study area, topographic effects on σ_0 were considered negligible and hence not corrected for. Images were filtered to reduce the effect of speckle — the inherent multiplicative noise of radar images. We found that applying a Lee filter iteratively using window sizes of 3×3 pixels, then 5×5 and 7×7 pixels gave the best speckle removal while still preserving edges. This method was recommended by Rio and Lozano-García (2000). Filtering was carried out on the intensity of the image (σ_0^2) and thereafter converted back to σ_0 values. Before analysis, σ_0 values were converted to dB. Image resolution after geocoding to UTM (zone 16, WGS84 datum) was 58 m by 61.5 m.

A notable difference in backscatter amplitude was immediately observed for known wetland and non-wetland areas. Since radar backscatter varies with degree of flooding we investigated the σ_0 values for the following flooding states: 'open water', meaning free water surfaces with negligible vegetation protruding through the water surface; 'flooded' areas, with vegetation protruding through the water surface, enabling a high backscatter of the radar signal; and 'not flooded' areas. On three wet season (Dec '06, early Sept '07, late Sept '07) and three dry season (Feb '07, Mar '07, May '07) images, two to five polygons were defined in each image for each flooding state and analyzed for mean and standard deviation of σ_0. Polygon size ranged from 340 to 30,230 pixels (median: 1,370 pixels). Similar techniques were used by Hess et al. (2003) and Martinez

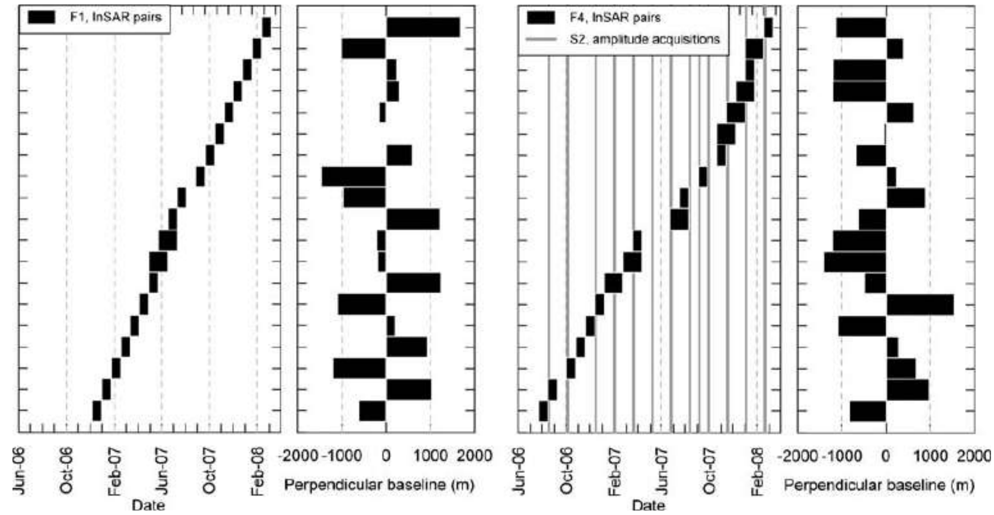

Fig. 2 InSAR image pairs, with their acquisition times, time spans and perpendicular baselines, for RADARSAT-1 F1 and F4 tracks, respectively. Acquisition times for RADARSAT-1S2 track, used for amplitude analysis, also shown

and Le Toan (2007). Since no ground truthing data were available, aerial photos, Landsat, and QuickBird images were used to confirm that polygons belonged to the different flooding categories. In Fig. 3, we indicate 95% confidence intervals for the σ_0 values, calculated for each polygon in each image, along with the standard deviation ranges of σ_0 for each category.

Clearly, both backscatter amplitudes and standard deviations are different for flooded and dry areas (Fig. 3). Values of σ_0 larger than −2.9 dB indicate flooded areas, whereas dry pixels have lower σ_0 values. It is however also obvious that the groups had some overlap. A Kruskal-Wallis *H* test indicated statistically significant differences among the three classes ($\chi^2=39.0$, $p<0.001$). Multiple comparison test using Scheffé's method showed that all three classes were significantly different ($P<0.05$). Based on the analyzed σ_0 values we chose the class thresholds shown in Table 1, using a stringent approach to avoid overlapping values. We included the 'unknown' category to accommodate for the overlap between 'not flooded' and 'flooded' categories.

The 'not flooded' and 'open water' groups, in particular, had a large overlap in σ_0 values; yet a clear difference in the standard deviations of open water and non-flooded pixels was evident (Fig. 3). Therefore, we calculated images of backscatter standard deviation using a 9×9 pixel window, and used these images to refine the classification, so that pixels with backscatter < −3.2 dB and standard deviation > 0.17 were also classified as open water. The blue 'open water' category and the dark green 'not flooded' category in Fig. 4 are the ones distinguished by standard deviation differences. The window size used for standard deviation calculations was optimized by trial-and-error.

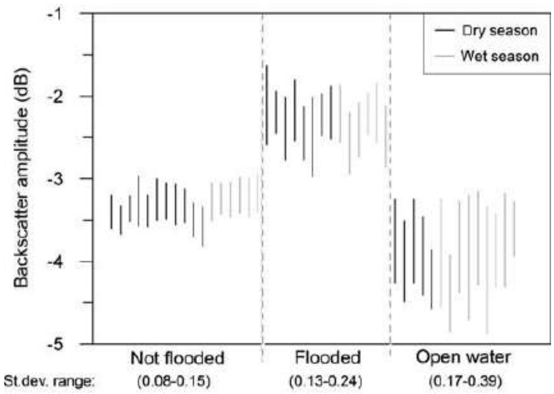

Fig. 3 Ninety-five % confidence intervals for the mean backscatter amplitude of polygons in both dry and wet season images for three different flooding states

Table 1 Classification criteria for backscatter amplitude (σ_0). Final classification also used differences in backscatter standard deviation to differentiate open water and not flooded areas

	Open water	< −3.8 dB
−3.8 dB ≤	Open water or not flooded	≤ −3.2 dB
−3.2 dB <	Not flooded	< −3.0 dB
−3.0 dB ≤	Intermediate/unknown status	≤ −2.9 dB
−2.9 dB <	Flooded	

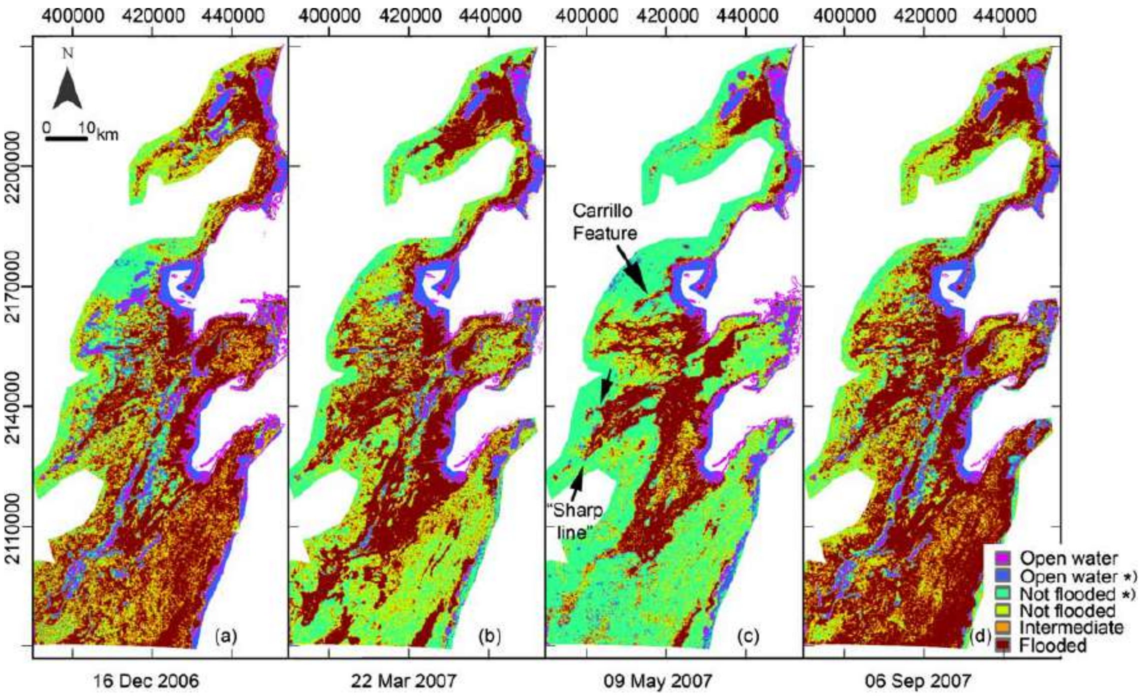

Fig. 4 Examples of flooding maps created from SAR backscatter amplitude images. **a** maximum flooding extent when no hurricane has passed, **b** a normal medium flooding extent example, **c** minimum, and **d** maximum flooding extent in the time series analyzed. Rough mask applied to disregard surrounding forest and ocean values. *Arrows* indicate the location of the Carrillo Feature and the sharp line west of the Tigritos slough. *indicates classes differentiated using standard deviation differences

InSAR Data and Analysis

The InSAR technique is well established for measuring surface displacement due to tectonic deformation (e.g., Massonnet et al. 1993) and glacier motion (e.g., Goldstein et al. 1993). Its application for wetland hydrology has only recently been recognized (Alsdorf et al. 2000). Interferograms are created by using two SAR images with nearly identical viewing geometries, co-registering them and subtracting the phases of the images for each pixel. Alsdorf et al. (2000, 2001, 2007) and Wdowinski et al. (2004, 2008) used L-band data for their interferograms over wetlands. Lu et al. (2005) and Kim et al. (2005) showed that C-band data are also useful for wetland interferometry over herbaceous wetlands. Kim et al. (2005) found that RADARSAT-1 data in particular maintain a good coherence over short time intervals due to their polarization (HH), which penetrates vegetation more easily, and due to the large incidence angle and high resolution of the Fine Beam modes. RADARSAT-1 data are advantageous for wetland InSAR due to the short orbit repeat cycle of 24 days because interferograms with short time spans can be constructed, so that coherence is more easily maintained over the often highly dynamic wetland surfaces.

We used RADARSAT-1 Fine Beam F1 and F4 modes data for the interferograms. Nineteen interferograms were formed with each of these tracks, covering the time interval July 2006 to March 2008. Image acquisition dates, time spans and perpendicular baselines are seen from Fig. 2. We used the ROI_PAC software (Buckley et al. 2000) to generate interferograms. Topographical phase was removed using the Shuttle Radar Topography Mission (SRTM) 3 arc-second digital elevation model. Based on the topography and baseline relation (Zebker and Villasenor 1992 – Eq. 25), and using perpendicular baselines of 800–1,500 m and slant range of 1,000 km, a 4–9 m topographic error will cause phase errors between 0.009 and 0.042 radians. This is negligible compared to the observed phase changes (1–7 phase cycles of 0 to 2π).

The resulting interferometric phase (φ) varies between $-\pi$ and $+\pi$. Unwrapping of the phase was done with the GZW algorithm (Goldstein et al. 1988), thus converting cycles of 0 to 2π to continuous surfaces of 0 to $n*2\pi$, where n is an integer depending on how many cycles ('fringes') follow each other.

We did not apply the spatial interferogram filtering typically used to improve interferogram quality, since we found that this smoothes out important densely spaced fringes that characterize the Sian Ka'an interferograms. To resolve this type of fringes we needed as high a spatial resolution as possible. For the same reason, use of "multi-look" processing, a standard signal-averaging procedure used to further reduce phase noise in interferograms, was minimized. Resulting resolution of our interferograms was 18 by 23 m (ungeocoded), and 58 by 61.5 m (geocoded to UTM, zone 16, WGS84 datum). Both were used in the image analysis.

The unwrapped interferogram phases (φ) were recalculated to water level changes (Δh) using the wavelength (λ) and incidence angle (θ, in radians) of each beam through the following formula, while assuming that all range changes are caused by vertical displacements only:

$$\Delta h = -\frac{\lambda \varphi}{4\pi \cos(\theta)} \tag{1}$$

For F1, θ=38.5° whereas for F4, θ=44.5° (RADARSAT International 1995), hence one phase cycle of 0–2π corresponds to 3.6 cm (F1) and 3.9 cm (F4) vertical displacement, respectively.

Results and Discussion

Flooding Extent as Determined from SAR Data

Within the investigated time interval, classification of the SAR amplitude images showed that the flooding extent in Sian Ka'an varied between 1,067 km^2 and 2,588 km^2 (mean: 2,030 km^2), when we totalled the area of 'flooded' and 'open water' pixels (Figs. 4 and 5). Of the pixels located within the official boundary of Sian Ka'an, between 25% and 48% (mean: 39%) were flooded during the year. This fits well with accounts that the wetlands take up roughly $^1/_3$ of RBSK's area (Olmsted and Duran 1990). The smallest flooding extent occurred at the end of the dry season (May 2007, Fig. 4c) whereas the largest extent occurred after Hurricane Dean (September 2007, Fig. 4d). In the year without extreme rainfall from hurricanes, the largest flooding extent occurred in December 2006, about 2 months after the end of the rainy season (Fig. 4a). Figure 4b is an example of medium flooding extent (March 2007).

We assessed the accuracy of the flooding maps by comparing them with processed Landsat ETM+ imagery. No Landsat data with sufficiently low degree of cloud cover were available for the exact SAR acquisition dates used. The closest date was 05 December 2007 (0–1% cloud cover), which was compared with the flooding map of 17 November 2007. Two Landsat scenes (path 19/row 46 and path 19/row 47) were used to cover the study area. We used an unsupervised classification (using the ER Mapper software) on the thermal infrared bands 6L and 6H and the mid-infrared band 5, combined. The thermal bands yield information about soil moisture whereas band 5 generally provides information about soil and plant moisture content (USGS 2003). We also calculated normalized difference vegetation index (NDVI) from the Landsat data as: (NIR−red)/(NIR + red), where 'NIR' is the near-infrared band 4 and 'red' is band 3. Negative NDVI values can either indicate water, snow (not applicable), or clouds (< 0.4% in scene row 47, 0% in scene row 46). We therefore used negative NDVI to identify 'open water'.

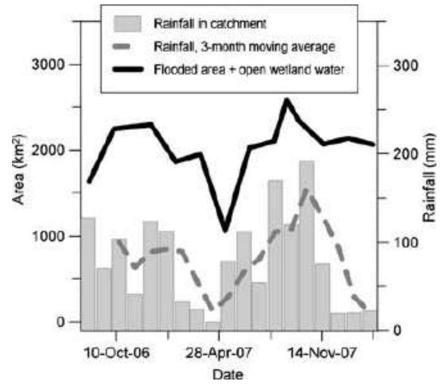

Fig. 5 Variations in flooding extent with time, as derived from classification of SAR imagery. Precipitation data (*histogram*) from the Tropical Rainfall Measuring Mission (TRMM, NASDA/NASA 2008), along with a 3-month backward moving average of this precipitation (*thick dashed line*). These data are a spatial average for the topographical catchment of Sian Ka'an (defined in Neuman and Rahbek 2007)

We classified 85% of our SAR flood maps' open water area as open water in the Landsat data. For the combined categories of 'flooded' and 'open water' the agreement was 63%, and for 'not flooded' pixels, agreement was 75%. Twenty-four percent of the area classified in the SAR flood maps had missing values in the Landsat images, since the instrument was operated in SLC-off mode. The percentages of agreement only considered pixels defined in both types of images. Considering that the two datasets were 18 days apart, the overlap in classifications between the Landsat classes and the SAR flood maps is satisfactory, and is in agreement with other studies (e.g., User's accuracies range from 65–95% in Hess et al. 2003 and 56–80% in Bourgeau-Chavez et al. 2005).

InSAR Images

Generally interferometric coherence was high over wetlands, whereas it was very low over forest areas, which means that the InSAR technique worked well over the Sian Ka'an wetlands. Between 78% and 91% of the area within the wetland mask was coherent in the produced interferograms. The high degree of coherence was partly attributable to the short time spans used. In contrast, a dry-season/wet-season interferogram could not be formed for the area, probably due to decorrelation over time, since the surface characteristics varied extensively, as exemplified by the flooding maps (Fig. 4). The degree of coherence is also related to the radar wavelength used compared to the dimensions of the dominant vegetation. Temporal changes in vegetation due to growing season were considered to have negligible influence on the coherence, since dominant vegetation was evergreen mangrove, perennial grasses, and sedges, with no leaf-off season.

Interferograms produced over Sian Ka'an were sometimes smooth, with few fringes and hence little relative water level change over the wetlands (Fig. 6b and e (wet season), Fig. 6c (dry season)), and at other times have complicated patterns due to greater variations in the relative water levels (Fig. 6a and d). Mostly, the Sian Ka'an interferograms showed irregular fringe patterns. This was also found by Alsdorf et al. (2007) for the Amazon flood plains and by Wdowinski et al. (2008) for the unregulated part of the Everglades wetlands. Like Alsdorf et al. (2007) found for the Amazon floodplains, we saw in Sian Ka'an that the smoothest interferograms patterns occurred at times when large water amounts occurred in the wetland, e.g., at the end of the rainy season in November and December (Fig. 6b and e). In contrast, the most irregular patterns were observed at the beginning and middle of the wet season, where surface water level changes were more localized (i.e., July–September). October had irregular patterns in 2006, while the patterns in October 2007 were smooth because hurricane Dean had recently provided large amounts of precipitation.

Interferogram fringes can be caused by water level changes in the wetlands, but can also be caused by atmospheric disturbances, topographical changes, and changes in the dielectric properties of the surface. The latter seems unlikely for the study area, and the topographic phase had been removed. Atmospheric disturbances at the latitudes of our study are mainly caused by large amounts of water vapor (clouds) in the local atmosphere that cause delay of the radar signal (Massonnet and Feigl 1998). An example of a fringe, which we attribute to atmospheric disturbances, is the circular pattern seen in the center of the interferogram in Fig. 6e. Kwoun and Lu (unpublished data, cited in Lu and Kwoun 2008) found 40–50% of interferograms over New Orleans to be influenced by atmospheric

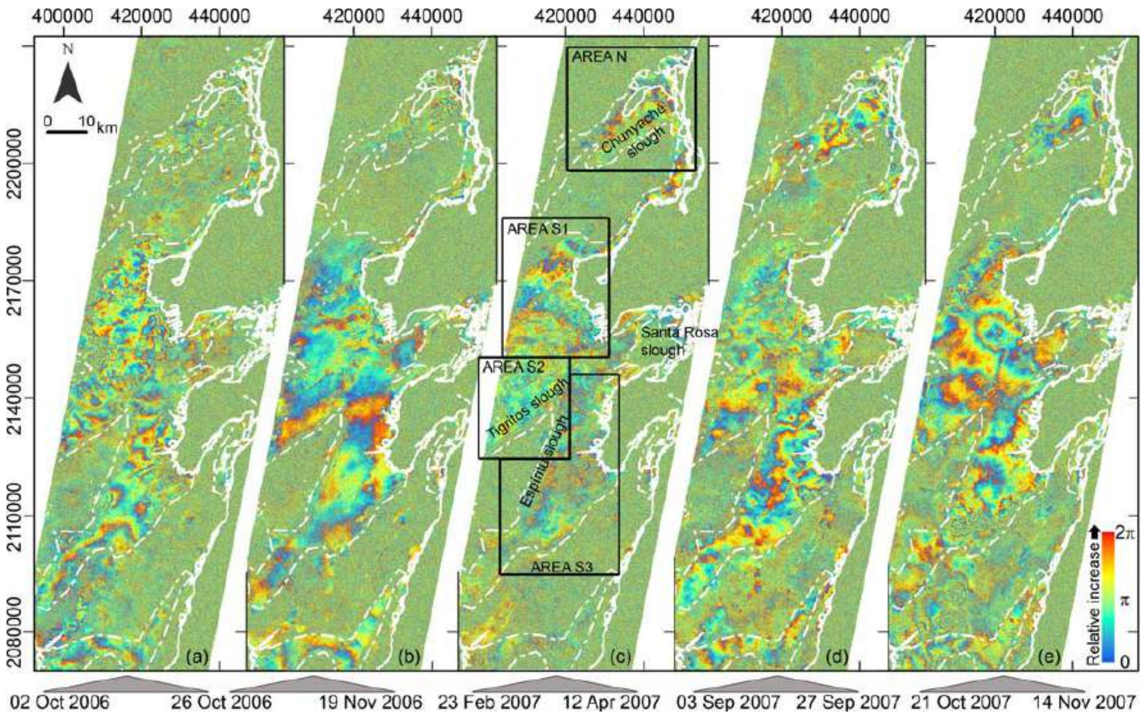

Fig. 6 Examples of the produced interferograms of the whole study area (Fine Beam F4), in the wet (**a**, **b**, **d**, **e**) and dry (**c**) season. Legend indicates direction of relative increase in water levels. *Full white line* is coast, *dashed white line* is the general outline of the wetlands. *Black boxes* show the location of the four different areas referred to in the text

delay patterns. Hence, in the analysis of our interferograms we only point out fringes and patterns that reoccur in the same places several times in interferograms that use different acquisitions, or patterns that can be associated with surface features such as tree barrier islands, channels etc.

Water Level Changes

Accuracy of InSAR-produced water level changes is usually derived by comparisons with *in situ* gauge height measurements. Gauge height measurements are also used to determine the offset between InSAR and absolute water level changes, transforming the relative InSAR changes to absolute changes (Wdowinski et al. 2008). Satellite altimetry can be used to measure absolute water levels over rivers, lakes, and wetlands (Berry et al. 2005). However, presently not enough suitable radar altimetry data are available over Sian Ka'an (R. G. Smith, Earth and Planetary Remote Sensing Laboratory, De Montfort University, UK, pers. comm. 2008).

We used our gauge height measurements to investigate the accuracy of the spatial pattern of water level changes obtained from InSAR. Table 2 displays water level changes as recorded on gauges and through interferograms (latest minus earliest date). We compared water level change differences between stations. Data were grouped in pairs of closest acquisition dates. There were 0–4 days difference in acquisition dates of InSAR and gauge height measurements. This should have negligible influence because water level changes varied slowly and smoothly where the gauges were located. InSAR water level changes between stations are within 0–2 cm of the gauge height measurements. Generally the InSAR data thus provide a good spatial representation of the water level changes.

Fringes in the interferograms relate to either local scale water divides or to water level changes, which are not spatially uniform. The latter can be caused by outflow, accumulation of water if flow into an area is faster than flow out of it, and tidal changes. The largest relative water level changes take place in the four sloughs of Sian Ka'an (Chunyaché, Tigritos, Espíritu, Santa Rosa), and at four main coastal outlets of the wetlands (an area between Chunyaché slough and Caapechen lagoon, a trapezoidal area in Area S1, the mouth of the Santa Rosa slough, and the bays in Area S3)(see Fig. 6c for the locations of these features). Fringes at the four coastal locations may partly or fully be caused by tidal changes. Detected water level changes were up to 28 cm (seven fringes) within 24 or 48 days (Fig. 7). Maximum hydraulic gradient changes were: Area near L. Caapechen — 78 ppm; Chunyaché slough — 46 ppm; trapezoidal area — 49 ppm; Santa Rosa slough — 13 ppm; mouth of Santa Rosa slough — 65 ppm; Tigritos slough — 8 ppm; Espíritu slough — 10 ppm; and bays in Area S3 — 117 ppm. Changes were thus 7 – 117% of the hydraulic gradient measured in the natural channel.

Timing of Sian Ka'an's Main Water Input

Catchment rainfall distribution during the time interval for the created flooding maps (Fig. 5) showed that flooding extent was related to the amount of rainfall. Interestingly, a 3-month backward moving average of the catchment rainfall data produced a pattern very similar to the flooding extent pattern (Fig. 5), which indicated that the flooding dynamics result from averaging and delaying the catchment response, and suggested that Sian Ka'an is indeed fed by ground water from a catchment larger than the area of the reserve itself. Water travel time from the catchment appears to be on the order of 3 months. Minimum flooding extent occurred slightly later than the minimum on the moving average curve, and might be explained by lower hydraulic gradients and slower ground-water flow during the dry season. Yet, not only the amounts of rain, but also the intensity of the rainfall influenced the extent of the wetland flooding. Hence, the

Table 2 Water levels change differences between gauge stations Muyil and Xlapak, derived from gauge height measurements and InSAR data. Gauge heights only read to nearest cm, hence no decimal places. As a rule of thumb, relative spatial accuracy of InSAR measurements is $^{1}/_{10}$ cycle, i.e. approx. 0.4 cm with the data used in this study

	Date (in 2007)	Diff. (cm) Muyil-Xlapak	Diff. (cm) Xlapak-Termite	Diff. (cm) Termite-Km7
Gauge heights	21Mar-10Apr	−1	*	*
InSAR data	19Mar–12Apr	−0.8	*	*
Gauge heights	29Apr–26May	0	*	*
InSAR data	30Apr–24May	0.1	*	*
Gauge heights	25May–10Jul	−1	*	*
InSAR data	24May–11Jul	0.5	*	*
Gauge heights	17Jun–07Jul	−2	3	−1
InSAR data	17Jun–11Jul	−1.4	1.1	−0.8

*Not presented due to lack of stage data

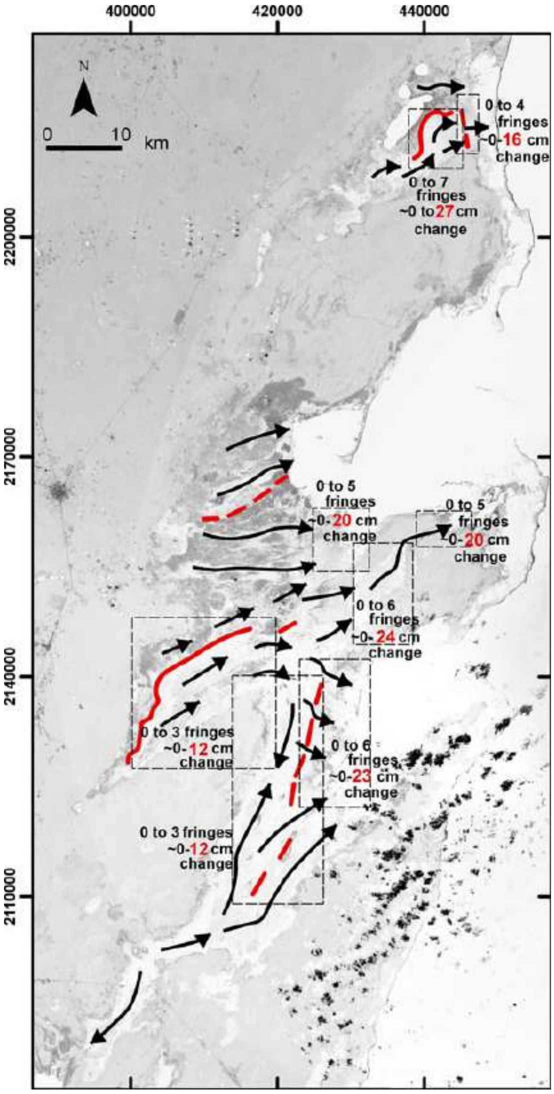

Fig. 7 *Black arrows*: Surface water flow directions, deduced from interferograms and visual inspection of Landsat imagery. *Red lines*: Semi- or impermeable water divides, deduced from abrupt phase changes and fringe lines. *Dashed boxes*: Areas with largest water level changes (most fringes). Background image: Grey-scaled Landsat TM Tri-Decadal mosaic, band 7

largest flooding extent occurred after an extreme rainfall event (the hurricane) and not after the largest amount of rain had fallen within the catchment (October 2007).

The smooth fringe patterns described for interferograms indicated that Sian Ka'an had the largest amounts of surface water in October, November, and December, as also indicated by the flood maps. Data from two ground-water hydrographs supported this finding. In Presidente Juarez, ground-water levels in a perched aquifer had their maximum in October 2007, whereas in Dzula, ground-water levels, measured in the regional aquifer, peaked in November–December 2007 (Fig. 8, locations shown in Fig. 1). Possibly the regional aquifer is partly recharged by the perched aquifer, which may explain the difference in timing of the maxima in the hydrographs.

Main Inflow Areas

Although the ground-water sources for the Sian Ka'an wetlands are diffuse, the flooding maps and interferograms revealed features from which we might deduce information about main water input zones to the wetlands. Below we propose three main water input areas, based on analysis of the SAR and InSAR data.

The flood map of the driest acquisition (Fig. 4c) indicates areas with main water input because areas still flooded during the peak of the dry season probably receive water from permanent input sources. The Tigritos slough (Area S2), the Chunyaché slough (Area N), and three channel-shaped flooded areas in Area S1 were flooded even at the driest times of the year. We therefore propose that these are main water input areas to Sian Ka'an.

The Tigritos slough always had water and high coherence east of a sharp line at the western end of the slough running SSW-NNE (Fig. 4c). Shapes of tree islands, seen in Landsat imagery, showed that the slough's predominant surface water flow direction is from west to east since the widest part of the teardrop-shaped tree islands indicates the upstream direction (Bazante et al. 2006). This suggests that the water source is at the western end. Likewise, fringes and tree islands in the Chunyaché slough showed that water flows

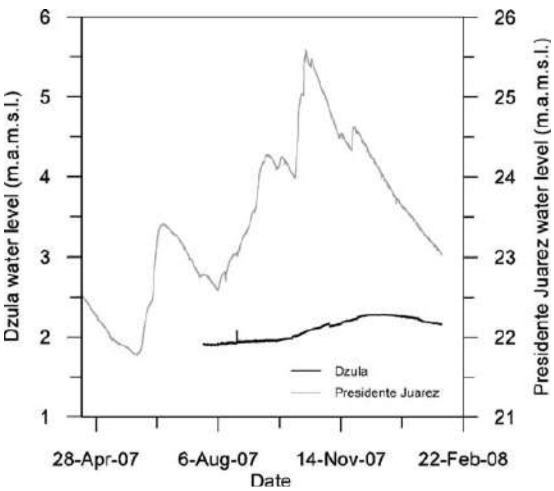

Fig. 8 Ground-water level changes in Presidente Juarez (perched aquifer) and Dzula (regional aquifer)

through the slough from west to east, indicating that the slough's source is located at its western boundary. In Area S1 the northern-most channel (named the Carrillo Feature in Fig. 4c) had dense fringes adjacent and parallel to it in a few interferograms (Fig. 9a), showing largest water level increase towards the feature and supporting the hypothesis that the feature feeds water into the surrounding wetlands.

The so-called Rio Hondo fault system is a series of sub-parallel normal faults, trending SSW-NNE (approx. N30E) (Weidie 1985). Some have their surface expression in the fault-guided lakes seen southwest of Sian Ka'an, of which the largest is Laguna de Bacalar (Fig. 10). The Rio Hondo faults may extend as far north as the northern part of Sian Ka'an (Weidie 1985), although no detailed maps of the location and extent of these faults exist. The Holbox fracture system, also trending SSW-NNE (approx. N5-10E) is located north of Sian Ka'an. Its southern terminus is not well determined, but possibly the Holbox and Rio Hondo fault systems intersect (Southworth 1985). Faults are known to guide the shape of the coast in the study area. The permanent water sources of Sian Ka'an proposed above may be connected to these fault systems. Based on geochemistry, Perry et al. (2002) established that Laguna de Bacalar does not have a direct hydrological connection to the ocean despite its proximity to the sea. We propose that the Rio Hondo fault system instead may be hydrologically connected to Sian Ka'an. The surprisingly linear western boundary of the Tigritos slough suggests that this slough may be fed by a ground-water-bearing fault. When this line is extended, it touches the most upstream point of the Carrillo Feature (Fig. 10). This line is parallel to the fault-guided coastline north of Sian Ka'an and the Holbox fracture system. Additionally, a line can be drawn following both the western edge of the depression forming the Area S2 wetlands and the ends of the two other permanently flooded channels in Area S1 (Fig. 10). This line parallels the coast at the bays and at the southern Mahahual Peninsula. Finally, the western edge of Chunyaché slough's permanently flooded part parallels the Holbox fracture zone as well as the series of lakes located on this line (Fig. 10).

Flow Directions and Local-Scale Water Divides

Water flow directions within the Sian Ka'an wetlands have not previously been described. InSAR data, combined with visual inspection of Landsat imagery, reveal flow paths, wetland dynamics, and local-scale water-divides. Figure 7 depicts dominant overall surface water flow paths within Sian Ka'an, interpreted from InSAR data and Landsat imagery. Flow is assumed perpendicular to main fringe directions.

The interferograms showed adjacent areas, which had individually uniform water level changes, but between

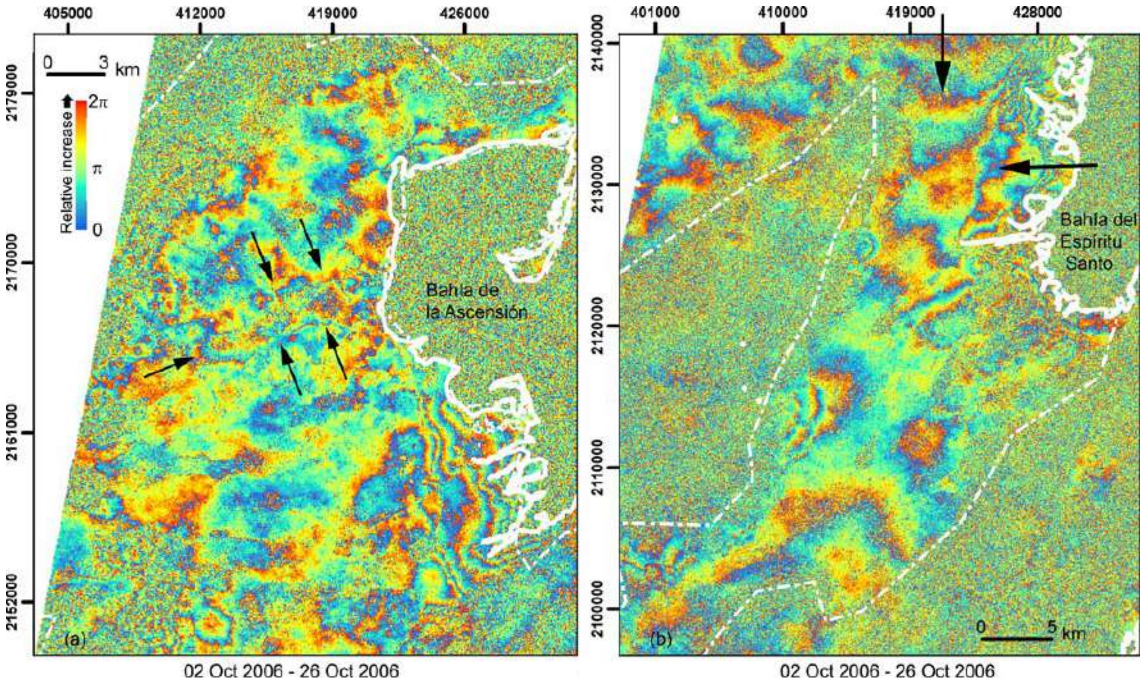

Fig. 9 **a** Interferogram over Area S1 with fringes parallel to the Carrillo Feature (*arrows*), and fringes in the trapezoidal area at the coast. **b** Interferogram over Area S3 showing that fringes in the Espíritu slough are normal to those in the bays area in the east (highlighted with *arrows*)

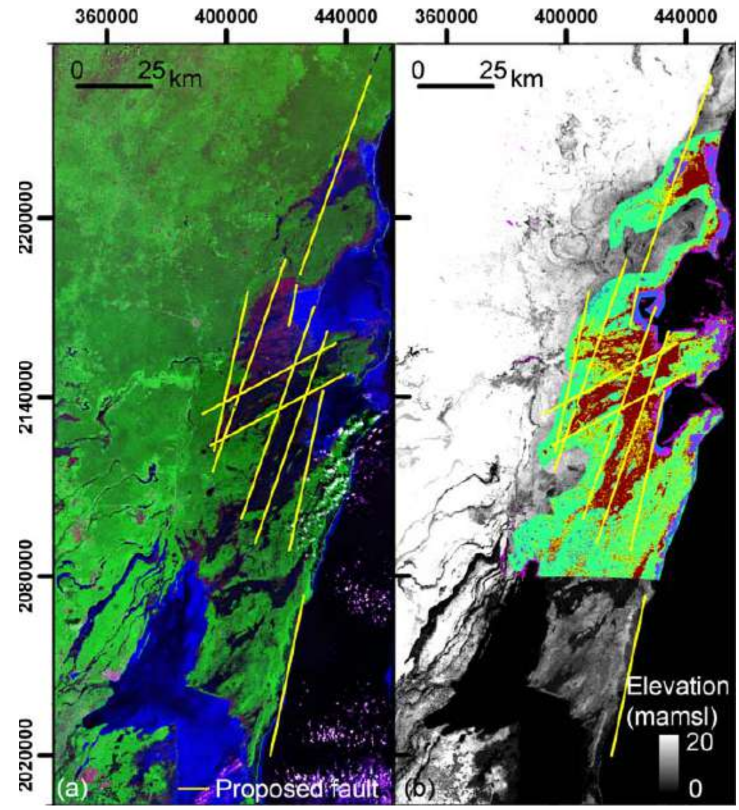

Fig. 10 The proposed faults as yellow lines, on the background of **a** Landsat TM Tri-Decadal mosaic, RGB: band 7, 4, 2; **b** topography data from the Shuttle Radar Topography Mission (SRTM) (grey-scale) and the May 2007 flooding map showing the smallest wetland extent. Color legend of the flooding map is seen in Fig. 4. Surface expression of the Rio Hondo faults are seen southwest of Sian Ka'an as elongated water bodies in (**a**) and depressions in (**b**). The Holbox fracture zone is partly seen in (**b**) as a line-shaped depression north of Sian Ka'an

which there was a sharp change in phase. Such features are interpreted as local scale water divides (red lines on Fig. 7). These divides may not be impermeable for water. The flooding regime however differs on each side of the divides. The divides may be caused by differences in vegetation cover (influencing the hydraulic resistance) and/or topographical relief (determining the flow direction).

The divide in Area N traces the boundaries of the Chunyaché slough (Fig. 11a and b). Part of the divide, sub-parallel and close to the Chunyaché lakeshore, had trees visible

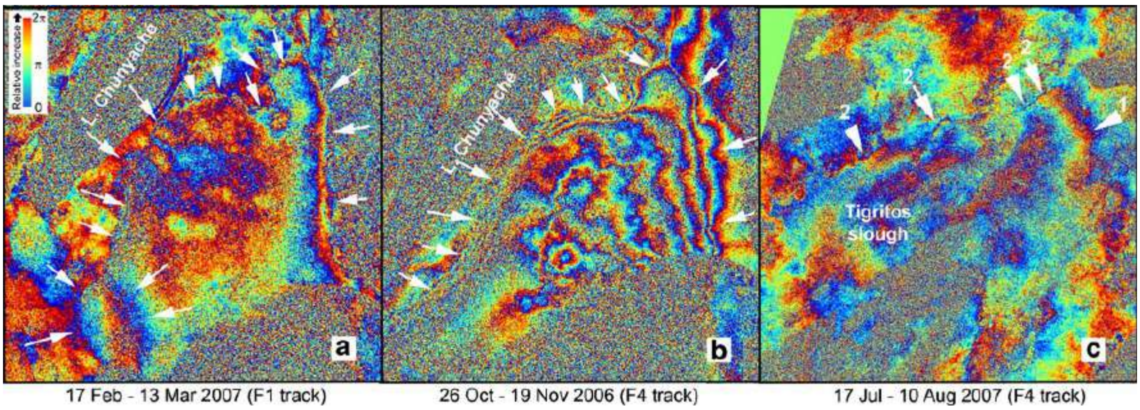

Fig. 11 **a** and **b**) Interferograms over the Chunyaché slough in Area N. *Arrows* highlight the fringes outlining the slough (**a** + **b**), and where it widens at the slough's western narrow part in (**a**). Many fringes within the slough are seen in (**b**), perpendicular to the flow direction. **c** Interferogram over Tigritos slough of Area S2. Arrow "1": Fringes indicating eastward flow direction from Tigritos to Santa Rosa slough. Arrows "2": Fringes indicating the divide between the outflow from the Tigritos slough and the area just north of this slough

on QuickBird imagery (Google Earth) indicating slightly higher topography here. Thus this water divide may be caused by minute differences in topography, which cannot be seen on the Shuttle Radar Topography Mission digital elevation model (SRTM DEM). Like other wetlands in low-relief landscapes (e.g., Everglades, Leonard et al. 2006; Okavango Delta, Gumbricht et al. 2005), water movement in Sian Ka'an is thus influenced by microtopography, which cannot be resolved by existing elevation models of the area.

The Tigritos slough was in many interferograms outlined by an abrupt phase change, or one or several fringes (e.g., Fig. 11c). At times of high water the boundary was somewhat further out, making the slough larger. The Tigritos slough's northern and southern boundaries are strikingly linear, and may also be fault guided (Fig. 10). At the slough's outlet, the water flow is partly directed towards the south and Area S3, and partly towards the east and the Santa Rosa slough (Fig. 7). This was supported by fringe directions (e.g., Fig. 11c) as well as the shape of tree islands seen on Landsat imagery. The change in flow direction could result from a tilt in topography, possibly caused by a fault forming the very linear western edge of the Espíritu slough (Fig. 10).

The fringe direction of the Espíritu slough and the bays near Bahía del Espíritu Santo were perpendicular to each other (Fig. 9b). This indicates an interesting flow pattern, bending off from a north–south direction in the slough to a west–east direction near to the bays. We suggest that this flow pattern is caused by a fault-induced tilt in topography at the eastern boundary of the slough (Fig. 10), yielding a steeper topographical gradient towards the bays.

Conclusions

Analysis of SAR and InSAR data over the Sian Ka'an wetlands showed that these remotely sensed data yield valuable information about this vast ground-water-fed wetland, for which hydrologic and hydrodynamic information is hard to obtain. Classification of SAR backscatter amplitude yielded time series of flooding extent maps, which can be used to calibrate hydrologic surface water models. Comparing these maps with catchment rainfall variations can give an order-of-magnitude estimate of ground-water travel time from the catchment to the wetlands.

Interferograms and flooding maps showed that sloughs are main water input areas, possibly fed by water-filled faults acting as main ground-water-transportation pathways. This has implications for protection of the wetlands, since transport of pollutants through such higher-permeability zones must be taken into account when planning and managing land use in the catchment of Sian Ka'an.

We found that information on water divides and flow directions can be obtained from interferogram fringe patterns. This type of information, or proxies for it (e.g., micro-topography), is often difficult or impossible to obtain for vast wetlands. Therefore this new utilization of InSAR data, as well as the water level changes obtained, is valuable for correct hydrological modeling of wetlands. Moreover, the information can guide water quality monitoring programs, with the aim to identify pollution transport pathways. Flow directions are also important for further studies on the interaction between ecology and hydrology in the wetlands.

InSAR and SAR data add significant information to our knowledge of the hydrologic dynamics of Sian Ka'an that will be useful for better management of this internationally important wetland. The approach presented in the present paper may also be useful for investigating other ground-water-dependent wetlands.

Acknowledgments RADARSAT data (Canadian Space Agency 2006, 2007, 2008) was distributed by the Center for Southeastern Tropical Advanced Remote Sensing, University of Miami, under Master License of RADARSAT International Inc. We thank CONANP staff for reading of gauge heights, Amigos de Sian Ka'an for logistical field help and Comisión Nacional del Agua for climate station data. Financial support was provided by WWF Verdensnaturfonden/Aase & Ejnar Danielsens Fond 2006 and 2007, Otto Mønsted's foundation, the COWIfoundation and NASA Cooperative Agreement No. NNX08BA43A (WaterSCAPES: Science of Coupled Aquatic Processes in Ecosystems from Space). Comments from anonymous reviewers and the Editor greatly improved this manuscript. This is CSTARS contribution #24.

References

Alsdorf DE, Melack JM, Dunne T, Mertes LAK, Hess LL, Smith LC (2000) Interferometric radar measurements of water level changes on the Amazon floodplain. Nature 404:174–177

Alsdorf DE, Smith LC, Melack JM (2001) Amazon floodplain water level changes measured with interferometric SIR-C radar. IEEE Transactions on Geoscience and Remote Sensing 39:423–431

Alsdorf D, Bates P, Melack J, Wilson M, Dunne T (2007) Spatial and temporal complexity of the Amazon flood measured from space. Geophysical Research Letters 34:L08402. doi:10.1029/2007GL029447

Bazante J, Jacobi G, Solo-Gabriele T, Reed D, Mitchell-Bruker S, Childers DL, Leonard L, Ross M (2006) Hydrologic measurements and implications for tree island formation within Everglades National Park. Journal of Hydrology 329:606–619. doi:10.1016/j.jhydrol.2006.03.011

Beddows PA (2004) Groundwater hydrology of a coastal conduit carbonate aquifer: Caribbean coast of the Yucatán Peninsula, México. Ph.D. Dissertation. University of Bristol, Bristol, UK

Berry PAM, Garlick JD, Freeman JA, Mathers EL (2005) Global inland water monitoring from multi-mission altimetry. Geophysical Research Letters 32:L16401. doi:10.1029/2005GL022814

Bourgeau-Chavez LL, Smith KB, Brunzell SM, Kasischke ES, Romanowicz EA, Richardson CJ (2005) Remote monitoring of regional inundation patterns and hydroperiod in the Greater Everglades using synthetic aperture radar. Wetlands 25:176–191

Buckley S, Rosen P, Persaud P (2000) ROI_PAC Documentation—Repeat Orbit Interferometry Package. Version 1.1. http://www.earth.ox.ac.uk/~timw/roi_pac/ROI_PAC_doc.pdf. Accessed 7 Mar 2008

Comisión Nacional del Agua (2008) Climate data 1952–2007 for the Yucatan Peninsula obtained from the database of Comisión Nacional del Agua, Merida, Mexico
Goldstein RM, Zebker HA, Werner CL (1988) Satellite radar interferometry—two-dimensional phase unwrapping. Radio Science 23:713–720
Goldstein RM, Engelhardt H, Kamb B, Frolich RM (1993) Satellite radar interferometry for monitoring ice-sheet motion—application to an Antarctic ice stream. Science 262:1525–1530
Gumbricht T, McCarthy TS, Bauer P (2005) The micro-topography of the wetlands of the Okavango Delta, Botswana. Earth Surface Processes and Landforms 30:27–39. doi:10.1002/esp.1124
Hess LL, Melack JM, Novo EMLM, Barbosa CCF, Gastil M (2003) Dual-season mapping of wetland inundation and vegetation for the central Amazon basin. Remote Sensing of Environment 87:404–428. doi:10.1016/j.rse.2003.04.001
Kim S-W, Wdowinski S, Amelung F, Dixon TH (2005) C-band interferometric SAR measurements of water level change in the wetlands: examples from Florida and Louisiana. Geoscience and Remote Sensing Symposium. IGARSS '05. IEEE International 4:2708–2710
Lang MW, Kasischke ES (2008) Using C-band synthetic aperture radar data to monitor forested wetland hydrology in Maryland's coastal plain, USA. IEEE Transactions on Geoscience and Remote Sensing 46:535–546. doi:10.1109/TGRS.2007.909950
Leonard L, Croft A, Childers D, Mitchell-Bruker S, Solo-Gabriele H, Ross M (2006) Characteristics of surface-water flows in the ridge and slough landscape of Everglades National Park: implications for particulate transport. Hydrobiologia 569:5–22
Lerer S (2008) Estimation of actual evapotranspiration using remote sensing data for the Yucatan Peninsula, Mexico. M. Sc. Thesis. Technical University of Denmark, Kgs. Lyngby, Denmark
Lesser JM (1976) Estudio hidrogeologico e hidrogeoquimico de la Peninsula de Yucatan. Proyecto Conacyt-NSF 704, Secretaria de Recursos Hidraulicos, Direccion de Geohidrologia y Zonas Aridas, Mexico
Lopez-Ornat A, Ramo C (1992) Colonial waterbird populations in the Sian Ka'an Biosphere Reserve (Quintana Roo, Mexico). Wilson Bulletin 104:501–515
Lu Z, Kwoun O (2008) Radarsat-1 and ERS InSAR analysis over southeastern coastal Louisiana: Implications for mapping water-level changes beneath swamp forests. IEEE Transactions on Geoscience and Remote Sensing 46:2167–2184. doi:10.1109/TGRS.2008.917271
Lu Z, Crane M, Kwoun O, Wells C, Swarzenski C, Rykhus R (2005) C-band radar observes water level change in swamp forests. EOS Transactions, AGU 86:141–144
Martinez J-M, Le Toan T (2007) Mapping of flood dynamics and spatial distribution of vegetation in the Amazon floodplain using multi-temporal SAR data. Remote Sensing of Environment 108:209–223
Massonnet D, Feigl KL (1998) Radar interferometry and its application to changes in the Earth's surface. Reviews of Geophysics 36:441–500
Massonnet D, Rossi M, Carmona C, Adragna F, Peltzer G, Feigl K, Rabaute T (1993) The displacement field of the Landers earthquake mapped by radar interferometry. Nature 364:138–142
Mazzotti FJ, Fling HE, Merediz G, Lazcano M, Lasch C, Barnes T (2005) Conceptual ecological model of the Sian Ka'an Biosphere Reserve, Quintana Roo, Mexico. Wetlands 25:980–997
Morales Barbosa JJ (1992) Los humedales, un mundo olvidado. Series: Sian Ka'an, Introducción a los Ecosistemas de la Península de Yucatan. Amigos de Sian Ka'an A. C.. Impresos MARCA, Mérida, Yucatán, Mexico
NASDA/NASA (2008) Tropical Rainfall Measuring Mission (TRMM), data product 3B43. TRMM algorithms were developed by the TRMM Science Team. TRMM data were processed by the TRMM Science Data and Information System (TSDIS) and the TRMM Office; archived and distributed by the Goddard Distributed Active Archive Center. TRMM is an international project jointly sponsored by the Japan National Space Development Agency (NASDA) and the U.S. National Aeronautics and Space Administration (NASA) Office of Earth Sciences
Neuman BR, Rahbek ML (2007). Modeling the groundwater catchment of the Sian Ka'an Reserve, Quintana Roo. Association for Mexican Cave Studies. Bulletin 18. AMCS bulletin publication
Olmsted I, Duran R (1990) Vegetación de Sian Ka'an. In: Navarro D, Robinson JG (eds) Diversidad biológica de la Reserva de la Biósfera de Sian Ka'an, Quintana Roo, Mexico. Centro de Investigaciones de Quintana Roo, Quintana Roo, pp 1–12
Perry E, Velazques-Oliman G, Marin L (2002) The hydrogeochemistry of the karst aquifer system of the northern Yucatan Peninsula, Mexico. International Geology Review 44:191–221
Pope K, Rejmankova E, Paris JF, Woodruff R (1997) Detecting seasonal flooding cycles in marches of the Yucatan Peninsula with SIR-C polarimetric radar imagery. Remote Sensing of Environment 59:157–166
Pozo de la Tijera C, Escobedo Cabrera JE (1999) Mamíferos terrestres de la Reserva de la Biosfera de Sian Ka'an, Quintana Roo, México. Revista de Biología Tropical 47:251–262
RADARSAT International (1995) RADARSAT illuminated—your guide to products and services. RADARSAT International Client Services, Richmond
Richards JA, Woodgate PW, Skidmore AK (1987) An explanation of enhanced radar backscattering from flooded forests. International Journal of Remote Sensing 8:1093–1100
Rio JNR, Lozano-García DF (2000) Spatial filtering of radar data (RADARSAT) for wetlands (brackish marshes) classification. Remote Sensing of Environment 73:143–151
Sass GZ, Creed IF (2008) Characterizing hydrodynamics on boreal landscapes using archived synthetic aperture radar imagery. Hydrological Processes 22:1687–1699. doi:10.1002/hyp.6736
Southworth CS (1985) Applications of remote-sensing data, eastern Yucatan. In: Ward WC, Weidie AE, Back W (eds) Geology and Hydrogeology of the Yucatan and Quaternary Geology of Northeastern Yucatan Peninsula. New Orleans Geological Society, New Orleans, pp 12–19
Ulaby FT, Dubois PC, van Zyl J (1996) Radar mapping of surface soil moisture. Journal of Hydrology 184:57–84
USGS (2003) Landsat: A global land-observing program fact sheet 023-03. http://egsc.usgs.gov/isb/pubs/factsheets/fs02303.html. Accessed 15 June 2008
USGS (2006) Shuttle Radar Topography Mission, 3 Arc Second, Finished 2.0. Global Land Cover Facility, University of Maryland, College Park, MD, USA. Accessed 15 June 2006
Wdowinski S, Amelung F, Miralles-Wilhelm F, Dixon TH, Carande R (2004) Space-based measurements of sheet-flow characteristics in the Everglades wetland, Florida. Geophysical Research Letters 31:L15503. doi:10.1029/2004GL020383
Wdowinski S, Kim S-W, Amelung F, Dixon T, Miralles-Wilhelm F, Sonenshein R (2008) Space-based detection of wetlands' surface water level changes from L-band SAR interferometry. Remote Sensing of Environment 112:681–696. doi:10.1016/j.rse.2007.06.008
Weidie AE (1985) Geology of Yucatan Platform. In: Ward WC, Weidie AE, Back W (eds) Geology and hydrogeology of the Yucatan and quaternary geology of northeastern Yucatan Peninsula. New Orleans Geological Society Publications, New Orleans, pp 1–12
Zebker H, Villasenor J (1992) Decorrelation in interferometric radar echoes. IEEE Transactions on Geoscience and Remote Sensing 30:950–959

II

Spatial mapping of submerged cave systems by means of airborne electromagnetics: an emerging technology to support protection of endangered karst aquifers

Supper, R., Motschka, K., Ahl, A., Bauer-Gottwein, P., Gondwe, B., Alonso, G.M., Romer, A., Ottowitz, D., Kinzelbach, W.

Near Surface Geophysics 2009, 7 (5–6), 613–327

Near Surface Geophysics, 2009, 613-627

Spatial mapping of submerged cave systems by means of airborne electromagnetics: an emerging technology to support protection of endangered karst aquifers

Robert Supper[1*], Klaus Motschka[1], Andreas Ahl[1], Peter Bauer-Gottwein[2], Bibi Gondwe[2], Gonzalo Merediz Alonso[3], Alexander Römer[1], David Ottowitz[1] and Wolfgang Kinzelbach[4]

[1] *Geological Survey of Austria, Neulinggasse 38, 1030 Vienna, Austria*
[2] *Department of Environmental Engineering, Technical University of Denmark, Miljovej, Building 113, 2800 Kgs Lyngby, Denmark*
[3] *Amigos de Sian Ka'an, Fuego # 2 Manzana 10 SM 4, Cancún, Quintana Roo, 77500, Mexico*
[4] *Institute of Environmental Engineering, ETH-Zürich, HIL G 37.3, 8093 Zurich, Switzerland*

Received October 2008, revision accepted February 2009

ABSTRACT
Karst aquifers represent important but very vulnerable sources for water supply to a significant part of the Earth's population. For sustainable use of these resources, development of integrated management tools based on numerical groundwater models is required. In principle karst aquifers are characterized by the presence of two distinct flow domains: the limestone matrix fractures and the conduits. A flow model of karst aquifers requires detailed, spatially distributed information on the hydrologic characteristics of the aquifer and flow paths. Geophysical methods determining the distribution of the electrical resistivities within the subsurface could provide such information. An international scientific research project was initiated to explore the potential of airborne electromagnetic mapping for providing such innovative information for improving groundwater modelling of karst aquifers. The project study area is located in the Sian Ka'an Biosphere Reserve located in Yucatán, Mexico, a coastal wetland of international importance. As a first step ground geoelectric and ground electromagnetic measurements were performed in March 2006 to determine the electrical properties of the Sian Ka'an Biosphere Reserve subsurface environment. These results were used for 3D forward modelling to calculate the expected airborne electromagnetic response. Based on these promising results, an airborne pilot survey was performed in 2007 to evaluate the applicability of airborne electromagnetic methodology. This survey covers an area of 40 square kilometres above the well-mapped Ox Bel Ha cave system. The results showed that the signature of the cave system could be clearly detected. The pilot survey offered as well the chance to define the limits of current state-of-the-art airborne data acquisition and inversion. The study helped to define the needs for further developments and improvements to establish the frequency domain electromagnetic method as a practical karst exploration method.

INTRODUCTION

Karst terrain covers approximately 12% of the Earth's land surface and karst aquifers are important water resources in many parts of the world (e.g., Williams 1993; Ford and Williams 2007). Due to the rapid water flow in karst aquifers and their limited capacity for retention of pollutants, these water resources are extremely vulnerable to environmental pollution. Therefore, protection of karst areas is of major concern to ensure adequate water supply for a significant portion of the Earth's population (e.g., Darnault 2008).

In order to protect karstic groundwater systems and associated ecosystems, it is necessary to develop integrated tools for sustainable management of these resources based on accurate coupled surface-/groundwater models. Although the mathematical formulation of such models is well established, results are mostly unsatisfactory. The reason for this is that both location and geometry of dominant karst features, controlling the flow, are either not known at all or not known with the required accu-

* robert.supper@geologie.ac.at

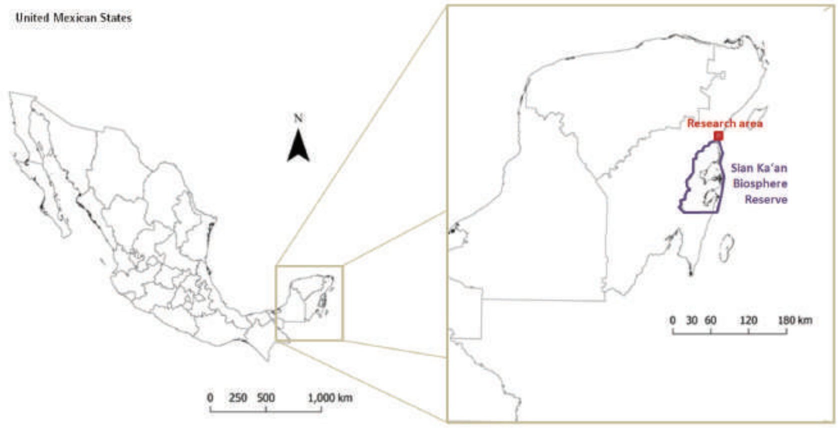

FIGURE 1
Location map of the SKBR and research area.

racy. Therefore, the results of hydrological modelling of karst aquifers could significantly advance if new and innovative technologies are developed to provide high-resolution constraints in groundwater models. The results of airborne electromagnetics could provide such information. The research project XPLORE was initiated to explore and improve the potential of airborne geophysical measurements and the associated interpretation techniques to provide such information.

The area around the Sian Ka'an Biosphere Reserve (SKBR) (for location see Fig. 1) was chosen as a test site as it offers favourable conditions for the application of the proposed frequency domain airborne electromagnetic techniques (FDEM) due to the following facts:

- The area is extremely flat and the karst is exposed right at the surface in the entire area, thus allowing low flight altitudes (60 m); almost no topographic effects are of concern.
- Topsoils are relatively thin and will not appreciably attenuate the electromagnetic signal.
- The dominant karst structures are located at shallow depth (max. 25 m).
- Though the karst conduit system in this area is largely unexplored, except in the Northern part, scuba diving for cave exploration has mapped the conduits. In this area the cave systems (e.g., Ox Bel Ha, Sac Actun) are known in great detail. The available cave maps can be used as ground truth for the interpretation of the airborne geophysical data.

These conditions form a perfect background for the evaluation of various technologies under simple boundary conditions.

First, ground geoelectric and electromagnetic measurements were applied to develop a general subsurface resistivity model for SKBR. Subsequently, forward modelling of frequency domain electromagnetic results using the above mentioned synthetic resistivity model was performed to evaluate the principal applicability of the methodology. Based on the promising results, a pilot airborne electromagnetic survey was conducted, covering an area north of the SKBR. The results of ground surveys, forward modelling and of the pilot airborne survey are presented here.

STATE-OF-THE-ART GEOPHYSICAL KARST EXPLORATION

Karstifiable rocks are a traditional focus of geophysical research (Bögli 1980). Several case studies can be found in the literature (e.g., McGath *et al.* 2002; Beck 2002; Cunningham 2002; Roth *et al.* 2002; Danbom 2005). Some successful results have been obtained using various geophysical methods, such as gravity (Debeglia and Dupont 2002), geoelectrics (Mingelli 1989; Zhou *et al.* 2002; Nyquist *et al.* 2007), coupled resistivity (Garmann and Purcell 2004), ground-penetrating radar (GPR) (Henson *et al.* 1997; Carreon-Freyre and Cerca 2006), proton magnetic resonance (Guérin and Benderitter 1995) and electromagnetics (Nyquist *et al.* 1999). On the Yucatán Peninsula, Steinich and Marin 1997 employed azimuthal resistivity surveys to identify directions of high permeability within the aquifer. Doolittle and Collins (1998) and Guerin and Benderitter (1995) demonstrated the application of two independent methods to improve the results of geophysical karst exploration.

As a shortcoming, all ground-based surveys are restricted by terrain accessibility. So far only a few studies are available where airborne geophysics has been applied to karst regions (Beard *et al.* 1994; Doll *et al.* 2000; Gamey *et al.* 2001, 2002; Mandell *et al.* 2003; Smith *et al.* 2003, 2005, 2008) we anticipate improvement for karst exploration results using airborne multi-sensor (electromagnetic (EM), very low frequency (VLF), Gamma) surveys, although their potential has not yet been explored exhaustively. Finally, two papers by Bosch and Müller (2001, 2005) suggested VLF gradient surveys for innovative high-resolution surveys over vulnerable karst regions. Most of these studies have focused on structural investigation and basement mapping in karst areas. However, the authors do not know of any study where results derived from airborne geophysical data have been used to characterize hydrological units for the modelling of karst aquifers.

To conclude, geophysics has shown that ground-based methods can identify aquifer units on a local basis. The ground-based data collection is only local and time- consuming and it is not realistic to apply it to the exploration of large groundwater systems, especially in inaccessible terrain. Airborne multi sensor platforms can be applied over large areas to map hydrostratigraphic units. However, results so far from airborne data have not been related to the characteristics of aquifer units. On a regional scale the role of geophysics and especially of remotely sensed data, has definitely not been fully exploited.

THE RESEARCH AREA

The Sian Ka'an Biosphere Reserve (SKBR), located on the Yucatán Peninsula, Mexico (Fig. 1), is a UNESCO World Heritage site, established in 1986. It is composed of a number of different ecosystems. The marine area of the SKBR includes parts of the widespread barrier reef system along the eastern coast of Central America (Morales 1993). The terrestrial ecosystems encompass evergreen and deciduous forests, savannahs, freshwater and saltwater marshes, mangroves and dunes (Morales 1992, 1995; see Fig. 2). The rainforests are part of the Gran Selva Maya, which is the world's largest continuous rainforest area north of the Amazon Basin. The reserve is home to a wide variety of wildlife including puma and jaguar and it hosts dozens of colonial water bird species.

SKBR is primarily fed by subsurface flow through the karstified limestone of the Yucatán plain. The general groundwater flow pattern on the Yucatán Peninsula is generally believed to be characterized by a radial flow pattern from the centre of the peninsula towards the coasts at the peninsula margins. However, locally, flow directions can be highly variable depending on the orientation of karst conduits and fractures.

The area receives precipitation of around 1000 to 1500 mm/year. Evapotranspiration is not well determined but estimates range between 40% (Beddows 2004) to 85% (Lesser 1976) of mean annual precipitation.

The underground hydrologic system in the study area is the key ecological link between the tropical forest, wetlands, coral reef and other marine ecosystems, as well as the human activities associated with those environments. Pressure on the reserve has been increasing over the years due to accelerated tourism development in the region, increased domestic water demand, contamination with agricultural fertilizers and pesticides as well as infrastructure projects, illegal hunting activities and extensive fishing. High population growth rates (over 10% per year in the region), high tourism activity (about 10 million visitors to the region in 2004) and poor waste water treatment (less than 30% of the total waste water produced in the region is treated in any way), makes water quality issues one of the area's most important and significant social and environmental problems and demands an integrated approach towards the management of SKBR.

On a local scale, the municipality of Tulum, located a few kilometres north of SKBR, is currently in the process of designing an urban development plan (Programa de Desarrollo Urbano del Centro de Población de Tulum (PDU), Gaceta Parlamentaria, (http://gaceta.diputados.gob.mx/Gaceta/60/2008/abr/20080430.html), año XI, número 2496, miércoles 30 de abril de 2008). The preliminary version of the PDU promotes the establishment of 60 000 hotel beds in Tulum. Presently Tulum has about 12 000 inhabitants and the PDU foresees an at least tenfold increase in the local population. The urban area is expected to expand significantly reaching the border of the SKBR in the south.

At the moment, knowledge on the hydrogeology of the area discussed in the PDU is fragmentary. Cave divers have explored parts of the karst conduits but up to date no systematic study on aquifer geometries and properties, groundwater flow directions and velocities exist. Two major problems are associated with the unknown aquifer structure in the area of the PDU: i) large karst cavities can collapse and are a potential hazard for the planned hotels and infrastructure in the area and ii) large quantities of wastewater will be generated by the increased permanent population and the visitors. A coherent concept for the treatment and disposal of the wastewater is lacking (Beddows *et al.* 2007;

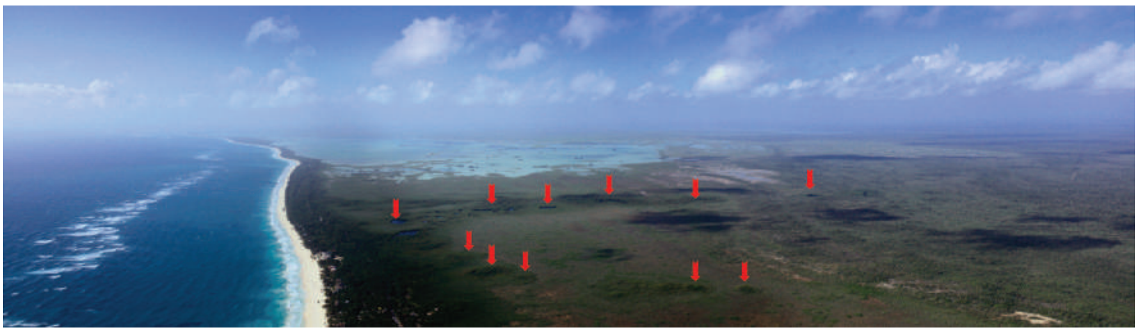

FIGURE 2

Airborne photograph showing part of the SKBR (photography: R. Supper, 02-2008; panorama stitching: A. Ahl) showing the different ecosystems: left side: Caribbean Sea with barrier reef and dunes, central back side: saltwater and freshwater lagoons, central foreground: mangrove woods and savannah, right side: rainforests of the Gran Selva Maya; in the central area, several cenotes can be recognized (red arrows), whose alignment marks the course of the main subsurface cave system.

Amigos de Sian Ka'an, Resultados de la Reunión. Document from the CD-Rom of the workshop: Construyendo las Bases Para la Conservación del Agua y su Biodiversidad Asociada en la Península de Yucatan. 10 y 11 de noviembre 2003, Cancún Quintana Roo Amigos de Sian Ka'an, The Nature Conservancy y la Comisión de Áreas Naturales Protegidas.; Krekeler *et al.* 2007). Local authorities favour re-injection of the wastewater into the deeper aquifer units, beneath the halocline (Beddows *et al.* 2007; Sam Mecham (pers. comm.) with the cave diver and director of Centro Investigador del Sistema Acquífero de Quintana Roo A.C. (CINDAQ) April 2006). However, due to its lower density compared to seawater, the wastewater may potentially resurface and pollute the freshwater lens that is currently serving as the backbone for water supply to the region. Wastewater discharge into the ocean will in turn endanger the ecological integrity of the coral reef, which is one of the prime economic assets of the region. Finally, it is presently unknown, whether some of the large subsurface conduits connect the area of the PDU to SKBR and whether the hydraulic gradient is directed towards or away from the reserve. In order to develop sustainable options for wastewater disposal and enhanced urban development of Tulum, an aquifer characterization and modelling study is urgently required.

GEOPHYSICAL KARST EXPLORATION RESULTS FOR THE SKBR

The application of airborne electromagnetic methods to map large-scale karst systems over wide-ranging areas seems promising to aid the above studies. However, karst conduits can only be detected by this method if the contrast between the resistivity of the carbonate host rock and the resistivity of the karst features is sufficiently high. Consequently, to start an airborne survey in Mexico without any preknowledge would pose a high financial and logistical risk. Therefore, a pilot ground based resistivity survey was performed in March 2006 to determine the electrical properties of

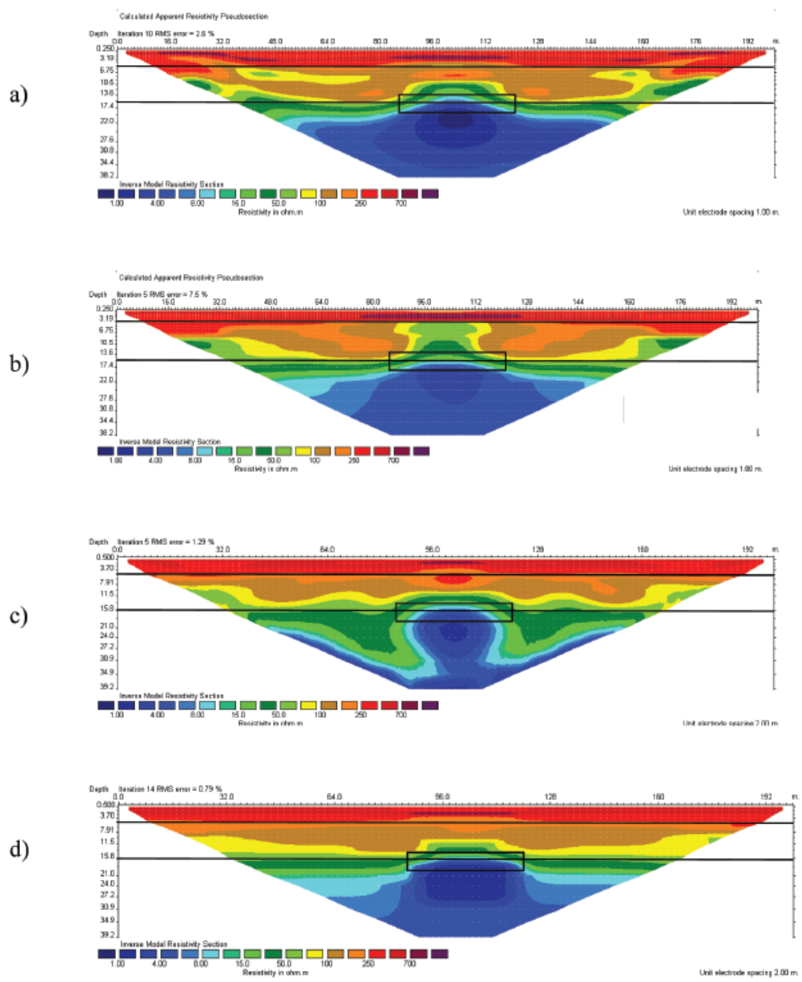

FIGURE 3
Results of inversion of synthetic geoelectrical data (Schlumberger configuration) with RES2DINV using different settings: a) smooth inversion, model block spacing: half electrode distance; b) robust inversion, model block spacing: half electrode distance; c) smooth inversion, model block spacing: unit electrode distance; d) robust inversion, model block spacing: unit electrode distance; black lines and rectangle indicate the shape of the initial model.

the SKBR subsurface environment. Subsequent forward modelling was applied to evaluate the potential success of applying airborne electromagnetic methods to map large-scale karst features within SKBR. On the other hand the inversion results gave important ground truth for the interpretation of the airborne electromagnetic field data from the airborne pilot survey.

The ground-based geoelectric survey campaign

Geoelectric multielectrode measurements and ground based electromagnetic (EM-34) profiles have been the method of choice to derive high-resolution 2D models of the subsurface resistivity structure, including cave systems, known from scuba diving exploration (based on the unpublished cave maps supplied by Sam Mecham (CINDAQ) and Robbie Schmittner (Xibalba Dive Center) (pers. comm.), for names of individual cave explorers see acknowledgements) at different locations.

Results of forward modelling and inversion of synthetic geoelectric data

Due to ambiguities inherent to the geoelectrical method, it is unlikely that the exact shape of a cave could be recovered from inversion of field data. However, the inversion could be improved by applying constrained inversion parameters. Based on a synthetic subsurface model, a geoelectric pseudosection was calculated for the Schlumberger configuration and subsequently inverted using different inversion parameters. The cave model used was set up according to the results of direct conductivity measurements over the cave system and field inspections performed during the first days of the field survey. The parameters were defined for a typical subsurface setting approximately 6–8 km inland from the Caribbean Sea. The average groundwater table at that location was found at a depth of 4.5 m, the depth to the halocline (interface between brackish (4 Ohmm) and marine (0.2 Ohmm) water) at 16 m. The cave was assumed to be located between a depth of 14 m and 20 m and to exhibit a width of 34 m (located between profile distance 86 m and 120 m). A bulk resistivity value of 500 Ohmm was assigned to dry limestone, 100 Ohmm to saturated limestone filled with brackish water and 6 Ohmm to saturated limestone with saline water filling. Subsequently the calculated values have been inverted using the RES2DINV (Loke and Dahlin 2002) and EarthImager 2D (http://www.agiusa.com/agi2dimg.shtml) software. Figure 3 presents the results for the RES2DINV software inversion using a) smooth, b) robust inversion based on model cells with width of half the unit electrode spacing (herein after referred to as 'smooth / robust half distance') and c) smooth, d) robust inversion based on model cells with a width of one unit electrode spacing (herein after referred to as 'smooth / robust normal distance'). The results showed that in all cases the horizontal location of the cave was reconstructed quite well whereas the exact geometry and depth below surface of the initial model could not be resolved. The depth to the top of the cave was generally underestimated (5–10 m). The depth to the bottom of the cave (27–30 m) as well as the actual resistivity of the brackish (15–50 Ohmm) and saline portion (1–4 Ohmm) of the cave, was overestimated. In the 'smooth half distance' case 3a) an intermediate low resistivity layer on either side of the cave at an average depth of 7 m was introduced. The best indication for the presence of a cave could be derived in the 'robust half distance' case 3b), whereas the most realistic representation of the input model could be obtained using the 'robust normal distance' d) parameter set. Results for the Earth Imager software show similar results, although edge effects are much smaller.

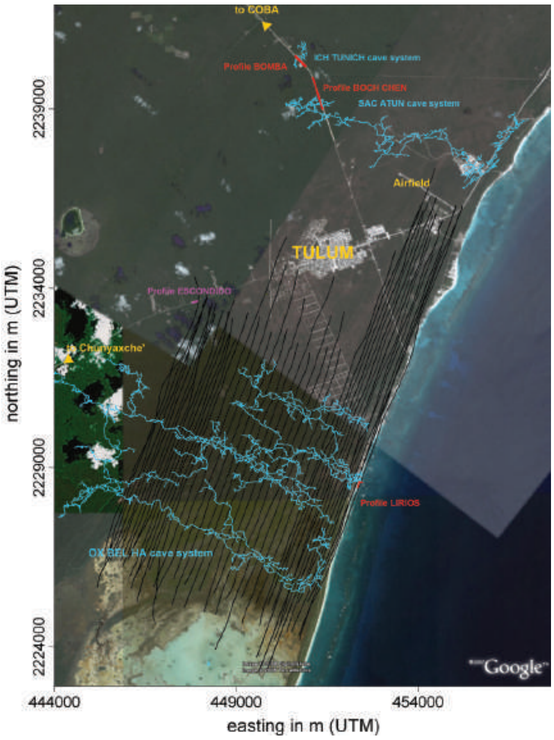

FIGURE 4
Location map showing the mapped cave systems (blue), geoelectrical profiles (red), the electromagnetic ground profile (purple) and airborne electromagnetic profiles (black). In the background, a satellite image taken from 'Google Earth' is shown.

The experience gained from these modelling studies, together with geological background information, was used to select inversion parameters and constraints for the inversion of the actual field data.

Results of geoelectric field measurements

Based on the results from scuba diving exploration several profiles were selected crossing known karst caves at different subsurface conditions. As most of the area is covered by dense vegetation, only a few locations over known cave systems were actually accessible to perform ground surveys. The locations of the measured profiles are indicated in Fig. 4. For this paper three profiles were selected as they investigate the subsurface resistivity structure at different constraints. The profile near Cenote Bomba investigates the near surface response from a well-known cave branch at 8 km distance from the sea whereas profile Cenote Boch Chen is intended to survey resistivities within the deeper subsurface below the halocline. Profile Lirios examines the typical subsurface resistivity pattern nearby the coastline.

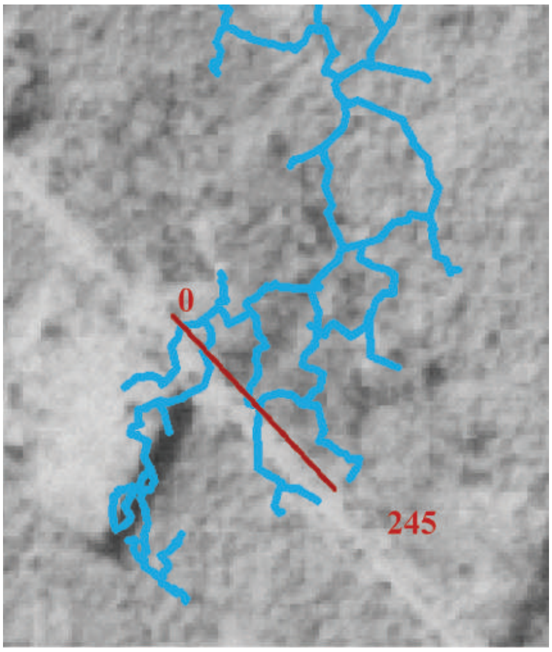

FIGURE 5
Location of the geoelectrical profile BOMBA in relation to the subsurface cave system, mapped by cave diving exploration (red line: geoelectric profile Bomba; light blue lines: mapped line inside cave system).

Profile Cenote Bomba

This profile was measured in an area 4–5 km north of Tulum, parallel to the main street to Coba between the two cenotes (Mexican word for sinkhole) 'Bomba' and 'High Voltage'. According to the scuba divers' exploration a large cave crosses the profile right in the middle (see Fig. 5, crossing point between profile distance 110 m and 150 m). The bottom of the cave could be expected at a depth of 16 m. Figure 6 shows the results of inversion for a) the Res2dinv (robust, half unit spacing) and for b) the EarthImager (smooth inversion, average resistivity of pseudosection was used as starting model) software. In both inversion results the existence of a cave could be detected quite clearly in the middle part of the section. The depth to the groundwater table was located at a depth of 5 m below ground level (bgl). The resistivity of the fresh/brackish groundwater layer was found to be relatively high (>150 Ohmm), suggesting a low porosity of the un-karstified limestone. The halocline is detected quite clearly as a resistivity gradient, although its depth (approximately 18 m) is overestimated by Earth Imager (25 m). The latter smooth inversion also detects three more caves at 33 m, 66 m and after 216 m along the profile, which can be correlated with caves known from the cave map. The similarity of the result shown in Fig. 6(a) with the forward modelling result of Fig. 3(b) is obvious. However, the result of the smooth inversion of Fig. 6(b) seems to enhance small variations in the measured resistances, eventually due to noise potentials, thus producing resistivity pattern with unrealistically high resolution.

Profile Cenote Boch Chen

This profile was measured near profile Bomba on the highway to Coba, starting near Gran Cenote and crossing the side tunnels of Cenote Boch Chen in the middle part of the profile between 300 m and 400 m. This profile was carried out to investigate the resistivity distribution at greater depths (>140 m). To reach these depths an electrode spacing of 10 m was used. Due to this large

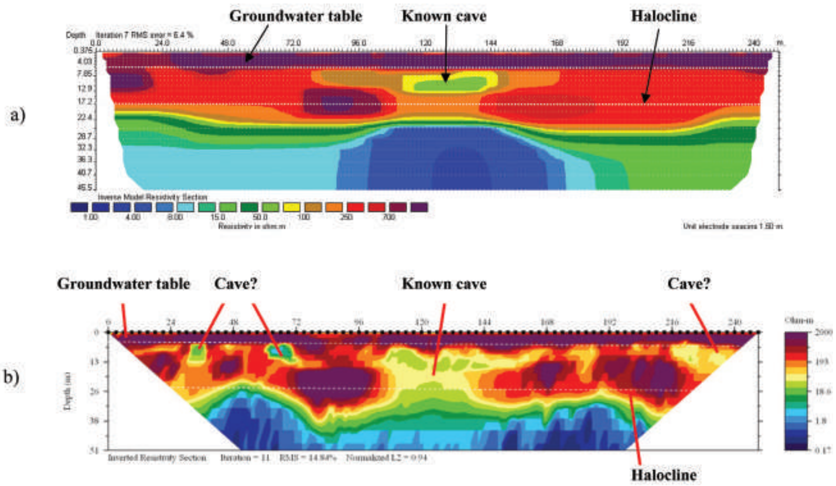

FIGURE 6
Results of inversion of geoelectrical data (Schlumberger-Wenner configuration) on profile Bomba: a) RES2DINV robust inversion, model block spacing: half electrode distance; b) EarthImager smooth inversion, starting model: average apparent resistivity.

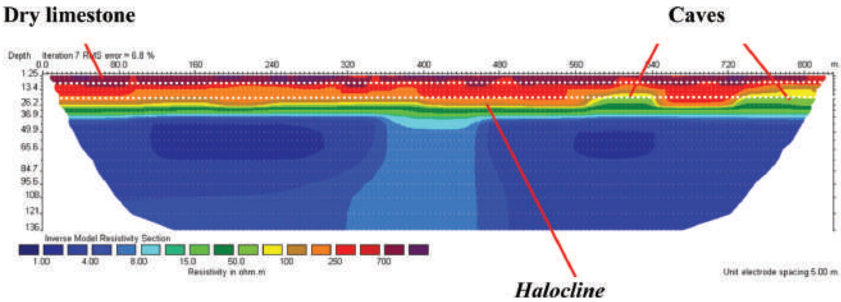

FIGURE 7
Results of inversion of geoelectrical data (Schlumberger-Wenner configuration) on profile Cenote Boch Chen: RES2DINV robust inversion, model block spacing: half electrode distance.

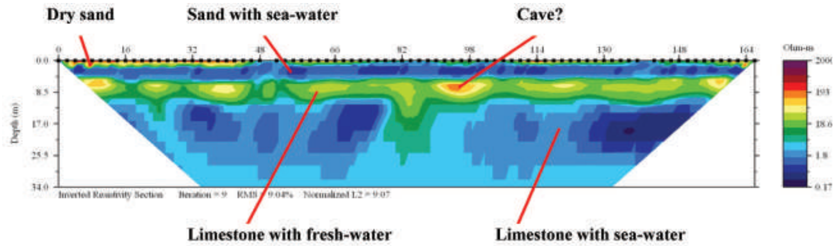

FIGURE 8
Results of inversion of geoelectrical data (Schlumberger-Wenner configuration) on profile Lirios: EarthImager robust inversion, starting model: average apparent resistivity.

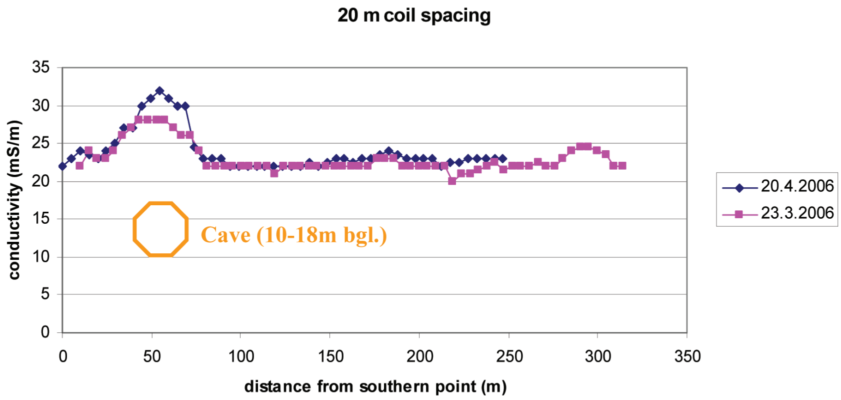

FIGURE 9
Results of EM-34 profiling (coil separation 20 m, frequency 1.6 kHz) over a known cave branch between cenote Cristal and cenote Escondido (apparent conductivities given).

electrode spacing no details about the shallow cave system could be expected. The data was inverted with a model block size of half the electrode spacing.

Figure 7 shows the result of the robust inversion. The high resistivity surface layer with values above 700 Ohmm suggests a thickness of almost 5–7 metres, corresponding well with the measured groundwater table in cenote Boch Chen at around 5 m bgl. Despite the large electrode spacing and therefore low resolution at near surface, several anomalies could be detected in the medium resistivity layer. The crossing of the known caves between 300 m and 320 m as well as between 345 m and 400 m are not very clearly seen although a slight decrease of resistivities is visible. Lower anomalies between 600–640 m and beyond 740 m suggest the existence of two caves but no scuba diving data is available yet.

From 21–31 m downwards we find a successive decrease of resistivities from 200–4 Ohmm. This transition zone corresponds to one model block thickness and might be an artefact of the inversion process, which is not able to reproduce such large and abrupt resistivity contrasts. Therefore, the depth of the halocline has to be fixed at around 21 m, which again corresponds well with the field and scuba diving observations. Below the halocline hardly any structures can be found except an increase in the middle part of the profile and a smooth increase with depth. No interpretation could be derived from the inversion results of the deeper parts, as the data for the field measurements were very noisy due to the nearby transformer station.

Profile Lirios

This profile was measured in the coastal area along the beach to investigate the resistivity distribution in an environment with a very thin freshwater aquifer. Here, brackish water filled caves, embedded in seawater filled background formations are expected. At greater depths seawater filled caves should be found. The results of the inversion (Fig. 8) show a thin, high resistivity top layer, correlating with dry beach sands. The groundwater table was found at 1.15 m below surface. Below, seawater filled dune-sands can be found, showing resistivities below 1 Ohmm and a thickness of 4–5 m. From 5–10 m depth, higher resistivity values between 5–200 Ohmm were detected, underlain by values below 2 Ohmm. A possible interpretation of the higher resistivity layer is that near the coastline, shallow karst areas are filled with brackish water, both in voids/caves (higher resistivity) whereas in the surrounding matrix (lower resistivity) salinity is higher due to mixing processes. However, interpretation is very difficult due to the ambiguities of the resistivity versus porosity/salinity relationship. In the deep low resistive layer, some extremely low resistivity anomalies can be estimated perhaps suggesting cave systems. We can conclude that due to the very low resistivities near to surface, most of the current is expected to be channelled within this layer. Consequently only some principal qualitative information about the resistivity structure below can be derived from geoelectric measurements, whereas quantitative conclusions on depths and thicknesses are very approximate.

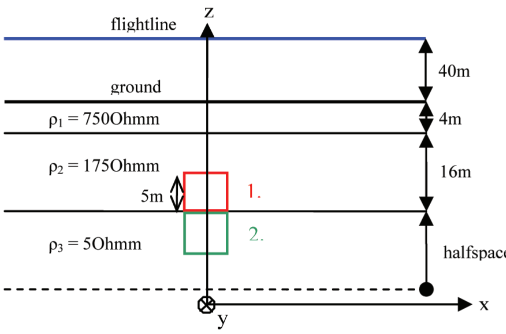

FIGURE 10
Cross-section of the model used for forward modelling, model case: deep situated halocline, cave located 1) inside limestone, saturated with brackish water (5 Ohmm) and 2) inside limestone, saturated with saline water (0.2 Ohmm), first layer: dry limestone.

Results of ground electromagnetic field measurements

Electromagnetic measurements using the Geonics EM-34 equipment were originally planned parallel to all geoelectric profiles. However, in most cases power lines were present in the vicinity of the profiles that produced a high noise level prohibiting reliable measurements. Only measurements along the profile Escondido, situated (see Fig. 4) along the highway Mex 307

TABLE 1
Specification of the Austrian airborne system

	Frequency (Hz)	a (m)	Configuration
Frequency 1 (f1)	340	4.53	Vertical-coplanar
Frequency 2 (f2)	3200	4.53	Horizontal-coaxial
Frequency 3 (f3)	7190	4.49	Vertical-coplanar
Frequency 4 (f4)	28850	4.66	Horizontal-coaxial

a = separation between transmitter and receiver coil.

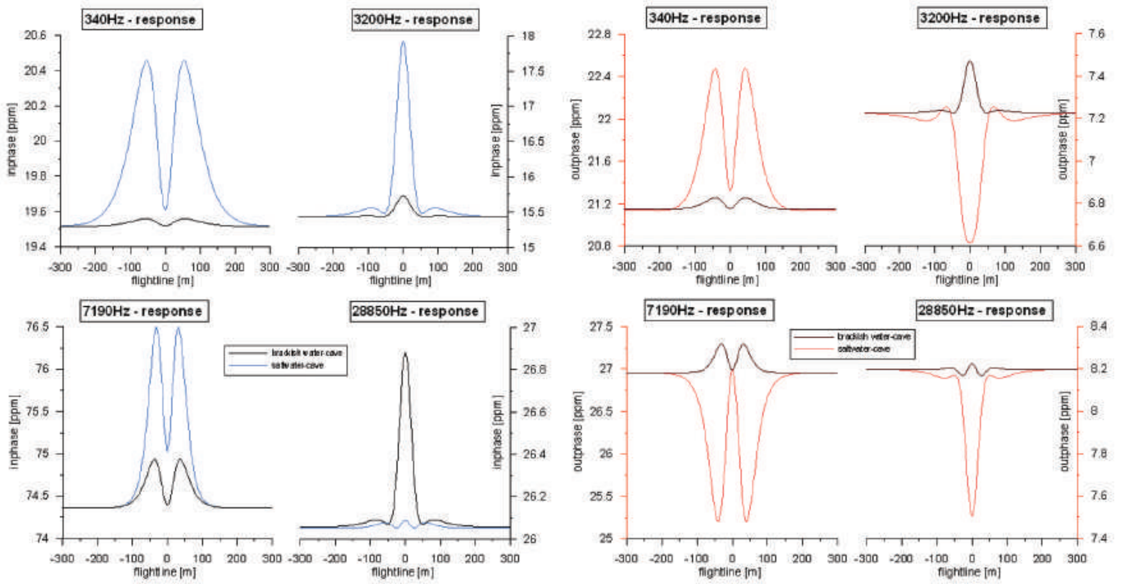

FIGURE 11
In-phase (black, blue) and out-of-phase (dark and light red) components calculated from the model of a brackish water- and saltwater-cave in case of a deep halocline.

between Chunyaxche' and Tulum, crossing one branch of the cave system connecting Cenote Naharon (Cristal) and Escondido (Mayan Blue) could be performed. Due to the heavy traffic on the road and limited space beside the highway, geoelectric measurements could not be carried out along this profile without endangering the field personal. The results (Fig. 9) show that a significant positive anomaly could be detected right above the cave. To prove reliability of the results, measurements along this profile were repeated one month later (blue curve), producing almost the same results.

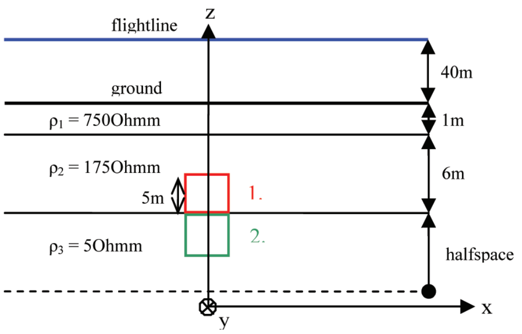

FIGURE 12
Cross-section of the model used for forward modelling, model case: shallow halocline, cave located 1) inside limestone, saturated with brackish water (5 Ohmm) and 2) inside limestone, saturated with saline water (0.2 Ohmm), first layer: dry limestone or dry sand.

The electrical model for the SKBR subsurface

The interpretation of geoelectric measurements showed that known caves in the research area could be detected by this technique. However, depth and size could be determined only very approximately. In the area near the coastline, where the brackish aquifer is very thin, no clear information about caves could be derived due to the ambiguity of the expected anomalies.

From a geoelectric point of view, the SKBR subsurface environment can be characterized as follows (see also Figs 10 and 12). Above the groundwater table, fractures and holes are mostly filled with air, thus representing a relatively high resistivity top layer (250–1000 Ohmm). Below, fractures are filled either with brackish (3–5 Ohmm) or saline (0.2 Ohmm) water. The halocline can be found at 4 m below ground level (bgl) nearby the sea (groundwater level 1 m bgl), dipping gently inland to a depth of approximately 20 m bgl at 7 km distance (groundwater level 6 m bgl). This corresponds well with halocline depths measured by Beddows (2004). The electrical resistivity of the saturated limestone matrix was determined to vary between 50–300 Ohmm (depending on actual porosity) above the halocline and 4–15 Ohmm below.

Due to these high resistivity contrasts, the applicability of an airborne frequency domain electromagnetic system, like the one operated by the Geological Survey of Austria (Motschka 2001), seemed very promising.

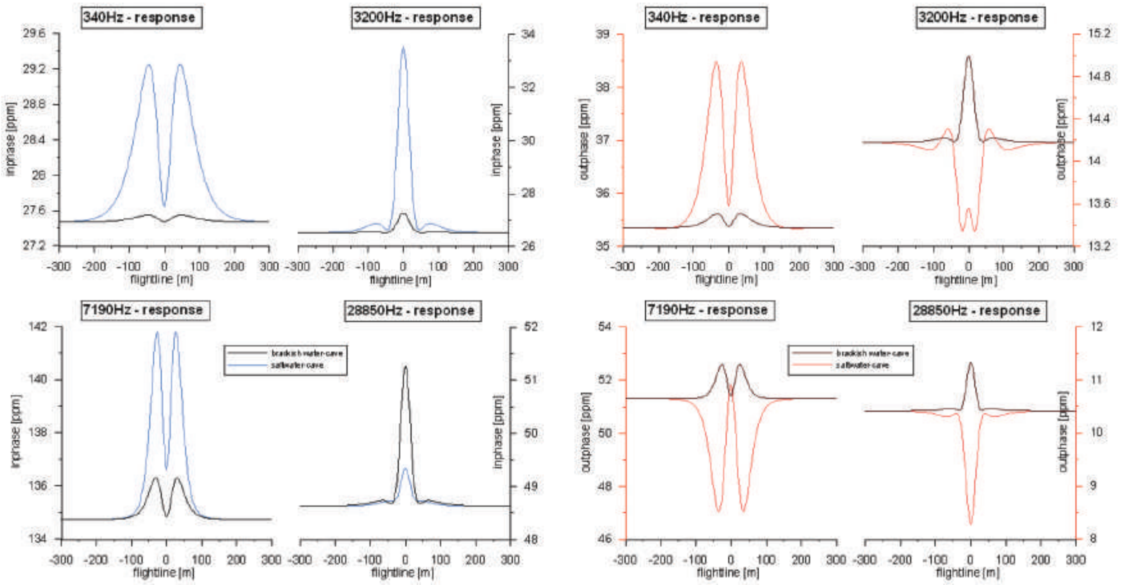

FIGURE 13
In-phase (black, blue) and out-of-phase (dark and light red) components calculated from the model of a brackish water- and saltwater-cave in case of a shallow halocline.

TABLE 2

Results of forward modelling, maximum amplitudes of anomalies in ppm for different EM-components are given for the different cases of forward modelling (shallow/deep/brackish-/saline-water filled cave), bold numbers indicate values above noise level and underlined numbers indicate highest anomaly amplitudes

	Shallow cave		**Deep cave**		**Amplitude difference shallow/deep**	
EM components	**Brack water**	**Saline water**	**Brack water**	**Saline water**	**Brack water**	**Saline water**
340Hz in-phase	0.1	**1.6**	0.1	**1**	0	0.6
340 Hz out-of-phase	0.25	**3**	0.2	**1.2**	0.05	**1.8**
3200 Hz in-phase	0.8	<u>7</u>	0.25	<u>2.5</u>	0.55	<u>4.5</u>
3200 Hz out-of-phase	0.8	0.8	0.3	0.6	0.5	0.2
7190 Hz in-phase	**1.2**	<u>7</u>	0.5	<u>2.2</u>	0.7	<u>4.5</u>
7190 Hz out-of-phase	**1.1**	**4**	0.3	**1.7**	0.8	**2.3**
28850 Hz in-phase	<u>2.7</u>	0.6	0.9	0.1	<u>1.6</u>	0.5
28850 Hz out-of-phase	0.8	**2.3**	0.02	0.7	0.75	**1.6**

All results are given in ppm.

THE AIRBORNE SURVEYING CAMPAIGN

Airborne electromagnetic forward modelling

To further evaluate the applicability of an airborne electromagnetic system for mapping karst features in the SKBR area, the theoretical response of a frequency domain airborne electromagnetic system (for system parameters see Table 1) over resistivity models derived from ground based geoelectric results (Figs 10 and 12) was calculated. Results for a large quantity of different model cases were calculated and analysed. For this paper we compare only cases highlighting the typical situation inside the investigation area of the pilot survey at two different distances (approximately 0.5 km and 8 km) from the sea. A rectangular cave (side length 5 m) was assumed to be located inside a limestone, saturated with brackish (red rectangle, case 1) or saline water (green rectangle, case 2). For details of the models, refer to Figs 10 and 12.

The software EMIGMA 7.5 (PetRos Eikon Inc.; Murray *et al.* 1999; Groom and Alvarez 2002) was used for the 3D-EM forward modelling. Results were verified using the AEM (version 2.2) software code developed by the AKP group (Avdeev *et al.* 1997, 1998; Pankratov *et al.* 1997). As results from both codes were basically identical, the outcome of the EMIGMA code was used for the figures of this paper.

Figures 11 and 13 show the results of forward modelling for the above models. The shape of the in-phase component anomaly clearly depends on the coil orientation: for horizontal-coaxial configuration the maximum of the anomaly is directly located above the centre of the cave. In case of vertical-coplanar arrangement a minimum marks the centre of the cave surrounded by two maxima. This is also valid for the shape of the 340 Hz out-of-phase component in vertical-coplanar orientation. For the other out-of-phase components, the shape is very much dependent on the depth and size of the caves. No general rules can be derived. For a good representation of the anomaly shape, different scales were used for the different components in Figs 11 and 13. To allow a comparison of absolute values, the results are summarized in Table 2. Black numbers indicate values above noise level and red and green bold numbers indicate highest anomaly amplitudes. The table clearly shows that the best response of a cave filled with saline water can be derived from the 3200 Hz and 7190 Hz in-phase components in case of a deep as well as a shallow cave. In both cases the maximum amplitude is far above the threshold defined by the general noise level (usually assumed around 1 ppm for the Austrian system). On the contrary a cave filled with brackish water can best be detected using the 28850 Hz in-phase component, although for the case of a deep situated cave the amplitude is at the edge of detectability.

The Austrian airborne system

Due to the promising results a pilot airborne survey was conducted in spring 2007 using the Austrian airborne electromagnetic (AEM) system. The main part of this system consists in a modified GEOTECH-'Bird' of 5.6 m length and 140 kg weight (Motschka 2001). It is towed on a cable 30 m below the helicopter. Inside the probe there are four transmitting coils as well as four receiving coils in different geometric arrangements (co-axial, coplanar loops; for details see Table 1). The transmitting coils generate an electromagnetic alternating field with frequencies of 340 Hz, 3200 Hz, 7190 Hz and 28850 Hz. This primary field induces eddy currents inside conductive subsurface layers. In turn the corresponding (secondary) magnetic field generated by these currents induces a current in the receiver coils. Based on the amplitude and the phase shift of the secondary field relatively to the primary field, conclusions can be drawn on the electrical resistivity of the subsurface. Variable frequencies and different geometric arrangements of the coils are used in order to allow depth-specific sounding of the subsurface. The lowest frequency determines the total penetration depth of the method (approximately 120 m below ground surface). The electromagnetic bird was supplemented by a

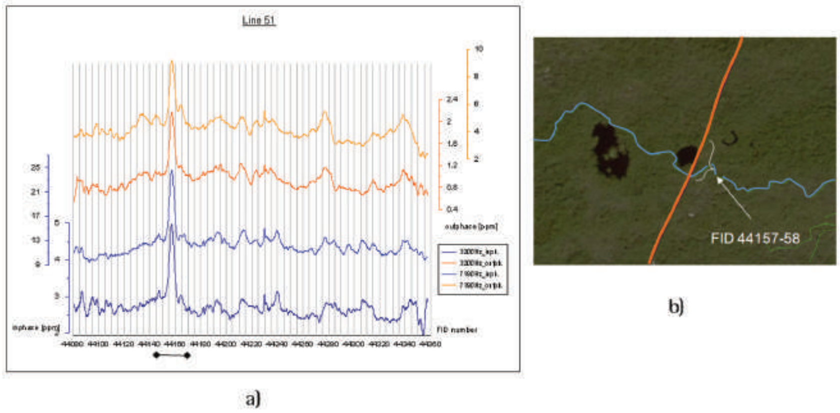

FIGURE 14
a) Results of drift corrected raw data (3200/7190 Hz in-phase (blue) and out-of-phase (orange)) over a known cave system (line 51, at 3.5–3.9 km distance to the coast) and a cenote; b) satellite image, showing several cenotes (black areas) inside the rain forest; location of mapped cave system (blue line) and flight path of survey helicopter (orange line) are overlain. Between fiducials 44157 and 44158 a significant anomaly due to the caves/cenotes influence can be detected.

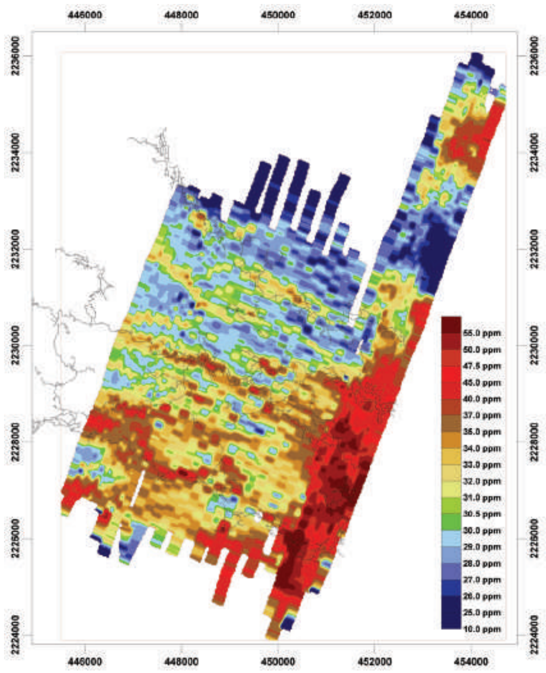

FIGURE 15
Results of the in-phase component of 7190 Hz after rough empirical altitude correction and profile levelling, colour bar chosen to highlight high- and low-amplitude areas; structure of known caves (black lines) are overlain.

laser altimeter and 2 differential GPS sensors, one located in the bird and one in the helicopter and a Cs-magnetometer. Additionally, gamma spectroscopy was applied.

The field survey

The pilot survey was carried out in April 2007 after half a year of intensive logistical preparations. An investigation area of almost 80 square kilometres (see Fig. 4) was selected between the town of Tulum and the lagoons of the SKBR (Fig. 2), partly covering the Ox Bel Ha cave system, which has been extensively mapped by cave divers. This area was covered with regularly spaced flight lines (for location of the flight lines see Fig. 4) at a separation of 100 m. In the middle part of the area a line spacing of 200 m had to be used due to limitations in available helicopter time. The target operating altitude of the helicopter was 70 m above ground surface, corresponding to a sensor altitude of 40 m. The distance between helicopter and ground surface was measured by a RIEGL LD90-3300HR laser-altimeter. The ground-distance of the helicopter was collected at a rate of 100 times per second. However, a laser ray is not only reflected from the ground surface but also from vegetation and manmade objects (for example buildings). Therefore, delicate processing algorithms had to be applied to compensate for this undesired effect. Basically, the maximum reflection times of all recordings within a time window of 0.1 second and along the profile were calculated and converted to distances between helicopter and ground surface. Based on these results and considering the length of the bird-cable and sensor displacements due to the speed of the helicopter, the distance between the bird and the ground surface was calculated.

As a first processing step, thermal drifts in each of the measured components (in-phase and out-of-phase components of all frequencies) were removed from the AEM-raw-data. Such drifts are long-term variations of the measured signal not caused by geological sources. Furthermore, parts of the AEM signal, which were disturbed by manmade noise (i.e., by power lines, electric motors, transformers) were removed.

Figure 14 shows one example of drift corrected measurements over a known sinkhole (cenote). Around fiducial number 44158, directly above the location of a cenote, a significant positive anomaly was recorded. Although the influence of variations in flight altitude is still inherent in the drift corrected data, altitude variations were not the cause for the detected EM anomaly in this case.

To derive a consistent picture of anomaly pattern for the detection of caves an empirical altitude correction and subsequent profile levelling (similar to the methodology of Huang (2008)) was applied to roughly compensate for variations in flight altitude. It has to be stated clearly that this algorithm was only used to enhance the pattern of the phase components with the goal to map the location of the caves. No further inversion can be applied on the resulting data. Figure 15 shows the results for the 7190 Hz in-phase component, overlain with the known cave system (black lines). Clearly a large quantity of linear structures can be delineated, which correlate with most of the well-mapped cave systems. Anomaly alignments in the 7190 Hz in-phase component suggest the existence of several other, so far unexplored, branches of the cave system. Within recent months, cave divers have already verified some of these new structures (R. Schmittner 2008, pers. comm.).

Finally the drift corrected AEM data were inverted assuming a homogeneous half-space as subsurface model. In this kind of inversion the electric resistivity of a homogeneous, laterally and downward infinitely expanded half-space is calculated for each single data point. This 'apparent' resistivity is calculated from the bird altitude plus one single component or any combination of AEM components. To obtain a lateral resistivity distribution, the resistivities of all of these 1D models are stitched together (Sengpiel and Siemon 1998; Zhang *et al.* 2000). In contrast to the recorded AEM components, the calculated resistivities should be independent of the sensor altitude. Therefore, variations in bird altitude no longer influence the derived anomaly pattern. A water (salt-water, fresh-water or brackish water) filled cave surrounded by a saturated limestone matrix, should then be highlighted as a low resistivity anomaly.

Based on the results from forward modelling (Table 2) distinct components and combination of components were selected as input parameter for inversion.

As known from forward modelling, the homogeneous half-space resistivity, calculated from the in-phase component of the 28850 Hz frequency and the bird altitude, mainly maps the surface karst layers (dry limestone or limestone saturated with brackish water) and caves filled with brackish water in most of the survey area (see Fig. 16). Due to the low penetration depth, only shallow caves can be seen. Especially in the NW part of the survey area, directly SSW of the town of Tulum, the rise of the topography additionally causes an increasing distance to the water level, indicated by high resistivities above 60 Ohmm in the results derived from the 28850 Hz in-phase signal.

Along the coastline and in the region of the lagoons remarkable low resistivity areas can be seen. These anomalies are most likely caused by near surface seawater intrusions along the coast (verified by the results from the geoelectric profile Lirios

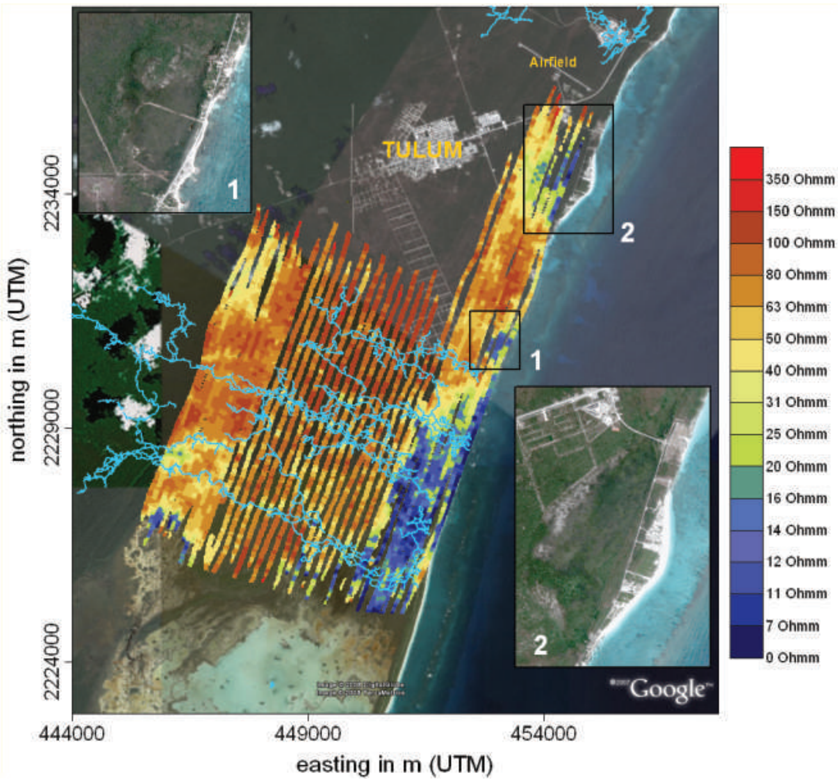

FIGURE 16
Homogeneous half-space calculated from in-phase component of the 28850 Hz frequency and the bird altitude. As an overlay, cave systems mapped by scuba-divers (light blue lines) are shown.

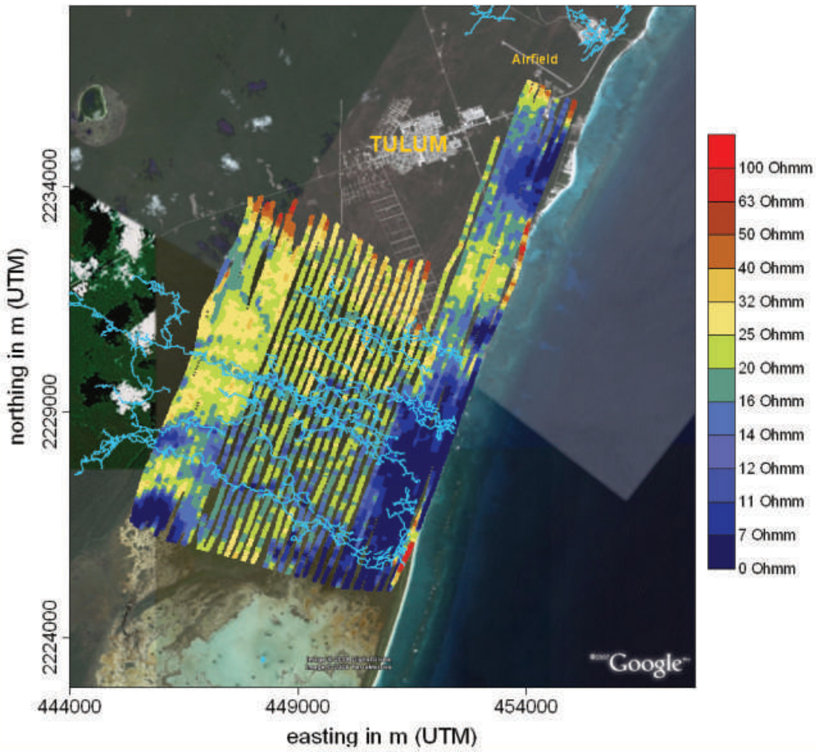

FIGURE 17
Results of homogeneous half-space inversion calculated from in-phase component of 3200 Hz and 7190 Hz frequency and the bird altitude. As an overlay, cave systems mapped by scuba-divers (light blue lines) are shown.

(Fig. 8)) or brackish water at the surface (in the area of the lagoon). The areas of low resistivity along the coastline in the northern part of the survey area are highlighted also by a visible change in vegetation (see satellite image as inlet to Fig. 16).

A good representation of the cave system is shown in the pattern of the half-space resistivities derived from the in-phase component of the 3200 Hz and 7190 Hz frequency (Fig. 17).

This behaviour was predicted by model calculations. In Figs 16 and 17 the caves can be seen as low resistivity anomalies. Anomalies aligned along the direction of the flight lines (SSW-NNE, Fig. 4) are mainly caused by non-linear drift components, which could not be corrected properly in the individual AEM components. These anomalies are particularly observed in areas flown with a line spacing of 200 m. This result emphasizes the need of a line spacing of not more than 100 m for such investigations and good drift/altitude correction.

CONCLUSIONS

The ability of airborne frequency domain EM measurements to localize and map karstic cave systems was demonstrated. For the investigated area the derived results could be verified by the available cave maps constructed by cave divers. Additionally, some previously unknown branches of the cave system were detected, of which some have recently been verified by divers guided by the prospective maps derived from the electromagnetic results. However, the results represent only a first step towards the definition of hydrological subsurface units. Inspection of the raw data and forward modelling indicate that additional information on the depth of the halocline, the resistivity of the limestone matrix and probably on the size and depth of the caves could be derived. To extract all inherent information from the field data multi-layer inversion algorithms constrained by boundary conditions have to be applied to make all information usable for advanced groundwater modelling. Additionally, the results have to be calibrated by ground measurements and borehole logs to better understand the relation between resistivity and matrix porosity of karst systems in order to allow proper interpretation of the results.

ACKNOWLEDGEMENTS

This survey was financially supported by the Austria Science Fund in frame of the project L524-N10 'XPLORE' and by ETH Zurich. We further acknowledge financial support by The Nature Conservancy, the Technical University of Denmark, the COWI Foundation, the WWF Verdensnaturfonden/Aase & Ejnar Danielsens Fond 2006 and 2007 and UNESCO. We would like to sincerely acknowledge the support of Sam Meacham, Centro Investigador del Sistema Acuífero de Quintana Roo (CINDAQ), Martin Heidovitsch, Joyce Coleman, Robbie Schmittner, Xibalba Dive Centre, Mario Rebolledo Vieyra, Centro de Investigación Científica de Yucatan (CICY), A.S. Gutierrez of NAFTA for importing and exporting the scientific equipment, Caribbean Air and Global Vision International Mexico.

We are very grateful to Grupo de Exploraction Ox Bel Ha for permission to use the Ox Bel Ha cave line maps. Line maps kindly provided by Quintana Roo Speleological Survey 2006. Principal explorers of the Ox Bel Ha system: B. Birnbach, S. Bogaerts, F. Devos, C. Le Maillot, S. Meacham, B. Philips, S. Richards, D. Riordan, S. Schnittger, G. Walten and K. Walten. We would like to thank Bruce D. Smith and Richard Smith for reviewing the paper. Their valuable suggestions and comments significantly improved the quality of the paper.

REFERENCES

Avdeev D.B., Kuvshinov A.V., Pankratov O.V. and Newman G.A., 1997. High-performance three-dimensional using modified Neumann series. Wide-band numerical solution and examples. *Journal of Geomagnetism and Geoelectricity* **49**, 1519–1539.

Avdeev D.B., Kuvshinov A.V., Pankratov O.V. and Newman G.A. 1998. Three-dimensional frequency domain modelling of airborne electromagnetic responses. *Exploration Geophysics* **29**, 111–119.

Beard L.P., Nyquist J.E. and Carpenter P.J. 1994. Detection of karst structures using airborne EM and VLF. 64th SEG meeting, Los Angeles, California, USA, Expanded Abstracts, 555–558.

Beck B. 2002. The karst conferences, consulting reports as science, and geophysical pitfalls. *Engineering Geology* **65**, 81–83.

Beddows P.A. 2004. *Groundwater hydrology of a coastal conduit carbonate aquifer: Caribbean coast of the Yucatán Peninsula, México*. PhD thesis. School of Geographical Sciences, University of Bristol.

Beddows P.A., Smart P.L., Whitaker F.F and Smith L.S. 2007. Decoupled fresh-saline groundwater circulation of a coastal carbonate aquifer: Spatial patterns of temperature and specific electrical conductivity. *Journal of Hydrology* **346**, 18–32.

Bögli A. 1980. *Karst Hydrology and Physical Speleology*. Springer.

Bosch F. and Müller I. 2001. Continuous gradient VLF measurements: a new possibility for high resolution mapping of karst structures. *First Break* **19**, 343–349.

Bosch F. and Müller I. 2005. Improved karst exploration by VLF-EM gradient surveys: comparison with other geophysical methods. *Near Surface Geophysics* **3**, 299–310.

Carreon-Freyre D. and Cerca M. 2006. Delineating the near-surface geometry of the fracture system affecting the valley of Querétaro, Mexico: Correlation of GPR signatures and physical properties of sediments. *Near Surface Geophysics* **4**, 49–55.

Cunningham K. 2002. Application of ground-penetrating radar, digital optical borehole images, and cores for characterization of porosity hydraulic conductivity and paleokarsts in the Biscayne aquifer, southeastern Florida. *Journal of Applied Geophysics* **55**, 61–76.

Danbom S. 2005. Techniques to evaluate shallow karst features. In: *Special Challenges Associated wit the Near Surface* (ed. D. Butler), pp. 13-22. SEG.

Darnault C.J.G. 2008. Karst aquifers: Hydrogeology and exploitation. In: *Overexploitation and Contamination of Shared Groundwater Resources Management, (Bio) Technological, and Political Approaches to Avoid Conflicts* (ed. C.J.G. Darnault), pp. 203–226. NATO Science for Peace and Security Series C: Environmental Security, Springer.

Debeglia N. and Dupont F. 2002. Some critical factors for engineering and environmental microgravity investigations. *Journal of Applied Geophysics* **50**, 435–454.

Doll W., Nyquist J., Beard L. and Gamey T. 2000. Airborne geophysical surveying for hazardous waste site characterization on the Oak Ridge Reservation, Tennessee. *Geophysics* **65**, 1372–1387.

Doolittle J. and Collins M. 1998. A comparison of EM and GPR methods in areas of karst. *Geoderma* **85**, 83–102.

Ford D.C. and Williams P. 2007. *Karst Hydrogeology & Geomorphology*. Wiley & Sons.

Gamey T.J., Thompson M., Mandell W. and Frano G. 2001. Karst pathway delineation using combined spatial and geophysical analysis at Camp Crowder, Missouri. GSA Annual Meeting, 5–8 November 2001, Boston, Massachusetts.

Gamey T.J., Thompson M., Mandell W., Frano G. and Miller S. 2002. Karst pathway delineation using combined spatial and geophysical analysis at Camp Crowder, Missouri. Proceedings of the SAGEEP 2002, Expanded Abstracts.

Garmann K. and Purcell S. 2004. Application for capacitively coupled resistivity surveys in Florida. *The Leading Edge* **23**, 697–698.

Groom R. and Alvarez C. 2002. 3D EM modelling application of the localized non-linear approximator to near surface applications. Proceedings of the SAGEEP 2002, Expanded Abstracts.

Guérin R. and Benderitter Y. 1995. Shallow karst exploration using MT-VLT and DC resistivity methods. *Geophysical Prospecting* **43**, 635–653.

Henson H., Sexton J., Henson M. and Jones P. 1997. Georadar investigation of karst in a limestone quarry near Anna. 67th SEG meeting, Dallas, Texas, USA, Expanded Abstracts, 763–767.

Huang H. 2008. Airborne geophysical data leveling based on line-to-line correlations. *Geophysics* **73**, F83–F89.

Krekeler M.P.S., Probst P., Samsonov M., Tselepis C.M., Bates W., Kearns L.E. and Maynard B. 2007. Investigations of subsurface flow constructed wetlands and associated geomaterial resources in the Akumal and Reforma regions, Quintana Roo, Mexico. *Environmental Geology* **53**, 709–726.

Lesser J.M. 1976. Estudio hidrogeologico e hidrogeoquimico de la peninsula de Yucatan. Unpublisched Technical Report. Proyecto Conacyt-NSF 704, Secretaria de Recursos Hidraulicos, Direccion de Geohidrologia y Zonas Aridas, Mexico.

Loke M.H. and Dahlin T. 2002. A comparison of the Gauss-Newton and quasi-Newton methods in resistivity imaging inversion. *Journal of Applied Geophysics* **49**, 149–162.

Mandell W., Gamey T.J. and Doll W. 2003. Groundwater pathway mapping using airborne geophysics: Two case studies. Proceedings of the the Sixth International Symposium and Exhibition on Environmental Contamination in Central and Eastern Europe and the Commonwealth of Independent States, Prague 2003.

McGath R.J., Syles P., Thomas E. and Neale S. 2002. Integrated high-resolution geophysical investigations as potential tools for water resource investigations in karst terrain. *Environmental Geology* **42**, 552–557.

Mingelli C. 1989. Application of the geoelectrical prospecting method for detection of Karst cavities. 59th SEG meeting, Dallas, Texas, USA, Expanded Abstracts, 424.

Morales J. J. 1992. *Los humedales, un mundo olvidado*. Amigos de Sian Ka'an, Cancun.

Morales J. J. 1993. *El mar y sus recursos*. Amigos de Sian Ka'an, Cancun.

Morales J. J. 1995. *La Gran Selva Maya*. Amigos de Sian Ka'an, Cancun.

Motschka K. 2001. Aerogeophysics in Austria. *Bulletin of the Geological Survey of Japan* **52**, 83–88.

Murray I.R., Alvarez C. and Groom R.W. 1999. Modelling of complex electromagnetic targets using advanced non-linear approximator techniques. 69th SEG meeting, Houston, Texas, USA, Expanded Abstracts.

Nyquist J.E., Peake J.S. and Roth M.J.S. 2007. Comparison of an optimized resistivity array with dipole-dipole soundings in karst terrain. *Geophysics* **72**, F139.

Nyquist J., Petruccione J. and Roth M. 1999. Characterization of shallow karst terrain using multifrequency electromagnetic induction: Two examples from eastern Pennsylvania. 69th SEG meeting, Houston, Texas, USA, Expanded Abstracts, 547–550.

Pankratov O.V., Kuvshinov A.V. and Avdeev D.B. 1997. High performance three-dimensional electromagnetic modelling using modified Neumann series. Anisotropic Earth. *Journal of Geomagnetism and Geoelectricity* **49**, 1541–1547.

Roth M., Mackey J., Mackey C. and Nyquist J. 2002. A case study of the reliability of multielctrode earth resistivity testing for geotechnical investigations in karst terrains. *Engineering Geology* **65**, 225–232.

Sengpiel K. and Siemon B. 1998. Examples of 1-D inversion of multifrequency HEM data from 3-D resistivity distributions. *Exploration Geophysics* **29**, 133–141.

Smith B.D., Gamey J.T. and Hodges G. 2005. Review of airborne electromagnetic geophysical surveys over karst terrains. Proceedings of the US Geological Survey Karst Interest Group, Rapid City, South Dakota, 12–15 September.

Smith B.D., Irvine R., Blome C., Clark A. and Smith D.V. 2003. Preliminary results, helicopter electromagnetic and magnetic survey of the Seco Creek area, Medina and Uvalde counties, Texas. Proceedings of SAGEEP 2003, Expanded Abstracts.

Smith B.D., Smith D.V. and Blome C.D. 2008. Helicopter electromagnetic surveys of carbonate karstic aquifers with emphasis on recent applications by the US Geological Survey. Proceedings of the 5th International Conference on Airborne Electromagnetics (AEM2008), Haikko Manor, Finland.

Steinich B. and Marín L. 1997. Determination of flow characteristics in the aquifer of the Northwestern Peninsula of Yucatan, Mexico. *Journal of Hydrobiology* **191**, 315–331.

Williams P.W. 1993. Environmental Change and Human Impact on Karst Terrains: An Introduction. Catena Supplement 25.Catena Verlag, Cremlingen-Destedt, Germany.

Zhang Z., Routh P.S., Oldenburg D.W., Alumbaugh D.L. and Newman G.W. 2000. Reconstruction of 1-D conductivivty from dual loop EM data. *Geophysics* **65**, 492–501.

Zhou W., Beck B. and Adams A. 2002. Effective electrode array in mapping karst hazards in electrical resistivity tomography. *Environmental Geology* **42**, 922–928.

III

Exploring regional-scale preferential flow paths in the karst aquifer of Southern Quintana Roo, Mexico

Gondwe, B.R.N., Ottowitz, D., Supper, R., Motschka, K., Merediz-Alonso, G., Bauer-Gottwein, P.

Manuscript submitted

Exploring regional-scale preferential flow paths in the karst aquifer of Southern Quintana Roo, Mexico

Bibi R. N. Gondwe[a*], David Ottowitz[b], Robert Supper[b], Klaus Motschka[b], Gonzalo Merediz Alonso[c], Peter Bauer-Gottwein[a].

[a] *Department of Environmental Engineering, Technical University of Denmark, Miljoevej, Building 113, DK-2800 Kgs. Lyngby, Denmark, pbg@env.dtu.dk.* [*)] Corresponding author: bng@env.dtu.dk; tel.: (+45) 4525 1570, fax: (+45)4593 2850

[b] *Geological Survey of Austria, Neulinggasse 38, 1030 Vienna, Austria david.ottowitz@geologie.ac.at, robert.supper@geologie.ac.at, klaus.motschka@geologie.ac.at*

[c] *Amigos de Sian Ka'an, Fuego # 2, Manzana 10 SM 4, Cancún, Quintana Roo, 77500, Mexico, gmerediz@amigosdesiankaan.org*

Abstract

The location of zones of high permeability is determining for groundwater flow patterns in karst. To ensure protection and management of groundwater-dependent ecosystems and well fields in karst aquifers, it is important to identify and map such structures. Using remote sensing imagery and topographic elevation data, regional-scale structures were delineated in the karstic catchment of the groundwater-fed Sian Ka'an wetlands, Yucatan Peninsula, Mexico. Airborne frequency-domain electromagnetic measurements across the structures revealed anomalous signals related to the structures. The Holbox fracture zone was shown to be a high-permeability zone with a lower bulk electrical resistivity than its surroundings. At and around structures delineated further inland a shallow low-resistivity layer was found, generally 1–5 Ωm and 5–6 m thick. This layer is proposed to be ejecta from the Chicxulub impact (Cretaceous/Paleogene boundary). Its signature corresponds well with the resistivity signature of borehole logs from the area. Electromagnetic measurements could not determine the geology beneath the low-resistive layer, but indicated the possibility of higher permeable zones beneath structures. Hydrologic modeling supported that the mapped structures are zones of high permeability. The method of combining local-scale HEM measurements with regional-scale remote sensing data analysis provides a suitable multi-scale methodology for mapping preferential flow paths in karst aquifers.

Keywords: remote sensing, frequency-domain EM, groundwater catchment, Yucatan, Sian Ka'an

1. Introduction

Karst aquifers are extremely vulnerable to pollution. The high permeabilities of karst geology cause rapid infiltration, fast water flow through caves and limited retention of contaminants. Contaminant sequestration from caves to the matrix and subsequent slow release means that recovery from pollution events may be particularly slow for karst aquifers (Li et al., 2008). Karst aquifers provide the main source of water for about 20–25 % of the world's population (Ford and Williams, 2007). The problem of karst groundwater protection is therefore globally relevant.

Delineating catchments of well fields and groundwater-dependent ecosystems is a vital step for water management. In karst aquifers the task is particularly challenging, because groundwater flow is heavily influenced by the location of underground high-permeable structures, such as caves and faults. It is generally difficult to obtain information about the location of such underground structures, and to produce detailed descriptions of the complex heterogeneous subsurface of karst aquifers. Karst aquifers may be conceptualized as a dual-domain conduit-matrix medium, with exchange between the two domains (e.g. Peterson and Wicks, 2005; Cornaton and Perrochet, 2002; Arfib and de Marsily, 2004; Liedl et al., 2003; Bauer et al., 2003; Birk et al., 2003). Storage and water transport takes place in both compartments, but typically conduit flow dominates over matrix flow, while water storage is larger in the matrix than in the conduits (Atkinson, 1977; Worthington, 2003).

Remotely sensed data and geophysical methods have been successfully used to locate subsurface karstic features, although success of the various methods always depends on local site conditions (Benson and Yuhr, 1993). Remote sensing studies typically utilize optical imagery for creating lineament maps, either by visual inspection or using computer algorithms (e.g. Tam et al., 2005; Hung and Batelaan, 2003; Süzen and Toprak, 1998; Kresic, 1995; Degirmenci and Günay, 1992). Surface lineaments are commonly correlated with subsurface faults, fractures or conduits. Also remotely sensed digital elevation models have been used to infer the location of subsurface karst features, as anomalies in geomorphology may be associated with karst structures (Masoud and Koike, 2006).

In contrast to the surface anomalies investigated through remotely sensed imagery, geophysical exploration methods can detect subsurface anomalies. A wide variety of ground-based geophysical methods have been applied to locate subsurface karst features, including microgravity (e.g. McGrath et al., 2002; Mochales et al., 2008), magnetic resonance sounding (e.g. Guérin et al., 2009; Vouillamoz et al., 2003), multielectrode resistivity (e.g. Roth et al., 2002; Nyquist et al., 2007), seismics (e.g. Guérin et al., 2009; Gamey et al., 2001), ground penetrating radar (e.g. Carreon-Freyre and Cerca, 2006; Henson et al., 1997), very-low-frequency gradient surveys (e.g. Bosch and Müller, 2005; Guérin and Benderitter, 1995), and electromagnetic methods (e.g. Vogelsang, 1987; Doolittle and Collins, 1998; Shah et al., 2008). Geophysics has also been used to detect the main azimuth angles of subsurface high-permeability structures (e.g. Steinich and Marin, 1997). The ground-based methods are applicable for local-scale studies. However, regional-scale studies require greater coverage. This is offered by airborne geophysics. The studies by Doll et al. (2000), Gamey et al. (2001), and Smith et al. (2005) successfully mapped general structures in karst aquifers with airborne electromagnetics (EM), whereas Supper et al. (2009) definitively showed the ability of airborne EM to map karst conduits on the Yucatan Peninsula.

This study presents a multi-scale integrated approach to karst structure mapping. The study area is located on the karstic Yucatan Peninsula, where groundwater-dependent wetlands are located in the 5280 km^2 Sian Ka'an Biosphere Reserve. The aquifer contains the world's longest submerged cave systems (http://www.caves.org/project/qrss/qrlong.htm; http://www.caverbob.com/uwcave.htm). On a local scale, Supper et al. (2009) successfully mapped the known Ox Bel Ha cave system, north of Sian Ka'an, with airborne electromagnetic measurements. The present study investigates the regional-scale catchment of the wetlands, to map potential regional-scale high-permeability structures. Remotely sensed data are used to locate and map the structures, whereas airborne geophysics is used to investigate the nature of these structures in relation to hydrogeologic properties. The findings are corroborated by geophysical inversions, forward modelling of the geophysical signal, local-scale field data and hydrologic modelling.

2. Methods and data

2.1. The study area

The study area is the tentative groundwater catchment of the Sian Ka'an Biosphere Reserve, located in Quintana Roo, Mexico (Fig. 1). The catchment was delineated based on topographic divides, assuming, as a first order approximation that these divides coincide with groundwater divides. Average precipitation ranges from 840 to 1550 mm/year, and groundwater recharge is approximately 15% of the rainfall (Gondwe et al., in review). The rainy season is from May to October. The groundwater consists of a thin freshwater lens (0–100 m thick) underlain by saltwater. Overall the lens shape follows the Ghyben-Herzberg relationship (Gondwe et al., in review; Marin et al., 2004; Steinich and Marin, 1996; Moore et al. 1992). Soil cover is limited and most of the area is covered by 15–30 m tall semi-evergreen forest. The study area contains a notable topographic contrast. The topographic relief is flat in the northern and coastal part (elevations 0–20 m above mean sea level (mamsl)), whereas the south-southwestern areas have an undulating relief with cone-karst landforms (elevations up to 340 mamsl). These two geomorphologic zones are called the flat and the hilly area in the remainder of this paper (see Fig. 2a). In between is a transition zone with moderately undulating relief (20–50 mamsl). Depressions forming seasonal swamps ('bajos', 'poljes') are found in the hilly area. Seasonal surface drainage connects some of these swamps. Saline, undrained and/or waterlogged soils are found in some of the swampy areas.

Further details on the study area are given in Gondwe et al. (in review) and references herein. Previous hydrogeologic studies of the area are scarce (Perry et al., 2002, 2009; Beddows, 2004). Gondwe et al. (in review) provides an integrated conceptual hydrogeologic model of the study area. The hydrology of Sian Ka'an's wetlands was studied by Gondwe et al. (2010).

2.2. Geological framework

The Yucatan Peninsula consists of limestones, dolomites and evaporites reaching thicknesses of >1500 m (Weidie, 1985). The surficial sediments spans Upper Cretaceous to Holocene in age, and are generally nearly horizontally layered and off-lapping, with gradually younger carbonates deposited towards the peninsula margins (Lopez-Ramos, 1975; SGM, 2007; Schönian et al., 2005). Kenkmann and Schönian (2006) emphasized that the geology of the southern peninsula is poorly constrained due to few exposures and difficulties in dating the sediments through biostratigraphy.

Ejecta associated with the Chicxulub meterorite impact, at the contact between Cretaceous and Paleogene sediments, have been found in southern Quintana Roo and neighboring Belize (Ocampo et al., 1996; Fouke et al., 2002; Pope et al., 2005; Schönian et al., 2005; Kenkmann and Schönian, 2006). The Chicxulub impact occurred in the northwestern Yucatan Peninsula (Hildebrand et al., 1991; Pope et al., 1991), 80–350 km from the study area. Based on geochemical data Perry et al. (2009) proposed that the ejecta blanket extends south and east of Lake Chichankanab. The extent of the possible ejecta blanket in the study area is not well known as Perry et al. (2009) only report three water sampling points in this region. It is believed to be a discontinuous blanket, possibly due to erosion following its deposition (Pope et al., 2005; Kenkmann and Schönian, 2006). In official geological maps some ejecta deposits in the hilly region appear to have been misdated to be Quaternary deposits, as some locations correlate with locations mapped by Kenkmann and Schönian (2006) as ejecta (Neuman and Rahbek, 2007; Perry et al., 2009). The ejecta is expected to have a low permeability to water, as it is clay-rich, and described to have a sealing or partially sealing effect (Ocampo et al., 1996; Grajales-Nishimura et al., 2000; Schönian, pers. comm., 2007; Perry et al., 2009). Ground-based transient electromagnetic measurements and geophysical borehole logs reported in Gondwe et al. (in review) show a geological unit with low resistivity and high natural gamma-radiation in the hilly area and the transition zone. The unit was generally encountered at around 0 to 13 m below surface (mbs) and was about 3–8 m thick. The unit was proposed to be the ejecta-layer (Gondwe et al., in review).

A series of sub-parallel faults, trending SSW-NNE exist in the southern part of the study area – The Río Hondo fault system. These faults have not been mapped in detail, but a surface expression is the fault-guided lakes in the study area, of which the largest is Laguna de Bacalar. The fault system has also shaped the Caribbean coastline in the study area, and sub-parallel horst and graben systems are present offshore (Rosencrantz, 1990). The Río Hondo fault system started forming in the late Jurassic, and continued to be active throughout the Cretaceous and Cenozoic. For this reason the rift structures are not hidden by sedimentary sequences (Dillon and Vedder, 1973). Another fault system is located in the northern part of the study area – the Holbox fracture zone, also trending SSW-NNE. Its southern terminus is not well determined but possibly the Holbox and the Río Hondo fault systems intersect (Southworth, 1985). Tulaczyk et al. (1993)

described swales in the Holbox fractures zone as solution corridors, and mapped them based on remotely sensed optical and infrared imagery.

2.3. Landsat and Shuttle Radar Topography Mission data

Visual inspection of Landsat ETM+ imagery revealed line-shaped features, resembling rivers, riverbeds or elongated structures on the land surface, and sometimes linking open water bodies. These structures were mapped manually. A nearly cloud-free true-color mosaic (RGB: band 3,2,1) of Landsat ETM+ data (NASA Landsat Program, 2000; 2001; 2002), and band 4 (near-infrared) from the Landsat TM Tri-Decadal mosaic (NASA Landsat Program, 1990) were used. Band 4 displayed distinct very dark elongated structures within the study area west and southwest of Sian Ka'an. Low reflectance in band 4 results from open water or high soil moisture. Fig. 2b shows the peninsula imaged with band 4. Clearly the dark structures feature in the central and southern part of the study area in band 4. Similar structures are only seen at the northern swales of the Holbox fracture zone; the rest of the peninsula lacks such features. In the visible bands, features appearing like rivers or river beds became visible as dark-green line-shaped features in the central and southern part of the study area when zooming further in (e.g. 1: 200,000) on the true color composite. Most of these features are not present on the most recent official map of perennial and ephemeral rivers (Fig. 1). The structures were therefore mapped partly as the very dark areas in band 4, and partly as these river-like features in the true-color composite. RGB combination 2,3,1 with histogram stretching was at times found to enhance the river-like features for easier delineation. Fig. 3a through c displays an example of some of the river-like features in visual Landsat bands (different band combinations and stretching) and Landsat band 4 (greyscaled). The corresponding surface elevation map and the structures outlined from the data are also shown (Fig. 3d and e). For visibility and to enable later incorporation into a hydrologic model with grid size 1 km^2 (not reported in this paper) identified structures have been outlined with a margin around them, making each feature some 3–5 km wide (Fig. 3e). Often this incorporates parts of, or all of, surrounding areas with a swamp-like expression on the true-color Landsat imagery and a low reflectance (higher soil moisture) on Landsat band 4.

Topographic data was obtained from the Shuttle Radar Topography Mission (SRTM) (USGS, 2006). To investigate the relation between topographic depressions and delineated structures, automatic river delineation was performed with the software ILWIS 3.3 Academic (ITC, 2005), using the built-in drainage network extraction routine, after automatically filling sinks in the SRTM data. Robustness of the automatically delineated rivers was tested by also carrying out the delineation routine on SRTM data added ± 0 to 10 m random noise. This essentially gave the same results as without noise added.

2.4. Helicopter-borne frequency-domain electromagnetic measurements – HEM

Helicopter-borne frequency-domain electromagnetic measurements (HEM) were carried out in selected transects across mapped structures in the dry season of 2007 and 2008. The Geological Survey of Austria system was used, consisting of a modified Geotech Hummingbird with 4 frequencies (340 Hz, 3200 Hz, 7190 Hz and 28850 Hz), four transmitter and four receiver coils in vertical co-axial and horizontal coplanar configuration. Motschka (2001) and Supper et al. (2009) provide further details on the equipment and data collection. Data leveling and processing was carried out by the Geological Survey of Austria.

Karst geology with cave structures is a three-dimensional geophysical inversion problem. Three-dimensional inversion codes to extract information on cave dimensions and depth currently do not exist. Hence the HEM data was analyzed using a qualitative approach, similar to Supper et al. (2009). As HEM data are sensitive to altitude, and sensor altitude (h [m]) varied during the survey, a data transformation was applied to convert the measured signal into the response parameters M and N (both [ppm]), which are much less sensitive to altitude (Huang, 2008):

$$M = I \cdot \left(\frac{h}{s} \right)^3 \quad \text{and} \quad N = Q \cdot \left(\frac{h}{s} \right)^3 \qquad \text{(Eq. 1)}$$

where I is the inphase and Q the quadrature component of the signal (both [ppm]), and s is the coil separation ([m]).

In some cases 1D layered inversions of the data were useful, and the software EM1DFM (UBC-GIF, 2000) was applied. Twenty-five layers of exponentially increasing thickness to a depth of 30 m gave the best results. Below this depth a homogeneous halfspace was assumed. In addition, 1D and 3D forward modelling with GeoTutor IV (PetroRos EiKon, 2008) was used for data interpretation.

3. Results

3.1. Structures identified on optical satellite imagery

The structures identified on the optical satellite imagery are shown in Fig. 2a. The longest structures were located in the hilly area and the transition zone, and few of them extended slightly into the flat area. In addition, some shorter structures were identified near the northern part of Sian Ka'an and one at the Holbox fracture zone. The structures in the hilly area and the transition zone were 50 km to >150 km long and transected the hilly area in a predominantly south-southwest to north-northeast direction. They were relatively densely located towards lower parts of the hilly area and the transition zone and were sub-parallel here. In the area near Presidente Juarez the structures had a braided pattern and intersected each other to some degree. Soils in the areas of the outlined structures were mainly gleysols (undrained and/or waterlogged soils) or vertisols (soils with high content of expansive clays), and were also saline in some cases, e.g. near the braided pattern (INEGI, 1997).

The result of the automatic river delineation showed some correspondence with the delineated structures, mainly in the hilly area and transition zone (Fig. 4). In the lower transition zone (elevations <25 mamsl) the automatically delineated rivers mostly corresponded to the location of roads, since these appear as 'depressions' in the SRTM topographical map, as roads have no vegetation. The rivers delineated automatically in the hilly area did not correspond to the location of roads. Only few of the automatically delineated rivers are termed perennial or ephemeral rivers on official maps (Fig. 1).

Whereas most delineated structures corresponded with topographical depressions, some structures had no distinct expression in the elevation data. One example is shown in Fig. 5 where river-like line-shaped features appeared in Landsat imagery, but no rivers were mapped by the automatic river delineation routine (highlighted with arrows).

The automatically delineated rivers terminated before reaching Sian Ka'an. The termination point was near the 20 m topographical contour line (Fig. 4). Possibly this shift in elevation demarks an ancient coastline, and no rivers were delineated beyond this point because of insignificant topographical relief here.

3.2. Results from airborne electromagnetic surveys

3.2.1 Survey over the Holbox fracture zone

About 1200 line-kilometers were flown over the area of the delineated proposed southern extension of the Holbox fracture zone, spanning an area from the coast to 12 km inland, 10 km wide. Line spacing was generally 100 m, but only 200 m in a 2 kilometer wide section covering part of the fracture zone. Fig. 6 presents the Holbox fracture zone's southern part, outlined based on topographic depressions in SRTM elevation data, dark areas in Landsat band 4 and high cenote (i.e. sinkhole) density. In addition the HEM results for frequencies 3200 Hz and 7190 Hz, transformed with Eq. 1, are shown. The HEM data displayed areas with markedly higher signal strength over the Holbox fracture zone, as indicated in the figure with large arrows and colored polygons. These areas were not fully alike in the two frequencies, nor in the inphase and quadrature components, but overlapped in the zone. When outlining the high-signal areas of each frequency, superposition of these polygons resulted in an area that corresponded well with the suggested location of the Holbox fracture zone's southern extension (Fig. 6e). The width of the anomalous zone was about 1–2 km. Both frequencies clearly outlined the open water body Laguna La Union, and its surroundings which do not have open water, but are known to have high soil moisture.

Additionally, the dataset showed four other areas of generally high signal strength. They are marked with numbered arrows in Fig. 6 and comprised: (1) an area with a line of small cenotes, located in immediate upstream extension from the Naranjal cave system; (2) the town of Tulum (likely caused by anthropogenic noise, e.g. electrical masts disturbing the HEM signal so that information about the subsurface can not be obtained); (3) a flooded area at the coast; and (4) part of the Sac Actun cave system.

Layered 1D-inversions of the Holbox dataset supported the qualitative findings above. Areas of generally lower resistivity corresponded with the location of the Holbox depression (sounding 170–510) and an agricultural field, probably irrigated (sounding 100–170) (Fig. 7). In the Holbox depression the bulk resistivity was about 50 Ωm, whereas outside the depression it was >130 Ωm. A layer of about 1 to 4 Ωm near -20 mamsl was seen, corresponding well with the expected depth of the halocline. Around Laguna La Union the zone of lower resistivity extended all the way to the surface, and was 5–15 Ωm, corresponding well with this surface freshwater body. Outside the Holbox fracture zone, the low bulk resistivity of 50 Ωm was generally not seen, except around cenotes (Fig. 7).

3.2.2 Survey over inland structures

Five transects over the inland structures were flown with HEM. Each transect consisted of 4–6 parallel flight lines, spaced 100 m apart. The measured signals, transformed with Eq. 1, showed high signal strength anomalies over most of the structures (Fig. 8). Anomalies were especially distinct in the inphase components of frequencies 3200 Hz and 7190 Hz, but were also present in most or all of the other signal components. The widths of the most significant anomalous areas ranged from 1 to 5.5 km.

The spectral gamma ray measurements also showed distinct anomalous composition of natural gamma radiation over structures, compared to away from the structures (Fig. 9). Over structures, the gamma-signal was predominantly composed of radiation from thorium and uranium, whereas outside structures, radiation from potassium constituted a major part of the signal. A strong correspondence existed between locations of anomalies in the spectral gamma ray measurements and in the EM measurements (compare Fig. 8 and 9).

In 1D layered inversions over the structures, the anomalous zones were either inverted as a low resistive layer (1–2 Ωm) of 5-7 m thickness located at shallow (e.g. 5–8 m) depth, or as a low resistive layer (1–2 Ωm) extending from about 10 mbs to the bottom of the inverted space (30 mbs). Generally, the inverted models did not fit the data very well.

To analyze the measured signals the possible subsurface configurations in Fig. 10 were forward calculated. Water level elevations and halocline depths were known from Gondwe et al. (in review), surface elevations from SRTM. Resistivity values from Supper et al. (2009) were used. The pertinent sensor heights at the points where the graph symbols are placed were used for the forward modelling. Forward modelling showed that measured signal levels were generally much higher than the ones obtained from the background model (Model A) (Fig. 11). Including multiple large freshwater-filled caves next to each other (Model B) could not bring the signal up to measured levels. These caves, although large, only increased the level by 10–15 ppm compared to Model A (Fig. 11). Furthermore, anomalies simulated with cave structures were much narrower (only ~150 m wide) than the measured anomalies. Modelling a freshwater cave as a full layer instead of separate anomalies (Model C), or using the conceptually unlikely Model D of saltwater in a high permeable zone, did also not yield a signal matching the measured (Fig. 11). Hence, the HEM anomalies were not likely caused by caves or high-permeable zones. Instead, a proposed ejecta-layer (Model E) was simulated. This gave a good fit to the measured data (Fig. 11–13), except to the 28850

Hz inphase and the 340 Hz quadrature components, which were often modelled higher than measured (Fig. 11c, 12c, 12e, 13c). Problems with data drift are however known for the dataset, and have not been fully compensated for in the data processing. The 3200 Hz and 7190 Hz have the best quality, and generally the quadrature components drift more than the inphase components.

Transect C was located in the lower transition zone, with elevations between 20 and 35 mamsl. In a borehole log only 1 km from the HEM transect, the ejecta layer has been detected extending from 5 to 13 mamsl, with a resistivity of about 5 Ωm (Fig. 11e and f) (Gondwe et al., in review). The HEM signal measured over Transect C was seen to correspond well with an ejecta layer of generally 5 Ωm, approx. 6 m thick, and generally located around 10 mamsl. Mildly varying the thickness of the ejecta layer or its resistivity could explain variations in measured anomaly strength.

Transect A was located in the transition zone at generally higher elevations, between 30 and 40 mamsl. The most western end transected a part of the hilly area (elevations >50 mamsl). Borehole logs with the anomalous layer, approx. 5–8 m thick at 10 to 25 mamsl, have been found 2 km (Nuevo Israel), 3 km (Las Panteras), 6 km (Emiliano Zapata) and 7 km (Presidente Juarez, only gamma log) from the transect (Gondwe et al., in review) (Fig. 12). The measured signals both above and away from structures could be modelled well with an ejecta layer of about 1.25 Ωm, and 5–6 m thick, located at around 15–20 mamsl. In the hilly area, the layer needed to be located much higher – around 60 mamsl – to match the measured signal. At x-coordinate 326000 and between x = 327500 and 340000 the 340Hz inphase component displayed larger signal strength which could not be explained by the ejecta-layer alone. The location corresponded well with the location of outlined structures. Adding a deeper low-resistive layer (5 Ωm, beginning at the elevation of the water table – 10 mamsl) could bring the 340 Hz inphase component up without affecting the other signal components. This solution is shown in Fig. 11. Alternatively, adding a surficial low-resistive layer (e.g. 1 m thick, 0.2 Ωm) could also bring the 340 Hz inphase component up, and affected all other signal components, requiring additional fitting. Conceptually, saline soil could be in agreement with the soil map at this location, but in spite of varying both resistivity and layer thickness of the saline soil layer, not as good fits could be obtained as in the case with ejecta and a low-resistive deeper layer.

The result from the 1D layered inversion, with a highly conductive layer extending from 10 mbs and beyond at the structures, was also forward modelled. This model fitted well to the 340 Hz inphase and quadrature components and the 7190 Hz quadrature, but gave too low signals in 3200 Hz and 7190 Hz inphase, and too high signals in 28850 Hz inphase.

Transect B, also located in the transition zone at elevations between 30 and 40 mamsl, could be modelled as for Transect A, i.e. with an ejecta layer around 15–20 mamsl, and in some cases additionally a low-resistive layer at depth. Transects D and E were located in the hilly area (elevations >50 mamsl). Fig. 13 gives an example of model fits to Transect D. An ejecta layer of generally about 3 Ωm located at shallow (<12 m) depth, but varying elevation (50 to 100 mamsl), could explain the measured signal well, and corresponds to that found in a borehole log 4 km from the transect (Fig. 13). In a ~7 km wide band around the small river crossing the transect a deeper low-resistive layer (5 Ωm) was needed in order to match measured signals. Most of this area overlaps with where the structure in this area has been delineated.

Adding a high-permeable freshwater cave (5 Ωm, width: 50 m, extending 10 m downwards from the water table) beneath the ejecta layer in the forward modelling gave detectable anomalies of the order of magnitude 2–7 ppm in the 3200 Hz and 7190 Hz components only if the sensor height was ≤ 30 m. The median sensor height in the transects flown across the structures was 60 to 70 m. At such a sensor height, freshwater-filled high permeable zones could only give detectable anomalies in the 340 Hz inphase, and only if the zone had a certain spatial and vertical extent. For example a 10 m deep 1 km wide anomalous zone of 5 Ωm extending downwards from the groundwater table gave an anomaly of 3 ppm in 340 Hz inphase, but was not at detectable levels in the other signal components. The width of the zone visibly affected the signal strength, but the thickness of the zone did not.

For comparison, forward modelling of the Ox Bel Ha dataset from Supper et al. (2009) was carried out using known depths of the water table and halocline. The ejecta layer is not present in the geology here, but the water-filled caves constitute the anomalous subsurface bodies. Also here, best models of known cave structures gave good fits in the 3200 Hz and 7190 Hz components, but modelled signals were higher than measured in the 28850 Hz and 340 Hz quadrature components.

4. Discussion

4.1 Feature at Holbox is a high-permeable zone

The proposed fault or fracture area over the Holbox zone's proposed southern extension appears with a lower resistivity. This zone is therefore likely to be a zone of higher matrix porosity, and, by inference, a zone of higher permeability to water flow. Archie's

Law (e.g. Telford et al., 1990) describes the dependency of a sedimentary rock's electrical resistivity on porosity. If assuming typical values for the constants in Archie's Law (a=1.5, m=n=2) and a freshwater resistivity between 4 and 10 Ωm (Beddows, 2004), the bulk resistivities found in the inversion within and outside the Holbox zone indicate a porosity within the zone about 0.1 to 0.15 larger than the surrounding. The HEM data set documents that the Holbox zone extends further south. Interestingly, this zone is aligned with larger lakes in the area (Laguna La Union, Laguna Ka'an Luum, Laguna Nopalito, Laguna Chunyaché), and with the fault suggested by Gondwe et al. (2010). The resistivity values of the freshwater-saturated bulk matrix outside and within the Holbox zone correspond well with values reported in Supper et al. (2009). Two cave systems, Aktun Ha and Tortuga, located in the zone further support the generally high permeability of this area (see cave maps in Smart et al., 2006). Dye tracing in Aktun Ha (Beddows and Hendrickson, 2008) and regional-scale hydrological modelling (Gondwe et al., submitted) indicates south-north-directed flow within the Holbox zone.

The Holbox dataset also confirms that caves can be mapped with HEM in the study area, as the Sac Actun cave system is clearly seen (Fig. 6). This application was first demonstrated by Supper et al. (2009).

4.2 Interpretation of inland structures

The structures delineated near the Bay of Chetumal (e.g. the Laguna de Bacalar depression) are known to be part of the Río Hondo fault system. The other inland structures in the lower part of the hilly area and in the transition zone are likely also related to this fault system, given their proximity and sub-parallel nature. The "S"-shape appearing in the transition zone on many of the structures is characteristic of *en echelon* faults, and supports the association between the structures and faults. *En echelon* faults in the studied region were described by Lara (1993).

The inland structures showed high EM signal anomalies, just as the Holbox fracture zone did. However, the anomalous signals were different in the cases of these structures. The signal measured over the structures appeared to be caused by a low-resistive material of about 1–5 Ωm and 5–6 m thick, located at different depths, but relatively close to the surface. It was however also possible to obtain a relatively good fit to the data by using a low-resistive thicker but deeper layer. The difference between the two inversion results arises because different components of the signal were being prioritized in the model fitting process. Based on forward modelling of the Ox Bel Ha system with its known caves, and on knowledge on the general data quality of the different signal components, fitting to the 3200 Hz and 7190 Hz components should be given more weight in the case of the HEM data obtained over Yucatan. Consequently, the inversion result yielding the geologic model with a low-resistive 5–6 m thick layer is preferred. This model is also the only one of the two which is consistent with borehole logs and measured halocline depths.

The low-resistive ~5 m thick layer was suggested in Gondwe et al. (in review) to be ejecta. From the HEM data and forward modelling it appears to be present at approximately the same depths, but varying elevations, in the hilly area, and at approximately the same elevations in the transition zone, with a slight tendency of being deeper buried the further away from the hilly area. The borehole logging and ground-based transient electromagnetic measurements from the area (Gondwe et al., in review) indicate the same. The proposed explanation is that at the time of the Chicxulub impact, only the hilly area was part of the land surface – a heavily karstified surface (Dillon and

Vedder, 1973; Pope et al., 2005), hence with a great variation in topographic relief. The ejecta was deposited on top of the Cretaceous surface; both on the land surface (hilly area) and in the shallow ocean (transition zone and flat area). The water-covered area was probably not as heavily karstified, and thus had a much more flat relief. Therefore, the anomalous layer is found at similar elevations here, whereas it is not in the hilly area. The steep drop in elevation between the hilly area and the transition zone – of more than 10 meters (from 50 to <40 mamsl) in less than a km suggests the presence of the ancient coastline here. Following the ejecta deposition, erosion may have taken place, reducing the thickness of the ejecta layer from the 200–400 m thick sequences found in wells near the crater (Rebolledo-Vieyra et al. 2000; Urrutia-Fucugauchi et al., 1996; 2004; 2008) to the thicknesses derived from the geophysics in this study and in Gondwe et al. (in review). Urrutia-Fucugauchi et al. (2008) also suggested significant erosion of the ejecta blanket following the finding of a ~34 m thick ejecta unit near Valladolid, and Pope et al. (2005) found Cenozoic sediments atop a weathered ejecta surface at one site. Reported ejecta thicknesses in southern Quintana Roo vary from the 3–8 m seen in most borehole logs (Gondwe et al., in review) and observed in outcrops by Pope et al. (2005) (4–8 m, bases not always observed) to 15 m (Reforma-log, Gondwe et al., in review) and 16 m (Albion Island, Ocampo et al., 1996), supporting the idea of erosion. Subsequently, Cenozoic sediments would have been deposited atop the ejecta in the areas covered by water – corresponding with the present geologic map (Fig. 1).

The reason why the inland structures appear anomalous in the HEM data is because the unsaturated zone is thinner above the structures than away from them. The structures in the transition zone are perfectly connected with preferential surface water flow paths in the hilly area delineated from topography. The observed HEM data can be explained by surface water runoff eroding depressions into the Cenozoic sediments in the transition zone and part of the flat area. Hence, over structures, a greater part of the Miocene-Pliocene geological strata overlying the ejecta has been eroded away (Fig. 11d). The initial focusing of surface runoff here may have been caused by slight depressions or rifts forming over the Río Hondo faults, as they were still active in the Cenozoic (Dillon and Vedder, 1973).

Due to the properties of the ejecta, water infiltrates slowly through this layer. When the layer is close to the surface, as it is at the inland structures, intermittent swamps and ephemeral rivers are formed. Storage capacity in the unsaturated zone is thus filled up faster over structures, and surface water is generated. The anomalous spectral-gamma ray signal may also be related to the ejecta. Ejecta from the Cretaceous/Paleogene boundary layer is known to have anomalously low potassium-values relative to thorium and uranium radiation (Paulsen and Lind, 1997). Since the measured spectral-gamma ray signal originates from the first ~35 cm of the soil, the anomalous gamma signal cannot be caused by a buried ejecta layer at ≥5 mbs. Yet, the ejecta layer is at/near the surface in the hilly area (no younger geologic deposits mapped atop it). Erosion of surface material may take place due to surface water runoff, and eroded material may be transported from the hilly area to the transition zone, through seasonal surface water flow in the structures. Flushing of ejecta material from the hilly area through these channels, may explain the observed gamma-signal. Alternatively, the measured gamma-signals may simply be caused by a different soil type in these seasonally waterlogged areas, but no information is available on the chemical constituents of the soils.

The 340 Hz EM signal was observed to be anomalously high in certain parts of the transects, corresponding with the location of delineated structures. The signal there was matched well with an additional low-permeability zone of ~5 Ωm at depth, suggesting a higher matrix porosity. The depth, extent and resistivity of the layer is relatively undetermined, due to equivalences and low sensitivity to geology beneath the very conductive ejecta-layer, so the data mainly suggest the possibility of 'something more conductive' at depth below structures than away from them. It is however notable that using the resistivity of freshwater in a cave, and the water table elevation at each transect as starting depth of this deeper layer, gave good fits to the data.

4.3. Under which conditions can HEM detect submerged high permeability zones?

The interesting question for the purposes of the present study is whether the delineated structures are high permeability zones for groundwater transmission. Analogue to the Holbox fracture zone, the structures could have higher permeability, since they are likely part of the Río Hondo fault system.

Although it has been seen that HEM can detect caves and larger-scale high permeability zones, this ability depends strongly on the local geological conditions. If the low-resistive layer (e.g. 5–10 mbs, 1–5 Ωm) is present, forward calculations showed that signal perturbations due to any high-permeable freshwater zone beneath it would only be observable in the most trusted 3200 Hz and 7190 Hz signal components if the sensor height was relatively low (≤ 30 m) – a sensor height somewhat difficult to obtain in the study area due to the tall vegetation. More significantly, such signal perturbations would not be distinguishable from changes caused by slight variation in the resistivity and/or thickness of the low-resistive layer. Since such changes are characteristic of the ejecta layer, HEM cannot be used to detect high-permeable freshwater filled zones in the inland parts of the study area, when the low-resistive shallow layer is present in the geology. The 340 Hz inphase component can by itself only ambiguously suggest the presence of such zones.

When the low-resistive layer is not present, the ability of HEM to detect high permeability zones, including caves, is not fully understood. Forward modelling of the Ox Bel Ha signal shows that using known cave dimensions cannot bring the modelled signal up to the level of that measured (Ottowitz, 2009). Instead, the matrix surrounding the caves may have an increased porosity, yielding a lower bulk matrix resistivity in the vicinity of caves, and increasing the signal magnitude. This topic has received very little attention in the literature. The limestone medium surrounding karst conduits has in one case been described as inhomogeneous, based on geophysical measurements (Guérin et al., 2009). A higher porosity surrounding cave conduits may also correspond to the proposed "annex-to-drain" conceptualization, where storage in the karst aquifer is believed to take place in large karstic voids with a high head loss connected to conduits (Mangin, 1974; Bakalowitz, 2005). Yet, since the surroundings of caves and high permeable zones are little known, and they influence the anomalous HEM signal significantly, it is presently not possible to say which conditions are determining for HEM to detect karstic voids. However, besides the matrix surrounding the caves, the HEM signal is sensitive to especially the following factors: the proportion of saltwater in the cave (for instance, the Ox Bel Ha caves are filled partly with fresh, partly with saline water); the size of the cave; the presence of several caves in the vicinity of each other; the shape and depth of the cave; the resistivity contrast in the geology; and, as always, the sensor height (Gondwe, unpubl. results of forward modelling experiments).

4.4 Hydrologic importance of the inland structures

4.4.1 Surface water hydrology and the inland structures

Clearly, the thinner unsaturated zone above the delineated structures and their lower elevation compared to surroundings, means that surface water bodies form atop them, due to runoff into depressions and limited infiltration capacity above the structures. This is corroborated by the fact that swamps, poljes, ephemeral streams, waterlogged soil types and the few lakes existing on the peninsula are associated with the delineated structures. The role of poljes and bajos in the regional hydrology, and how they were formed, has not previously been described in the existing literature on the Yucatecan inland swamps (e.g. Pope and Dahlin 1989; Gunn et al., 2002; Tun-Dzul et al., 2008; Beach et al., 2008). Runoff is observed in many structures during parts of the year, and is evidenced by the presence of culverts and bridges across them. The structures are thus important for surface water generation and flow in the study area.

Looking at the official geologic maps and topography, poljes and flat-bottomed valleys are also seen to exist in Campeche's hilly regions. They were also followed by the automatic river-delineation routine. However, in Campeche only the flat-bottomed polje-features are seen. In Quintana Roo the structures have remained more incised, due to the formation in association with the Río Hondo fault system. The incision also shows in the Landsat Band 4, where only the incised structures appear dark; the flat-bottomed poljes in Campeche and in the hilly parts of the study area (Morocoy and Nuevo Becak poljes) do not. Hence, surface drainage is more focused in the study area, and more diffuse in the Campeche side. It is interesting to note how the incised structures of the study area seem to point towards Sian Ka'an – the only extensive wetland on the peninsula.

4.4.2 Groundwater hydrology and the inland structures

Due to the ejecta-layer, HEM measurements cannot tell us if the inland structures are associated with high permeable zones for groundwater transport. Yet, faults elsewhere in the study area appear to be high permeable zones. Besides the Holbox zone, also the fault in which Laguna de Bacalar is located is proposed to be related to underground water circulation through a connected karst system (Gischler et al., 2008). This lake has the same width as most of the delineated structures (1–2 km). It is up to 15 m deep, and freshwater-filled cenotes up to 90 m deep are associated with it (Gischler et al., 2008), indicating underground groundwater circulation as well. Karstic caves are generally known to often form along faults and fracture systems (Ford and Williams, 2007). In the study area, breakdown-features near Ocom, on one of the delineated structures, form seven lakes 'on-a-string', known to be fed by submerged sinkholes, and indicating the likely presence of underground caves. In the hilly area, some sinking streams (ponors, e.g. Río Escondido) have been observed, disappearing into sinkholes. In neighboring Belize poljes are associated with ponors and underground caves (Miller, 1996). All these attributes suggest the possibility that the structures may be underlain by high-permeable zones.

With the presently available data, the only way to investigate the permeability of the structures is by inverse groundwater modelling. Multiple Model Simulation (Refsgaard et al., 2006) was used to compare hydrologic models of the area with or without assigning a hydraulic conductivity contrast between the structures and the matrix

(Gondwe et al., submitted). Automatic calibration of the models to measured heads from 59 groundwater wells yielded a hydraulic conductivity of the structures which was one to two orders of magnitude higher than the hydraulic conductivity of the matrix. Simulated flows in these structures had the same order of magnitude as those measured in Quintana Roo conduits (Gondwe et al., submitted). Hence, it is plausible that the delineated structures may be associated with high permeable zones, yielding faster transmission of groundwater. However, Gondwe et al. (submitted) showed that equally good fits to heads could be achieved with a uniform hydraulic conductivity and a variable coastal flow resistance. The nature of the structures must therefore be investigated further to determine whether they *do* conduct water more easily than the matrix.

5. Conclusions

Remote sensing data combined with geomorphologic analysis and HEM measurements can be used to map regional-scale high permeability structures in karst. Remote sensing can be used to delineate overall structures, and to interpolate local-scale HEM results to the catchment scale. Remote sensing and geomorphology can guide HEM exploration when total coverage of HEM measurements is not feasible due to the size of the groundwater catchment. The method of combining local-scale HEM measurements with regional-scale remote sensing data analysis may be applicable for analysis of other karst catchments as well.

The ability of HEM to detect underwater caves is not fully understood but depends partly on the resistivity contrast between high-permeability zone and bulk rock matrix, size of the anomalous zone and proportion of saline water 'infill'. Further studies are required to determine the nature of the rock matrix immediately surrounding high-permeability zone, as this zone may have an important influence on the measured EM signals.

The large-scale high permeability structures in the Sian Ka'an catchment are possible pathways for rapid groundwater flow to the wetland, and for seasonal surface water flow. Protecting well fields and groundwater-dependent ecosystems hence requires that attention is given to these structures.

6. Acknowledgements

Financial support from the Austrian Science Fund (project L524-N10 'XPLORE'), The Nature Conservancy, UNESCO, Geological Survey of Austria, the COWIfoundation, WWF Verdensnaturfonden/Aase & Ejnar Danielsens Fond 2006 and 2007, ETH Zürich, and Technical University of Denmark is gratefully acknowledged. We thank S. Bogaerts, K. Davidson, D. Jones, B. Phillips and R. Schmittner for permission to use the Sac Actun cave map. Andreas Ahl carried out the HEM data leveling and processing prior to the data analysis and inversion presented herein.

7. References

Arfib, B., de Marsily, G., 2004. Modeling the salinity of an inland coastal brackish karstic spring with a conduit-matrix model. Water Resour. Res. 40 (11), W115061–W1150610.

Atkinson, T.C., 1977. Diffuse flow and conduit flow in limestone terrain in the Mendip Hills, Somerset (Great Britain). J. Hydrol. 35, 93–110.

Bakalowicz, M., 2005. Karst groundwater: a challenge for new resources. Hydrogeol. J. 13, 148–160. doi: 10.1007/s10040-004-0402-9.

Bauer, S., Liedl, R., Sauter, M., 2003. Modeling of karst aquifer genesis: influence of exchange flow. Water Resour. Res. 39 (10), SBH61–SBH612.

Beach, T., Luzzadder-Beach, S., Dunning, N., Cook, D., 2008. Human and natural impacts on fluvial and karst depressions of the Maya Lowlands. Geomorphol. 101, 308–331. doi: 10.1016/j.geomorph.2008.05.019.

Beamish, D., 2004. 3D modelling of near-surface, environmental effects on AEM data. J. of App. Geophys. 56, 263–280.

Beddows, P.A., 2004. Groundwater hydrology of a coastal conduit carbonate aquifer: Caribbean coast of the Yucatán Peninsula, México. PhD thesis. Sch. of Geogr. Sci.. Univ. of Bristol, UK.

Beddows, P.A., Hendrickson, M.R., 2008. When the survey is not enough: temperature, salinity, and dye tracing reveal flow paths. In: Elliot, W.R., (Ed.). Proc. 2007 Natl. Cave and Karst Manage. Symp., St. Louis, Mo., USA. 198–203.

Benson, R.C., Yuhr, L., 1993. Spatial sampling considerations and their applications to characterizing fractured rock and karst systems. Environ. Geol. 22, 296–307.

Birk, S., Liedl, R., Sauter, M., Teutsch, G., 2003. Hydraulic boundary conditions as a controlling factor in karst genesis: a numerical modeling study on artesian conduit development in gypsum. Water Resour. Res. 39 (1), SBH21–SBH214.

Bosch, F., Müller, I., 2005. Improved karst exploration by VLF-EM gradient surveys: comparison with other geophysical methods. Near Surf. Geophys. 3, 299–310.

Carreon-Freyre, D., Cerca, M., 2006. Delineating the near-surface geometry of the fracture system affecting the valley of Querétaro, Mexico: Correlation of GPR signatures and physical properties of sediments. Near Surf. Geophys. 4, 49–55.

Cornaton, F., Perrochet, P., 2002. Analytical 1D dual-porosity equivalent solutions to 3D discrete single-continuum models. Application to karstic spring hydrgraph modelling. J. Hydrol. 262, 165–176.

Degirmenci, M., Günay, G., 1992. Analysis of hydrologic relations between Egirdir-Beysehir-Sugla lakes system and adjacent basins by means of remote sensing techniques (Southern Turkey). Environ. Geol. Water Sci. 19 (1), 41–45.

Dillon, W.P., Vedder, J.G., 1973. Structure and development of the continental margin of British Honduras. Geol. Soc. Am. Bull. 84, 2713–2732.

Doll, W.E., Nyquist, J.E., Beard, L.P., Gamey, T.J., 2000. Airborne geophysical surveying for hazardous wast site characterization on the Oak Ridge Reservation, Tennessee. Geophys. 65 (5), 1372–1387.

Doolittle, J., Collins, M., 1998. A comparison of EM and GPR methods in areas of karst. Geoderma 85, 83–102.

Ford, D.C., Williams, P., 2007. Karst hydrogeology and geomorphology. Chichester, Wiley. ISBN: 978-0-470-84997-2. 576 pp.

Fouke, B.W., Zerkle, A.L., Alvarez, W., Pope, K.O., Ocampo, A.C., Wachtman, R.J., Grajales Nishimura, J.M., Claeys, P., Fischer, A.G.., 2002. Cathodoluminescence petrography and isotope geochemistry of KT impact ejecta deposited 360 km from the Chicxulub crater, at Albion Island, Belize. Sedimentol. 49, 117–138.

Gamey, T. J., Thompson, M., Mandell, W., Frano, G., 2001. Karst pathway delineation using combined spatial and geophysical analysis at Camp Crowder, Missouri. In Abstracts with Programs, Geol. Soc. Am. 33 (6), 132.

Gischler, E., Gibson, M.A., Oschmann, W., 2008. Giant Holocene freshwater microbialites, Laguna Bacalar, Quintana Roo, Mexico. Sedimentol. 55, 1293–1309.

Gondwe, B.R.N., Hong, S.-H., Wdowinski, S., Bauer-Gottwein, P., 2010. Hydrologic dynamics of the ground-water-dependent Sian Ka'an wetlands, Mexico, derived from InSAR and SAR data. Wetl. (in press).

Gondwe, B.R.N, Lerer, S., Stisen, S., Marin, L., Rebolledo-Vieyra, M., Merediz-Alonso, G., Bauer-Gottwein, P. (in review). Hydrogeology of the south-eastern Yucatan Peninsula: new insights from water level measurements, geochemistry, geophysics and remote sensing. Submitted to J. Hydrol.

Gondwe, B.R.N., Merediz-Alonso, G., Bauer-Gottwein, P., (submitted). The influence of conceptual model uncertainty on management decisions for a groundwater-dependent ecosystem in karst. Submitted to J. Hydrol..

Grajales-Nishimura, J.M., Cedillo-Pardo, E., Rosales-Domínguez, C., Morán-Zenteno, D.J., Alvarez, W., Claeys, P., Ruíz-Morales, J., García-Hernández, J., Padilla-Avila, P., Sánchez-Ríos, A., 2000. Chicxulub impact: the origin of reservoir and seal facies in the southeastern Mexico oil fields. Geol. 28 (4), 307–310.

Guérin, R., Baltassat, J.-M., Boucher, M., Chalikakis, K., Galibert, P.-Y., Girard, J.-F., Plagnes, V., Valois, R., (2009). Geophysical characterization of karstic networks - Application to the Ouysse system (Poumeyssen, France). Comptes Rendous Géoscience. doi: 10.1016/j.crte.2009.08.005.

Guérin, R., Benderitter, Y., 1995. Shallow karst exploration using MT-VLF and DC resistivitiy methods. Geophys. Prospect. 43, 635–653.

Gunn, J.D., Foss, J.E., Folan, W.J., Carrasco, M.R.D., Faust, B.B., 2002. Bajo sediments and the hydraulic system of Calakmul, Campeche, Mexico. Anc. Mesoam 13, 297–315.

Henson, H., Sexton, J., Henson, M., Jones, P., 1997. Georadar investigation of karst in a limestone quarry near Anna. 67th Ann. Internat. Meet. SEG, 763–767.

Hildebrand, A.R., Penfield, G.T., Kring, D.A., Pilkington, M., Camargo Z., A., Jacobsen, S.B., Boynton, W.V., 1991. Chicxulub crater: A possible Cretaceous/Tertiary boundary impact crater on the Yucatan Peninsula, Mexico. Geol. 19, 867–871.

Huang, H., 2008. Airborne geophysical data leveling based on line-to-line correlations. Geophys. 73 (3), F83–F89.

Hung L. Q., Batelaan O., 2003. Environmental geological remote sensing and GIS analysis of tropical karst areas in Vietnam. Int. Geosci. and Remote Sens. Symp. 2003 (IGARSS '03). Proc. IEEE Int. 4, 2964–2966.

INEGI, 1997. Carta edafológica (soil map). Recursos electónicos. Escala 1:250,000. Instituto Nacional de Estadística Geogrfía e Informática (INEGI). Shape file.

ITC, 2005. ILWIS 3.3 Academic. International Institute for Geo-Information Science and Earth Observation (ITC). Software for remote sensing and GIS.

Kenkmann, T., Schönian, F., 2006. Ries and Chicxulub: Impact craters on Earth provide insights for Martian ejecta blankets. Meteorics and Planet. Sci. 41 (10), 1587–1603.

Kresic, N, 1995. Remote sensing of tectonic fabric controlling groundwater flow in Dinaric karst. Remote Sens. Environ. 53, 85–90.

Lara, M.E., 1993. Divergent wrench faulting in the Belize southern lagoon: implications for Tertiary Caribbean plate movements and Quaternary reef distribution. Am. Assoc. Petrol. Geol. Bull. 77, 1041–1063.

Li, G., Loper, D. E., Kung, R., 2008. Contaminant sequestration in karstic aquifers: Experiments and quantfication. Wat. Resour. Res. 44, W02429, doi: 10.1029/2006WR005797.

Liedl, R., Sauter, M., Hückinghaus, D., Clemens, T., Teutsch, G., 2003. Simulation of the development of karst aquifers using a coupled continuum pipe flow model. Water Resour. Res. 39 (3), SBH61-SBH611.

Lopez-Ramos, E., 1975. Geological summary of the Yucatan Peninsula. Chap. 7. In: Nairn, A.E.M., Stehli, F.G. (Eds.) The ocean basins and margins. Vol. 3 The Gulf of Mexico and the Caribbean. Plenum Press, NY, USA.

Mangin, A., 1974. Contribution à l'étude hydrodynamique des aquifers karstiques (Contribution the hydrodynamics of karst aquifers). Ann. de Spéléol. 29 (3), 283–332; 29 (4), 495–601; 30 (1), 21–124.

Marin, L.E., Perry, E.C., Essaid, H.I., Steinich, B., 2004. Hydrogeological investigations and numerical simulation of groundwater flow in the karstic aquifer of northwestern Yucatan, Mexico. p. 257–278. In: Cheng, A., H.-D., Ouazar, D., 2004. Coastal aquifer management: monitoring, modeling and case studies. CRC Press LLC. ISBN 1-56670-605-X.

Masoud, A., Koike, K., 2006. Tectonic architecture through Landsat-7 ETM+/SRTM DEM-derived lineaments and relationship to the hydrogeologic setting in Siwa region, NW Egypt. J. of Afr. Earth Sci. 45, 467–477.

McGrath, R.J., Styles, P., Thomas, E., Neale, S., 2002. Integrated high-resolution geophysical investigations as potential tools for water resource investigations in karst terrain. Environ. Geol. 42: 552–557. doi: 10.1007/s00254-001-0519-2.

Miller, T.E., 1996. Geologic and hydrologic controls on karst and cave development in Belize. J. of Cave and Karst Stud. 58 (2), 100–120.

Mochales, T., Casas A.M., Pueyo, E.L., Pueyo, O., Román, M.T., Pocoví, A., Soriano, M.A., Ansón, D., 2008. Detection of underground cavities by combining gravity, magnetic and ground penetrating radar surveys: a case study from the Zaragoza area, NE Spain. Environ. Geol. 53, 1067–1077. doi: 10.1007/s00254-007-0733-7.

Moore, Y.H., Stoessell, R.K., Easley, D.H., 1992. Fresh-water/sea-water relationship within a ground-water flow system, northeastern coast of the Yucatan Peninsula. Ground Water 30 (3), 343–350.

Motschka, K., 2001. Aerogeophysics in Austria. Bull. of Geol. Surv. of Jpn. 52 (2–3), 83–88.

NASA Landsat Program (1990) Tri-Decadal Landsat Orthorectified TM Mosaic of circa year 1990 (1985 to 1996) cloud-free images, N-16-15_loc. USGS, Sioux Falls. Downloaded from http://glovis.usgs.gov/

NASA Landsat Program (2000) Landsat ETM+ scenes p019r045_7x20000421, p019r046_7x20000421, p019r047_7x20000421, p020r045_7x20001106, p020r046_7x20001106, p020r047_7x20000327, p020r048_7x20000327. Orthorectified. USGS, Sioux Falls, 14 Mar, 21 Apr, and 6 Nov 2000. Downloaded from http://glcf.umiacs.umd.edu/data/landsat/.

NASA Landsat Program (2001) Landsat ETM+ scene p020r046_7x20010314. Orthorectified. USGS, Sioux Falls, 14 Mar 2001. Downloaded from http://glcf.umiacs.umd.edu/data/landsat/.

NASA Landsat Program (2002) Landsat ETM+ scene p019r048_7x20020918. Orthorectified. USGS, Sioux Falls, 18 Sept 2002. Downloaded from http://glcf.umiacs.umd.edu/data/landsat/.

Neuman, B.R., Rahbek, M.L., 2007. Modeling the groundwater catchment of the Sian Ka'an Reserve, Quintana Roo. Assoc. for Mex. Cave Stud.. Bull. 18. AMCS bulletin publication. Austin, TX, USA.

Nyquist, J.E., Peake, J.S., Roth, M.J.S., 2007. Comparison of an optimized resistivity array with dipole-dipole soundings in karst terrain. Geophys. 72, F139.

Ocampo, A.C., Pope, K.O., Fischer, A.G., 1996. Ejecta blanket deposits of the Chicxulub crater from Albion Island, Belize. p. 75–88. In: Ryder, G., Fastovsky, D., Gartner, S. (Eds.) The Createaceous-Tertiary event and other catastrophes in Earth history. Geol. Soc. Am. Spec. Pap. 307.

Ottowitz, D., 2009. 3-D Modellrechnung der Karststrukturen des Ox Bel Ha Höhlensystems zur Methodenevaluierung - Aeroelektromagnetic. M.Sc. Thesis, Univ. of Vienna, Austria.

Paulsen, D.E., Lind, I.L., 1997. Gammaspectral scanning of Creatceous/Tertiary boundary sections, Site 999 and Site 1001. Proc. Ocean Drill. Program Init. Reps. 165, 7–13, 36, 186, 336.

Perry, E., Velazquez-Oliman, G., Marin, L., 2002. The hydrogeochemistry of the karst aquifer system of the northern Yucatan Peninsula, Mexico. Int. Geol. Rev. 44, 191–221.

Perry, E., Paytan, A., Pedersen, B., Velazquez-Oliman, G., 2009. Groundwater geochemistry of the Yucatan Peninsula, Mexico: constraints on stratigraphy and hydrogeology. J. Hydrol. 367 (1–2), 27–40. doi: 10.1016/j.jhydrol.2008.12.026.

Peterson, E.W., Wicks, C.M., 2005. Fluid and solute transport from a conduit to the matrix in a carbonate aquifer system. Mathematical Geology 37 (8), 851–867. doi: 10.1007/s11004-005-9211-5.

PetRos EiKon, 2008. GeoTutor IV, Emigma Version 6.4. Geophysical forward modelling software. Ont., Can.

Pope, K.O., Dahlin, B. H., 1989. Ancient Maya wetland agriculture: new insights from ecological and remote sensing research. J. of Field Archeol. 16 (1), 87–106.

Pope, K.O., Ocampo, A.C., Duller, C.E., 1991. Mexican site for K/T impact crater? Nat. 351, 105.

Pope, K.O., Ocampo, A.C., Fischer, A.G., Vega, F.J., Ames, D.E., King Jr., D.T., Fouke, B.W., Wachtman, R.J., Kletetschka, G., 2005. Chicxulub impact ejecta deposits in southern Quintana Roo, México, and central Belize. p. 171–190. In: Kenkmann, T., Hörz, F., Deutsch, A. (Eds.) Large meteorite impacts III. Geol. Soc. Am. Spec. Pap. 384.

Refsgaard, J.C., van der Sluijs, J.P., Brown, J., van der Keur, P., 2006. A framework for dealing with uncertainty due to model structure error. Adv. in Water Resour. 29, 1586–1597.

Rosencrantz, E., 1990. Structure and tectonics of the Yucatan Basin, Caribbean Sea, as determined from seismic reflection studies. Tectonics 9 (5), 1037–1059.

Roth, M.J.S., Mackey, J.R., Mackey, C., Nyquist, J.E., 2002. A case study of the reliability of multielectrode earth resistivity testing for geotechnical investigations in karst terrains. Eng. Geol. 65 (2–3), 225–232.

Schönian, F., Stöffler, D., Kenkmann, T., Wittmann, A., 2004. The fluidized Chicxulub ejecta blanket, Mexico: Implications for Mars. Poster, 35th Annu. Lunar and Planet. Sci. Conf., Leag. City, TX, USA.

Schönian,F., Tagle, R., Stöffler, D., Kenkmann, T., 2005. Geology of southern Quintana Roo (Mexico) and the Chicxulub ejecta blanket. Abstract #2389. 36th Annu. Lunar and Planet. Sci. Conf., Leag. City, TX, USA.

SGM, 2007. Carta geológica de México. Escala 1:2,000,000. 6a edición. Servicio Geológico Mexicano (SGM).

Shah, S.D., Smith, B.D., Clark, A.K., Kress, W.H., 2008. A multi-tool geophysical and hydrogeological investigation of a karst aquifer system, Cibolo Canyon Deveopment Area, Bexar County, Texas. In:

Kuniansky, E. (Ed.). U. S. Geol. Surv. Karst Interest Group Proc., Bowling Green, Kentucky, USA. p. 107–116.

Smart, P.L., Beddows, P.A., Coke, J., Doerr, S., Smith, S., Whitaker, F.F., 2006. Cave development on the Caribbean coast of the Yucatan Peninsula, Quintana Roo, Mexico. In: Harmon, R.S., Wicks, C. (Eds.) Perspectives on karst geomorphology, hydrology and geochemistry – A tribute volume to Derek C. Ford and William B. White. Geol. Soc. Am.. Spec. Pap. 404, 105–128.

Smith, B.D., Cain. M.J., Clark, A.K., Moore, D.W., Faith, J.R., Hill, P.L., 2005. Helicopter electromagnetic and magnetic survey data and maps, Northern Bexar County, Texas. U. S. Geol. Surv. Open-File report 05-1158. pp. 122.

Southworth. C.S., 1985. Applications of remote-sensing data, eastern Yucatan. p. 12–19. In: Ward, W.C., Weidie, A.E., Back, W. (Eds.) Geology and hydrogeology of the Yucatan and Quaternary geology of northeastern Yucatan Peninsula. New Orleans Geol. Soc. Publ., New Orleans, LA, USA.

Steinich, B., Marin, L.E., 1996. Hydrogeological investigations in northwestern Yucatan, Mexico, using resistivity surveys. Ground Water 34 (4), 640–646.

Steinich, B., Marin, L.E., 1997. Determination of flow characteristics in the aquifer of the Northwestern Peninsula of Yucatan, Mexico. J. Hydrol. 191, 315–331.

Supper, R., Motschka, K., Ahl, A., Bauer-Gottwein, P., Gondwe, B., Merediz Alonso, G., Römer, A., Ottowitz, D., Kinzelbach, W., 2009. Spatial mapping of submerged cave systems by means of airborne electromagnetics: an emerging technology to support protection of endangered karst aquifers. Near Surf. Geophys. 7 (5), 613–627. doi: 10.3997/1873-0604.2009008.

Süzen, M.L., Toprak, V., 1998. Filtering of satellite images in geological lineament analyses: an application to a fault zone in Central Turkey. Int. J. Remote Sens. 19 (6), 1101–1114.

Tam, V.T., De Smedt, F., Batelaan, O., Hung, L.Q., Dassargues, A., 2005. Study of cavernous underground conduits in Nam La (Northwest Vietnam) by an integrative approach. Hydrogeol. J. 13, 675–689. doi: 10.1007/s10040-005-0452-7.

Telford., W. M., Geldart, L. P., Sheriff, R. E., 1990. Applied Geophysics, Second Edition. Camb. Univ. Press, ISBN 0-521-33938-3.

Tulaczyk, S.M., Perry, E.C., Duller, C.E., Villasuso, M., 1993. Influence of the Holbox fracture zone on the karst geomorphology and hydrogeology of northern Quintana Roo, Yucatan Peninsula, Mexico. p. 181–189. In: Beck, B.F. (Ed.) Applied karst geology. Balkema, Rotterdam, NL.

Tun-Dzul, F.J., Vester, H., García, R.D., Schmook, B., 2008. Estructura arbórea y variabilidad temporal del NDVI en los "bajos inundables" de la Península de Yucatán, México. Polibotánica 25, 69–90.

Tølbøll, R.J., Christensen, N.B, 2007. Sensitivity functions of frequency-domain magnetic dipole-dipole systems. Geophys. 72 (2), F45–F56.

UBC-GIF, 2000. A program library for forward modelling and inversion of frequency domain electromagnetic data over 1D structures, version 1.0. Developed by the UBC-Geophysical Inversion Facility, Dep. of Earth and Ocean Sci., Univ. of Br. Columbia, Vanc., Br. Columbia. Can.

Urrutia-Fucugauchi, J., Marin, L., Trejo-Garcia, A., 1996. UNAM Scientific drilling program of Chicxulub impact structure: Evidence for a 300 kilometer crater diameter. Geophys. Res. Lett. 23(13), 1565–1568.

Urrutia-Fucugauchi, J., Morgan, J., Stöffler, D., Claeys, P., 2004. The Chicxulub Scientific Drilling Project (CSDP). Meteorics and Planet. Sci. 39 (5), 787–790.

Urrutia-Fucugauchi, J., Chavez-Aguirre, J.M., Pérez-Cruz, L., De la Rosa, J.L., 2008. Impact ejecta and carbonate sequence in the eastern sector of the Chicxulub crater. C. R. Geosci. 340, 801–810.

USGS. 2006. Shuttle Radar Topography Mission, 3 Arc Second, Finished 2.0. U.S. Geol. Surv. Glob. Land Cover Facil., Univ. of Maryland, College Park, Md. February 2000.

Vogelsang, D., 1987. Examples of electromagnetic prospecting for karst and fault systems. Geophys. Prospect. 35, 604–617.

Vouillamoz, J.M., Legchenko, A., Albouy, Y., Bakalowicz, M., Baltassat, J.M., Al-Fares, W., 2003. Location of saturated karst aquifer with magnetic resonance sounding and resistivity imagery. Ground Water 41 (5), 578–586.

Weidie, A.E., 1985. Geology of Yucatan Platform. p. 1–12. In: Ward, W.C., Weidie, A.E., Back, W. (Eds.) Geology and hydrogeology of the Yucatan and Quaternary geology of northeastern Yucatan Peninsula. New Orleans Geol. Soc. Publ., New Orleans, LA, USA.

Worthington, S.R.H., 2003. A comprehensive strategy for understanding flow in carbonate aquifer. Speleogenesis and Evol. of Karst Aquifers 1 (1), 1–8.

FIGURE CAPTIONS

Fig. 1 Geology of the Yucatan peninsula, modified from SGM (2007). Topography from SRTM (USGS, 2006) overlain as grey-scaled transparent. Study area outlined with thick grey polygon. Coordinates are UTM zone 16N, WGS84 datum and ellipsoid

Fig. 2 a) Topography from SRTM (USGS, 2006), highlighting the hilly and the flat areas referred to in the text. Structures outlined from visual inspection of satellite imagery also shown. b) Landsat Tri-Decadal TM mosaic band 4 (NASA, 1990) in grey-scale, white indicating highest brightness. Structures are seen as elongated black and white lines in southern-central part of the study area

Fig. 3 Example of how the structures appear and have been mapped. a) Landsat TM band 4, grayscale. Bright indicates high reflectance, b) Landsat ETM+, RGB: band 2, band 3, band 1, histogram stretched, c) Landsat ETM+ true color composite (RGB=3,2,1), contrast and brightness enhanced for improved display, d) topography from SRTM, e) the delineated structures (black areas) displayed on Landsat ETM+ band 4 for orientation. Location of the image subsections is displayed in Fig. 5

Fig. 4 Location of the rivers automatically delineated based only on topographical relief. Topography shown as background map. The structures delineated from inspection of satellite imagery are outlined in white

Fig. 5 Example of how in some cases river-like linear features can be seen in Landsat imagery but in some cases the automatic river delineation does not always put a river atop of such features (highlighted in a) with green arrows). In b) the equivalent image is given without the automatically delineated rivers overlain, so the structures marked by the automatic river delineation can be seen more clearly. Background image as in Fig. 3b

Figure 6. a+b) Response parameters *M* and *N* for the 3200 Hz signal components, and c+d) for the 7190 Hz signal components, over the southern end of the Holbox fracture zone. Large arrows highlight anomalous areas above the Holbox zone; small numbered arrows highlight other features mentioned in the text. e) Holbox fracture zone outlined as described in text (thick white line). Anomalous areas with high signal strength in 3200 Hz inphase signal (blue polygons) and 7190 Hz inphase signal (green polygons). Sac Actun cave system, (curving red lines) courtesy of S. Bogaerts, K. Davidson, D. Jones, B. Phillips and R. Schmittner. Naranjal cave system and Aktun Ha and Tortuga cave systems (location coarsely indicated, straight red lines) modified from Smart et al. (2006). Dashed grey line outlines area

surveyed with HEM. Background image: Landsat TriDecadal TM band 4; dark areas indicate high soil moisture or open water

Fig. 7 Inversion results from profiles over the Holbox fracture zone. In a) soundings 170 to ~500 are within the delinated Holbox zone and appear as higher conductive than surroundings. Sounding 100–170 likely represents an irrigated field. In b) the line only crosses a higher conductive part of the Holbox zone at sounding 0 to ~110. The "c"s indicate location of known cenotes. Location maps at right side show topographic relief from SRTM (brown: elevations > 20 mamsl, green: elevations < 0 mamsl. Numbers are the sounding numbers of each profile

Fig. 8 HEM signal measured over inland structures, transformed with Eq. 1. 7190 Hz *M* parameter (a,b,c,e) and 3200 Hz *M* parameter (d). Thin yellow lines outline structures. Background of a-c): Landsat TriDecadal TM band 4; background of d): SRTM topograph, brown is high elevation, dark green is low elevation; background of e): Landsat ETM+, RGB: band 2, band 3, band 1, histogram stretched

Fig. 9 Spectral gamma-ray across Transect A, B, D and E, displayed as red-green-blue ternary ratio. c) shows how to interpret the colors

Fig. 10 Possible subsurface configurations modelled. Water levels and depths to halocline from Gondwe et al. (in review). *): Not measured, but estimated from the Ghyben-Herzberg relation and measured water table elevations. **): Realistic higher-end cave sizes from Smart et al. (2006). ***): Estimated through fitting and comparison with nearby borehole logs. Not to scale

Fig. 11 a-c) HEM data (lines) from a flight line in Transect C, along with forward modelled signals (symbols). d) Topographic relief of the transect and earth models corresponding to x-symbols on above graph. e) Nearest borehole log, from Gondwe et al. (in review). f) Location map, displayed on topographic background (dark green is lower elevation). HEM data legend as in Fig. 8. Black dot: Location of logged borehole. White dot: Point where water level was measured. Numbers indicate measured water levels in mamsl from Gondwe et al. (in review)

Fig. 12 a-c+e) HEM data (lines) from a flight line in Transect A, along with forward modelled signals (symbols). d) Topographic relief of the transect and earth models corresponding to x-symbols on above graph. f-g) Nearest borehole log, from Gondwe et al. (in review). h) Location map, displayed on topographic background (dark green is lower elevation, brown is higher elevation). HEM data legend as in Fig. 8. Black dot: Location of logged boreholes. White dot: Point where water level was measured. Numbers indicate measured water levels in mamsl from Gondwe et al. (in review). Small black squares: Wells with perched water encountered, levels not shown (from Gondwe et al., in review)

Fig. 13 a-c+e) HEM data (lines) from a flight line in Transect D, along with forward modelled signals (symbols). d) Topographic relief of the transect and earth models corresponding to x-symbols on above graph. f) Nearest borehole log, from Gondwe et al. (in review). g) Location map, displayed on topographic background (dark green is lower elevation, brown is higher elevation). HEM data legend as in Fig. 8. Black dot: Location of logged boreholes. White dot: Point where water level was measured. Numbers indicate measured water levels in mamsl from Gondwe et al. (in review). Small black square: Wells with perched water encountered, levels not shown (from Gondwe et al., in review). Black stars: Sites with ejecta according to Schönian et al. (2004) and Kenkmann and Schönian (2005)

FIGURES

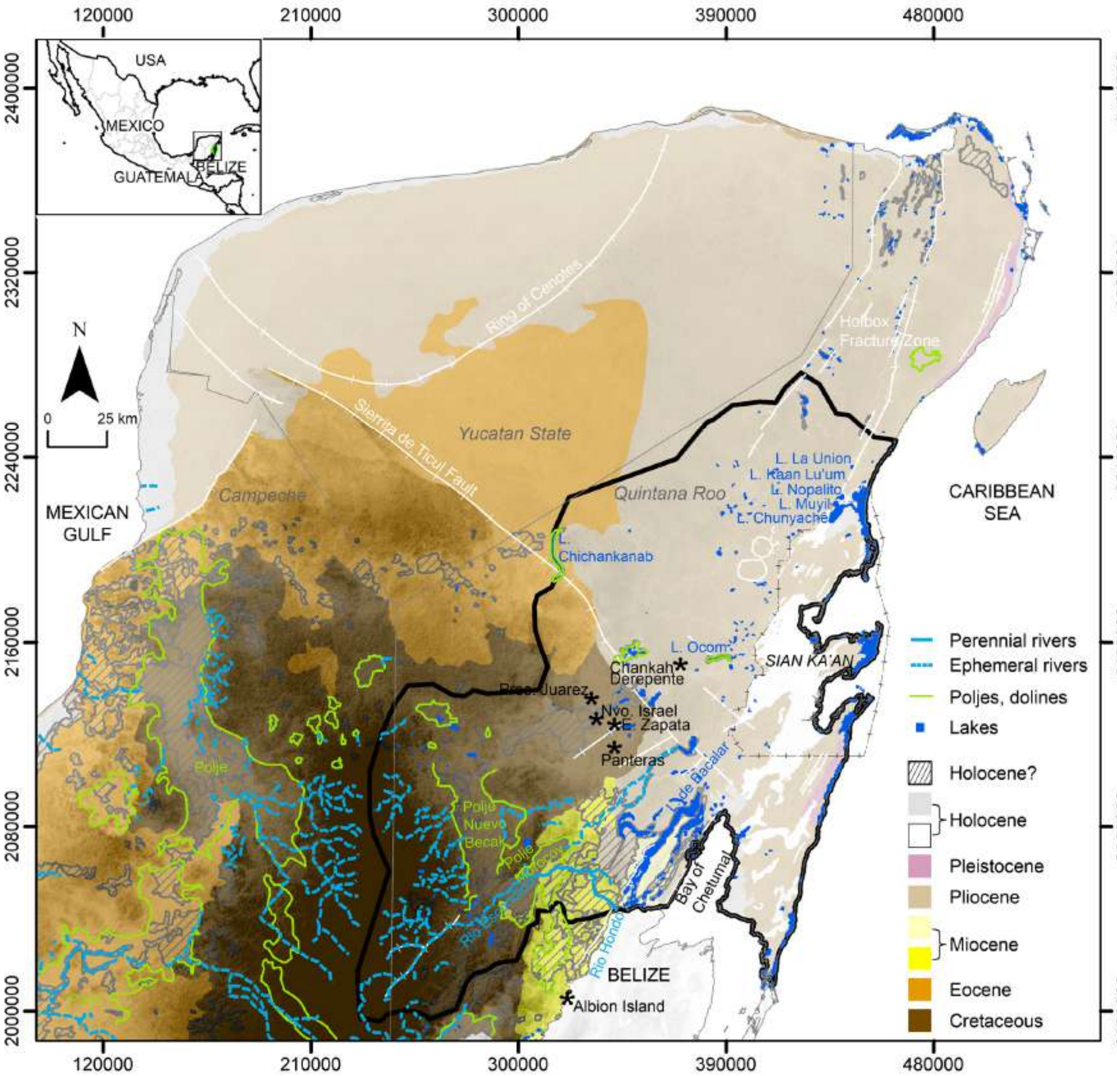

Fig. 1

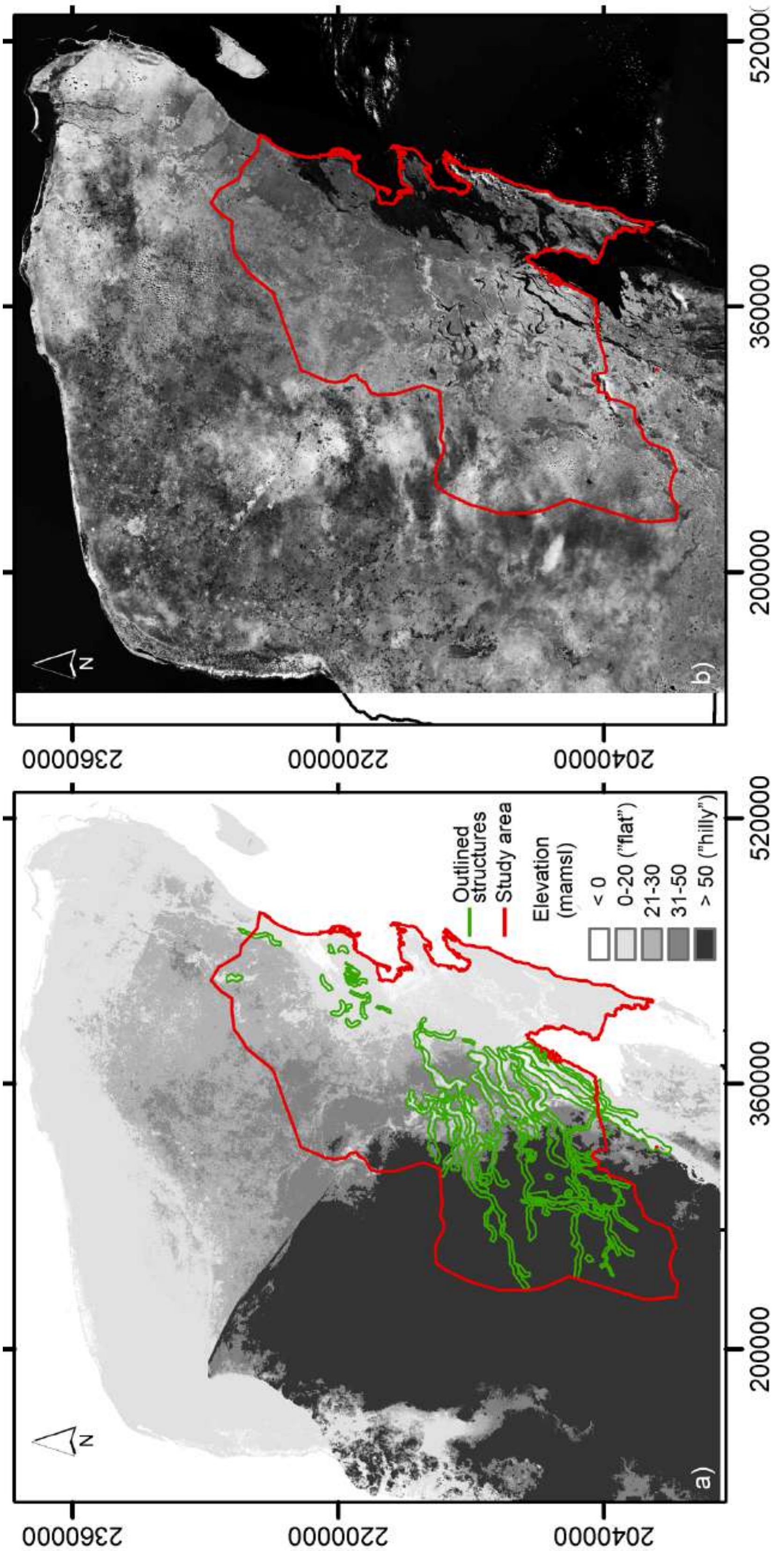

Fig. 2 (rotated 90 degrees)

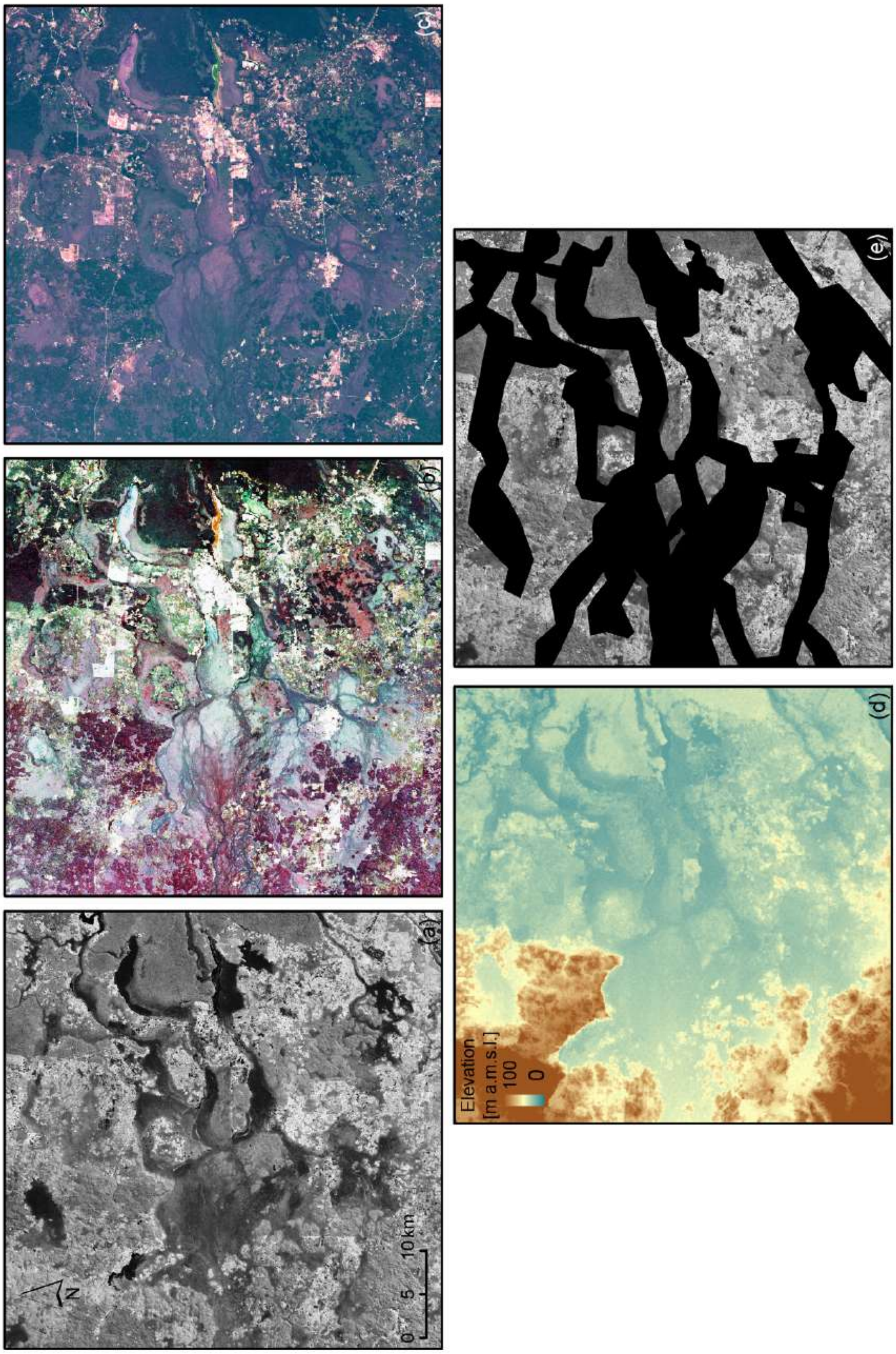

Fig. 3 (rotated 90 degrees)

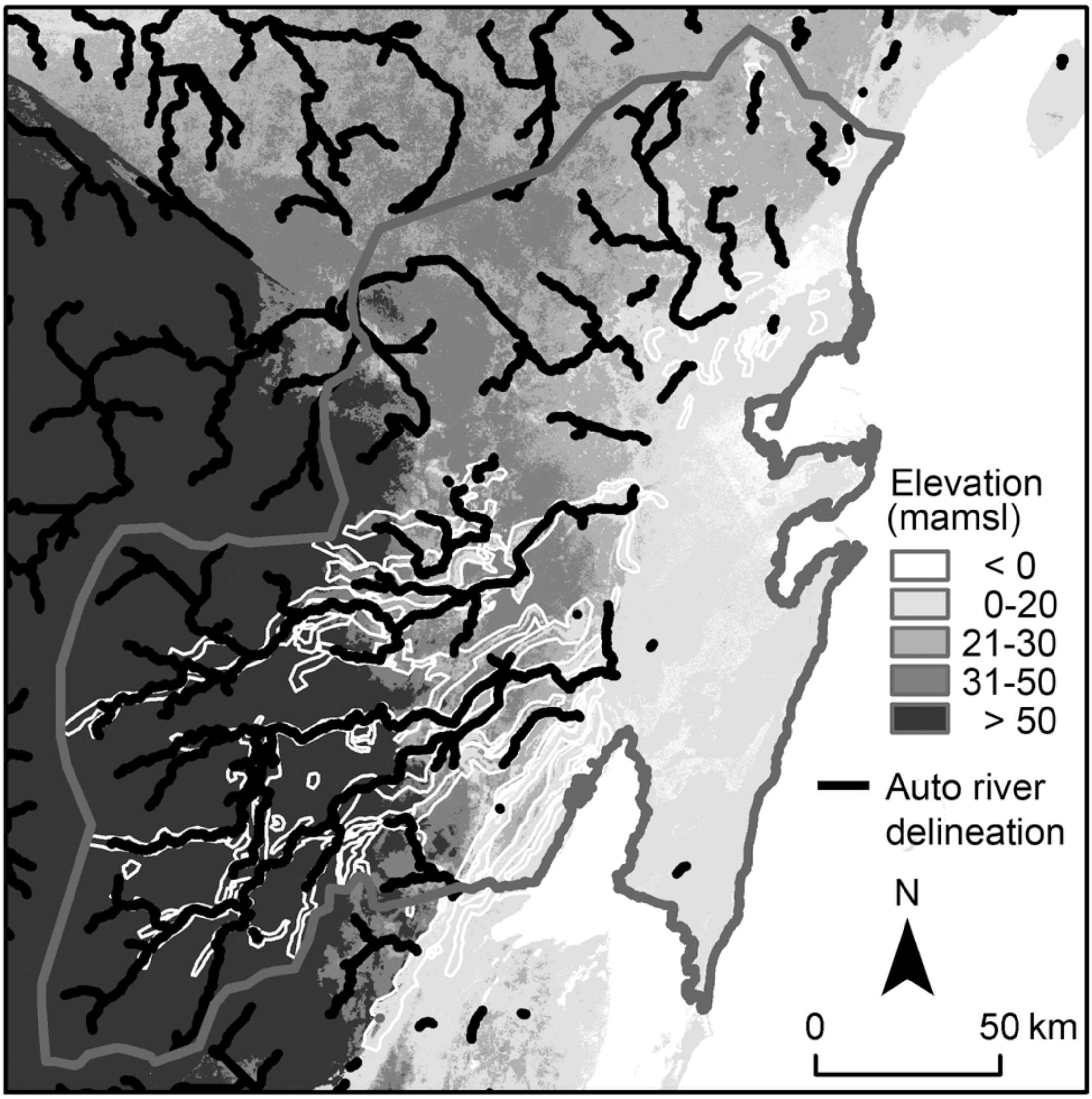
Elevation
(mamsl)
< 0
0-20
21-30
31-50
> 50
Auto river
delineation
N
0
50 km

Fig. 4

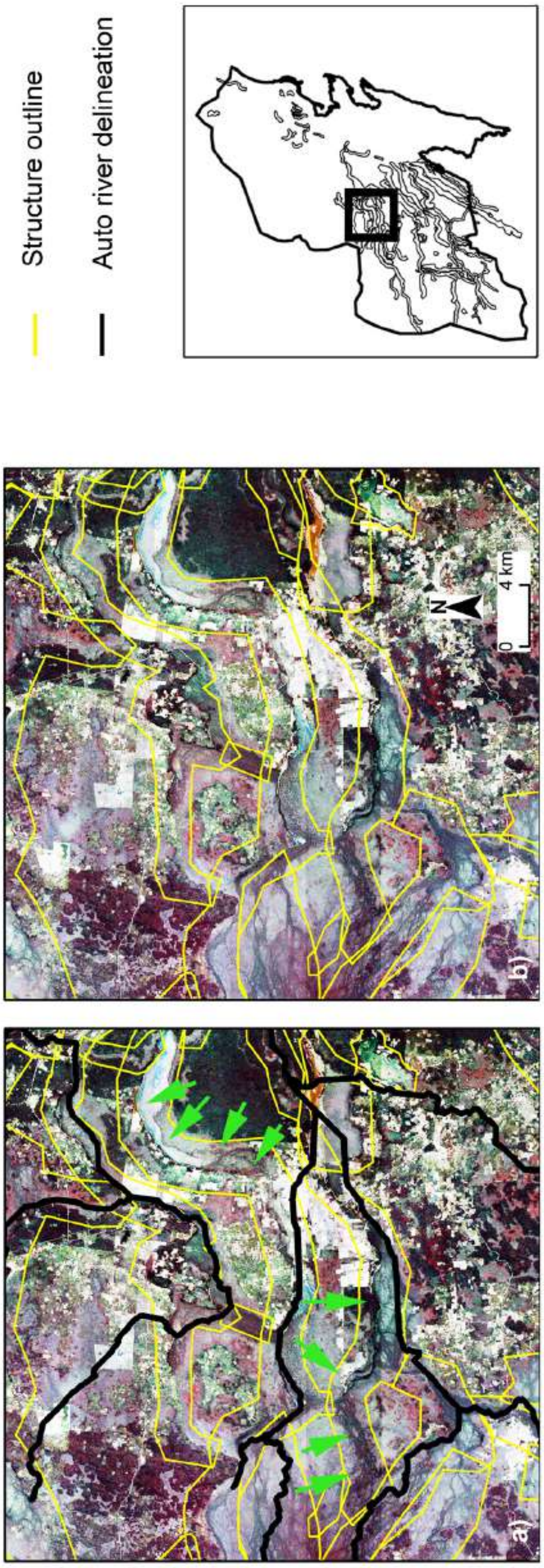

Fig. 5 (rotated 90 degrees)

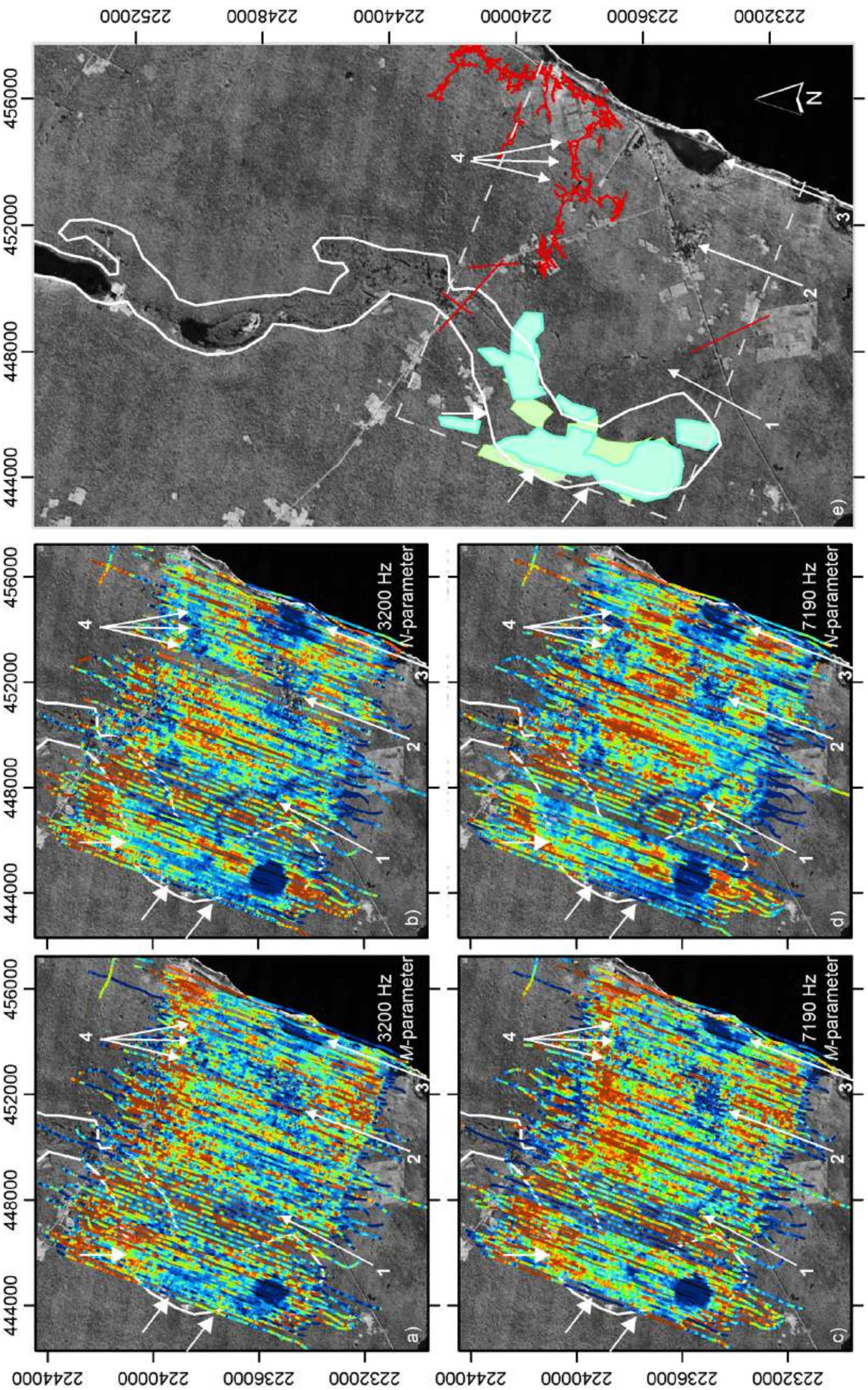

Figure 6 (rotated 90 degrees)

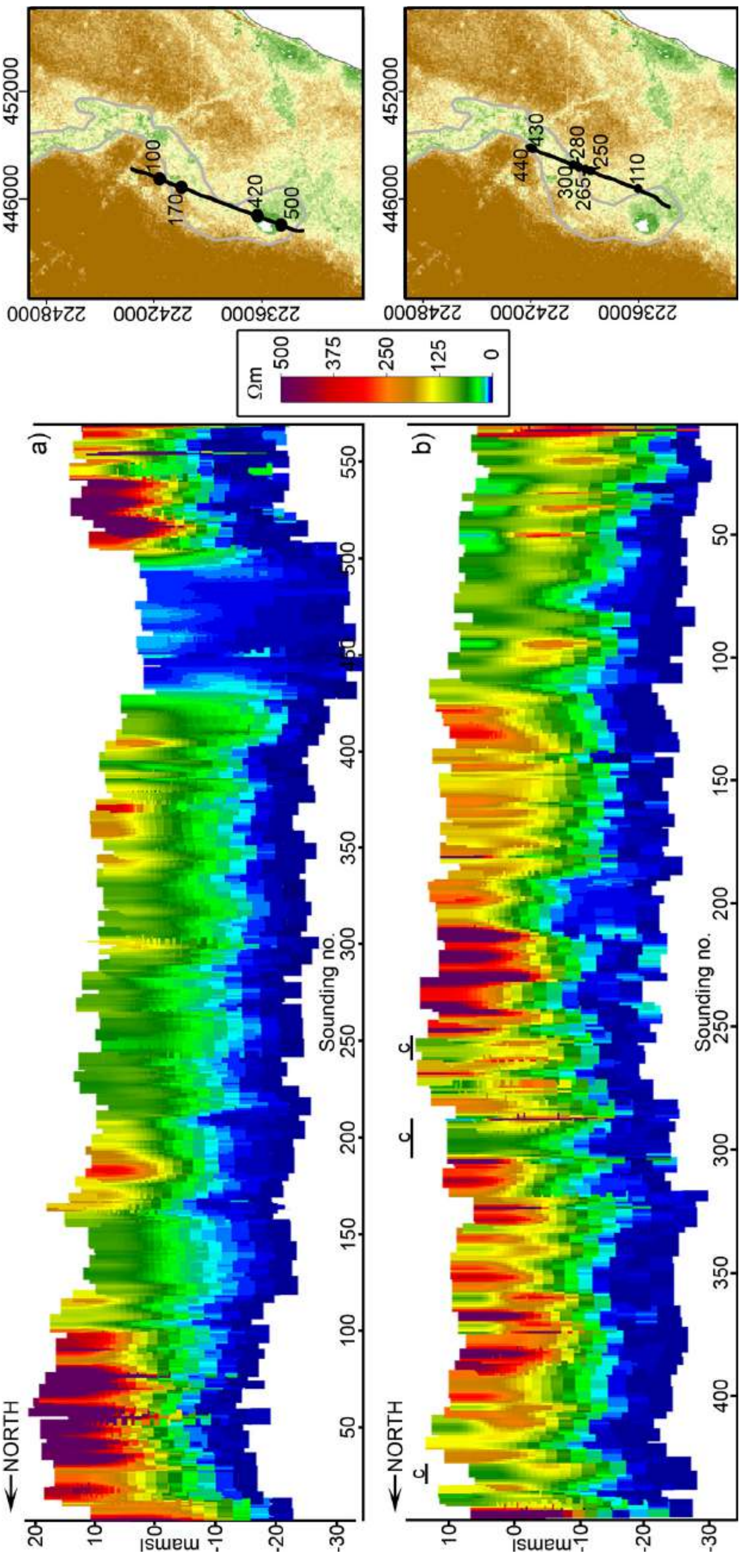

Fig. 7 (rotated 90 degrees)

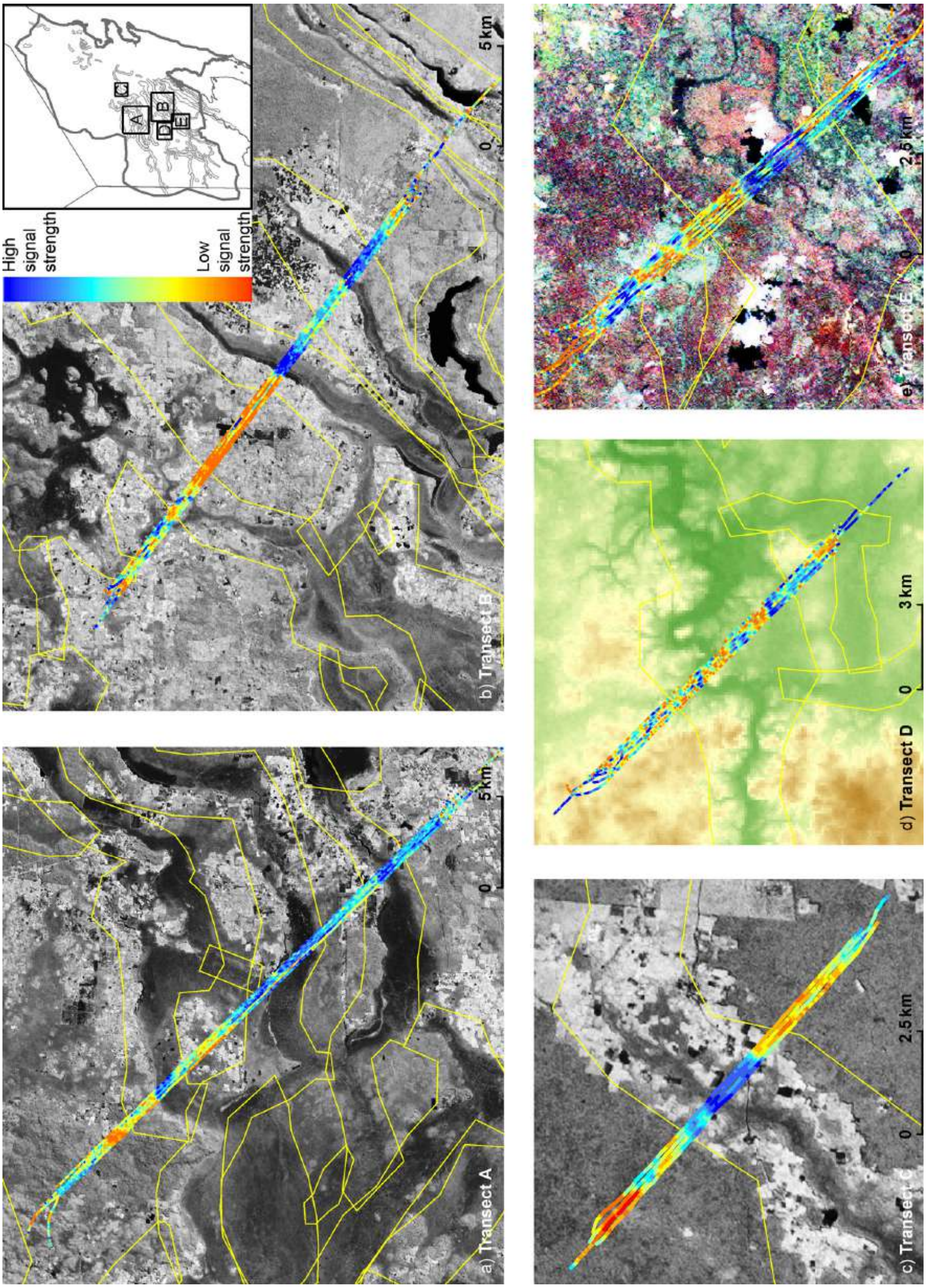

Fig. 8 (rotated 90 degrees)

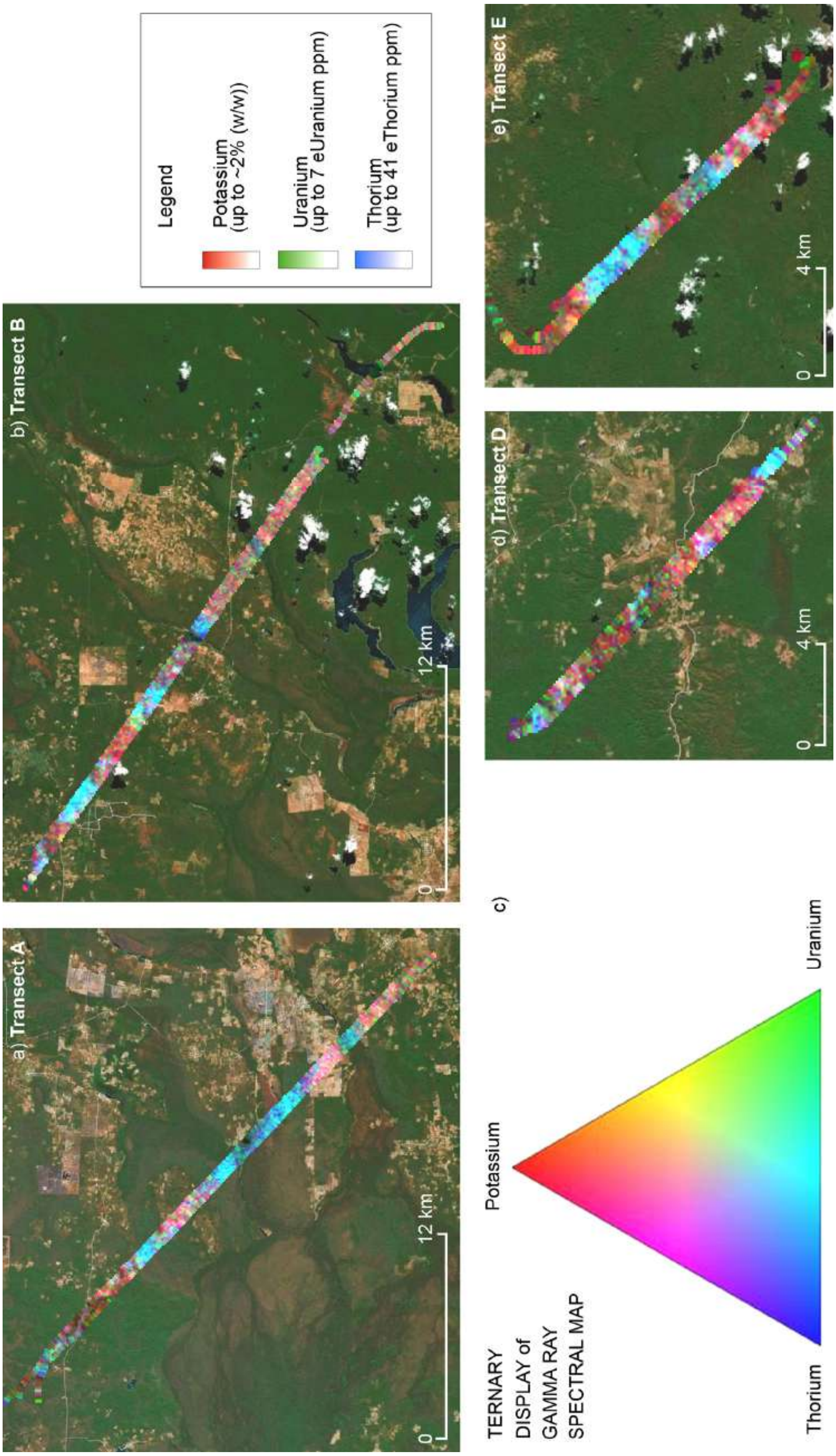

Fig. 9 (rotated 90 degrees)

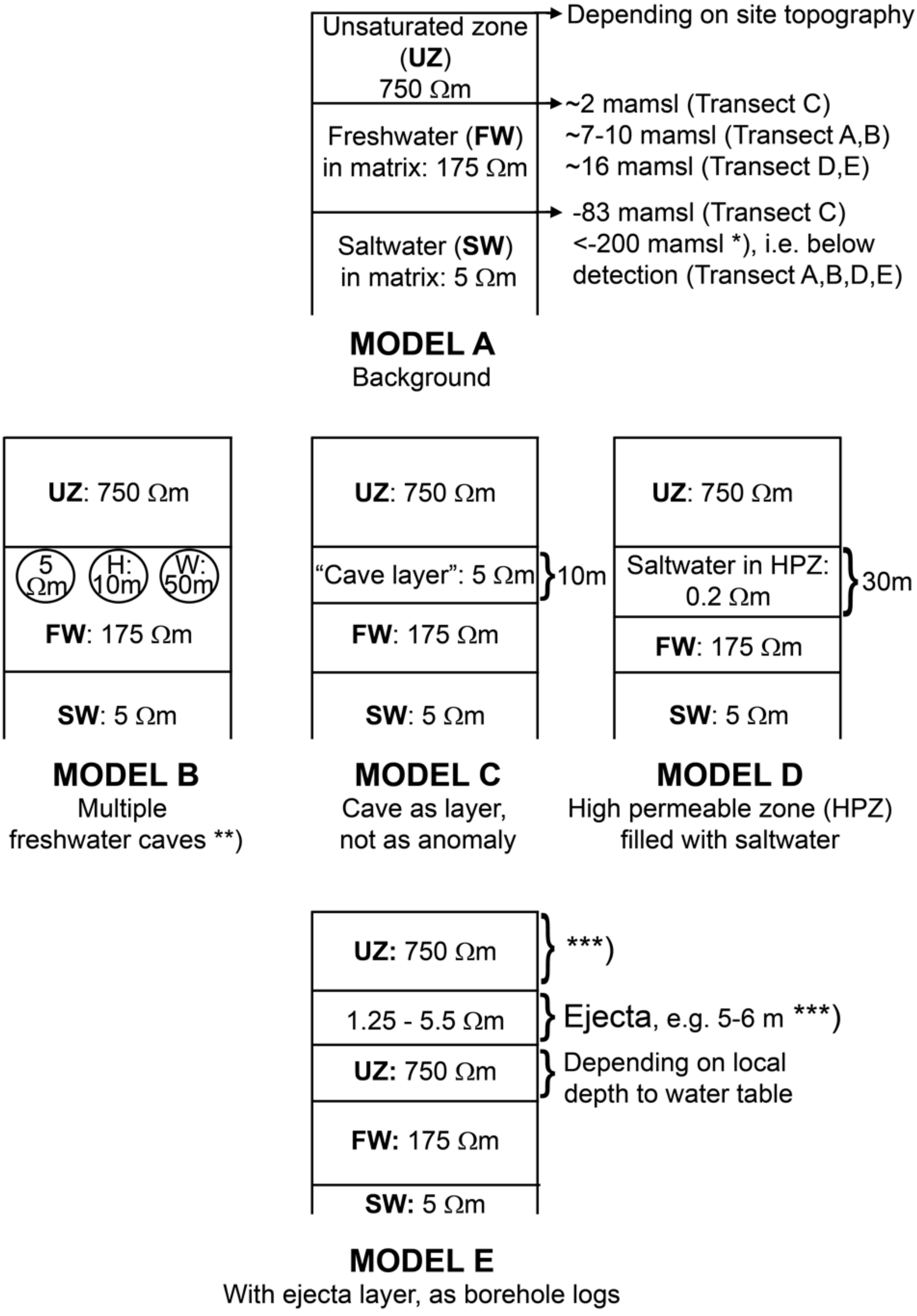
Unsaturated zone
(UZ)
750 Ωm
Depending on site topography
Freshwater (FW)
in matrix: 175 Ωm
~2 mamsl (Transect C)
~7-10 mamsl (Transect A,B)
~16 mamsl (Transect D,E)
Saltwater (SW)
in matrix: 5 Ωm
-83 mamsl (Transect C)
<-200 mamsl *), i.e. below
detection (Transect A,B,D,E)
MODEL A
Background
UZ: 750 Ωm
5 Ωm
H: 10m
W: 50m
FW: 175 Ωm
SW: 5 Ωm
MODEL B
Multiple
freshwater caves **)
UZ: 750 Ωm
"Cave layer": 5 Ωm
10m
FW: 175 Ωm
SW: 5 Ωm
MODEL C
Cave as layer,
not as anomaly
UZ: 750 Ωm
Saltwater in HPZ:
0.2 Ωm
30m
FW: 175 Ωm
SW: 5 Ωm
MODEL D
High permeable zone (HPZ)
filled with saltwater
UZ: 750 Ωm
***)
1.25 - 5.5 Ωm
Ejecta, e.g. 5-6 m ***)
UZ: 750 Ωm
Depending on local
depth to water table
FW: 175 Ωm
SW: 5 Ωm
MODEL E
With ejecta layer, as borehole logs

Fig. 10

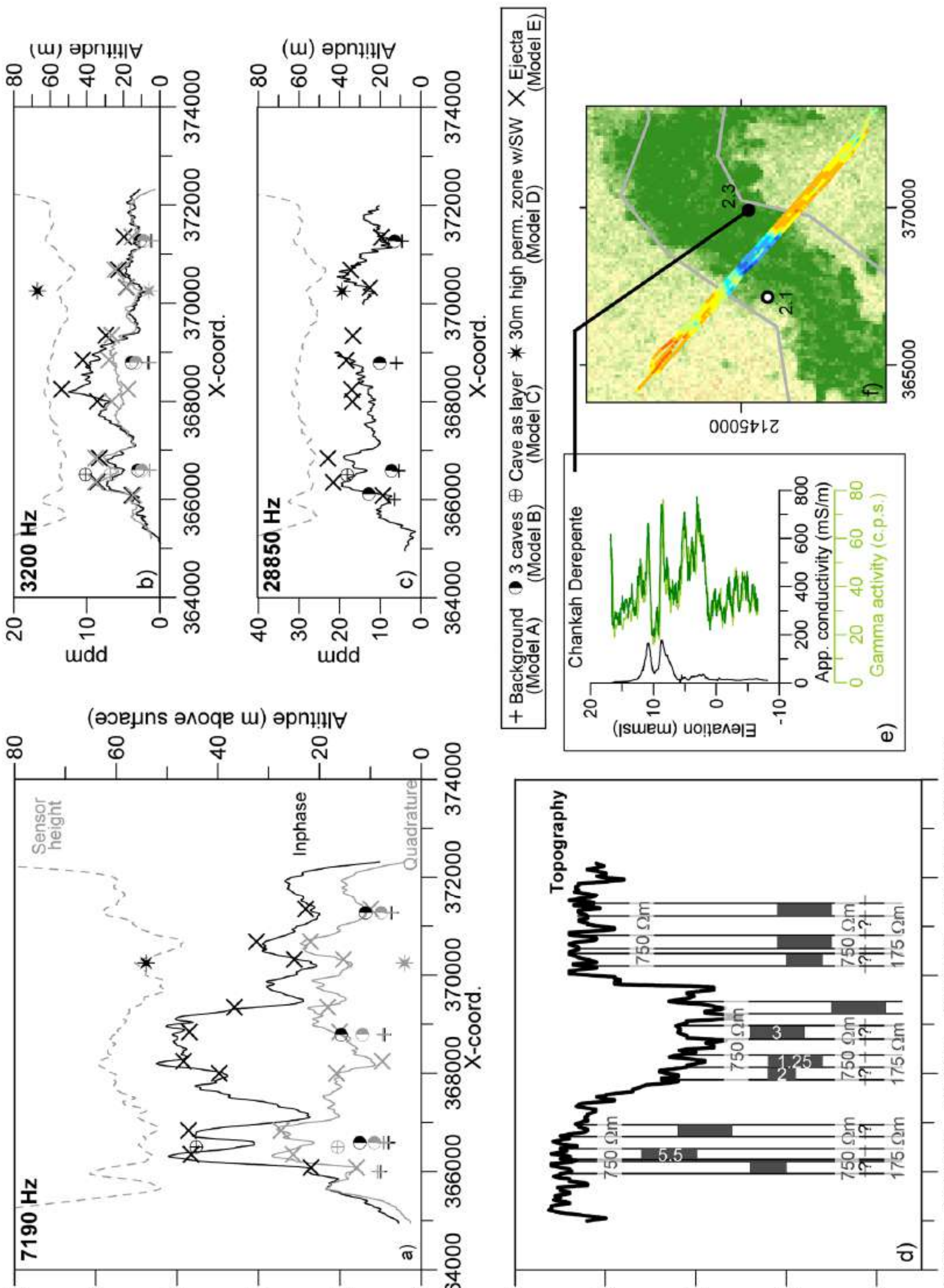

Fig. 11 (rotated 90 degrees)

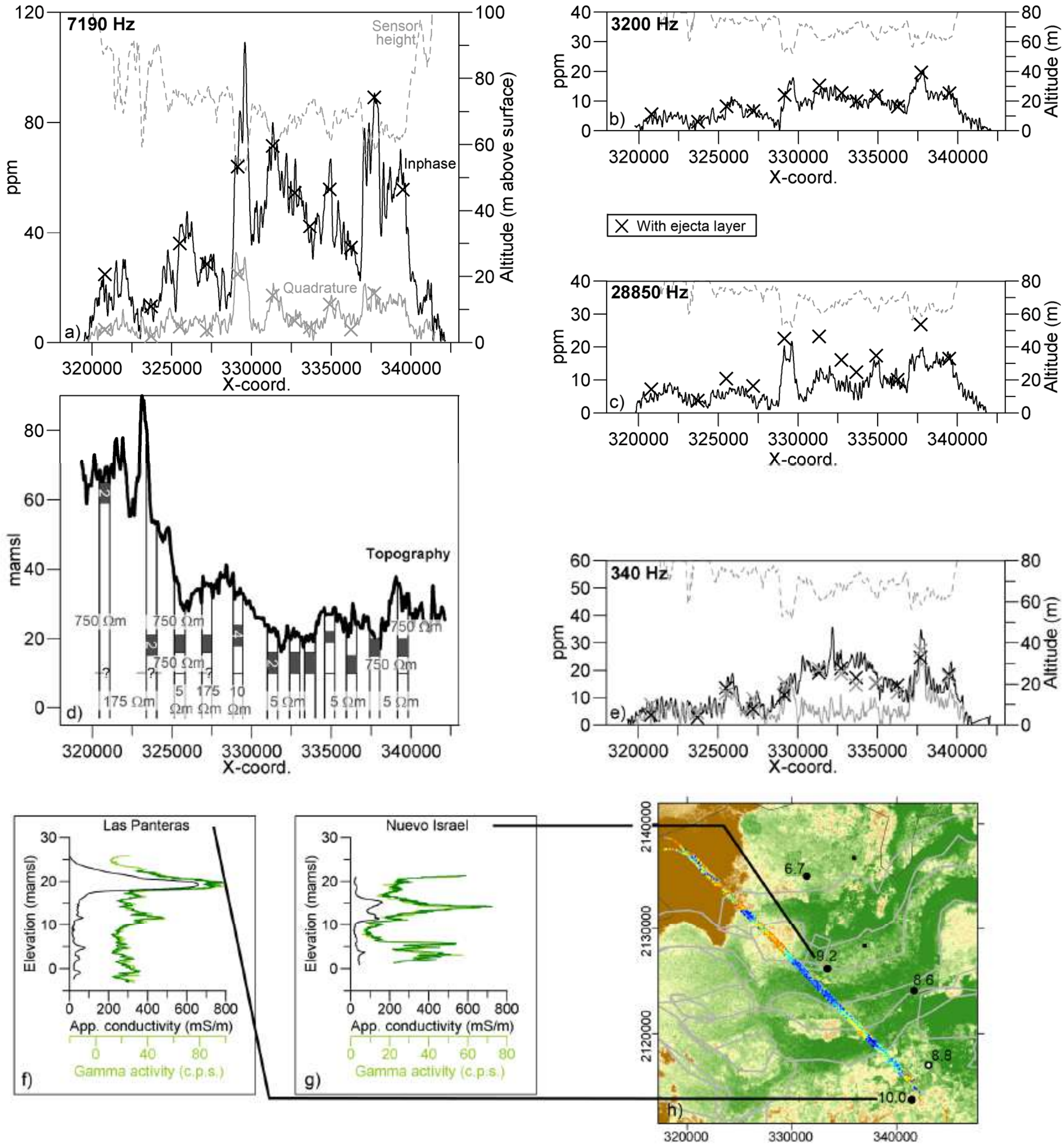

7190 Hz
Sensor height
Inphase
Quadrature
ppm
Altitude (m above surface)
X-coord.
a)
3200 Hz
b)
Altitude (m)
With ejecta layer
28850 Hz
c)
Topography
mamsl
750 Ωm
175 Ωm
5 Ωm
10 Ωm
d)
340 Hz
e)
Las Panteras
Nuevo Israel
Elevation (mamsl)
App. conductivity (mS/m)
Gamma activity (c.p.s.)
f)
g)
6.7
9.2
8.6
8.8
10.0
h)

Fig. 12

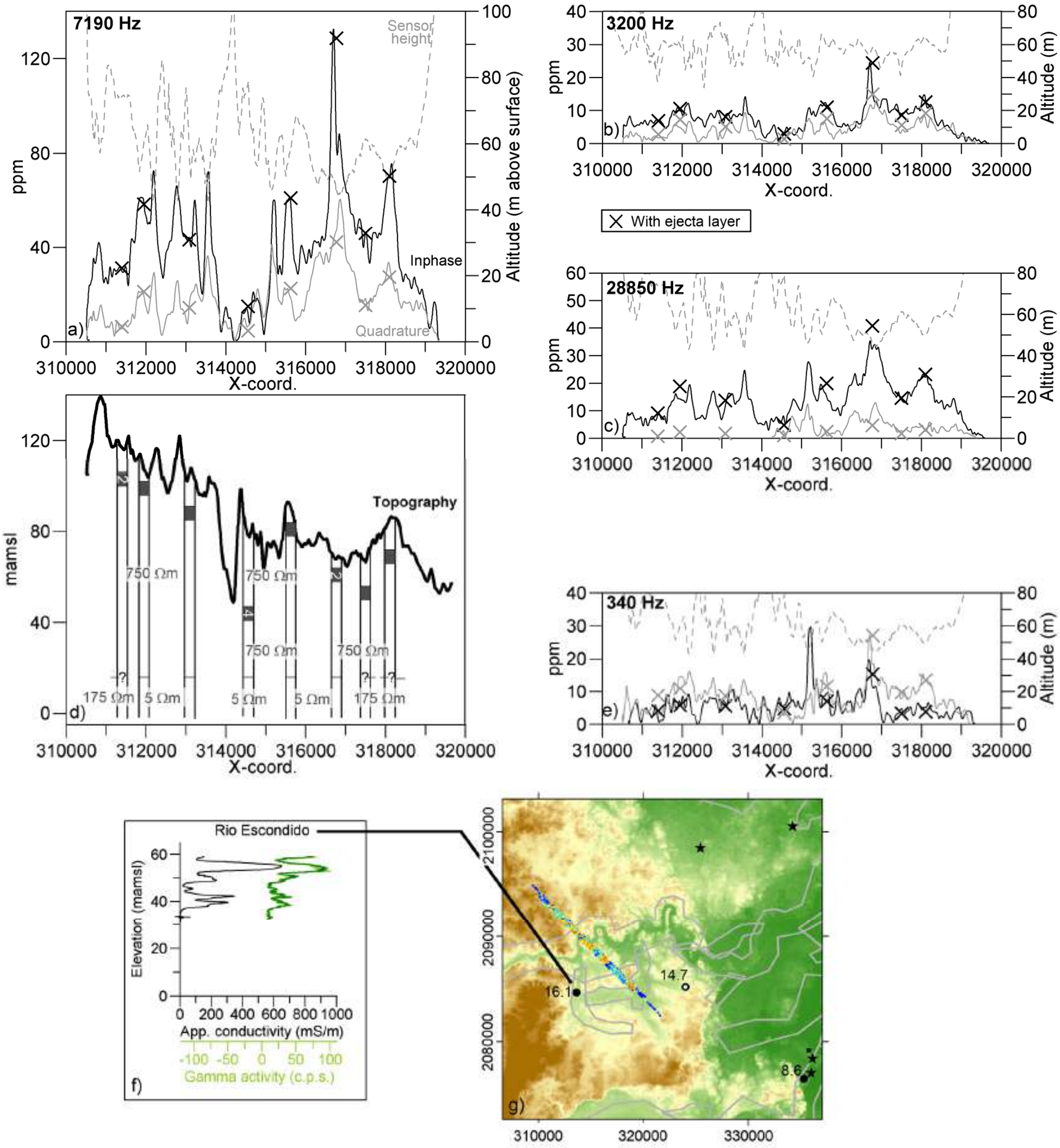

7190 Hz
Sensor height
Inphase
Quadrature
ppm
Altitude (m above surface)
X-coord.
a)
3200 Hz
b)
Altitude (m)
With ejecta layer
28850 Hz
c)
Topography
mamsl
750 Ωm
175 Ωm
5 Ωm
d)
340 Hz
e)
Rio Escondido
Elevation (mamsl)
App. conductivity (mS/m)
Gamma activity (c.p.s.)
f)
16.1
14.7
8.6
g)

Fig. 13

IV

Hydrogeology of the south-eastern Yucatan Peninsula: New insights from water level measurements, geochemistry, geophysics and remote sensing

Gondwe, B.R.N., Lerer, S., Stisen, S., Marín, L., Rebolledo-Vieyra, M., Merediz-Alonso, G., Bauer-Gottwein, P.

Manuscript submitted

Hydrogeology of the south-eastern Yucatan Peninsula: New insights from water level measurements, geochemistry, geophysics and remote sensing

Bibi R. N. Gondwe[a*], Sara Lerer[a], Simon Stisen[b], Luis Marín[c], Mario Rebolledo-Vieyra[d], Gonzalo Merediz-Alonso[e], Peter Bauer-Gottwein[a].

[a] *Department of Environmental Engineering, Technical University of Denmark, Miljoevej, Building 113, DK-2800 Kgs. Lyngby, Denmark. pbg@env.dtu.dk.*

[b] *Geological Survey of Denmark and Greenland (GEUS), Oester Voldgade 10, DK-1350 Copenhagen, Denmark sst@geus.dk*

[c] *Instituto de Geofísica, Universidad Nacinal Autónoma de México, Cd. Universitaria, México, D.F.,04510, México. lmarin@geofisica.unam.mx*

[d] *Centro para el Estudio del Agua, CICY-Quintana Roo, Calle 8, Lote 1, No. 39, Manzana 20 SM 64, Cancún, Quintana Roo, 77500, México. marior@cicy.mx*

[e] *Amigos de Sian Ka'an, Calle Fuego No. 2, Manzana 10 SM 4, Cancún, Quintana Roo, 77500, México. gmerediz@amigosdesiankaan.org*

[*)] Corresponding author: bng@env.dtu.dk; tel.: (+45) 4525 1570, fax: (+45)4593 2850

Abstract

The Yucatan Peninsula is one of the world's largest karstic aquifer systems. It is the sole freshwater source for human users and ecosystems. The region hosts internationally important groundwater-dependent ecosystems (GDEs) in the 5280 km^2 Sian Ka'an Biosphere Reserve. The GDEs are threatened by increasing groundwater abstractions and risks of pollution. Hydrogeological exploration work is needed as basis for sound groundwater management. A multidisciplinary approach was used to study this data-scarce region. Geochemical data and phreatic surface measurements showed distinct hydrogeological units in the groundwater catchment of Sian Ka'an. The hilly southwestern areas had a low hydraulic permeability, likely caused by a geology containing gypsum, whereas the transition zone and flat areas in the east and north had a high permeability. In the latter areas, the fresh groundwater could be described by a Dupuit-Ghyben-Herzberg lens. Geophysical borehole logging and time-domain electromagnetic soundings identified a shallow, low-resistive and high-gamma-radiation layer present throughout the hilly area and transition zone. Its thickness was 3–8 meters, apparent conductivity was 200–800 mS/m and natural gamma-radiation about 80 counts pr. second. The layer is proposed to be ejecta from the Chicxulub impact (Cretaceous/Paleogene boundary). Spatial estimates of recharge were calculated from MODIS imagery using the 'triangle method'. Average recharge constituted 17% of mean annual precipitation in the study area. Recharge was greatest in the hilly area and towards Valladolid. Near the coast, average actual evapotranspiration exceeded annual precipitation. The multidisciplinary approach used in this study is applicable to other catchment-scale studies.

Keywords: conceptual model, karst, aquifer, Sian Ka'an, Mexico

1. Introduction

Globally, groundwater-dependent terrestrial ecosystems are receiving increased attention due to growing recognition that water must be available for ecosystems as well as for people (Eamus and Froend, 2006; Münch and Conrad, 2007; Krause et al., 2007). Groundwater-dependent ecosystems (GDEs) in karst environments are recognized as important ecosystems, and are the target of restoration and protection efforts (Wolfe, 1996; Loftus et al., 2001; Kilroy et al., 2005; Mazzotti et al., 2005). These ecosystems are extremely vulnerable to pollution due to the rapid infiltration, the fast water flow through caves and the limited retention of contaminants in karst geology.

One of Mexico's largest protected areas, the 5280 km^2 Sian Ka'an Biosphere Reserve, is a groundwater-dependent ecosystem in karst. Located in the eastern part of the Yucatan Peninsula, it hosts vast wetlands, fed by groundwater, taking up roughly ⅓ of the reserve. These wetlands are internationally valued and listed as UNESCO World Heritage and a Ramsar site (http://whc.unesco.org/en/list; www.ramsar.org). Their diverse ecosystems and recreational value make them important for the region. Their groundwater source is a thin freshwater lens, only up to 100 m thick. Effectively it is the only fresh water resource available for human use and ecosystems on the Yucatan Peninsula.

On the Peninsula, water demands are growing, along with threats from pollution. Escolero et al. (2000) and Pacheco et al. (2001) documented groundwater pollution problems and significant water abstraction in the northwestern Yucatan Peninsula. Along the eastern coast the tourism industry is expanding, which leads to a rapid increase in population density and water demands (Fideicomiso, 2004). Agricultural activities are intensifying (Mazzotti et al., 2005). Wastewater treatment in the region is poorly implemented. Typically, wastewater is re-injected into the aquifer (ASK, 2003; Marín et al., 2000; Krekeler et al., 2007). Trading off ecosystem water use and human water use emerges as one of the major groundwater management problems on the Yucatan Peninsula.

For sound management of groundwater-dependent ecosystems, a catchment-scale focus is important. However, delineating catchments in karst poses a challenge, due to the complex and heterogeneous nature of karst aquifers. Comprehensive hydrogeologic datasets are required for this purpose. Hydrogeological data are generally scarce in the (south)eastern part of the Yucatan Peninsula. Existing data on the region primarily concentrate on the State of Yucatan, the Cancun area in northern Quintana Roo and the Riviera Maya (e.g. González-Herrera et al., 2002; Graniel et al., 1999; Marín, 1990; Méndez Ramos, 1991; Moore et al., 1992; Beddows, 2004; Steinich and Marín, 1996; 1997; Back and Hanshaw, 1970; Lesser, 1976; Hanshaw and Back, 1980). Only Perry et al. (2002; 2009) and Kenkmann and Schönian (2006) reported geologic and hydrogeologic aspects for the central and southeastern parts of the Peninsula. They indicated that the (hydro)geology here is different from that in Yucatan State, due to the occurrence of an incompletely mapped ejecta layer originating from the late Cretaceous Chicxulub meteorite impact (Hildebrand et al., 1991; Pope et al., 1991). The presence of lakes and seasonally inundated forests and swamps in southern Quintana Roo also indicates a hydrogeology different from the highly permeable geology of the northern part of the Peninsula. With the pressure to further develop tourism activities north and south of the Sian Ka'an Biosphere Reserve, it is important to develop a quantitative understanding of the regional hydrology. Groundwater flow patterns towards Sian Ka'an need to be established. Without knowing where catchment boundaries and main recharge zones are located, management and preservation of these unique wetlands is difficult.

To develop a quantitative hydrogeological understanding of Sian Ka'an's catchment, this study uses a multidisciplinary approach. Geophysical, remotely sensed, water chemical and water level surveys are combined and identify important hydrogeologic differences between the flat and hilly parts of the catchment. Groundwater recharge in the catchment is quantified and its spatial distribution is mapped. A shallow layer of low permeability in parts of the catchment is mapped comprehensively for the first time, and is proposed to be ejecta from the Chicxulub meteorite impact. The collected hydrogeologic data are then combined into a consistent conceptual model of the karstic groundwater catchment of Sian Ka'an.

2. Methods and data

2.1 The study area

The study area is the tentative groundwater catchment of the Sian Ka'an Biosphere Reserve, located in Quintana Roo, Mexico (Fig. 1). The study area was delineated based on topographic divides, assuming, as a first order approximation, that these divides coincide with groundwater divides. The groundwater head data presently available for the Peninsula are in agreement with these boundaries. Geochemical findings of Perry et al. (2002) support the water divide location at Lake Chichankanab.

Average precipitation ranges from 840 to 1550 mm/year. Three quarters of the precipitation falls between May and October (unpubl. climate data from Comisión Nacional del Agua (CONAGUA)). Actual evapotranspiration is poorly estimated; estimates range from 40 to 85% of mean annual precipitation (Lesser, 1976; Beddows, 2004). Average monthly temperatures range from 23 to 27 °C. The area is subject to tropical storms. Soil cover is limited and most of the area is covered by 15–30 m tall semi-evergreen forest (Sánchez-Sánchez and Islebe, 2002; INEGI (1997). Sian Ka'an contains coastal savannas, swamps, marches and mangrove, in addition to tropical forests, and hosts endangered and endemic species (Morales Barbosa, 1992; Mazzotti et al., 2005). From August 2006 to February 2008 the wetland extent varied between 1 067 and 2 588 km^2. Smallest extent was in May and largest in December in a typical year (Gondwe et al., 2010).

The study area contains a notable topographic contrast. The topographic relief is flat in the northern and coastal part (elevations 0–20 meters above mean sea level (mamsl)), whereas the south-southwestern areas have an undulating relief with cone-karst landforms (elevations 50–340 mamsl). In between is a transition zone with moderately undulating relief (20–50 mamsl). These areas are called the flat area, the hilly area, and the transition zone in the remainder of this paper (Fig. 6b). Depressions forming seasonal swamps ('bajos', 'poljes') are found in the hilly area (Pope and Dahlin 1989; Gunn et al., 2002; Tun-Dzul et al., 2008; Beach et al., 2008). Seasonal surface drainage connects some of these swamps (Fig. 1; SGM, 2007) yet not all ephemeral streams appear to have been officially mapped. No perennial rivers are present within the study area, but the majority of the Peninsula's relatively few lakes are found in the centre of the study area. In contrast, no lakes are present in the northern Peninsula. The only surface water bodies in the north are sinkholes ('cenotes'). Cenotes are also present throughout the study area, most abundantly in the flat area and transition zone. The total number of cenotes on the Peninsula is unknown but exceeds one thousand.

Previous studies have established significant seawater intrusion into the aquifer for the Yucatan State and Riviera Maya (Back and Hanshaw, 1970; Perry et al., 1989;

1995; Steinich and Marín, 1996; Moore et al. 1992; Beddows, 2004; Beddows et al., 2007). In Yucatan State the saltwater has been detected up to ~90 km inland (Back and Hanshaw, 1970; Steinich and Marín, 1996), whereas only the near-coastal zone has been studied in Quintana Roo. Groundwater levels referenced to mean sea level have only been mapped in Yucatan State (Marín, 1990).

2.2 Geological framework

The Yucatan Peninsula consists of limestones, dolomites and evaporites reaching thicknesses of >1 500 m (Weidie, 1985). The sediments exposed at the ground surface spans Upper Cretaceous to Holocene in age, and are generally nearly horizontally layered and off-lapping, with gradually younger carbonates deposited towards the Peninsula margins (Lopez-Ramos, 1975; SGM, 2007; Schönian et al., 2005). The Cretaceous age of the oldest sediments sediments exposed at the ground surface is a recent interpretation (Schönian et al., 2005) but the possibility was already mentioned by Lesser (1976). The age of the sediments exposed at the ground surface will be used to refer to various parts of the study area (e.g. Pliocene area) in the remainder of this paper. Kenkmann and Schönian (2006) emphasized that the geology of the southern Peninsula is poorly constrained due to few exposures and difficulties in dating the sediments through biostratigraphy. The Yucatecan carbonates are heavily karstified. They host abundant caves, including the world's longest underwater cave system (http://www.caves.org/project/qrss/qrlong.htm; http://www.caverbob.com/uwcave.htm). Mapped caves are mainly found on the Riviera Maya; possibly as a result of its vicinity to population centers, rather than lack of cave systems inland (Smart et al., 2006;

Beddows, 2004). Regional-scale zones of higher permeability were investigated in Gondwe et al. (in prep.).

Ejecta associated with the Chicxulub meterorite impact, at the contact between Cretaceous and Paleogene sediments, have been found in southern Quintana Roo and neighboring Belize (Ocampo et al., 1996; Fouke et al., 2002; Pope et al., 2005; Schönian et al., 2005; Kenkmann and Schönian, 2006). The Chicxulub impact occurred in the northwestern Yucatan Peninsula (Hildebrand et al., 1991; Pope et al., 1991), 80–350 km from the study area. The extent of the possible ejecta blanket in the study area is not well known. Based on geochemical data Perry et al. (2009) proposed that the ejecta blanket extends south and east of Lake Chichankanab. It appears that in official geological maps some ejecta deposits in the hilly region may have been misdated to be Quaternary deposits, as some locations correlate with locations mapped by Kenkmann and Schönian (2006) as ejecta (Neuman and Rahbek, 2007; Perry et al., 2009). The ejecta is expected to have a low hydraulic permeability, as it is clay-rich, and described to have a sealing or partially sealing effect (Ocampo et al., 1996; Grajales-Nishimura et al., 2000; Perry et al., 2009).

2.3 Water level measurements

Static groundwater levels were measured at 89 hand-dug and drilled wells within the study area. Surface water levels were measured at 12 locations in wetlands and permanent lakes near Sian Ka'an, and at 2 locations in the hilly area. Water levels were referenced to EGM96 mean sea level using static carrier phase GPS. Data processing was carried out in the Trimble Total Control software (Trimble, 2003) using IGS final ephemeris from http://igscb.jpl.nasa.gov/components/prods_cb.html. Estimated uncertainty on the z-coordinate was ±1–7 cm (absolute average: 4 cm), based on reoccupation of 7 rover points. Four water level measurement campaigns were carried out; two in the dry season (Feb-Apr 2007, Feb 2008), one in the early wet season (Jul 2007) and one in the late wet season (Nov-Dec 2008). Not all 103 locations were measured in each campaign. Water level measurements were carried out to the nearest cm from marked geo-referenced points, yielding an uncertainty of ±0.5 cm on temporal water level variations. At three different locations Schlumberger Mini-Diver pressure transducers were employed to measure temporal water level variation in detail. Measurements were compensated for barometric changes measured with Schlumberger Baro-Divers. Uncertainty on Mini-Diver measurements were ±5 mm.

2.4. Geophysical measurements

Twenty-one time-domain electromagnetic measurements (TEM) were carried out to investigate geology and map the depth to the freshwater-saltwater interface – the halocline. The flat area and transition zone were sampled representatively, whereas the hilly part was not sampled, due to time constraints. A ProTEM47 instrument (Geonics Ltd., Canada) with a 40x40 m^2 transmitter coil in central loop configuration was employed. Repetition frequencies of 285 Hz (1 A current), 75 Hz and 30 Hz (both 3 A current) were used. Decay of the secondary magnetic field was sampled in 20 time gates covering 35 μs to 7 ms after end of current turn-off ramp. Data processing and least squares 1D layered inversion was carried out with the SiTEM-SEMDI software (HGG, Denmark 2001; 2007; Munkholm and Auken, 1996; Effersø et al., 1999). For each sounding location the inversion result with best compromise between model simplicity and model fit was chosen. The ability of the TEM method to detect depths to the halocline depends on local geologic conditions and goodness-of-fit of the inversion to data. In a previous study, the depth to halocline obtained from TEM was within 5 m of that observed in boreholes (Goldman et al., 1991). Elevations from Shuttle Radar Topography Mission (SRTM) data (USGS, 2006) were used to convert depths to elevation (mamsl), as elevations determined by GPS were not available for the TEM sites. Error bars given by the inversion routine were added 5 m in each direction to compensate for possible SRTM error (typically e.g. 4–9 m according to Kocak et al., 2005; Gorohkhovich and Voustianiouk, 2006; Weydahl et al., 2007).

Geophysical borehole logging was carried out at 17 sites, mostly wells belonging to private ranches. Fluid temperature and fluid specific electrical conductivity (SEC) was carried out with a Solinst 107 Temperature Level Conductivity meter. Electromagnetic induction log was carried out with an EM39 probe, and natural gamma logging with a GAMMA39 probe (both Geonics Ltd., Canada). Reported induction log results have been adjusted according to the calibration curve given in McNeill (1986). Gamma logs were repeated at least two times to obtain a more certain determination of the highly variable natural gamma radiation. Repetitions were essentially equal. At one site (Presidente Juarez) an induction log could not be carried out due to metal well casing. All other well casings were PVC.

2.5 Water chemistry

Twenty-eight groundwater samples were taken from actively pumping municipal wells, after pumping out at least 1 m^3 of water through the hose to avoid stagnant water. Three surface water samples were obtained as grab samples at locations with active flow of water. At Cenote Azul water 0.5 m below the surface was sampled. Samples were filtered in the field through 0.45 μm filters, and stored in air-tight PE bottles. Bottles for cation analysis had been acid-rinsed in 5% nitric acid, and were stored full of deionized water, which was decanted immediately prior to each sampling. Bottles were rinsed with sample water before being filled. After filling it was ensured that there was no headspace. Separate bottles for alkalinity, cation and anion analysis were used. Samples for alkalinity and sulfate were stored in an ice cooler after sampling, and refrigerated at 5 °C until analysis. Alkalinity was determined 8–28 days after sampling by titration to pH 4.5 using 1.6 N H_2SO_4 acid and a Hach digital titrator following APHA (1998a). Expected precision is approx. ± 1 mg $CaCO_3$/L. Sulfate was determined 7–27 days after sampling using the turbidimetric method (APHA, 1998b), with precision of approx. ± 0.3 meq SO_4/L, based on repeatability test. Remaining samples were transported by air and stored frozen until analysis. For cations, samples were stabilized with concentrated HNO_3 (concentration in sample: 1% v/v), and left for two weeks at 5 °C before analysis to ensure dissolution of any precipitated carbonate. Cations were analyzed on a Varian Vista MPX Axial View Inductively Coupled Plasma Optical Emission Spectrometer (ICP-OES). Three replicates were run, and one was spiked with all the cations for control. Anions, except sulfate, were analyzed on a Dionex ion chromatograph ICS-1500 with an AMMS anion suppressor. Analytical precision ranged at or below ±7% for cations, ±5% for anions.

The PHREEQC software (Parkhurst and Appelo, 1999) was used to calculate mineral saturation indices. Since pH and temperature had not been measured in the field, most recent values available from Comisión de Agua Potable y Alcantarillado (CAPA) (unpubl. data) measured for the same wells were used. Where no values were available from CAPA or Perry et al. (2002), an average of the values for the other localities was used (pH: 7.3, temperature: 28.5 °C). Equilibrium constants from the database phreeqc.dat were used. Measured alkalinity was assumed equal to the HCO_3- concentration, since at the samples' pH values the contribution from other anions to alkalinity can be neglected.

2.6. Remote sensing

2.6.1 Soil water balance

The water balance equation for the soil zone in the catchment can be written as:

$$\frac{dV}{dt} = P - ET_a - Q - R \qquad \text{(Eq. 1)}$$

where *V*: volume of water stored in the soil zone [e.g. mm], *dt*: change in time [e.g. year], *P*: precipitation rate, ET_a: actual evapotranspiration rate, *Q*: rate of surface runoff, *R*: groundwater recharge rate [all e.g. mm/year]. In the present case the recharge rate is equal to the sum of groundwater outflow from the catchment to the coast and the groundwater abstracted. All quantities in Eq. 1 may be a function of space and time. When considering long-term averaged conditions based on several years, the change in volume of water stored in the soil zone over time becomes zero, as storage can be assumed constant. *Q* can also be assumed zero within the catchment studied, as any (ephemeral) runoff created is expected to infiltrate to the groundwater in a steady-state long-term average scenario. Thus recharge can be estimated as the difference of precipitation and actual evapotranspiration.

2.6.2 Rainfall data

Daily precipitation data were obtained by summing the Tropical Rainfall Measuring Mission (TRMM) 3B42 3-hour precipitation product in the period 2004 to 2008

(NASDA/NASA, 2008). TRMM product 3B43 was used for monthly precipitation for 1998–2008. Comparison with monthly station data from CONAGUA showed good agreement with respect to timing of rainfall, but showed TRMM estimates to be generally lower than station data. Before use, TRMM data were therefore adjusted to ground truth measurements following Wolff et al. (2005), utilizing monthly data from 23 CONAGUA precipitation stations located in the study area. TRMM spatial resolution is 0.25°x0.25°.

2.6.3 Evapotranspiration determined from MODIS imagery

Actual evapotranspiration (ET_a) was estimated using the 'triangle method' and the Priestly-Taylor equation, following Jiang and Islam (2001) and Stisen et al. (2008). The Priestley-Taylor equation takes its basis in the Penman-Monteith equation (Monteith, 1965) and defines ET_a as:

$$ET_a = \phi\left[(R_n - G)\frac{\Delta}{\Delta+\gamma}\right] \quad \text{(Eq. 2)}$$

where ET_a is here in [W/m^2], ϕ is the Priestley-Taylor parameter (Priestley and Taylor, 1972) [dimensionless], R_n is net radiation [W/m^2], G is soil heat flux [W/m^2], Δ is the slope of the saturated vapour pressure curve [kPa/K] and γ is the psychrometric constant [kPa/K]. ϕ is assumed to represent the aerodynamic term. It is an effective surface resistance to evapotranspiration, not related to a single surface attribute (Jiang and Islam, 1999). ϕ may vary between 0 and $(\Delta+\gamma)/\Delta$, yielding ET_a between 0 and the maximum available energy (R_n - G). The evaporative fraction (*EF*) [dimensionless], i.e. the amount of energy used on evapotranspiration compared to available energy can be written as:

$$EF = \frac{ET_a}{(R_n - G)} \tag{Eq. 3}$$

or

$$EF = \phi \left[\frac{\Delta}{\Delta + \gamma} \right] \tag{Eq. 4}$$

In the 'triangle method' a physical relation is assumed between ϕ and the T_s–VI space. T_s is land surface temperature, VI is a vegetation index. T_s is plotted versus VI for all pixels in the area studied. The plot will show a triangular space. The lower horizontal edge of the triangle ('wet edge', i.e. constant T_s, varying VI) represents potential ET; temperature is reduced to a minimum in these pixels because of maximum evaporative cooling. The upper, slanting, edge of the triangle ('dry edge') represents minimum ET_a for each VI class (cp. Fig. 1 in Stisen et al., 2008). The position of each pixel in the triangle hence reveals information on its degree of EF. $\phi_{\max}$ is assigned to pixels where T_s is minimum and VI is maximum. $\phi_{\min}$ is assigned to pixels where T_s is maximum and VI is minimum. The VI axis is divided into intervals of equal size. Then ϕ_i of each pixel can be calculated as:

$$\phi_i = \frac{T_{ii,\max} - T_i}{T_{i,\max} - T_{i,\min}} \cdot \left(\phi_{\max} - \phi_{i,\min}\right) + \phi_{i,\min} \tag{Eq. 5}$$

where $T_{i,\,max}$ and $T_{i,\,min}$ are the maximum and minimum temperatures, respectively, for the VI interval in question, and $\phi_{i,\min}$ is the lower bound of ϕ for each VI interval. $\phi_{i,\min}$ is here established using the relation proposed in Stisen et al. (2008):

$$\phi_{i,\min} = \phi_{\max} \cdot \left[\frac{VI_i - VI_{\min}}{VI_{\max} - VI_{\min}} \right]^2 \tag{Eq. 6}$$

When ϕ_i is obtained for each pixel, Eq. 4 and 3 are used to calculate first the *EF* of each pixel, and next the ET_a of each pixel.

The ‘triangle method’ requires that minimum and maximum evaporative fractions can be observed in the analyzed area, because both the dry edge and the wet edge of the triangle must be defined by the data. Therefore, the spatial area used for $\mathrm{ET_a}$ estimation was the whole Peninsula, so that both the drier north-western Yucatan Peninsula with less dense vegetation, and the more humid study area with more dense vegetation, were included. The period 2004–2008 was covered. As VI the MODIS enhanced vegetation index (EVI) (in the 16-day product MYD13A2) was used, since EVI has a higher sensitivity over dense vegetation, such as the study area, than other often used VIs such as the normalized difference vegetation index (NDVI) . Difference in daily day and night land surface temperature was used (dT_s), as this is preferred to using daytime land surface temperature only in the triangle method (Anderson et al., 1997; Wang et al. 2006). The MODIS Aqua product MYD11A1 was used, as these overpass times (approx. 1am and 1.30pm local time) were better suited than MODIS Terra’s. Spatial resolution of MODIS products was 1x1 km^2. To calculate ET_a from evaporative fraction, net radiation (R_n) was calculated as the sum of net shortwave and net longwave radiation obtained from the European Center for Medium-Range Weather Forecast (ECMWF) 12-hour accumulated daytime forecast data (Surface Solar Radiation, SSR, ECMWF parameter #176, and Surface Thermal Radiation, STR, ECMWF parameter #177, respectively). Comparison with net radiation measured by automatic climate stations from CONAGUA showed good agreement. ECMFW data products had 0.5°x0.5° resolution in 2004 and 2005, and 0.25°x0.25° resolution from

2006 onwards. Soil heat flux, G, was calculated using the empirical relationship of Kustas et al. (1993):

$$G = R_n \cdot (0.40 - 0.33 \cdot NDVI) \qquad \text{(Eq. 7)}$$

Due to cloud cover, ET_a could not be calculated daily for all pixels. Instead, the adjusted crop coefficient (K_{c_adj}) for the available days was calculated for each pixel (Allen et al., 1998):

$$K_{c\_adj} = \frac{ET_a}{ET_{ref}} \qquad \text{(Eq. 8)}$$

The 'adjusted' term is used when dealing with crops grown under non-standard conditions; see Allen et al. (1998). The reference evapotranspiration (ET_{ref}) needed was calculated with Hargreaves's equation (Hargreaves and Samani, 1985; Allen et al., 1998) for every 10 days using the ECMWF reanalysis data product 2T (2 meter temperature, ECMWF parameter #167). Hargreaves' equation was chosen because parameters for using the FAO Penman-Monteith equation were not available. Subsequently, the crop coefficients were interpolated in time following Brunner et al. (2004) to provide temporally variable K_c estimates for all days for all pixels. Finally, daily ET_a could be calculated for the missing days in each pixel by using Eq. 8 and the interpolated daily crop coefficients and reference ET at each pixel.

The root mean square error (RMSE) of the used 'triangle method' was found in Stisen et al. (2008) to be 41.45 W/m^2 = 1.5 mm/day, which is the same order of magnitude as that found by most other authors, cited in Stisen et al. (2008). Recalculating this to the uncertainty on a yearly average estimate by dividing with $\sqrt{365}$ yields an RMSE of 0.08 mm/day (= 29 mm/year).

3. Results

3.1 Water levels and water level changes

Water level measurements showed a regional difference in groundwater levels, coinciding with the geological difference in age of the sediments exposed at the ground surface (cp. Fig. 2 and Fig. 1). In the Pliocene area, groundwater levels ranged below 3 mamsl whereas groundwater encountered in the Cretaceous geology ranged from about 4 to 260 mamsl. This regional difference was observed during both wet and dry seasons. Water levels indicated that the general groundwater flow direction was SW-NE from the Cretaceous area to the Pliocene area, whereas in the Pliocene area, the groundwater flow direction was W-E towards the coast.

A regional difference in the magnitude of temporal water level changes was also seen between the Pliocene and Cretaceous areas. Largest increases between dry and late wet season 2008 were all seen to take place in the Cretaceous geology (20 to 954 cm) (Fig. 2d). In contrast, no or little change (0–5 cm increases) were generally seen to occur in the Pliocene area (Fig. 2d).

The continuous hydrographs from the locations of Presidente Juarez (Cretaceous area) (Fig. 3a) and Dzula (Pliocene area) (Fig. 3b) were notably different. Whereas Presidente Juarez showed water level variations of about 350 cm within Apr 2007 to Feb 2008, Dzula only showed water level variations of approx. 40 cm within Jul 2007 to Feb 2008. The Presidente Juarez hydrograph was jagged, and showed many steep changes of e.g. 150 cm within two weeks, whereas the Dzula hydrograph showed smooth transitions. The Petcacab hydrograph (Pliocene area) was short but had the same smooth pattern as the Dzula hydrograph (Fig. 3c). The jagged pattern of Presidente

Juarez corresponded very well with times when rainfall events had occurred in the local area (Fig. 3a). Every time a large rainfall event occurred, the water levels reacted instantaneously. At Dzula, increases also took place following a large rainfall event in the local area, but increases occurred more smoothly. The Petcacab hydrograph showed similar behavior. All hydrographs reacted more closely to the rainfall falling in the TRMM pixel in which they were located (approx. 27.5 km x 26 km), than to the average rainfall falling in the study area (Fig. 3).

Presence of water relatively close to the surface in the Cretaceous geology, and the jagged patterns of the Presidente Juarez hydrograph, indicated that perched aquifers may be present in parts of the study area. The Cretaceous geology is characterized by generally higher elevations than the other geologies, but, as mentioned, geological boundaries on Fig. 1 are only approximate. Two criteria – ground elevation larger than 30 mamsl (as surrogate for geology) and proximity of water table to ground surface $\leq$ 10 m – were therefore used to map locations which likely have perched aquifers (Fig. 2a). All these locations had large temporal water level changes (mostly > 1 m, frequently several meters). That is consistent with having localized perched aquifers, since they would respond more abruptly to precipitation and runoff effects than a regional aquifer in a highly transmissive medium would. Five additional localities had similarly large water level changes, but did only approximately fulfill the two criteria. These locations are marked as 'possibly perched' in Fig. 2a.

When excluding these perched or possibly perched localities the hydraulic gradient in the Cretaceous area was 10–190 cm/km. This is significantly larger than that of the Pliocene area, which had a hydraulic gradient of 3–7 cm/km. This again showed the regional difference between the Pliocene and the Cretaceous areas.

3.2 TEM results

3.2.1 Depth to the halocline

Depth to halocline, determined from inversion of TEM measurements, revealed the expected freshwater lens shape (Fig. 4a). The lens reached a thickness of 80–100 meters 50–70 km from the coast. Ground truthing at site "Eden" (Fig. 1) showed good agreement. At Eden, Beddows (2004) found the halocline at 12 m below the water table during multiple measurements in wet and dry seasons. The TEM measurement yielded a depth to halocline of 16 m ± 1 m below ground surface. Ground surface was 4–5 m above the water table.

The Dupuit-Ghyben-Herzberg model can be used to describe the position of the halocline in a homogeneous medium, if the interface is sharp, and the saltwater and freshwater bodies are in a steady state condition. The model describes the depth to the halocline, with respect to mean sea level, as a function of the elevation of the water table above mean sea level (Vacher, 1988):

$$z_i = 40 \cdot h_f \qquad \text{(Eq. 9)}$$

$$h_f = \sqrt{\frac{r}{41K}\left(L^2 - x^2\right)} \qquad \text{(Eq. 10)}$$

where z_i: depth to the halocline [mamsl], h_f: head of the freshwater lens [mamsl], K: homogeneous hydraulic conductivity [m/day], r: recharge [m/day], L: distance from water divide to coast [m], x: distance from water divide to point where halocline depth is calculated [m].

Water level observations were available within 2 km from the TEM sites. These water levels were plotted vs. depths to halocline (Fig. 4b). If the Dupuit-Ghyben-

Herzberg relationship was valid, the points should be distributed along a line with slope -40 (Eq. 9). Linear regression showed that the points followed a line with slope -39.2 (R^2=0.67). A statistical F-test showed that there is a significant relationship between the response (depth to halocline) and the regressor (water levels) (F-ratio: 32.86, *p*-value: $3\cdot10^{-5}$). A statistical individual t-test showed that the 95% confidence interval for the slope was [-47.8;-30.7] ($t_{16,0.975}$=2.120).

The Dupuit-Ghyben-Herzberg model (Eq. 9 and 10) was fitted to the data, using an estimated L=100 km and r=$5.5\cdot10^{-4}$ m/day (~17% of mean annual precipitation). Although the Dupuit-Ghyben-Herzberg model is only valid for a homogeneous medium and steady state conditions, this was done to obtain a first order K-estimate of 0.3 m/s (Fig. 4a, root mean square error: 11.2 m).

3.2.2 A low-resistive shallow layer

The expected geology with a highly resistive top layer (unsaturated limestone, e.g. >100 Ωm), a medium-resistive middle layer (limestone saturated with freshwater, e.g. ~50 Ωm) and a low-resistive bottom layer (limestone saturated with saltwater, e.g. ≤ 5 Ωm) was observed in many TEM soundings (e.g. Fig. 5a). Some soundings were noisy in the first 285 Hz gates, and were therefore only trusted at depth. In contrast, 7 sites revealed a lower-resistive layer (e.g. <20 Ωm) clearly present at shallow depth (e.g. Fig. 5b–d). The location of the sites is shown in Fig. 6b. The resistivity, depth and thickness of this layer at each site was not well determined using TEM. The method cannot accurately describe shallow layers, due to the time that passes from current turn-off till beginning of the first gate. Elevation of the top and bottom of the layer is shown in Fig. 6a – where error bars are not shown the depth is relatively undetermined from the inversion (infinite uncertainty).

3.3 Borehole logging results

The borehole logging results showed a difference in geology between the flat area and the hilly area/transition zone. In the five borehole logs carried out in the flat area, there were no significant anomalies. Two typical examples of flat area borehole logs are shown in Fig. 7a and b. These were the only two wells deep enough to penetrate the halocline (Fig. 7a) or the top of the saltwater/freshwater mixing zone (Fig. 7b), seen as an increase in the SEC fluid log and the induction log. The gamma logs did not have anomalies at the same depth as the induction log anomalies, therefore the induction anomalies here are clearly due to saltwater entering the rock matrix.

Eleven borehole logs from the hilly area and transition zone showed some highly conductive layers with corresponding anomalies in the gamma-logs. Examples of borehole logs with the anomalous layer are shown in Fig. 7d-f. The electronic supplement material contains graphs of all eleven borehole logs containing the anomalous layer. Gamma-anomalies generally reached levels of about 80 counts pr. second (cps) and were located at the same depths as measured induction-log anomalies. Induction anomalies had values between approx. 200 and 800 mS/m (i.e. ~5 Ωm down to ~1.3 Ωm). The anomalies were generally 0-13 m below surface (mbs), 3-8 m thick, and located in the unsaturated zone. Elevation of the anomalies varied between sites (Fig. 6a). The Reforma site was an exception, with the anomaly located in the upper part of the aquifer, at 20–35 mbs.

One well, Xpichil, was located in the transition zone but did not encounter the anomalous layer. This well was only logged down to 20 mbs (down to 0.82 mamsl).

Metal clamps on most PVC well casings were responsible for the regularly spaced thin positive and negative anomalies seen in the induction log and the inphase component. The inphase thus indicated which anomalies were due to geology and which were due to well casing features.

3.4 Geochemical results

Full water chemical results and saturation indices calculated with PHREEQC are given in the electronic supplement material. Here only the most relevant results are described. An electrical balance between 1.0 and 7.5 meq/L (1.0–12.7%) showed that no major elements were missing from the chemical analysis.

The ratio 1000·Sr/Cl (Fig. 8a) indicates the degree of influence of modern day sea water. Modern day seawater at Yucatan has a 1000·Sr/Cl-ratio of 0.11 (Stoessell, no year). If this ratio is >10 there is little or no mixing with modern day sea water. Fourteen of the 31 sampling points fell within this category. These points were mainly located in the Cretaceous geology. The remaining seventeen samples had 1000·Sr/Cl-ratio between 1 and 10. This category mainly encompassed water from the Pliocene area, but some sites in the Cretaceous area also had values between 1 and 10.

Samples with Cl/Na-ratios between 1 and 1.17 indicates that the source of Cl is seawater dilution or halite dissolution. This was only the case for six samples: Andres Quintana Roo, Limones, Pedro A. Santos and Polinkin in the Pliocene area, and Nicholas Bravo and Veinte de Noviembre in the Cretaceous area. No value of the Cl/Na ratio occurred distinctly more often than the others (Fig. 8b), and most Cl/Na-ratios were below the halite or seawater values.

All water samples had a relatively high content of the strontium-ion. The Sr-content was much larger than it would be if seawater was the sole contributor of this ion to the water (Fig. 9a and b), and there was no correlation between Sr and Cl contents (Fig. 9b). An excellent linear correlation however existed between the concentration of the Sr and the SO_4 ions (R^2 = 0.95, Fig. 9a). The Sr concentrations were higher than the seawater value of 0.16 meq/L (Stoessell, no year) for ten of the thirty-one samples; all of these were located in the Cretaceous geology.

The 100·SO_4/Cl-ratios were grouped into three categories (Fig. 10a): Ratios >100, ratios between 10 and 100 and ratios below 10. The ratios >100 were found in the Cretaceous area and the transition zone part of the Pliocene area. The ratios between 10 and 100 were found in the flat area and in a belt at the southern part of the hilly region (Fig. 10a). In the same places where this ratio was >100, high absolute concentrations of the sulfate ion were found (Fig. 10c) and these waters were very close to or at saturation with gypsum, celestite and anhydrite (Fig. 10b, Fig. 11b, c and d). Furthermore, a strong linear correlation was seen between the dominant cations Ca and Mg and the sulfate concentration (R^2=0.98, Fig. 11a).

3.5 ET and recharge results

The estimated daily ET_a for the whole Peninsula (spatial average) was rather stable from year to year, and varied temporally from 1.56 to 3.90 mm/day (mean: 2.63 ± 0.51 mm/day) (Fig. 12a). Lowest values were encountered in the late wet season (Nov–Jan) whereas highest values occurred in the late dry and early wet season (Mar–Aug). The correspondence with ET_{ref} shows that the net radiation is the main determining factor for the temporal variation (Fig. 12a). On a spatial average, ET_a exceeded average monthly precipitation during Nov–Apr (Fig. 12a). Spatially, the temporal average ET_a for 2004–2008 varied between 0.99 and 6.93 mm/day (mean: 2.62 ± 0.52 mm/day) throughout the Peninsula. When considering only the study area, ET_a varied between 1.42 and 5.74 mm/day (mean: 2.88 ± 0.42 mm/day). The highest ET_a-rates were seen at the coast, where elevations <10 mamsl, and hence water table was relatively close to ground surface. Lowest rates were seen in the drier and less densely vegetated Yucatan State.

Recharge was estimated according to Eq. 1 by subtracting estimated ET_a from precipitation. A comparison of the two quantities for 2004–2008 showed that mean annual ET_a constituted 70–89% of mean annual precipitation on a Peninsula average (Fig. 13a). The variation was chiefly due to yearly variation in precipitation amounts. On average, recharge on the Yucatan Peninsula was thus estimated to be 23% of mean annual precipitation. When considering only the study area, the average value was 17%, when considering an ET_a average of years 2004–2008 and average precipitation covering the same time period. Spatial distribution of recharge showed that ET_a exceeded mean annual rainfall along the coasts (Fig. 13b). In the study area, main recharge areas were located in the hilly area and the area towards Valladolid. Yearly average recharge for the whole Peninsula was 0.79 ± 0.70 mm/day (max.: 3.16 mm/day, min.: -4.01 mm/day); average recharge for the study area was 0.56 ± 0.55 mm/day (max.: 2.24 mm/day, min. -2.49 mm/day).

4. Discussion

4.1 Hydrogeological differences across the study area

The observed regional difference in water levels and hydraulic gradients indicates a difference in transmissivity across the study area. The low hydraulic gradient of the Pliocene area (3–7 cm/km) corresponds well with hydraulic gradients measured elsewhere in the Yucatan Peninsula (Yucatan State: 2 cm/km (Back and Hanshaw, 1970), 0.7–1 cm/km (Marín, 1990); Riviera Maya: 10-15 cm/km (Moore et al., 1992), 6 cm/km (Beddows, 2004)). The water level variations have the same magnitude as those reported for Yucatan State (5–61 cm within 2.5 years, Marín, 1990). These low values indicate high transmissivity of the geology in the Pliocene area. The small and smooth variations in hydrographs from the Pliocene areas support a high transmissivity here. The relatively large K = 0.3 m/s estimated from data and Eq. 10 has the same order of magnitude as that calculated from field data by Moore et al. (1992) and that used in hydrological modelling by González-Herrera et al. (2002).

In the Cretaceous geology the transmissivity may be much lower. Low transmissivity could explain the much higher hydraulic gradient and the large spatial variation in the believed regional water table, e.g. at La Lucha (91.7 mamsl) and Nuevo Becar (34.7 mamsl), located only 30 km apart (Fig. 2b and c). Another option could be that all water in the Cretaceous geology is perched. This however still indicates low transmissivity of the Cretaceous geology or of beds herein.

A geological difference between the two areas is supported by geochemistry. The Cretaceous geology appears to contain significant amounts of evaporites, e.g. gypsum and anhydrite. Firstly, this is seen from the clear correlation between Ca^{2+} and

SO_4^{2-} (Fig. 15a). Gypsum dissolution would give such a clear correlation, and in all points the 100·SO_4/Cl-ratio were higher than that of seawater (=10.3, Perry et al. (2002)), indicating some up-concentration compared to the marine environment. Secondly, sampling points located in the Cretaceous geology were close to saturation with gypsum and anhydrite (Fig. 10b, Fig. 11b and d). Thirdly, the spatial distribution of the highest 100·SO_4/Cl -ratios (>100) indicates the region affected by evaporites (Fig. 10a) (Perry et al., 2002). The spatial distribution of these geochemical indications of evaporites corresponds very well with the location of the Cretaceous geology (Fig. 1), and the gypsum quarries shown in Perry et al. (2009). Likely this area may belong to the evaporitic Ichaiche formation (e.g. Lopez-Ramos, 1975). Schönian et al. (2005) described that the Ichaiche formation is probably Cretaceous of age, instead of the Paleocene age which has been proposed for it, and his boundary to the Ichaiche formation corresponds well with the boundary between Cretaceous and Miocene sediments in Fig. 1. Deep drilled wells in Yucatan State have also encountered Cretaceous sediments with gypsum, anhydrite and halite (Lefticariu et al., 2006; Rebolledo-Vieyra et al., 2000). The belt with lower 100·SO_4/Cl-ratios corresponds with the location of Miocene sediments. This area also has generally low gypsum saturation indices and SO_4^{2-}-concentrations. Two sites in this Miocene geology stand out by having the same water-chemical signature as the Cretaceous sediments (Fig. 10a, b, c). This may be due to inadequate placement of geological boundaries, so that the points are in fact located in Cretaceous geology. Another explanation may be that these sites are influenced by water from deeper geological layers, as they are located close to the fault that forms Laguna de Bacalar, mapped as up to 15 m deep and associated with four surrounding cenotes >90 m deep (Gischler et al., 2008). The southern end of the fault (outside the study area) extends close to the Cretaceous boundary, making transport of water affected by Cretaceous sediments through the fault another possibility. Gypsum is known to have low primary porosity, with water flow mainly taking place through developed karst features, if any (Klimchouk, 1997). Cretaceous anhydrite samples from a borehole in Yucatan State generally have a porosity < 2% (Mayr et al., 2008). This supports the proposed lower transmissivity suggested by the water level data. Perry et al. (2002) defined the 'Evaporite Region' as extending south and east of Lake Chichankanab "from somewhere between Tulum and Felipe Carrillo Puerto south to the Belize border". Due to denser sampling this study can now define the region influenced by evaporites more precisely. The $100 \cdot SO_4^{2-}/Cl$-ratios og SO_4^{2-} concentrations are in agreement with those found by Perry et al. (2002, 2009) (also plotted in Fig. 10 for completeness).

The measured high sulfate concentrations likely originate from gypsum dissolution, since their locations correspond to the gypsum-associated areas mentioned above. The geological control on water quality is important to realize for the water management authorities, because high sulfate concentrations (e.g. concentrations >9.4 meq/L, Marfia et al., 2004) may impair water quality. Twelve samples exceeded 6 meq SO_4^{2-}/L, seven of which had concentrations >20 meq/L. These sites coincided with places in the Cretaceous geology where local residents complained about bad taste of the water.

The geochemical results also indicate some heterogeneity. For instance large differences in water chemistry were seen between Presidente Juarez and Nuevo Israel, located only 9 km apart. A similar example has been reported in Chunhuhub (Perry et al., 2009), and local-scale heterogeneity was also indicated in the geological mapping of

Kenkmann and Schönian (2006). Limited hydraulic permeability may explain such water quality heterogeneity, as also suggested by Perry et al. (2009). Alternatively, geochemical heterogeneity may be caused by rapid water flow through preferential flow paths (caves, faults), enabling water from different geochemical regions to be transported to other regions without equilibrating with the surrounding matrix.

A last regional difference in hydrogeology is the suggested presence of perched aquifers mainly found in the Cretaceous geology or close to its boundaries. To our knowledge, this is the first time that perched aquifers in the region have been mapped (Fig. 2a). Other authors (Perry et al., 2009; Pope and Dahlin, 1989) have only in general terms mentioned presence of perched water tables. The large temporal water level changes in the perched aquifers are caused by direct recharge by local precipitation and likely also by (seasonal) surface water runoff. A barrier of low permeability reducing infiltration rates from the perched aquifer to deeper geological layers must necessarily exist in this area. Likely different types of recharge and storage pertain to the perched aquifers and the regional aquifer in the Pliocene area. The jagged hydrograph (Fig. 3a) indicates concentrated recharge and/or low storage and/or concentrated flow (Kiraly, 2003). The smooth hydrographs (Fig. 3b and c) indicate the opposite.

4.2 Areas influenced by saltwater intrusion

In the Pliocene area the TEM measurements clearly detected saltwater underlying the freshwater. Together with the distribution of the $1000 \cdot Sr/Cl$-ratios < 10 the TEM data support that the Pliocene area is influenced by saltwater intrusion. Since the Dupuit-Ghyben-Herzberg slope of -40 falls within the 95% confidence interval of the slope calculated from the data, the Dupuit-Ghyben-Herzberg model is valid for the sampled area when taking a large-scale perspective. The freshwater can therefore be conceptualized as a lens, and Eq. 9 may be used to define the lower level of the freshwater aquifer in the Pliocene area, based on measured and modelled water levels. In Yucatan State Eq. 9 and 10 were also found valid at a regional scale (Steinich and Marín, 1996). On a local scale the model may not be valid because the basic assumptions of the model are not fulfilled. Geological heterogeneity, non-stationary conditions etc. may account for the fluctuation of points around the Dupuit-Ghyben-Herzberg model curve. On a local scale, neither Moore et al. (1992) nor Beddows (2004) found Eq. 9 and 10 to fit their measured depths to halocline. Both studies were conducted on a local scale and relatively close to the coast (max. 20 km inland, most sampling undertaken within 10 km of the coast). On a local scale coastal caves may truncate the depths to the halocline (Wicks and Herman, 1995), and an outflow face (Van der Veer, 1977; Vacher, 1988), affecting Eq. 10, may need to be applied as a boundary at the coast (Beddows, 2004).

In the Cretaceous geology there is no evidence for the presence of saltwater beneath the freshwater in the regional aquifer. The 1000·Sr/Cl-ratios are generally > 10 here, indicating little influence by modern day seawater. At the same time most Cl/Na-ratios in this area do not indicate influence of seawater dilution. Perry et al. (2002) found Cenote Azul, located in the Miocene geology, to have an unusually low chloride-content (1.2 meq/L). This study shows that a low chloride-content is not unusual in the areas with surface geology older than Pliocene. Eight sites had Cl-concentrations < 2 meq/L (see electronic supplement). In Cenote Azul, scuba divers have so far found 74 m of freshwater column, and have not encountered any saltwater despite the proximity to the coast (P. Widmann, freelance cave diver, pers. comm., 2008). Two possibilities exist. Either the saltwater is very deep down in the older geology (water table elevations and Eq. 9 would indicate a halocline 400–3600 m below mean sea level; whether such a thick water column is realistic could be disputed) or there is no saltwater intrusion in this region. Whichever the possibility, it remains that the older geology does not appear affected by saltwater intrusion. Perry et al. (2009) came to the same conclusion, but defined the unaffected area as being "along the southernmost Caribbean coast from somewhere south of Tulum to the Belize border and probably much farther south". This study has mapped the unaffected and affected areas more precisely.

Six sites had Cl/Na-ratios that indicated the source of chloride to be either seawater dilution or halite dissolution. Four of the sites were in the Pliocene area, favoring the former explanation. The remaining two sites were located in the Cretaceous and Miocene areas. Possibly local halite deposits may explain their data.

4.3 The low-permeable shallow geological layer - interpretation and hydrogeological effect

The similar magnitude of the borehole log anomalies at the 11 different sites, and their generally similar depths indicate that these anomalous layers likely represent the same stratigraphic unit. Furthermore, the gamma anomaly (90 cps) at 1–4 mbs in the Presidente Juarez borehole log is at the same depth interval as a highly conductive layer found using TEM at a different site in the same village (~313 mS/m=3.2 Ωm, top of layer located 3.4 to 6.2 m below surface (= one standard deviation interval), Fig. 5c). The depths and thicknesses of the low-conductive layers detected with TEM are in the same range as those detected in the borehole logs (Fig. 6a). The low-conductive layer detected with TEM is thus likely to be the same stratigraphic unit as the anomalous layer found in the borehole logs.

The low resistivity and high natural gamma activity of the layer indicates that the layer is possibly a fine-grained, clayey material. It has not previously featured in geological maps of the area. One possibility is that this layer is ejecta from the Chicxulub impact at the Cretaceous/Paleogene boundary. The apparent properties of the layer correspond with ejecta properties in general. The ejecta is reported to consist of larger clasts deposited in a fine-grained matrix (Ocampo et al., 1996; Pope et al., 2005). Clayey and silty material characteristically exhibit high natural gamma radiation. The ejecta layer is characterized by high conductivity and gamma anomalies in other borehole logs (Grajales-Nishimura et al., 2000; Wohlgemuth et al., 2004; Mayr et al., 2008). Furthermore, one ejecta location mapped by Schönian (2004, 2005) is 2 km from one of the logged wells where the anomalous layer was found (Reforma).

Additionally, the geochemistry indicates the possible presence of ejecta. The lack of correlation between Sr and Cl, and the excellent correlation between Sr and SO_4 ions indicates that the Sr-content likely originates from dissolution of celestite present in evaporite and/or in ejecta (Perry et al., 2002; 2009). Perry et al. (2002) found the same correlation for their groundwater samples taken south and west of Lake Chichankanab. Especially where Sr-concentrations are higher than seawater's, water may be in contact with evaporite or ejecta layers (Perry et al., 2009). This was the case for ten samples. Application of the following formula (Perry et al., 2009):

$$m_{SrE} = m_{SrGwtr} - (Cl_{Gwtr}/Cl_{Sea}) \cdot m_{SrSea} \qquad \text{(Eq. 11)}$$

where, m_{SrE}: mmol evaporite Sr pr. L of sample

m_{SrGwtr}: Sr-concentration in sample [mmol/L]

(Cl_{Gwtr}/Cl_{Sea}): ratio of Cl-concentration in sample to that in seawater [-]

m_{SrSea}: Sr-concentration in seawater [mmol/L]

reveals that the amount of "excess" strontium (m_{SrE}) contributed to a water sample by dissolution of evaporite was ≥ 0.05 mmol/L at ten sites; in seven cases even as large as 0.13-0.18 mmol/L. All these sites were again located in the hilly area and transition zone, mainly in the Cretaceous geology. Of these, the sites in the hilly area were close to saturation with celestite, gypsum and anhydrite.

A way to prove presence of Chicxulub ejecta in the anomalous layers is by microscopy of thin sections, e.g. to confirm presence of shocked quartz, altered glass and "peening texture" (Ocampo et al., 1996; Pope et al., 2005; Schönian et al., 2004; Marshall et al., 1998). This has not been possible within this study. Nevertheless, whether the anomalous layer in borehole logs and TEM specifically represents the ejecta layer or merely "a clay layer", the results indicate that this layer is widespread in the hilly region and the transition zone. Airborne frequency-domain electromagnetic measurements (HEM) over 5 transects in the hilly area and transition zone also indicate the presence of the high-conductive layer throughout these areas. The HEM data were modelled well with an anomalous layer of the same thickness, depth and resistivity as seen in nearby borehole logs (Gondwe et al., in prep.).

The ejecta was deposited atop a karstified Cretaceous surface (Pope et al., 2005). Possibly only the present hilly area was land surface, permitting weathering and karstification to create greater variation in the topographic relief here compared to surrounding areas. The surrounding water-covered areas would have had a more modest relief. Assuming that the anomalous layer is ejecta, these circumstances may explain why the anomalous layer is found at widely varying elevations in the hilly area, but at similar elevations in the transition zone (Fig. 6a and results in Gondwe et al., in prep.). Between the hilly area and the transition zone there is today a steep drop in elevation of more than 10 meters (from 50 to <40 mamsl) within less than a km suggesting the presence of an ancient coastline here, and distinguishing the two areas of notably different topographic relief.

If the anomalous layer is ejecta, erosion may have taken place following the deposition, reducing the thicknesses of the layer from the 200–400 m thick deposits found in wells near the impact crater (Rebolledo-Vieyra et al., 2000; Urrutia-Fucugauchi et al., 1996; 2004; 2008) to the 3–8 m seen in most borehole logs. A weathered ejecta surface beneath Cenozoic sediments has been found (Pope et al., 2005) and Urrutia-Fucugauchi et al. (2008) also suggested significant erosion of the ejecta blanket after finding a ~34 m thick ejecta unit beneath Cenozoic sediments near Valladolid. Other ejecta findings away from the crater have reduced thicknesses too (Pope et al. (2005): 4–8 m, bases not always observed; Ocampo et al. (1996): 16 m). After erosion, the transition zone and the most southern part of the hilly area near the Bay of Chetumal would have been covered by Cenozoic sediments, according to the geologic map (Fig. 1).

In the flat area no anomalous layer has been found at the depths explored in this study, and the geochemical results do not indicate interaction with ejecta/evaporite. Likely the layer is buried deeper here. Furthermore, the freshwater lens is thinner in this near-coastal zone, reducing the likelihood of freshwater interacting with ejecta layers. The ejecta layer has in Yucatan State been encountered at 222, 250, 257, 332 and 795 mbs, corresponding to about -190 to -780 mamsl (Urrutia-Fucugauchi et al., 2008; Rebolledo-Vieyra et al., 2000; Lefticariu et al., 2006).

Whether or not the anomalous layer is ejecta, a hydrogeological implication of the documented shallow and likely clayey (i.e. low-permeable) layer may be the formation of perched aquifers and ephemeral swamps and streams seen in the transition zone and hilly area. The anomalous layer appears widespread, and may be continuous. However karstic features such as cenotes may interrupt the layer and locally erosion may have removed the layer completely. The layer likely does not generally inhibit infiltration on a regional scale. Locally, it may however reduce infiltration. Examples are the formation of the ephemeral surface water bodies, and the flooding of villages and roads, which occurs in and near the hilly area during the rainy season and lasts for several weeks to months after rainfall events. A recent study by Perry et al. (in press) has similarly found evidence of an extensive clay-rich aquitard in neighboring Campeche.

4.4 Conceptual hydrogeological model

The hydrogeological results are summarized in the conceptual model presented in Fig. 14. If the anomalous shallow geologic layer is interpreted as ejecta, the underlying material must necessarily be of Cretaceous age. As the transition zone has a high hydraulic permeability, the rather shallow Cretaceous material here is likely not evaporitic, but rather karstified limestone and/or dolomite, for instance the Barton Creek formation or the Cerro de Pavo formation (Pope et al., 2005; Schönian, 2005; Butterlin, 1958). In contrast, the Cretaceous formation in the hilly area appears to generally have a low matrix permeability and evaporitic geochemical signature, and could for instance be the evaporitic Ichaiche formation (Schönian, 2005; Lopez-Ramos, 1975). If the anomalous geologic layer is not ejecta, the Cenozoic sediments (likely the Carrillo Puerto formation (e.g. Butterlin, 1958; Lopez-Ramos, 1975)) could solely account for the high permeability of the transition zone and flat area throughout the depth of the freshwater lens. No boreholes have yet documented the thickness of the Cenozoic sediments in the study area, so both scenarios are plausible.

Saltwater intrusion is documented in the flat area and transition zone, but is unknown in the hilly area. Fresh groundwater flow takes place in both rock matrix and preferential flow paths, such as caves. Large-scale structures and faults, discernable from remote sensing imagery, is present throughout the hilly area and transition zone, and may represent large-scale preferential flow paths within the study area (Gondwe et al., in prep.; 2010). Ephemeral surface water flow takes place in the hilly region and in part of the transition zone, mainly atop the large-scale structures. The surface water eventually infiltrates to the groundwater, through the unsaturated zone and through sinkholes, except the little surface water which connects to Río Hondo and flows out into the Bay of Chetumal. The overall groundwater levels and the presence of the structures indicate the possibility of significant above- and underground transfer of groundwater from the hilly area to the transition zone.

The spatial distribution of recharge is dominated by vegetation patterns. The high recharge areas in the hilly area and towards Valladolid are characterized by less dense or smaller vegetation, reflected in relatively lower EVI. In the hilly area, most of the high-recharge locations correspond to the structures outlined in Gondwe et al. (in prep.), owing to the generally smaller vegetation of the swampy areas (Tun-Dzul et al., 2008). Near the coast average evapotranspiration rates exceed average precipitation rates. That is possible due to flow of groundwater from the inland areas to the coast. The comparatively higher evapotranspiration rates at the coast may be related to the water table being closer to the ground surface in these areas, yielding a thinner unsaturated zone. Possibly, the groundwater becomes accessible to plant roots in these areas, providing an unlimited source for evapotranspiration. A spatial view of evapotranspiration has not previously been presented for the Yucatan Peninsula.

Average recharge is relatively high, but agrees well with previous estimates. Lesser (1976) calculated ET_a to be 900 mm/year using Turc's method for the northern half of the Yucatan Peninsula, meaning that recharge would constitute 15% of the average rainfall in his area of study. This study found average ET_a for the whole Peninsula to be between 937 and 995 mm/year. Thomas (1999) estimated recharge to be 21% and 23% of mean annual precipitation for Chetumal and Valladolid. This is in the same range as the average annual values calculated in this paper for the study area and for the whole Peninsula. Beddows (2004) suggested that recharge should be > 30% of mean annual precipitation at the coast to match field data of outflow from two cave systems, and to match halocline depths in an area <10 km from the coast. In contrast, this study suggests limited average recharge rates at the coast. Flow of groundwater from distant parts of the catchment to the coast might instead explain Beddows' data.

5. Conclusions

Water level data and geochemistry show that there is a distinct hydrogeologic divide within the study area, related to a topographic divide and a change in the age of sediments exposed at the ground surface. The hilly area, with Cretaceous sediments, has a lower hydraulic permeability, whereas the transition zone and flat area, which includes younger sediments, has a high permeability. The transition zone and flat area is influenced by saline intrusion, and the freshwater can here be conceptualized as a Dupuit-Ghyben-Herzberg lens. In the hilly area evidence of saline intrusion has not been found.

A shallow low-resistive layer is present in the hilly area and the transition zone, evidenced from geophysical measurements. The layer also has high natural gamma activity. This is the first time this layer is documented throughout the region. The layer is proposed to be continuous or nearly continuous in the region. It is suggested that the layer may be ejecta from the Cretaceous/Paleogene Chicxulub meteorite impact. The dataset thus represents an input to the ongoing discussion on the distribution of the ejecta blanket. Two different conceptual hydrogeological models are proposed, depending on whether the layer is ejecta or rather an unspecified clayey layer, previously unmapped in the region (Fig. 14). The anomalous layer is likely responsible for the formation of local perched aquifers and ephemeral surface water bodies in the region.

The developed conceptual model contributes with new hydrogeological knowledge of the region, and is an important prerequisite for hydrological modelling and sound groundwater management within the study area. The multi-disciplinary methodology applied is applicable for other catchment-scale studies in karst and unmonitored regions.

6. Acknowledgements

We gratefully acknowledge financial support from the WWF Verdensnaturfonden/Aase & Ejnar Danielsens Fond 2006 and 2007, the COWIfoundation, and the Technical University of Denmark. This study would not have been possible without field support (equipment and/or field assistants) from Amigos de Sian Ka'an, UNAM, CICY-CEA, the Geological Survey of Austria and ETH Zürich. We thank CONAGUA for climate data, access to CONAGUA boreholes and for a list of licensed private boreholes in Quintana Roo, which strongly helped us locate useful boreholes for logging. We thank CAPA for access to log the Carrillo Puerto well and for water chemical data from municipal water wells. We thank well operators and private ranch owners for granting us access to sample water from and log in their wells. Oxygen isotope analyses of water samples (results shown in the electronic supplement material) were kindly performed at Centre for Ice and Climate, Niels Bohr Institute, University of Copenhagen, Denmark. We are thankful for the thorough comments from two anonymous reviewers, which greatly improved this manuscript.

7. References

Allen, R.G., Pereira, L.S., Raes, D., Smith, M., 1998. Crop evapotranspiration. Guide-lines for computing crop water requirements. FAO irrigation and drainage paper, 56. Rome, FAO. ISBN 92-5-104219-5.

Anderson, M.C., Norman, J.M. Diak, G.R., Kustas, W.P., Mecikalski, J.R., 1997. A two-source time-integrated model for estimating surface fluxes using thermal infrared remote sensing. Remote Sens. Environ. 60, 195–216.

APHA, 1998a. Method 2320-B. Alkalinity. Titration Method. Standard Methods for the Examination of Water and Wastewater, American Public Health Association. Washington, DC. 20th Edition, pp. 2-27.

APHA, 1998b. Method 2320-B. Sulfate. Turbidimetric Method. Standard Methods for the Examination of Water and Wastewater, American Public Health Association. Washington, DC. 20th Edition, pp. 4-1888.

ASK, 2003. Tratamiento de Aguas Residuales. Report prepared by Amigos de Sian Ka'an A. C. (ASK). Available on the cd-rom of the workshop: Construyendo las Bases Para la Conservación del Agua y su Biodiversidad Asociada en la Península de Yucatan". 10 y 11 de noviembre 2003, Cancún Quintana Roo, Organizado por Amigos de Sian Ka'an, The Nature Conservancy y la Comisión de Áreas Naturales Protegidas.

Back, W., Hanshaw, B.B., 1970. Comparison of chemical hydrogeology of the carbonate peninsulas of Florida and Yucatan. J. Hydrol. 10, 330–368.

Beach, T., Luzzadder-Beach, S., Dunning, N., Cook, D., 2008. Human and natural impacts on fluvial and karst depressions of the Maya Lowlands. Geomorphol. 101, 308–331. doi: 10.1016/j.geomorph.2008.05.019.

Beddows, P.A., 2004. Groundwater hydrology of a coastal conduit carbonate aquifer: Caribbean coast of the Yucatán Peninsula, México. PhD thesis. Sch. of Geogr. Sci.. Univ. of Bristol, UK.

Beddows, P.A., Smart, P.L., Whitaker, F.F., Smith, S.L., 2007. Decoupled fresh-saline groundwater circulation of a coastal carbonate aquifer: Spatial patterns of temperature and specific electrical conductivity. J. Hydrol. 346, 18–32. doi: 10.1016/j.jhydrol.2007.08.013.

Brunner, P., Bauer, P., Eugster, M., Kinzelbach, W., 2004. Using remote sensing to reginalize local precipitation recharge rates obtained from the Chloride Method. J. Hydrol. 294, 241–250.

Butterlin, 1958. Reconocimiento geologico preliminary del territorio de Quintana Roo. Bol. de la Asoc. Mex. de Geólog. Petroleros 10, 531–570.

Eamus, D., Froend, R., 2006. Groundwater-dependent ecosystems: the where, what and why of GDEs. Aust. J. of Bot. 54, 91–96.

Effersø, F., Auken, E., Sørensen, K.I., 1999. Inversion of band-limited TEM responses. Geophys. Prospect. 47 (4), 551–564.

Escolero, O.A., Marín, L.E., Steinich, B., Pacheco, J., 2000. Delimitation of a hydrogeological reserve for a city within a karstic aquifer: the Merida, Yucatan example. Landsc. and Urban Plan. 51, 53–62.

Fideicomiso para la Promoción Turística de la Rivera Maya, 2004. Estadísticas de Riviera Maya.

Fouke, B.W., Zerkle, A.L., Alvarez, W., Pope, K.O., Ocampo, A.C., Wachtman, R.J., Grajales Nishimura, J.M., Claeys, P., Fischer, A.G.., 2002. Cathodoluminescence petrography and isotope geochemistry of KT impact ejecta deposited 360 km from the Chicxulub crater, at Albion Island, Belize. Sedimentol. 49, 117–138.

Gischler, E., Gibson, M.A., Oschmann, W., 2008. Giant Holocene freshwater microbialites, Laguna Bacalar, Quintana Roo, Mexico. Sedimentol. 55, 1293–1309.

Goldman, M., Gilad, D., Ronen, A., Melloul, A., 1991. Mapping of seawater intrusion into the coastal aquifer of Israel by the time domain electromagnetic method. Geoexplor. 28 (2), 153–174. doi: 10.1016/0016-7142(91)90046-F.

Gondwe, B.R.N., Hong, S.-H., Wdowinski, S., Bauer-Gottwein, P., 2010. Hydrologic dynamics of the ground-water-dependent Sian Ka'an wetlands, Mexico, derived from InSAR and SAR data. Wetl. (in press).

Gondwe, B.R.N., Ottowitz, D., Supper, R., Merediz Alonzo, G., Bauer-Gottwein, P., (in prep.). Exploring regional-scale preferential flow paths in the karst aquifer of southern Quinana Roo, Mexico. (in prep.)

González-Herrera, R, Sánchez-y-Pinto, I., Gamboa-Vargas, J., 2002. Groundwater-flow modeling in the Yucatan karstic aquifer, Mexico. Hydrogeol. J. 10, 539–552.

Gorohkhovich, Y., Voustianiouk, A., 2006. Accuracy assessment of the processed SRTM-based elevation data by CGIAR using field data from USA and Thailand and its relation to the terrain characteristics. Remote Sens. Environ. 104, 409–415.

Grajales-Nishimura, J.M., Cedillo-Pardo, E., Rosales-Domínguez, C., Morán-Zenteno, D.J., Alvarez, W., Claeys, P., Ruíz-Morales, J., García-Hernández, J., Padilla-Avila, P., Sánchez-Ríos, A., 2000. Chicxulub impact: the origin of reservoir and seal facies in the southeastern Mexico oil fields. Geol. 28 (4), 307–310.

Graniel, C. E., Morris, L. B., Carrillo-Rivera, J.J., 1999. Effects of urbanization on groundwater resources of Merida, Yucatan, Mexico. Environmental Geology, 37 (4), 303–312.

Gunn, J.D., Foss, J.E., Folan, W.J., Carrasco, M.R.D., Faust, B.B., 2002. Bajo sediments and the hydraulic system of Calakmul, Campeche, Mexico. Anc. Mesoam 13, 297–315.

Hanshaw, B.B., Back, W.,1980. Chemical mass-wasting of the northern Yucatan Peninsula by groundwater dissolution. Geology, 8, 222-224.

Hargreaves, G.H., Samani, Z.A., 1985. Reference crop evapotranspiration from temperature. Appl. Eng. in Agric. 1 (2), 96–99.

HGG, Denmark, 2001. SEMDI Version 3.1.14.88. Software for geophysical inversion of time-domain electromagnetic measurements. HydroGeophysics Group, Aarhus, Denmark.

HGG, Denmark 2007 SiTEM Version 3.1.13.86. Software for processing of time-domain electromagnetic measurements. HydroGeophysics Group, Aarhus, Denmark.

Hildebrand, A.R., Penfield, G.T., Kring, D.A., Pilkington, M., Camargo Z., A., Jacobsen, S.B., Boynton, W.V., 1991. Chicxulub crater: A possible Cretaceous/Tertiary boundary impact crater on the Yucatan Peninsula, Mexico. Geol. 19, 867–871.

INEGI, 1997. Carta de uso de suelo y vegatación (vegetation map). Recursos electónicos. Escala 1:250,000. Instituto Nacional de Estadística Geogrfía e Informática (INEGI). Shape file.

Jiang, L., Islam, S., 1999. A methodology for estimation of surface evapotranspiration over large areas using remote sensing observations. Geophys. Res. Letters 26, 2773–2776.

Jiang, L., Islam, S., 2001. Estimation of surface evaporation map over southern Great Plains using remote sensing data. Water Resour. Res. 37 (2), 329–340.

Kenkmann, T., Schönian, F., 2006. Ries and Chicxulub: Impact craters on Earth provide insights for Martian ejecta blankets. Meteorics and Planet. Sci. 41 (10), 1587–1603.

Kilroy. G., Coxon, C., Ryan, J., O'Connor, A., Daly, D., 2005. Groundwater and wetland management in the Shannon river basin (Ireland). Environ. Sci. & Policy 8, 219–225.

Kiraly, L., 2003. Karstification and groundwater flow. Speleogenesis and Evolut. of Karst Aquifers 1 (3). 26 pp.

Klimchouk, A.B., 1997. The role of karst in the genesis of sulfur deposits, Pre-Carpathian region, Ukraine. Environ. Geol. 31 (1/2), 1–20.

Kocak, G., Buyuksalih, G.,Oruc, M., 2005. Accuracy assessment of interferometric digital elevation models derived from the Shuttle Radar Topography Mission X- and C-band data in a test area with rolling topography and moderate forest cover. Opt. Eng. 44 (3), 036201.1-036201.7.

Krause, S., Heathwaite, A.L., Miller, F., Hulme, P., Crowe, A., 2007. Groundwater-dependent wetlands in the UK and Ireland: controls, functioning and assessing the likelihood of damage from human activities. Water Resour. Manage. 21, 2015–2025. doi: 10.1007/s11269-007-9192-x.

Krekeler, M.P.S., Probst, P., Samsonov, M., Tselepis, C.M., Bates, W., Kearns, L.E., Barry Maynard, J., 2007. Investigations of subsurface flow constructed wetlands and associated geomaterial resources in the Akumal and Reforma regions, Quintana Roo, Mexico. Environ. Geol. 53, 709–726. doi: 10.1007/s00254-007-0684-z.

Kustas, W.P., Daughtry, C.S.T., Van Oevelen, P.J., 1993. Analytical treatment of the relationships between soil heat flux7net radiation ratio and vegetation indices. Remote Sens. Environ. 46, 319–330.

Lefticariu, M., Perry, E.C., Ward, W.C., Lefticariu, L., 2006. Post-Chicxulub depositional and diagenetic history of the northwestern Yucatan Peninsula, Mexico. Sediment. Geol. 183, 51–69.

Lesser, J. M., 1976. Estudio hidrogeologico e hidrogeoquimico de la Peninsual de Yucatan. Proyecto Conacyt-NSF 704, Secretaria de Recursos Hidraulicos, Direccion de Geohidrologia y Zonas Aridas, Mexico. 64 p.

Loftus, W.F., Bruno, M.C., Cunningham, K.J., Perry, S., Trexler, J.C., 2001. The ecological role of the karst wetlands of Southern Florida in relation to system restoration. In Kuniansky, E. (Ed.). Water-Resources Investigations Report 01-4011, U.S. Geological Survey. 8–15.

Lopez-Ramos, E., 1975. Geological summary of the Yucatan Peninsula. Chap. 7. In: Nairn, A.E.M., Stehli, F.G. (Eds.) The ocean basins and margins. Vol. 3 The Gulf of Mexico and the Caribbean. Plenum Press, NY, USA.

Marfia, A.M., Krishnamurthy, R.V., Atekwana, E.A., Panton, W.F., 2004. Isotopic and geochemical evolution of ground and surface waters in a karst dominated geological setting: a case study from Belize, Central America. Appl. Geochem. 19, 937–946.

Marín, L.E., 1990. Field investigations and numerical simulation of ground-water flow in the karstic aquifer of northwestern Yucatan, Mexico. PhD thesis. Dept. of Geol., North. Ill. Univ., USA.

Marín, L.E., Steinich, B., Pacheco, J. Escolero, O.A., 2000. Hydrogeology of a contaminated sole-source karst aquifer, Mérida, Yucatán, Mexico. Geofís. Int. 49 (4), 359–365.

Marshall, J.R., Bratton, C., Pope, K.O., Ocampo, A.C., 1998. Diagnostic clast-texture criteria for recognition of impact deposits. Abstract #1134. 29th Annu. Lunar and Planet. Sci. Conf., Houston, TX, USA.

Mayr, S.I., Burkhardt, H., Popov, Y., Wittmann, A., 2008. Estimation of hydraulic permeability considering the micro morphology of rocks of the borehole YAXCOPOIL-1 (Impact crater Chicxulub, Mexico). Int. J. Earth Sci. (Geol. Rundsch.) 97, 385–399.

Mazzotti, F.J., Fling, H.E., Merediz, G., Lazcano, M., Lasch, C., Barnes, T., 2005. Conceptual ecological model of the Sian Ka'an Biosphere Reserve, Quintana Roo, Mexico. Wetl. 25 (4), 980–997.

McNeill, J.D., 1986. Geonics EM39 borehole conductivity meter. Theory of operation. Technical Note TN-20. Geonics Ltd, Ontario, Canada.

Méndez Ramos, R., 1991. Modelo de comportamiento del acuífero de la ciudad de Mérida, Yucatán. Comisión Nacional del Auga, Gerencia Estatal Yucatán, Subgerencia de Administración del Agua, Mérida, Yucatán, Mexico.

Monteith, J.L., 1965. Evaporation and environment. Proc. 19th Symp. of the Society of Experimental Biol. New York: Cambridge University Press.

Moore, Y.H., Stoessell, R.K., Easley, D.H., 1992. Fresh-water/sea-water relationship within a ground-water flow system, northeastern coast of the Yucatan Peninsula. Ground Water 30 (3), 343–350.

Morales Barbosa, J.J., 1992. Los humedales, un mundo olvidado. Series: Sian Ka'an, Introducción a los Ecosistemas de la Península de Yucatan. Amigos de Sian Ka'an A. C. Impresos MARCA, Mérida, Yucatán, Mexico.

Münch, Z., Conrad, J., 2007. Remote sensing and GIS based determination of groundwater dependent ecosystems in the Western Cape, South Africa. Hydrogeol. J. 15, 19–28. doi: 10.1007/s10040-006-0125-1.

Munkholm M.S. and Auken E., 1996. Electromagnetic noise contamination on transient electromagnetic soundings in culturally disturbed environments. J. of Environ. and Eng. Geophys. 1, 119–127.

NASDA/NASA, 2008. Tropical Rainfall Measuring Mission (TRMM), data products 3B42 and 3B43. TRMM algorithms were developed by the TRMM Science Team. TRMM data were processed by the TRMM Science Data and Information System (TSDIS) and the TRMM Office; archived and distributed by the Goddard Distributed Active Archive Center. TRMM is an international project jointly sponsored by the Japan National Space Development Agency (NASDA) and the U.S. National Aeronautics and Space Administration (NASA) Office of Earth Sciences.

Neuman, B.R., Rahbek, M.L., 2007. Modeling the groundwater catchment of the Sian Ka'an Reserve, Quintana Roo. Assoc. for Mex. Cave Stud.. Bull. 18. AMCS bulletin publication. Austin, TX, USA.

Ocampo, A.C., Pope, K.O., Fischer, A.G., 1996. Ejecta blanket deposits of the Chicxulub crater from Albion Island, Belize. p. 75–88. In: Ryder, G., Fastovsky, D., Gartner, S. (Eds.) The Createaceous-Tertiary event and other catastrophes in Earth history. Geol. Soc. Am. Spec. Pap. 307.

Pacheco, J., Marín, L., Cabrera, A., Steinich, B., Escolero, O., 2001. Nitrate temporal and spatial Patterns in 12 water-supply wells, Yucatan, Mexico. Environ. Geology 40 (6), 708–715.

Parkhurst, D.L., and Appelo, C.A.J., 1999. User's guide to PHREEQC (version 2)– A computer program for speciation, reactionpath, 1D-transport, and inverse geochemical calculations: U.S. Geol. Surv. Water-Resour. Investig. Rep. 99-4259.

Perry, E., Swift, J., Gamboa, J., Reeve, A., Sanborn, R., Marín, L, Villasuso, M., 1989. Geologic and environmental aspects of surface cementation, north coast, Yucatan, Mexico. Geol. 17, 818–821.

Perry, E.C., Marín, L.E., McClain, J., Velazquez, G., 1995. The Ring of Cenotes (sinkholes) northwest Yucatan, Mexico: Its hydrogeologic characteristics and association with the Chicxulub Impact Crater. Geol. 23, 17–20.

Perry, E., Velazquez-Oliman, G., Marin, L., 2002. The hydrogeochemistry of the karst aquifer system of the northern Yucatan Peninsula, Mexico. Int. Geol. Rev. 44, 191–221.

Perry, E., Paytan, A., Pedersen, B., Velazquez-Oliman, G., 2009. Groundwater geochemistry of the Yucatan Peninsula, Mexico: constraints on stratigraphy and hydrogeology. J. Hydrol. 367 (1–2), 27–40. doi: 10.1016/j.jhydrol.2008.12.026.

Perry, E., Velazquez Oliman, G., Wagner, N. Geoquímica del agua subterránea y superficial en la península de Yucatán. Retos de la Investigación del Agua en México. In press.

Pope, K.O., Dahlin, B. H., 1989. Ancient Maya wetland agriculture: new insights from ecological and remote sensing research. J. of Field Archeol. 16 (1), 87–106.

Pope, K.O., Ocampo, A.C., Duller, C.E., 1991. Mexican site for K/T impact crater? Nat. 351, 105.

Pope, K.O., Ocampo, A.C., Fischer, A.G., Vega, F.J., Ames, D.E., King Jr., D.T., Fouke, B.W., Wachtman, R.J., Kletetschka, G., 2005. Chicxulub impact ejecta deposits in southern Quintana Roo, México, and central Belize. p. 171–190. In: Kenkmann, T., Hörz, F., Deutsch, A. (Eds.) Large meteorite impacts III. Geol. Soc. Am. Spec. Pap. 384.

Priestley, C.H.B., Taylor, R.J., 1972. On the assessment of surface heat flux and evaporation using large scale parameters. Monthly Weather Review 100, 81–92.

Rebolledo-Vieyra, M., Urrutia-Fucugauchi, J., Marín, L.E., Trejo-García, A., Sharpton, V.L., Soler-Arechalde, A.M., 2000. UNAM scientific shallow-drilling program of the Chicxulub impact crater. Int. Geol. Rev. 42, 928–940.

Sánchez-Sánchez, O., Islebe G.A., 2002. Tropical forest communities in south eastern Mexico. Plant Ecol. 158, 183–200.

Schönian, F., Stöffler, D., Kenkmann, T., Wittmann, A., 2004. The fluidized Chicxulub ejecta blanket, Mexico: Implications for Mars. Poster, 35th Annu. Lunar and Planet. Sci. Conf., Leag. City, TX, USA.

Schönian,F., Tagle, R., Stöffler, D., Kenkmann, T., 2005. Geology of southern Quintana Roo (Mexico) and the Chicxulub ejecta blanket. Abstract #2389. 36th Annu. Lunar and Planet. Sci. Conf., Leag. City, TX, USA.

SGM, 2007. Carta geológica de México. Escala 1:2,000,000. 6a edición. Servicio Geológico Mexicano (SGM).

Smart, P.L., Beddows, P.A., Coke, J., Doerr, S., Smith, S., Whitaker, F.F., 2006. Cave development on the Caribbean coast of the Yucatan Peninsula, Quintana Roo, Mexico. In: Harmon, R.S., Wicks, C. (Eds.) Perspectives on karst geomorphology, hydrology and geochemistry – A tribute volume to Derek C. Ford and William B. White. Geol. Soc. Am.. Spec. Pap. 404, 105–128.

Steinich, B., Marín, L.E., 1996. Hydrogeological investigations in northwestern Yucatan, Mexico, using resistivity surveys. Ground Water 34 (4), 640–646.

Steinich, B., Marín, L.E., 1997. Determination of flow characteristics in the aquifer of the Northwestern Peninsula of Yucatan, Mexico. J. Hydrol. 191, 315–331.

Stisen, S., Sandholt, I., Nørgaard, A., Fensholt, R., Høegh Jensen, K., 2008. Combining the triangle method with thermal intertia to estimate regional evapotranspiration – Applied to MSG-SEVIRI data in the Senegal River basin. Remote Sens. Environ. 112, 1242–1255.

Stoessell. R. et al., no year. Yucatan water chemistry collected by Ronald Stoessell and co-workers. Data from 1980s to 1990s. Publicly available at http://www.ronstoessell.org/Stoessell_Yucatan.pdf. Accessed Jan 2009.

Thomas, C., 1999. Aspects hydrologiques du Yucata (Mexique). Karstologia 34, 9–22.

Trimble, 2003 .Trimble Total Control Version 2.73. Software for GPS data processing.

Tun-Dzul, F.J., Vester, H., García, R.D., Schmook, B., 2008. Estructura arbórea y variabilidad temporal del NDVI en los "bajos inundables" de la Península de Yucatán, México. Polibotánica 25, 69–90.

USGS, 2006. Shuttle Radar Topography Mission, 3 Arc Second, Finished 2.0. Global Land Cover Facility, University of Maryland, College Park, MD, USA. Accessed 15 June 2006.

Urrutia-Fucugauchi, J., Marin, L., Trejo-Garcia, A., 1996. UNAM Scientific drilling program of Chicxulub impact structure: Evidence for a 300 kilometer crater diameter. Geophys. Res. Lett. 23(13), 1565–1568.

Urrutia-Fucugauchi, J., Morgan, J., Stöffler, D., Claeys, P., 2004. The Chicxulub Scientific Drilling Project (CSDP). Meteorics and Planet. Sci. 39 (5), 787–790.

Urrutia-Fucugauchi, J., Chavez-Aguirre, J.M., Pérez-Cruz, L., De la Rosa, J.L., 2008. Impact ejecta and carbonate sequence in the eastern sector of the Chicxulub crater. C. R. Geosci. 340, 801–810.

Vacher, H.L., 1988. Dupuit-Ghyben-Herzberg analysis of strip-island lenses. Geol. Soc. Am. Bull. 100 (4), 580–591.

Van der Veer, P., 1977. Analytical solution for steady interface flow in a coastal aquifer involving a phreatic surface with precipitation. J. Hydrol. 34, 1–11.

Wang, K., Li, Z., Cribb, M., 2006. Estimation of evaporative fractin from a combination of day and night land surface temperatures and NDVI: A new method to determine the Priestley–Taylor parameter. Remote Sens. Environ. 102, 293–305.

Weidie, A.E., 1985. Geology of Yucatan Platform. p. 1–12. In: Ward, W.C., Weidie, A.E., Back, W. (Eds.) Geology and hydrogeology of the Yucatan and Quaternary geology of northeastern Yucatan Peninsula. New Orleans Geol. Soc. Publ., New Orleans, LA, USA.

Weydahl, D.J., Sagstuen, J., Dick, Ø.B., Rønning, H., 2007. SRTM DEM accuracy assessment over vegetated areas in Norway. Int. J. Remote Sens. 28 (16), 3513–3527.

Wicks, C.M., Herman, J.S., 1995. The effect of zones of high porosity and permeability on the configuration of the saline-freshwater mixing zone. Ground Water 33 (5), 733–740.

Wohlgemuth, L., Bintakies, E., Kück, J., Conze, R., Harms, U., 2004. Integrated deep drilling, coring, downhole logging, and data management in the Chicxulub Scientific Drilling Project (CSDP), Mexico. Meteorics and Planet. Sci. 39 (6), 791–797.

Wolfe, W.J., 1996. Hydrology and tree-distribution patterns of karst wetlands at Arnold Engineering Development Center, Tennessee. Water-Resources Investigations Report 96–4277. United States Geological Survey. Nashville, Tennessee. 50 pp.

Wolff, D.B., Marks, D.A., Amitai, E., Silberstein, D.S., Fisher, B.L., Tokay, A., Wang, J., Pippit, J.L., 2005. Ground validation for the Tropical Rainfall Measuring Mission (TRMM). J. Atmos. and Ocean. Technol. 22, 365–380.

Figure captions

Fig. 1 Geology of the Yucatan Peninsula, modified from SGM (2007). Oldest sediments dated as Cretaceous instead of Paleocene, based on Schönian (2005) and Lopez-Ramos (1975) (Ichaiche Formation). Topography from SRTM (USGS, 2006) overlain as grey-scaled transparent. Study area outlined with thick grey polygon. Coordinates are UTM zone 16N, WGS84 datum and ellipsoid

Fig. 2 a), b) and c): Water levels measured in the dry season (Feb) 2008, interpolated using Natural Neighbor algorithm. (a+b) include the points believed to be perched water; (c) excludes these points. The different legends of (a) and (b) are made to more clearly show the overall regional water level differences in the hilly area, and in the flat area, respectively. Water levels refer to meters above mean sea level, and measured values are labeled in b). The "Perched?" label in a) indicates localities with possibly perched aquifers. d): Water level changes between the dry (Feb) and the wet (Nov-Dec) season 2008, given in meters. Positive values indicate an increase in water levels from the dry to the wet season

Fig. 3 Hydrographs from a) Presidente Juarez, b) Dzula and c) Petcacab, measured with pressure transducers. Mean daily precipitation in the study area is given in every figure along with daily precipitation over the locality itself. Precipitation derived from TRMM 3B42 3-hr product (NASDA/NASA 2008)

Fig. 4 a) Depth to halocline measured with TEM as a function of distance from coast. Grey line indicates best fit of the Dupuit-Ghyben-Herzberg model to data. b) Depth to halocline as a function of measured water levels, both with respect to mean sea level. Best linear regression curve shown as bold black line

Fig. 5 Geological models inverted from TEM data. a) shows the expected model, with only three layers, found in the flat area; b), c) and d) exemplify the locations where a shallow anomalous layer was found. Depth refers to depth below ground surface

Fig. 6 a) Elevation of the anomalous layer from TEM measurements and borehole logs. Surface elevation also shown, along with the max. measurement depth of the measurements which did not find the anomalous layer. Location of presumed Cretaceous coastline indicated, characterized by steep drop in elevation from 50 mamsl to <40 mamsl over less than one kilometer; b) Location of TEM and logging measurements, with indications of which encountered the anomalous layer (green), which did not (red) and which were too noisy in the first gates to determine this (yellow). Background is SRTM topography, F = flat area, H = hilly area

Fig. 7 Example results from the borehole logging. a) and b) represent typical results from the flat area (no anomalous layer detected). d) through f) show the logs with the anomalous layer detected. Results from remaining wells with anomalous layer given in the Electronic supplementary material. SEC: specific electrical conductivity of the well fluid - its top indicates location of water table. Location map at top right

Fig. 8 a) Molal ratio of 1000·Sr/Cl vs. 1/Sr in L/mmol. b) Histogram of Cl/Na ratio (in equivalents). If the water obtained its Cl from saltwater or halite, this ratio would be between 1 an d 1.17, a criteria only fulfilled by 6 samples

Fig. 9 a) Sr-concentration vs. SO_4-concentration, along with linear fit (bold black line and equation given) and the distribution for seawater (grey line). b) Sr-concentration vs. Cl-concentration, along with the distribution typical for seawater (grey line)

Fig. 10 Spatial distribution within the study area of a) 100·SO_4/Cl-ratios (in equivalents), b) Gypsum saturation indices,and c) SO_4-concentrations (meq/L). The ten small grey dots indicate results from Perry et al. (2002) (mainly) and Stoessell (no year) (only Chumkopo site)

Fig. 11 a) Ca, Mg and (Ca+Mg) concentrations vs. SO_4-concentrations (meq/L), b), c) and d): Gypsum, celestite and anhydrite saturation indices (no unit) vs. SO_4-concentrations (mmol/L)

Fig. 12 a) ET_a temporal daily variation; b) ET_a spatial variation (average of years 2004-2008). a) also includes ET_{ref} estimated using Hargreave's equation, and monthly average precipitation from TRMM

Fig. 13 Recharge, calculated as mean annual precipitation subtracted ET_a (both average of 2004–2008); a) temporal variation, displayed together with average Peninsula precipitation from TRMM and calculated ET_a, b) spatial variation (mm/day)

Fig. 14 Conceptual model with the anomalous layer interpreted as ejecta

Figures

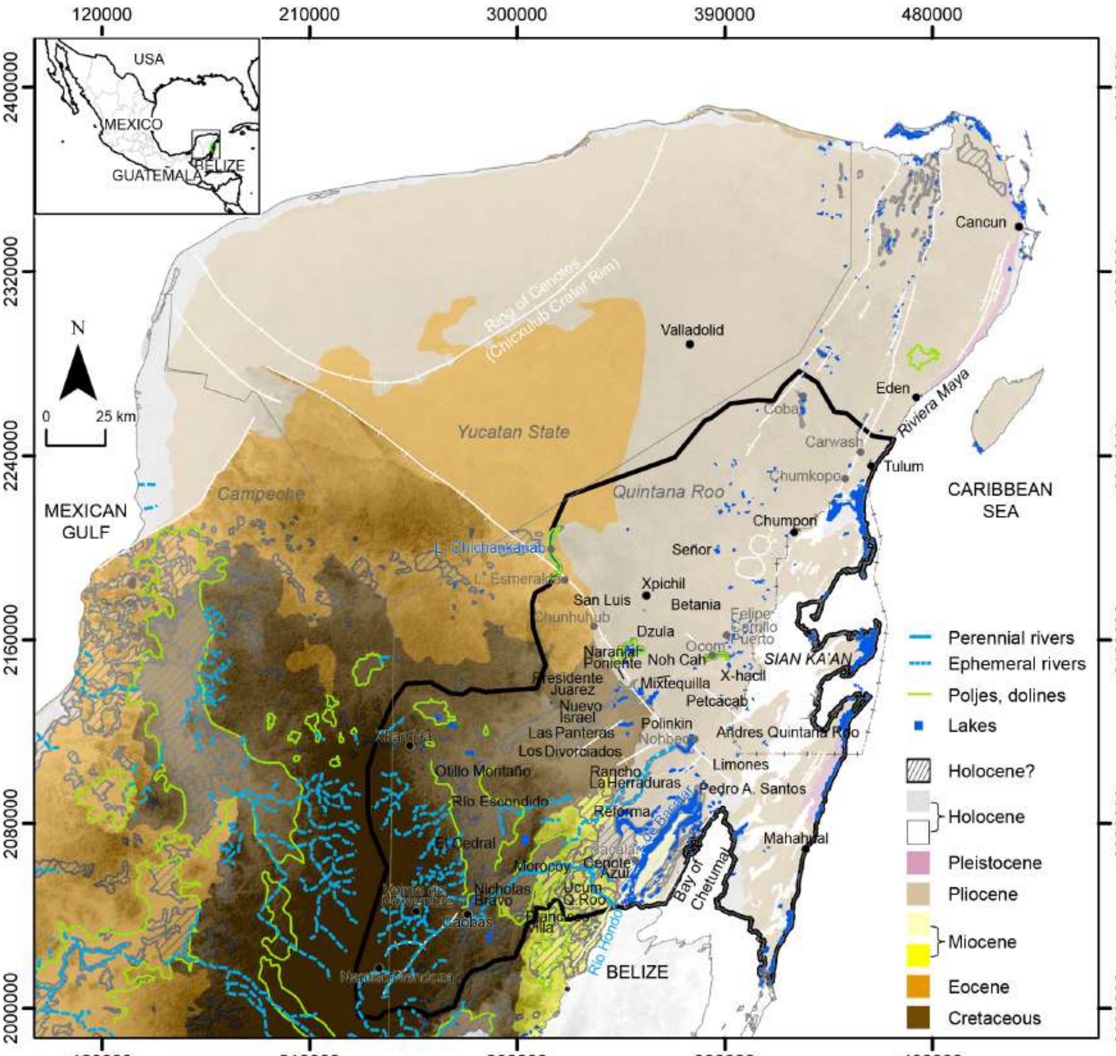

Fig. 1

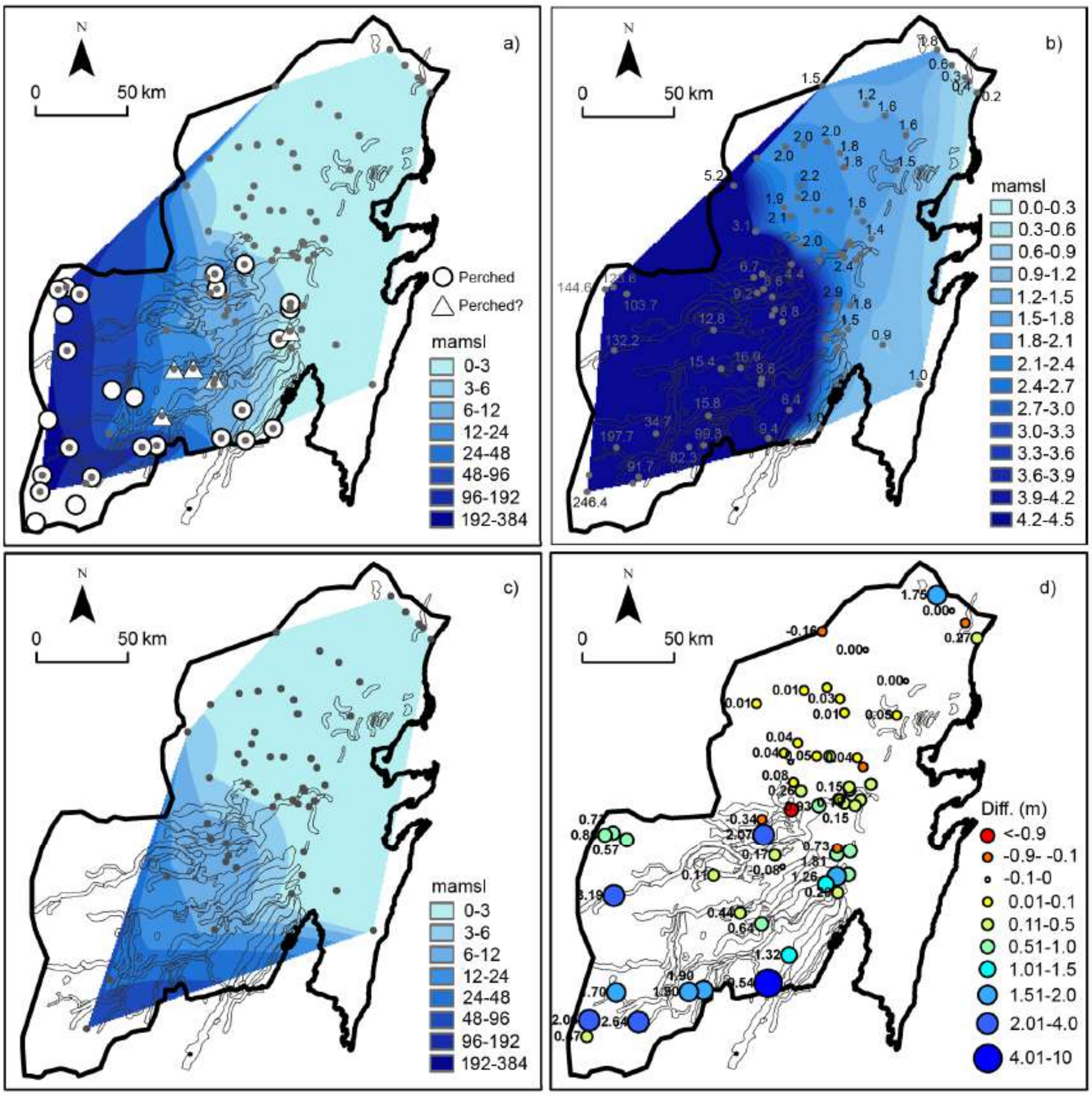

a)
b)
c)
d)
0
50 km
Perched
Perched?
mamsl
0-3
3-6
6-12
12-24
24-48
48-96
96-192
192-384
0.0-0.3
0.3-0.6
0.6-0.9
0.9-1.2
1.2-1.5
1.5-1.8
1.8-2.1
2.1-2.4
2.4-2.7
2.7-3.0
3.0-3.3
3.3-3.6
3.6-3.9
3.9-4.2
4.2-4.5
Diff. (m)
<-0.9
-0.9- -0.1
-0.1-0
0.01-0.1
0.11-0.5
0.51-1.0
1.01-1.5
1.51-2.0
2.01-4.0
4.01-10

Fig. 2

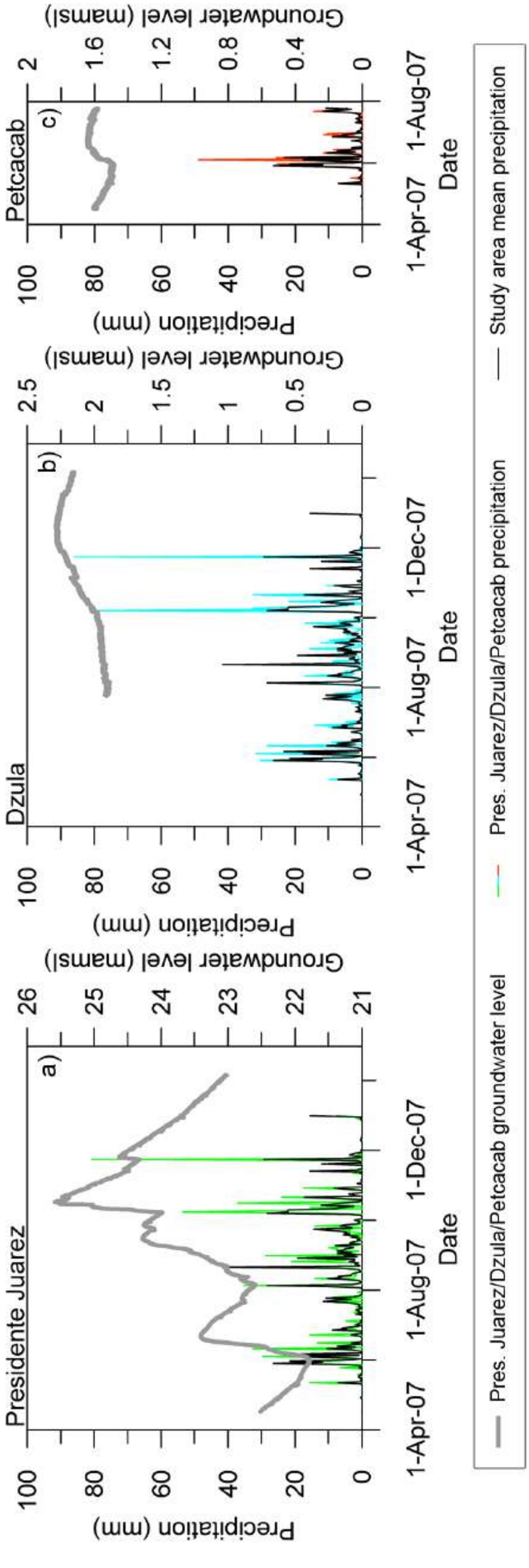

Fig. 3 (rotated 90 degrees)

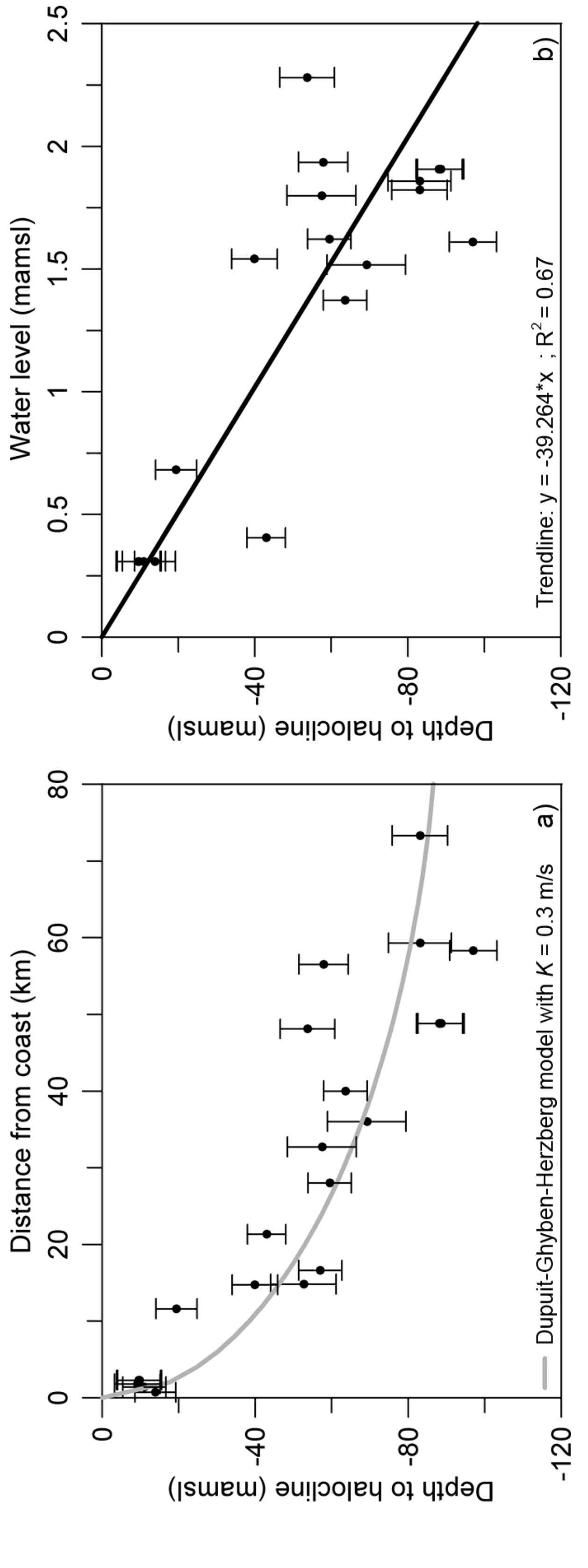

Fig. 4 (rotated 90 degrees)

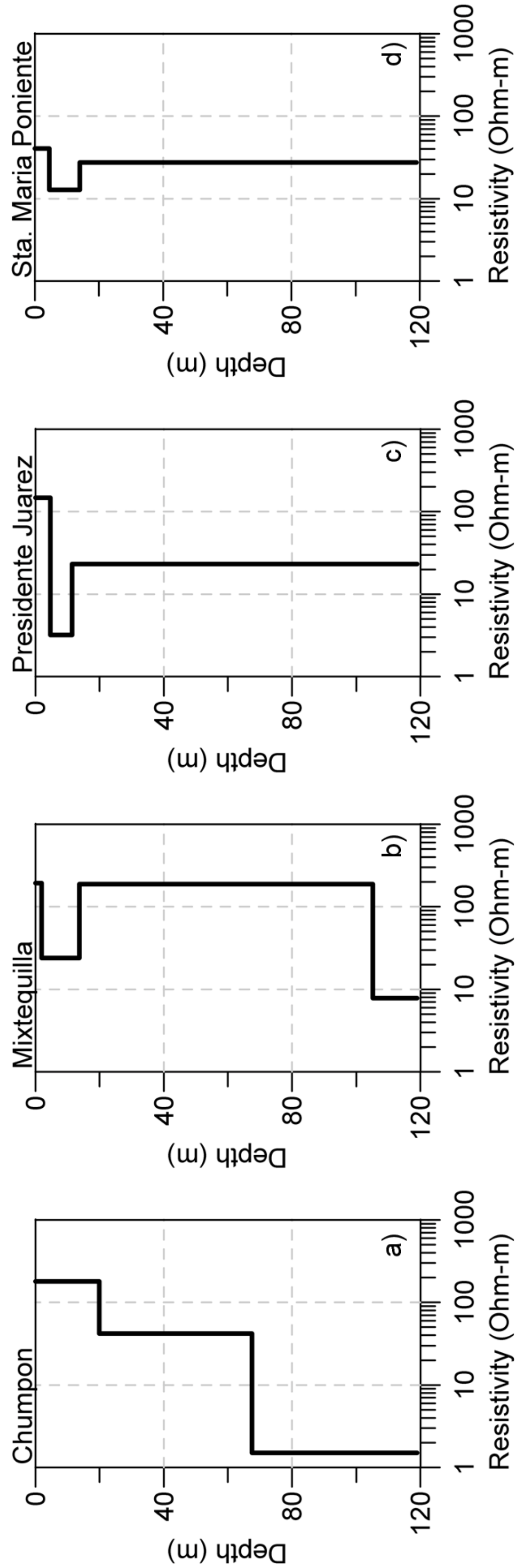

Fig. 5 (rotated 90 degrees)

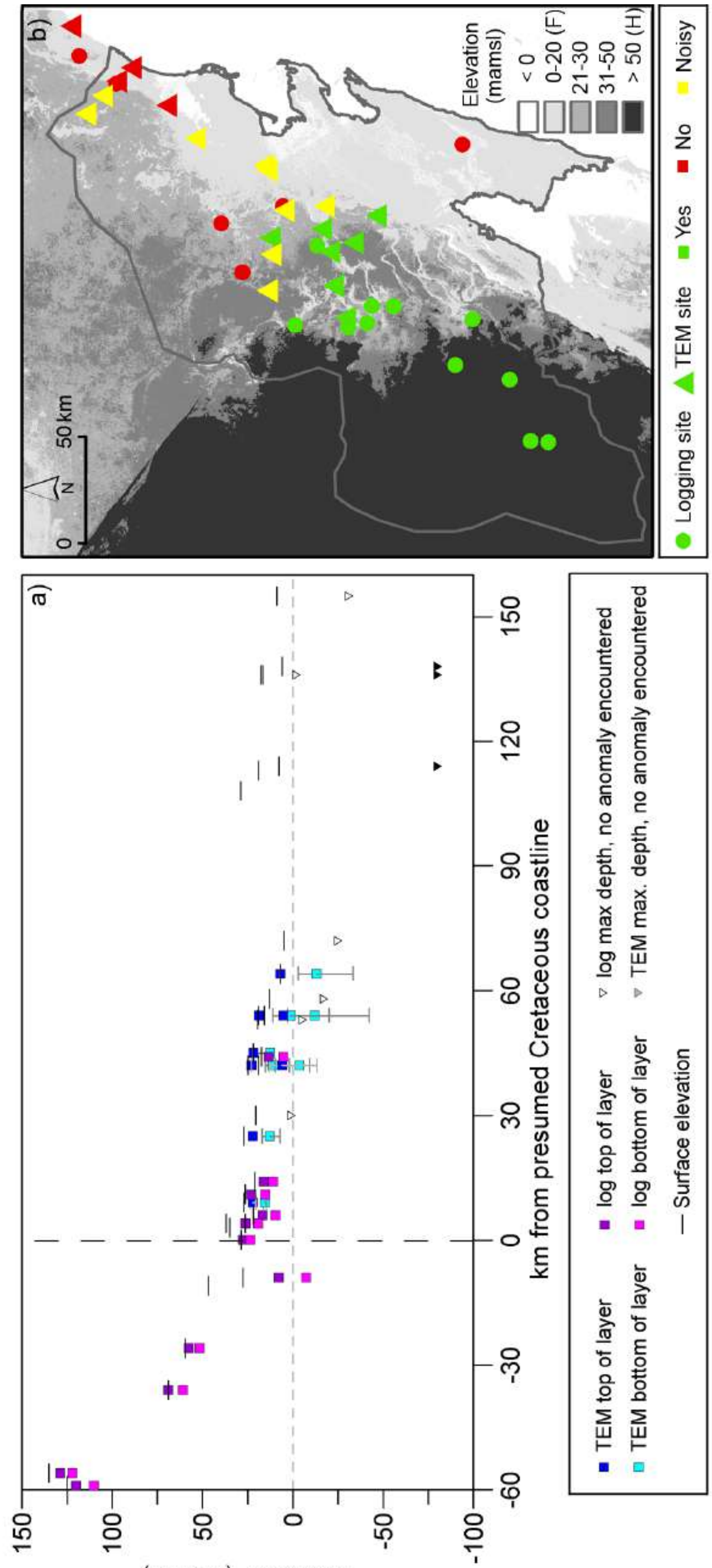

Fig. 6 (rotated 90 degrees)

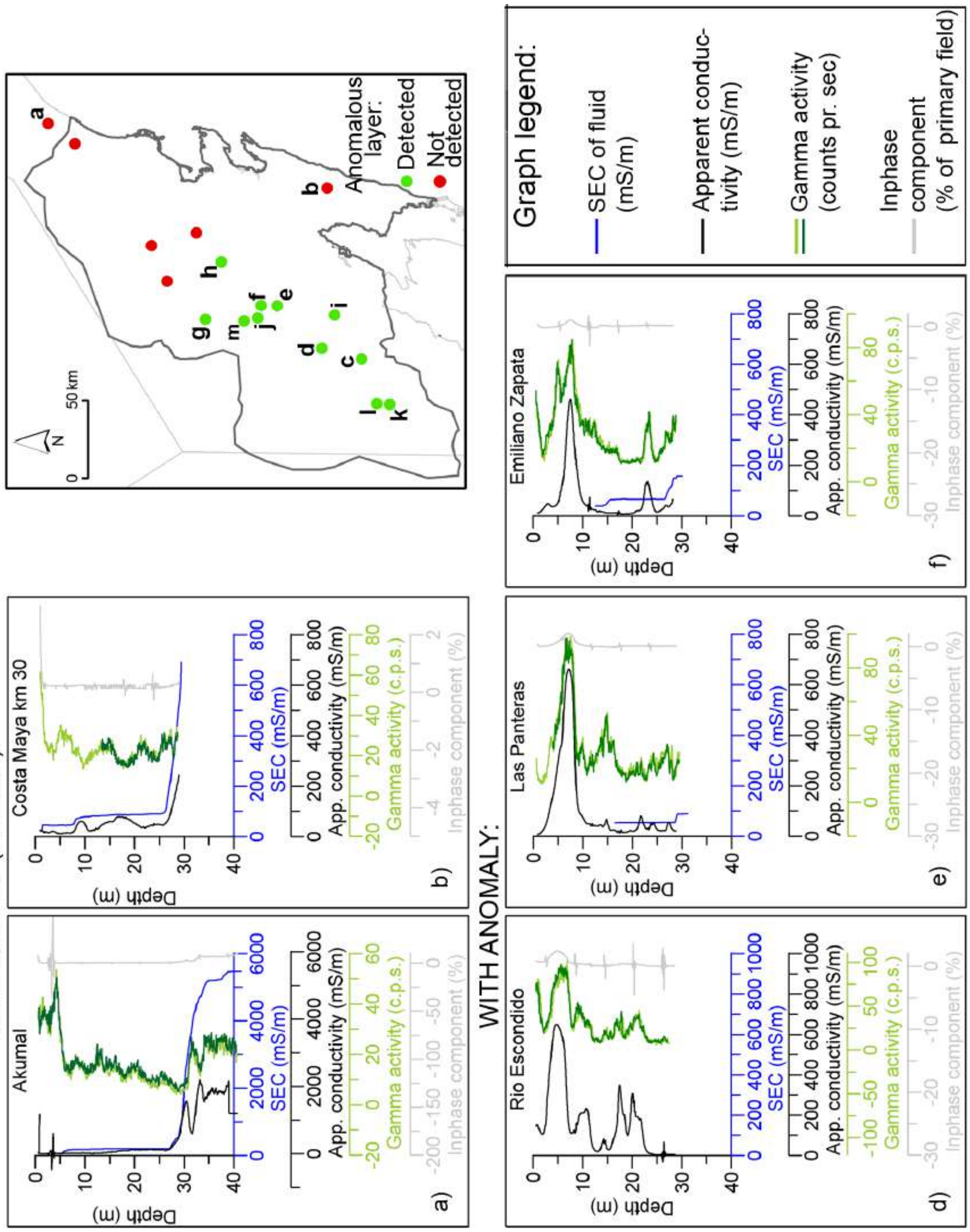

Fig. 7 (rotated 90 degrees)

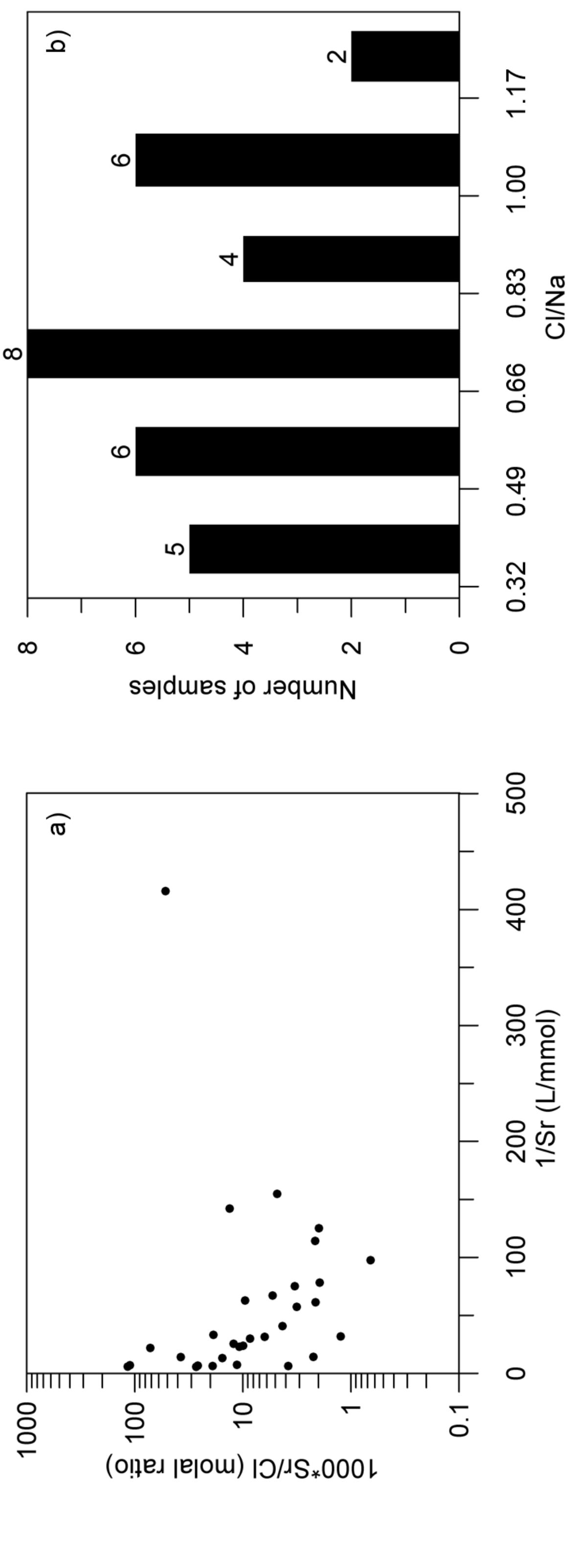

Fig. 8 (rotated 90 degrees)

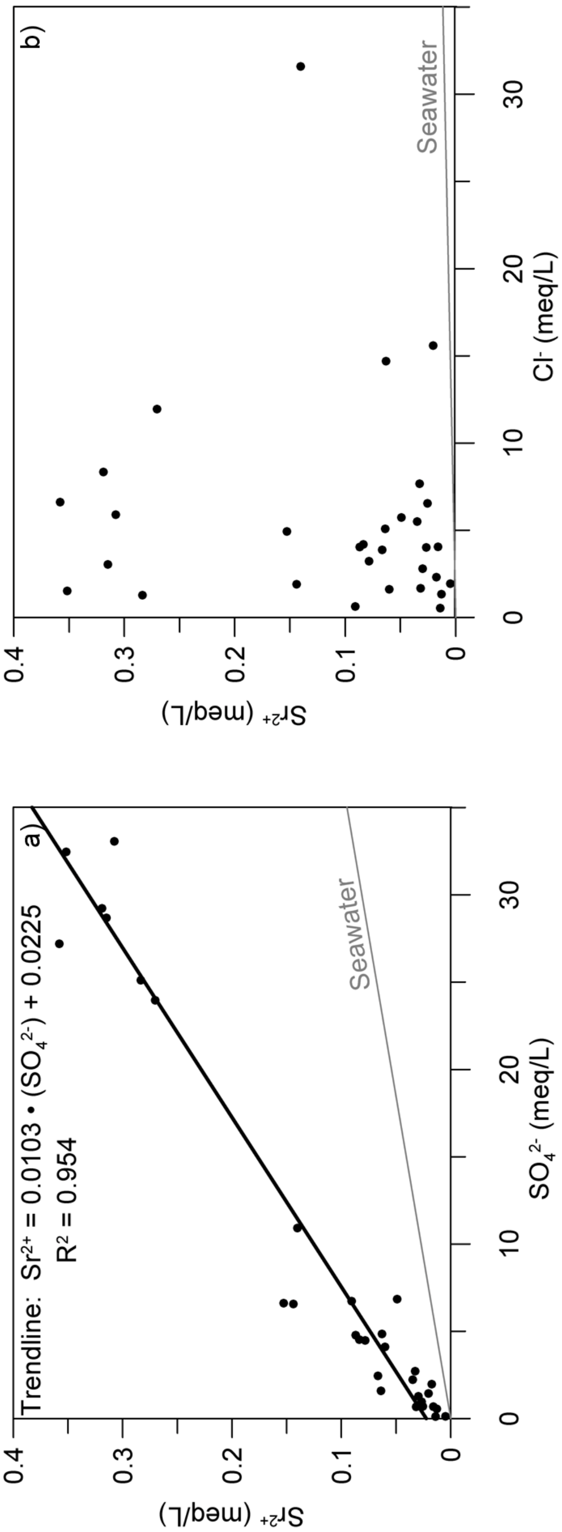

Fig. 9 (rotated 90 degrees)

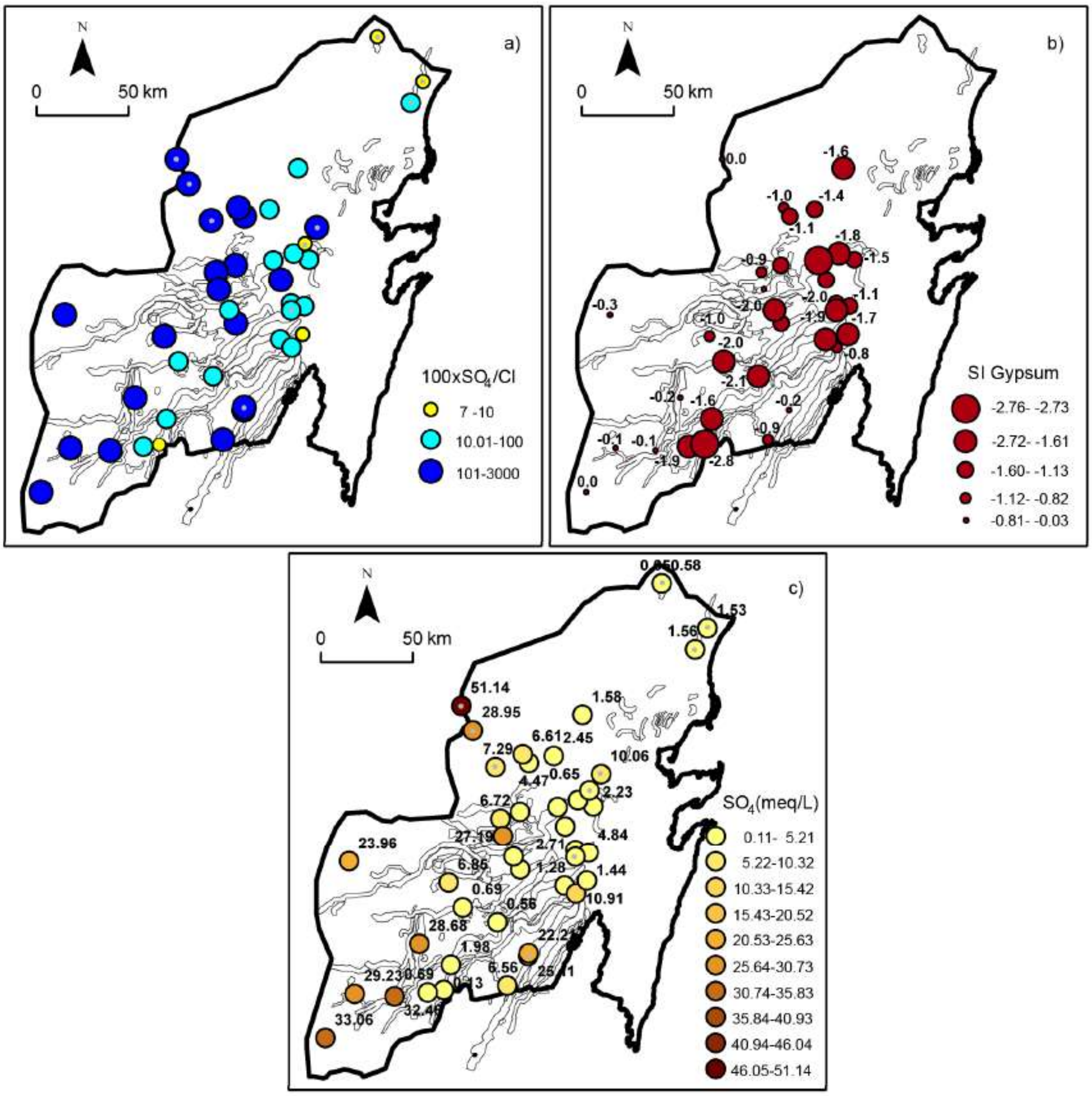

a)
b)
c)
N
0
50 km
100xSO4/Cl
7 -10
10.01-100
101-3000
SI Gypsum
-2.76- -2.73
-2.72- -1.61
-1.60- -1.13
-1.12- -0.82
-0.81- -0.03
SO4(meq/L)
0.11- 5.21
5.22-10.32
10.33-15.42
15.43-20.52
20.53-25.63
25.64-30.73
30.74-35.83
35.84-40.93
40.94-46.04
46.05-51.14

Fig. 10

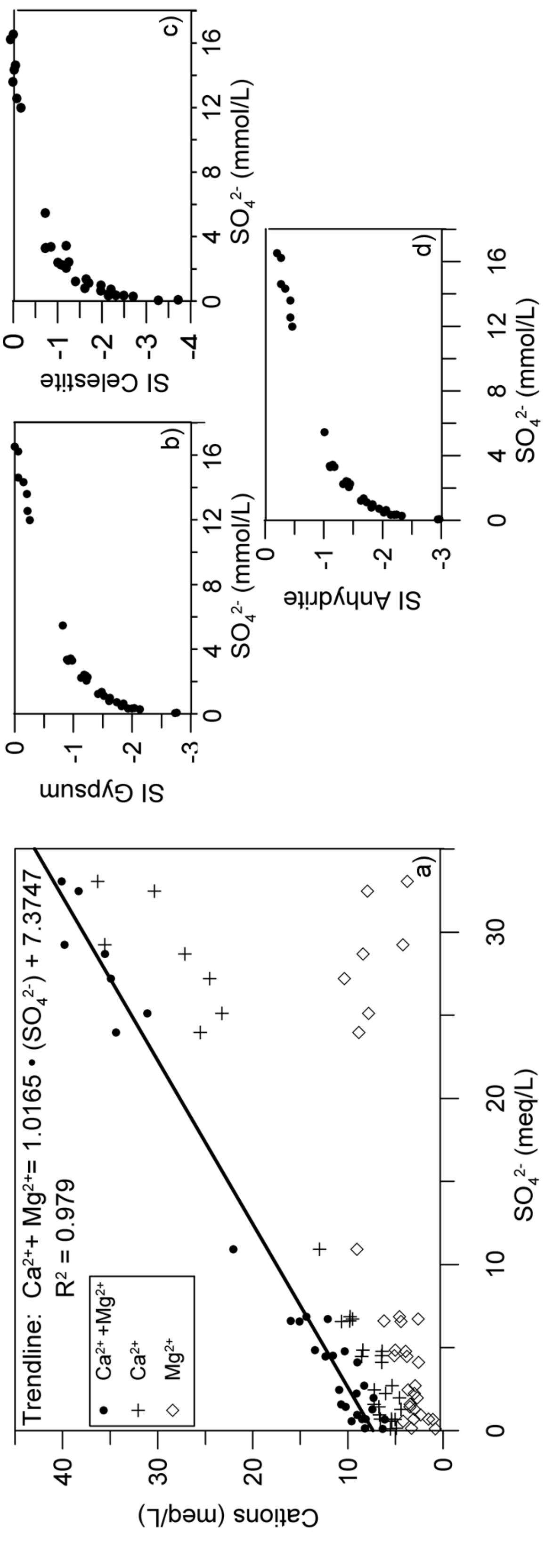

Fig. 11 (rotated 90 degrees)

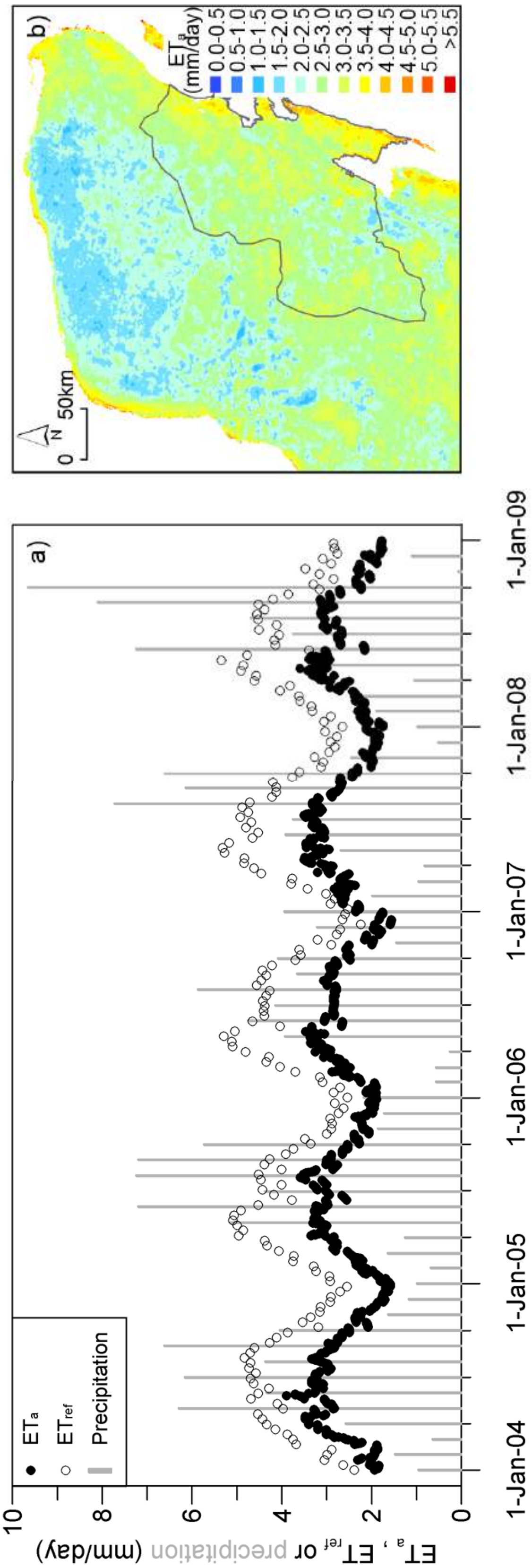

Fig. 12 (rotated 90 degrees)

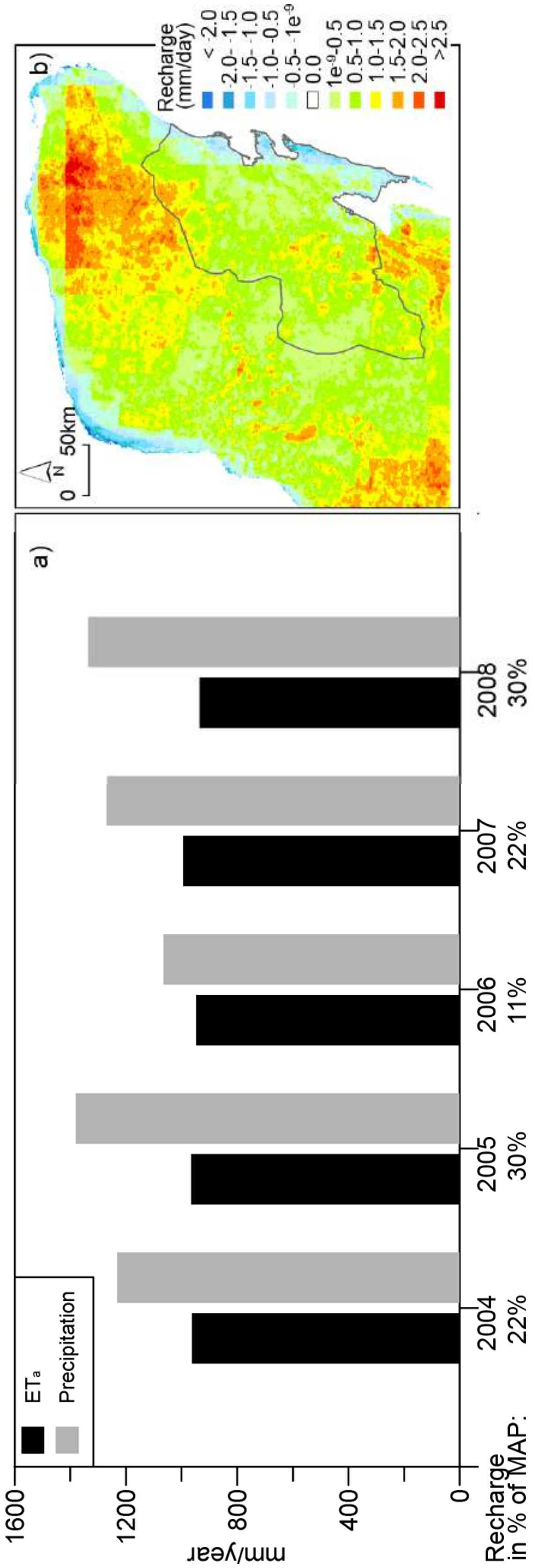

Fig. 13 (rotated 90 degrees)

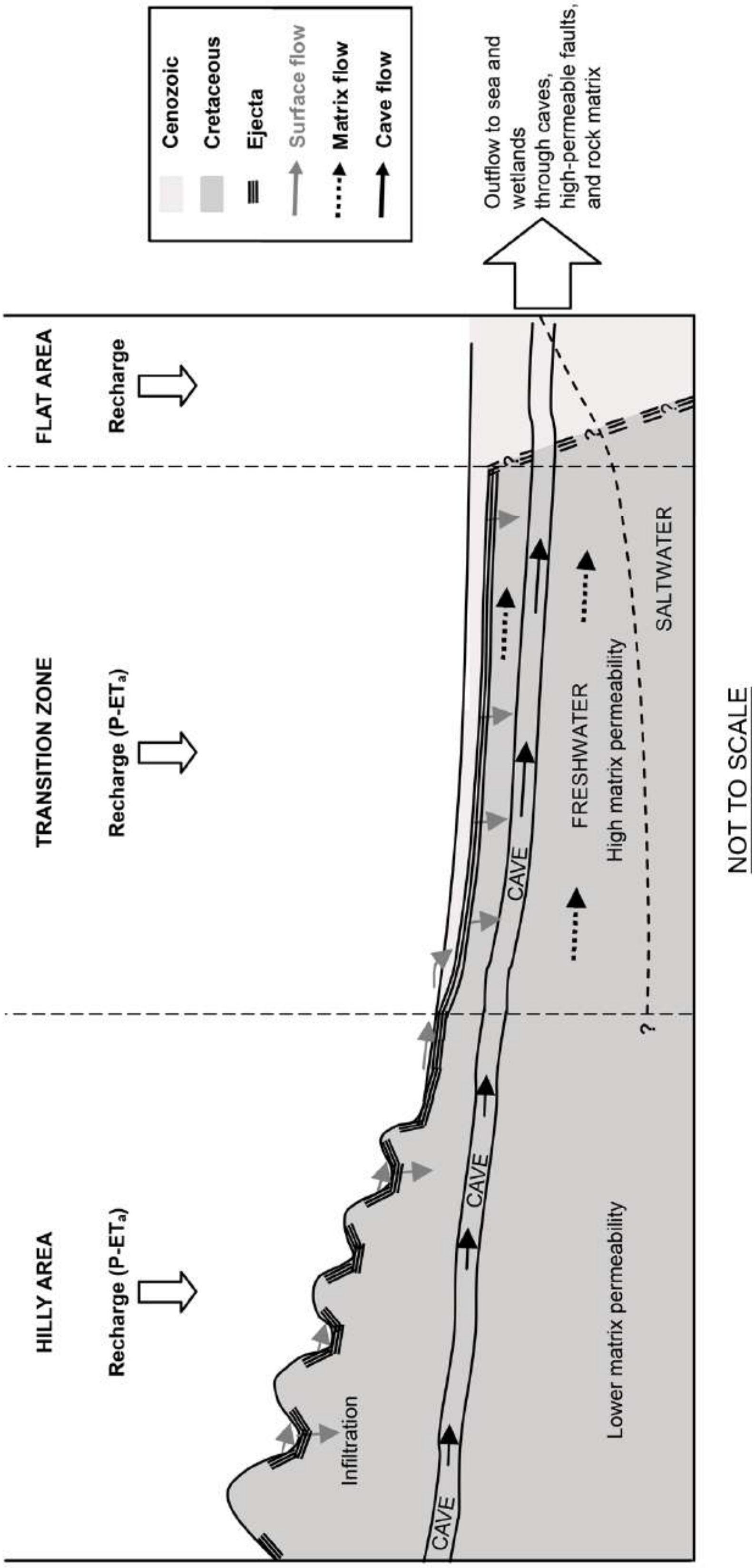

Fig. 14 (rotated 90 degrees)

Electronic supplement material

Tab. A1 Results of water chemistry analyses.

Location	Northing	Easting	Collect	Ca^{2+}	Mg^{2+}	Sr^{2+}	K^{+}	Na^{+}	Ba^{2+}	SO_4^{-}	Cl^{-}	NO_3^{-}	Br^{-}	HCO_3^{-}	IonBal	ElecBal	Temp.[a]	pH[a]	$\delta^{18}O$
	(UTM)	(UTM)	date in 2008	(meq/L)	(meq/L)	(meq/L)	(meq/L)	(meq/L)	(meq/L)	(meq/L)	(meq/L)	(meq/L)	(meq/L)	(meq/L)	(%)	(meq/L)	(°C)		(‰) SMOW
Groundwater																			
Andres Quintana Roo	2119078	384045	24-Feb	8.44	5.03	0.063	0.32	13.36	0.001	4.84	14.70	0.019	0.023	5.72	3.64	1.91	-	7.20	-3.63
Betania	2171991	364995	19-Feb	7.25	3.67	0.067	0.10	4.32	0.001	2.45	3.87	0.121	N.D.	6.93	7.07	2.04	-	7.30	-4.73
Caobas	2040402	278072	25-Feb	30.35	7.97	0.352	0.08	2.68	0.000	32.46	1.51	0.018	N.D.	4.13	4.16	3.31	29.0	7.12	-5.29
Dzula	2168188	351530	19-Feb	8.56	3.80	0.078	0.34	4.62	0.001	4.47	3.23	0.298	N.D.	6.10	10.47	3.30	29.5	7.00	-4.42
El Cedral	2069065	291628	23-Feb	27.14	8.41	0.315	0.10	4.72	0.000	28.68	3.03	0.046	N.D.	4.32	6.02	4.62	30.0	-	-5.00
Francisco Villa	2043887	305022	23-Feb	4.90	3.32	0.005	0.05	2.13	0.025	0.13	1.94	0.035	N.D.	6.47	9.78	1.86	28.0	7.50	-5.10
Las Panteras	2116954	343030	20-Feb	5.06	1.07	0.032	0.13	3.58	0.004	0.67	1.67	0.019	N.D.	5.30	12.70	2.23	-	-	-4.22
Limones	2103575	383133	20-Feb	6.77	3.48	0.020	0.38	14.49	0.001	1.44	15.59	0.028	0.032	5.68	4.96	2.38	28.0	7.88	-4.48
Los Divorciados	2109676	346734	07-Feb	6.46	5.13	0.084	0.19	4.94	0.001	4.52	4.19	0.092	N.D.	6.92	3.33	1.08	28.0	7.17	-4.10
Mixtequilla	2144153	367118	18-Feb	5.54	0.82	0.014	0.11	1.20	0.001	0.11	0.53	0.026	N.D.	5.93	7.56	1.08	-	7.40	-4.20
Morocoy	2057464	308879	23-Feb	4.59	2.72	0.018	0.10	3.43	0.001	1.98	2.31	0.020	N.D.	4.50	10.39	2.04	27.4	7.29	-4.71
Naranjal Poniente	2141533	346663	18-Feb	6.45	2.58	0.060	0.13	4.03	0.001	4.10	1.61	0.027	N.D.	6.05	5.84	1.46	-	7.30	-2.91
Nicholas Bravo	2042505	296143	25-Feb	6.59	1.54	0.016	0.16	4.01	0.007	0.69	4.05	0.117	0.008	5.25	9.84	2.21	27.5	7.42	-4.91
Noh Cah	2147855	378229	24-Feb	6.70	2.35	0.027	0.14	5.21	0.001	0.96	4.01	0.016	N.D.	6.73	10.35	2.71	-	7.40	-4.46
Nuevo Israel	2128250	337357	20-Feb	24.52	10.40	0.358	0.19	9.23	0.000	27.19	6.61	0.109	0.012	5.27	6.57	5.51	-	7.50	-3.76
Otillo Montaño	2102587	307561	22-Feb	9.80	4.58	0.049	0.11	6.93	0.001	6.85	5.73	0.097	0.009	7.08	4.14	1.71	29.3	7.03	-4.44
Pedro A. Santos	2096556	377217	20-Feb	12.98	9.08	0.140	0.53	26.94	0.001	10.91	31.59	0.014	0.065	6.08	1.03	1.01	31.0	7.00	-4.47
Petcacab	2133494	371269	21-Feb	6.41	3.94	0.087	0.20	6.31	0.001	4.77	4.04	0.050	N.D.	5.70	7.59	2.39	29.0	7.76	-3.55
Polinkin	2120565	376854	21-Feb	5.36	2.92	0.033	0.26	7.05	0.001	2.71	7.66	N.D.	0.015	3.95	4.31	1.29	28.0	7.14	-2.13
Presidente Juarez	2137762	335917	20-Feb	9.51	2.61	0.091	0.11	1.31	0.000	6.72	0.63	N.D.	N.D.	5.07	4.68	1.22	-	7.30	-3.71
Rancho Las Herraduras	2100867	370950	20-Feb	4.43	3.00	0.030	0.12	6.58	0.001	1.28	2.80	0.015	N.D.	7.05	11.93	3.02	-	-	-4.21
Reforma	2080887	334274	23-Feb	5.42	4.21	0.013	0.17	2.42	0.003	0.56	1.34	0.194	N.D.	7.48	12.22	2.67	29.3	7.29	-4.14
Rio Escondido	2088921	315400	22-Feb	5.45	3.07	0.026	0.11	5.35	0.004	0.69	6.55	0.043	0.013	5.60	4.12	1.11	28.0	7.00	-4.83

San Luis	2172936	348052	19-Feb	9.82	6.20	0.153	0.14	6.91	0.001	6.61	4.92	0.046	0.008	6.80	11.62	4.83	-	7.40	-4.55
Señor	2194275	380703	22-Feb	7.27	3.46	0.064	0.09	5.91	0.001	1.58	5.08	0.076	0.009	6.36	12.30	3.68	-	-	-4.68
Ucum Q.Roo	2046238	339617	23-Feb	10.67	4.44	0.144	0.08	3.20	0.001	6.56	1.91	0.090	N.D.	6.80	9.32	3.16	29.0	6.76	-4.83
Xhacil	2144613	386587	18-Feb	6.05	3.04	0.035	0.14	6.75	0.001	2.23	5.49	0.022	0.009	6.48	5.88	1.78	27.0	7.38	-4.37
Xkan-Ha	2114278	253374	27-Feb	25.52	8.86	0.270	0.14	14.42	0.000	23.96	11.94	0.619	0.020	5.20	8.21	7.47	-	-	-4.26
Surface water																			
Cenote Azul	2062367	350932	23-Feb	23.26	7.84	0.283	0.09	2.27	0.000	25.11	1.27	0.003	N.D.	4.70	4.10	2.66	27.4[b]	7.35[b]	-4.05
Narciso Mendoza	2017596	240428	26-Feb	36.31	3.79	0.308	0.14	5.00	0.001	33.06	5.89	0.014	0.416	3.60	2.89	2.56	-	-	-3.79
Veinte de Noviembre	2041661	256369	26-Feb	35.57	4.23	0.319	0.20	8.05	0.000	29.23	8.33	0.080	0.015	9.15	1.64	1.56	-	-	-4.20

[a] Value from CAPA's waterchemical analysis, 2005 (unpublished), unless otherwise noted.
[b] Value from Perry et al. (2002), March 1996
N.D. : Not detected
- : Not available.

Tab. A2 Saturation indices (SI) calculated with PHREEQC

Location	Northing (UTM)	Easting (UTM)	Collect date	SI Gypsum	SI Anhydrite	SI Celestite	SI Calcite	SI Aragonite	SI Dolomite
Groundwater									
Andres Quintana Roo	2119078	384045	24-Feb-08	-1.17	-1.38	-1.24	0.36	0.22	0.66
Betania	2171991	364995	19-Feb-08	-1.42	-1.63	-1.40	0.55	0.40	0.97
Caobas	2040402	278072	25-Feb-08	-0.06	-0.27	0.06	0.51	0.37	0.59
Dzula	2168188	351530	19-Feb-08	-1.13	-1.33	-1.11	0.25	0.11	0.33
El Cedral	2069065	291628	23-Feb-08	-0.15	-0.34	-0.02	0.69	0.55	1.03
Francisco Villa	2043887	305022	23-Feb-08	-2.76	-2.97	-3.72	0.60	0.46	1.21
Las Panteras	2116954	343030	20-Feb-08	-2.00	-2.20	-2.14	0.35	0.21	0.20
Limones	2103575	383133	20-Feb-08	-1.73	-1.94	-2.19	0.96	0.82	1.80
Los Divorciados	2109676	346734	07-Feb-08	-1.24	-1.45	-1.07	0.33	0.19	0.72
Mixtequilla	2144153	367118	18-Feb-08	-2.73	-2.94	-3.27	0.56	0.42	0.46

Morocoy	2057464	308879	23-Feb-08	-1.62	-1.83	-1.98	0.19	0.04	0.30
Naranjal Poniente	2141533	346663	18-Feb-08	-1.22	-1.43	-1.19	0.44	0.29	0.64
Nicholas Bravo	2042505	296143	25-Feb-08	-1.93	-2.14	-2.49	0.54	0.40	0.61
Noh Cah	2147855	378229	24-Feb-08	-1.82	-2.02	-2.16	0.63	0.48	0.97
Nuevo Israel	2128250	337357	20-Feb-08	-0.21	-0.43	0.01	0.87	0.73	1.50
Otillo Montaño	2102587	307561	22-Feb-08	-0.95	-1.15	-1.19	0.36	0.22	0.55
Pedro A. Santos	2096556	377217	20-Feb-08	-0.82	-1.01	-0.72	0.30	0.16	0.63
Petcacab	2133494	371269	21-Feb-08	-1.21	-1.41	-1.01	0.84	0.70	1.64
Polinkin	2120565	376854	21-Feb-08	-1.48	-1.68	-1.64	0.02	-0.13	-0.07
Presidente Juarez	2137762	335917	20-Feb-08	-0.89	-1.10	-0.85	0.50	0.35	0.59
Rancho Las Herraduras	2100867	370950	20-Feb-08	-1.85	-2.06	-1.97	0.37	0.23	0.75
Reforma	2080887	334274	23-Feb-08	-2.13	-2.33	-2.70	0.50	0.36	1.07
Rio Escondido	2088921	315400	22-Feb-08	-2.04	-2.24	-2.31	0.06	-0.08	0.04
San Luis	2172936	348052	19-Feb-08	-0.98	-1.18	-0.73	0.69	0.55	1.35
Señor	2194275	380703	22-Feb-08	-1.61	-1.81	-1.61	0.52	0.38	0.88
Ucum Q.Roo	2046238	339617	23-Feb-08	-0.91	-1.11	-0.72	0.12	-0.02	0.03
Xhacil	2144613	386587	18-Feb-08	-1.52	-1.73	-1.70	0.50	0.36	0.86
Xkan-Ha	2114278	253374	27-Feb-08	-0.26	-0.46	-0.17	0.73	0.59	1.15
Surface water									
Cenote Azul	2062367	350932	23-Feb-08	-0.22	-0.43	-0.08	0.70	0.56	1.07
Narciso Mendoza	2017596	240428	26-Feb-08	0.00	-0.20	0.00	0.69	0.55	0.54
Veinte de Noviembre	2041661	256369	26-Feb-08	-0.06	-0.27	-0.05	1.08	0.94	1.39

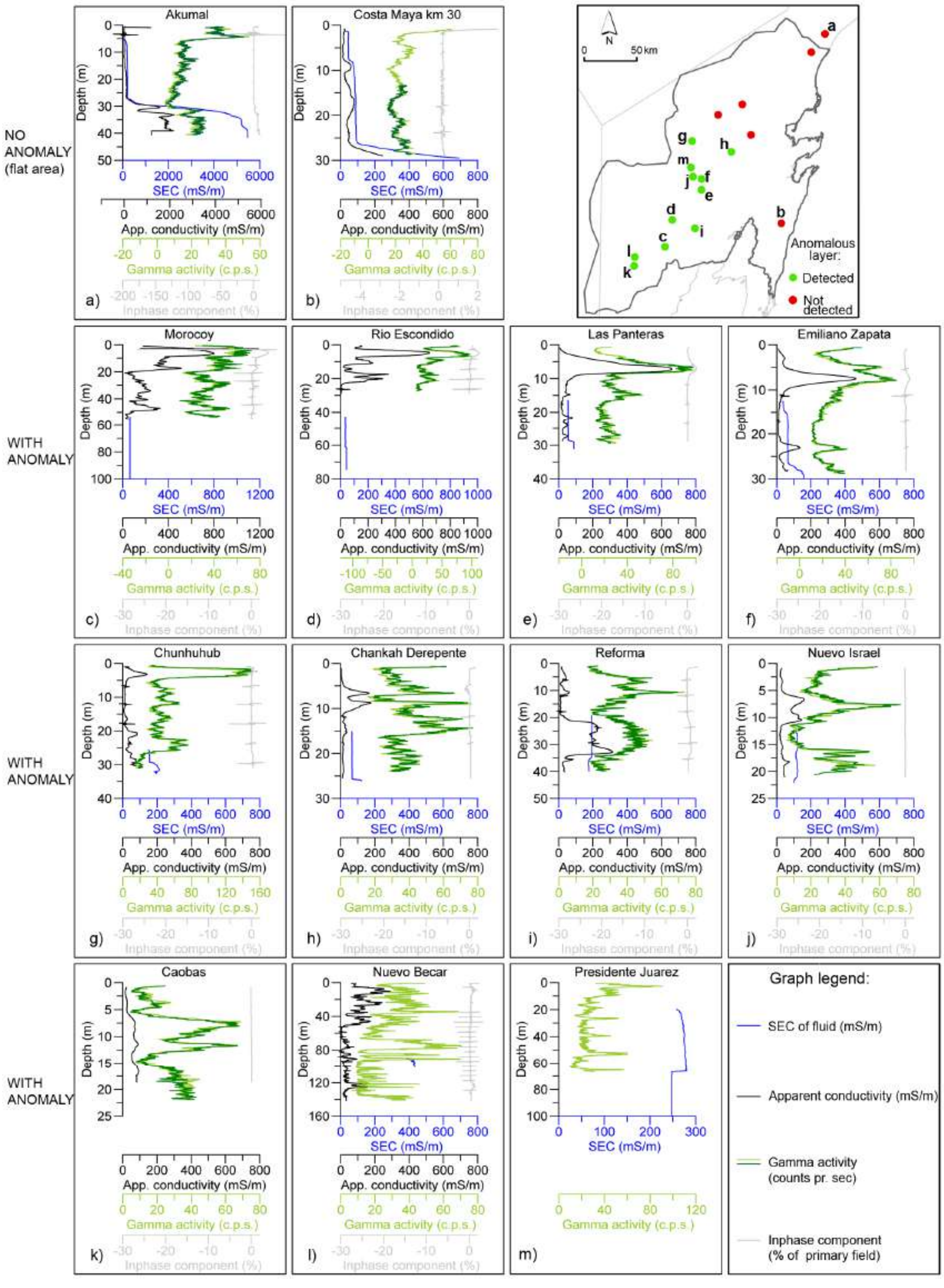

Fig. A1 Borehole logging results showing all the logs with the anomalous layer detected (c-m), as well as two examples of boreholes without the anomalous layer (a-b).

V

The influence of conceptual model uncertainty on management decisions for a groundwater-dependent ecosystem in karst

Gondwe, B.R.N., Merediz-Alonso, G., Bauer-Gottwein, P.

Manuscript submitted

The influence of conceptual model uncertainty on management decisions for a groundwater-dependent ecosystem in karst

Bibi R. N. Gondwe[a*], Gonzalo Merediz-Alonso[b] and Peter Bauer-Gottwein[a]

[a] *Department of Environmental Engineering, Technical University of Denmark, Miljoevej, Building 113, DK-2800 Kgs. Lyngby, Denmark. pbg@env.dtu.dk.* [*)] Corresponding author: bng@env.dtu.dk; tel.: (+45) 4525 1570, fax: (+45)4593 2850

[b] *Amigos de Sian Ka'an, Calle Fuego No. 2, Manzana 10 SM 4, Cancún, Quintana Roo, 77500, México. gmerediz@amigosdesiankaan.org*

Abstract

Groundwater management in karst is often based on limited hydrologic understanding of the aquifer. The geologic heterogeneities controlling the water flow are often insufficiently mapped. As karst aquifers are very vulnerable to pollution, groundwater protection and land use management are crucial to preserve water resources and maintain ecosystem services. Multiple Model Simulation (MMS) highlights the impact of model structure uncertainty on management decisions using several plausible conceptual models. MMS was used for this purpose on the Yucatan Peninsula, which is one of the world's largest karstic aquifers. The aquifer is the only available fresh water source for human users and ecosystems on the Peninsula. One of Mexico's largest protected areas, the groundwater-dependent Sian Ka'an Biosphere Reserve (5280 km^2) is fed by the aquifer's thin freshwater lens. Increasing groundwater abstractions and pollution threatens the fresh water resource, and consequently the ecosystem integrity of both Sian Ka'an and the adjacent coastal environment. Seven different catchment-scale conceptual models were implemented in a distributed hydrological modelling approach.

Single-continuum and dual-continuum equivalent porous medium conceptualizations were used. The models demonstrated that Sian Ka'an's wetlands are indeed groundwater-fed. The water quantities in the wetlands and the flooding dynamics are determined by the larger groundwater catchment. The overall water balance for the model domain showed that recharge constitutes 4400 mio. m^3/year ± 700 mio. m^3/year. Of this, 4–12% exits as overland flow, and 88–96% exits as groundwater flow. Net groundwater outflow from the model domain to the north via the Holbox fracture zone appears as an important cross-basin transfer between regions of the Peninsula. Probability maps of Sian Ka'an's catchment were obtained through automatic calibration and stochastic modelling. Groundwater travel time zones were calculated based on different calibrated effective porosities. The spatial modelling results highlight the impact of regional-scale structures on the flow field and transport times.

Keywords: catchment modelling, model structure, equivalent porous medium, aquifer, Sian Ka'an, Mexico

1. Introduction

The need to provide water both for human demands and for ecosystems is increasingly being recognized worldwide, placing interaction between groundwater and surface water in political and scientific focus (Kilroy et al., 2005; Eamus and Froend, 2006; Münch and Conrad, 2007; Krause et al., 2007). Terrestrial groundwater-dependent wetland ecosystems are some of the world's most productive ecosystems, and therefore the target of protection and restoration efforts. Groundwater-dependent ecosystems (GDEs) in karst are particularly vulnerable to pollution because of rapid groundwater flow and contaminant transport in karst geology.

In Mexico, one of the largest protected areas is a GDE in karst. The 5280 km^2 Sian Ka'an Biosphere Reserve on the Yucatan Peninsula includes large wetlands taking up about ⅓ of the area (Fig. 1). Their rich ecosystem diversity and recreational value is internationally and regionally valued, and the area is listed as a Ramsar site and UNESCO World Heritage. The wetlands are fed by a thin fresh groundwater lens, only up to 100 m thick, which effectively is the only fresh water resource available on the Yucatan Peninsula.

Peninsula-wide, groundwater demands and groundwater pollution problems are growing. Both in northwestern Yucatan Peninsula (Escolero et al., 2000) and along the eastern coast (Fideicomiso, 2004), significant and rapid increases in population density and water demands are taking place, partly due to an expanding tourism industry in the east. Groundwater pollution in Yucatan State has been documented by Pacheco et al. (2001), while agricultural activities are intensifying in the state of Quinana Roo (Mazzotti et al., 2005). Wastewater is typically re-injected into the Peninsular aquifer, and often does not undergo prior treatment (ASK, 2003; Beddows 2002; Beddows et al., 2005; Marín et al., 2000; Krekeler et al., 2007). Thus, the tradeoff between human water use and ecosystem water use appears as a major groundwater management problem on the Yucatan Peninsula.

To manage the water resources of the GDE soundly, it is necessary to delineate its catchment. Distributed hydrological modelling is the method of choice, but in the highly heterogeneous karst aquifers, catchment delineation poses a particular challenge. A karst aquifer is a triple porosity medium, consisting of the rock matrix (intergranular porosity), the fractures and bedding planes and the karstic conduits (White, 1999). Most karstic groundwater flow takes place in the conduits, whereas the matrix is the prime compartment for water storage (Atkinson, 1977; Worthington, 2003). The unknown heterogeneities make it difficult to predict karstic groundwater flow accurately. Groundwater management initiatives, such as land use zonation, are therefore often made based on limited hydrogeologic understanding of the aquifer.

Conceptual model uncertainty can be addressed using Multiple Model Simulation (MMS). The impact of uncertainty in the conceptual model is usually far greater than the impact of any model parameter uncertainty (Neuman and Wierenga, 2003; Højberg and Refsgaard, 2005). In MMS a number of different plausible conceptual models are formulated and calibrated. Based on validation tests, models are accepted or rejected. All accepted models are subsequently used for prediction and uncertainty assessment (Refsgaard et al., 2006). MMS increases the robustness of model predictions and yields explicit analyses of the consequences of using alternative models. The limitations of the MMS approach are that the selection of conceptual models is necessarily subjective and often incomplete. Important plausible conceptual models may be left out, and it is not possible to quantify the probability of each alternative model (Refsgaard et al., 2006; 2007).

Numerically, karst aquifers may be represented in various ways. Here we consider only distributed models. Distributed hydrological modelling studies that take all three aquifer continua into account are limited (e.g. Cheng and Chen, 2005). However, a relatively common numerical modelling method is to consider two continua, the matrix and the conduits, and include an exchange component between the two (e.g. Arfib and de Marsily, 2004; Birk et al., 2003; Liedl et al. 2003). Flow in the larger apertures may be turbulent, while the flow in the matrix is laminar. These conduit-matrix models are physically sound but also complex and computationally expensive. Problems occur in the parameterization of the highly variable caves (e.g. cave location, course, roughness, dimensions) and in quantifying the exchange between the continua, particularly at larger scales. Slight changes in some cave parameterizations can change model output notably (Peterson and Wicks, 2006), and the exchange between conduits and matrix is still little understood (Martin and Screaton, 2001; Bauer et al., 2003; Peterson and Wicks, 2005). Catchment-scale applications of conduit-matrix models are limited by the high computational load. Moreover, sufficiently detailed data are typically not available for large areas.

The simplest way of modelling a distributed karst aquifer is to assume that the aquifer can be represented by an equivalent porous medium. This assumption is reasonable if the numerical cell size is 'large enough', i.e. equals or exceeds a "representative elementary volume" (REV). The hydraulic conductivity (*K*) assigned to a cell represents the combined effect of matrix, fractures and conduits within the cell. In a few cases the equivalent porous medium approach, using only one *K* for the whole domain (single-continuum models), has been successful (e.g. Larocque et al., 1999; 2000; Scanlon et al., 2003), but it is also often criticized as too simplistic to represent karst flow (e.g. Kovacs et al., 2005). A modification of this method is the dual-continuum equivalent porous medium model, where important conduits are represented as zones with a higher *K* than the matrix, and there is exchange between the two continua. This approach still models only laminar flow in both compartments, but incorporates some of the important heterogeneity of karst aquifers. Assigning such "block permeabilities" to different zones gives a higher accuracy than single continuum models, if the zonation and assignment of values is reasonably reliable (Durlofsky, 1992). The dual continuum approach has been successfully used by e.g. Teutsch and

Sauter (1991), Knochenmus and Robinson (1996), Lindgren et al. (2005) and Kiraly (2003). Its simplified approach is applicable especially for regional-scale studies.

The present study aims to illustrate the effects of model structure uncertainty on management decisions in karst. For the catchment of the Sian Ka'an Biosphere Reserve we test different conceptual models of the area using both single- and dual-continuum equivalent porous medium approaches. Models are accepted or rejected based on quantified fluxes and model fits to measured heads. The accepted hydrological models are then used to delineate the catchment that contributes with groundwater to Sian Ka'an using stochastic modelling. The implications for groundwater management are discussed.

2. Methods and data

2.1 The study area

The study area is the 35000 km^2 large tentative groundwater catchment of the Sian Ka'an Biosphere Reserve (SKBR), located in Quintana Roo, Mexico (Fig. 1). The study area was delineated based on topographic divides, assuming, as a first order approximation, that these coincide with groundwater divides. The boundary perpendicular to the coast north of Tulum was not based on topography, but on an assumed flow line, far enough away from SKBR to ensure that areas further away would not contribute groundwater to the Reserve. The groundwater head data presently available for the peninsula are in agreement with these tentative catchment boundaries. Geochemical findings of Perry et al. (2002) support the water divide at Lake Chichankanab.

Average precipitation ranges from 840 to 1550 mm/year. Three quarters of the precipitation falls between May and October (unpubl. climate data from Comisión Nacional del Agua). A spatial estimate of actual evapotranspiration, using the 'triangle method' and MODIS data, showed that average recharge equals about 17% of mean annual precipitation in the study area (Gondwe et al., in review). Average monthly temperatures range from 23 to 27 °C. The area is subject to tropical storms. Soil cover is limited and most of the area is covered by 15–30 m tall semi-evergreen forest (Sánchez-Sánchez and Islebe, 2002; INEGI, 1997). Sian Ka'an contains coastal savannas, swamps, marches and mangrove, in addition to tropical forests, and hosts endangered and endemic species (Morales Barbosa, 1992; Mazzotti et al., 2005). From August 2006 to February 2008 the wetland extent varied between 1067 km^2 and 2588 km^2. Smallest extent was in May and largest in December in a typical year (Gondwe et al., 2010).

The Yucatan Peninsula consists of limestones, dolomites and evaporites reaching thicknesses of >1500 m (Weidie, 1985). The surficial sediments span Upper Cretaceous to Holocene in age, and are generally nearly horizontally layered and off-lapping, with gradually younger carbonates deposited towards the Peninsula margins (Lopez-Ramos, 1975; SGM, 2007; Schönian et al., 2005) (Fig. 1). The geology is poorly constrained in the southern and central Peninsula due to few exposures and difficulties in dating the sediments through biostratigraphy (Kenkmann and Schönian, 2006). The Yucatecan carbonates are heavily karstified and host abundant caves, including the world's longest underwater cave system (http://www.caves.org/project/qrss/qrlong.htm; http://www.caverbob.com/uwcave.htm). Extensive cave systems have mainly been mapped in the northern part of Sian Ka'an, along the coast north of SKBR, and up to roughly 10 km inland. This is likely a result of sampling bias, as most cave divers live in this area, thus concentrating most exploration efforts there (Beddows, 2004). However, the possibility also exists that the extensive cave systems are related to the Pleistocene geology only deposited in this area (Neuman and Rahbek, 2007 and references herein). In neighboring Belize, cave development in the Tertiary sediments is practically unknown, despite an abundance of mapped cave systems in other geologies (Miller, 1996).

The study area contains a notable topographic contrast. The topographic relief is flat in the northern and coastal parts of the Pliocene geology (elevations 0–20 meters above mean sea level (mamsl)) whereas the south-southwestern, mainly Cretaceous, areas have an undulating relief with cone-karst landforms (elevations 50–340 mamsl). In between there is a transition zone with moderately undulating relief (20–50 mamsl). A similar divide exists in the groundwater phreatic surface (Gondwe et al., in review). The Pliocene area has a very low hydraulic gradient (3–7 cm/km) with relatively small water level variations (5–40 cm within a year). This indicates a high transmissivity. In contrast, the Cretaceous geology has perched aquifers, and higher hydraulic gradients (10–190 cm/km). Water level variations have not been recorded here. Geochemistry shows groundwater dominated by gypsum in the Cretaceous part of the study area, which supports a lower transmissivity in this geology (Gondwe et al., in review). The main groundwater flow direction deduced from phreatic surface measurements is SW-NE from the Cretaceous area to the Pliocene area, and W-E towards the coast within the Pliocene area.

In the Pliocene geology, the fresh groundwater forms a lens floating on top of saline water. The Dupuit-Ghyben-Herzberg model can be used to describe the thickness of the freshwater lens on a regional scale in the study area's Pliocene geology (Gondwe et al., in review). However, only 100 m from the coast at Tulum, Beddows (2004) showed that the freshwater lens is 4.6 m to 7 m thick. This is thicker than predicted from the Dupuit-Ghyben-Herzberg model, and may be due to outflow restrictions. Coastal caves explored by cave divers north of Tulum are smaller than inland caves. Moreover, they are often parallel to the coast because they developed along joints (Smart et al., 2006). In the Cretaceous hilly area saline intrusion has not been documented, and is not reflected in the geochemistry (Gondwe et al., in review; Perry et al., 2009). Thus the thickness of the fresh aquifer in this area is unknown.

Important physiographic features characterize the study area. The Río Hondo faults are a series of sub-parallel faults, trending SSW-NNE, and located in the southern part of the study area (Fig. 1). They have not been mapped in detail but fault-guided lakes are a surface expression of the faults (e.g. Laguna de Bacalar). The Río Hondo faults are normal faults with the downthrown side to the east. They have shaped the Caribbean coastline in the study area, and sub-parallel horst and graben systems are present offshore (Rosencrantz, 1990). Another fault system is located in the northern part of the study area – the Holbox fracture zone, also trending SSW-NNE. Its southern terminus is not well determined but possibly the Holbox and Río Hondo fault systems intersect (Southworth, 1985). Sharp linear wetland boundaries within Sian Ka'an have been proposed to be fault-controlled (Gondwe et al., 2010), outlining additional possible sub-regional faults within Sian Ka'an between the two main regional fault systems.

Regional-scale structures have been delineated within the study area using remote sensing imagery and topographic elevation data (Gondwe et al., submitted) (Fig. 1). Most of these structures are sub-parallel to the Río Hondo faults and may constitute a part of this system. Possibly these structures may be regional high-permeability zones.

Airborne electromagnetic investigations have been carried out over the structures but could not definitively determine their hydraulic character because of a shallow, highly conductive geologic layer (Gondwe et al., submitted). Seasonal surface water runoff takes place in these structures, but infiltrates into the aquifer before reaching the coast (Gondwe et al., submitted; SGM, 2007; Pope and Dahlin, 1989). The shallow geologic layer with high electrical conductivity and likely high clay content is the proposed reason for the reduced infiltration capacity over the structures (Gondwe et al., submitted). This layer is probably discontinuous, due to erosion following its deposition (Pope et al., 2005; Kenkmann and Schönian, 2006; Urrutia-Fucugauchi et al., 2008; Gondwe et al., submitted). Despite its general presence throughout the hilly area and transition zone the layer does not appear to inhibit rapid infiltration to the aquifer at the regional scale. This is confirmed by rapid groundwater level responses to local rainfall (Gondwe et al., in review).

Previous hydrogeologic, geologic and hydrologic studies of the area are limited. Beddows (2003; 2004) and Beddows et al. (2007) studied cave hydrology on a local scale in Riviera Maya. Smart et al. (2006) and Supper et al. (2009) investigated the cave systems in the same area using direct inspection and airborne geophysical methods, respectively. The geology of a section in the southern part of the study area was characterized by Schönian et al. (2004; 2005) and Kenkmann and Schönian (2006), whereas geochemistry was investigated by Perry et al. (2002; 2009) on a regional scale. Hydrologic dynamics of the Sian Ka'an wetlands were investigated by Gondwe et al. (2010), and regional-scale multidisciplinary field investigations of the tentative catchment were carried out by Gondwe et al. (in review; submitted), as an antecedent to the hydrological modelling presented in this paper. Hydrological modelling of Sian Ka'an's catchment has not been carried out in any previous studies.

Based on the findings of Gondwe et al. (in review), the Pliocene geology of the study area can be considered one continuous aquifer, with a clearly defined lower level. The relation between this aquifer and any aquifer in the Cretaceous geology is undetermined. It is not known whether there is groundwater flow between the Cretaceous area with the low transmissivities and the Pliocene area with the high transmissivities. In addition, data on regional groundwater heads in the Cretaceous area are limited to 3 measurement points in the hilly area and 8 in the transition zone, and it is not clear whether some of these are connected to perched aquifers. Moreover, the thickness of the freshwater aquifer in the Cretaceous area is unknown. Therefore, only the Pliocene part of the study area was simulated with a distributed hydrological model. The effects of the Cretaceous geology aquifer were represented as lumped boundary inflows. The model area of the distributed model was outlined based on geological boundaries from SGM (2007) and the 50 mamsl topographic contour line, as it was assumed that the rugged topography >50 mamsl near Lake Chichankanab did not belong to the generally more smooth Pliocene geology. Outside the delineated model area, the water levels were much higher than the 0.5– 3 mamsl that characterize the Pliocene area aquifer. The total area of the distributed model was 21000 km^2 (Fig. 1).

2.2 Design of the numerical hydrological models

An equivalent porous medium modelling approach was chosen because of the regional scale of the model area. Different conceptual models were developed. They differed with respect to two main criteria: A) Whether there is flow between the Cretaceous and the Pliocene area; and B) whether the structures and faults delineated in Gondwe et al. (submitted; 2010) are regional-scale zones of higher permeability. Consequently, four conceptual models were set up and compared (Fig. 2): Model 1) No inflow from the Cretaceous area, and hydraulic conductivity (*K*) of the structures equal to that of the matrix. Model 2) Same as Model 1 but with structures having a different *K* than the surrounding equivalent porous medium matrix. Model 3) With inflow from the Cretaceous area to the discretized model domain. *K* of structures equals that of the matrix. Model 4) Same as Model 3, but with structures having a different *K* than the matrix.

The coupled surface-water/groundwater finite-difference code MIKE SHE (Refsgaard and Storm, 1995; Graham and Butts, 2006) was used. Darcian flow was assumed throughout the saturated zone. Grid cell size was 1x1 km^2 and hydraulic conductivity was assumed to be isotropic. The aquifer was assumed unconfined throughout the model domain. Mainly, steady state conditions were analyzed. The unsaturated zone was disregarded in the model setup. Fast infiltration of recharge directly into the aquifer is considered a valid assumption for the average conditions represented by the steady state models.

The top of the aquifer was set as the topographic level obtained from the Shuttle Radar Topography Mission (SRTM) (USGS, 2006), resampled to the 1 km^2 grid. The simulated extent of overland flow was sensitive to topographic level. Moreover, the SRTM may measure to top of canopy instead of ground level. Therefore, the 2-percentile topographic value within each 1 km^2 grid cell was used as the topographic level. The simulated extent of flooding was then similar to that observed from remote sensing data (Gondwe et al., 2010). A few coastal cells with topography < 0 mamsl at some narrow coastal land tongues at the extremes of the model area were removed from the model domain, since they showed inflow from the sea in all modelling experiments.

The lower level of the aquifer was defined by using the Dupuit-Ghyben-Herzberg principle (Vacher, 1988) to convert modelled freshwater heads to depths to the halocline. This modelled depth to the halocline corresponded well with measured values obtained from time-domain electromagnetic measurements (root mean square error (RMSE) = 10.3 m (Fig. 3), which is in the same range as the uncertainty of the measurements (5–15 m, Gondwe et al., in review)). At the coast, the lower level was set to -4.6 mamsl based on measurements in Beddows (2004). Next to the coastal cells minimum depth was set to -14.3 mamsl, based on Dupuit-Ghyben-Herzberg computations.

Boundary conditions were set to fixed head = 0 mamsl at the coast. Conceptual Model 1 had zero flux boundaries elsewhere. The Conceptual Models 3 and 4 were given inflow (flux) boundaries near the Cretaceous area (see below). Conceptual Models 2 and 4 further had a fixed head boundary of 0.4 mamsl at the Holbox fracture zone. This fixed head value was obtained from neighboring water level measurements. Model sensitivity to uncertainty in this parameter was investigated by adding or subtracting an estimated standard deviation, σ_{Holbox_bound}, of 4 cm (Gondwe et al., in review) to/from the fixed head boundary, and calibrating these model scenarios. Discharge thus took place along the coast via saturated zone and overland flow, and could also take place through the Holbox fracture zone, when structures were included. Discharge through groundwater abstractions were not included in the model due to lack of data. Hydrological modelling studies of the largest abstractions in Quintana Roo – at Cancun (outside the model area) have shown that even such relatively large abstractions

(1.9 m^3/s distributed over 70 km^2) do not cause appreciable modification of the groundwater heads, because of the high transmissivity of the Pliocene geology (Charvet, 2009).

Spatial estimates of yearly average recharge from Gondwe et al. (in review) were used directly in the model (mean: 0.5 mm/day, max.: 1.8 mm/day, min.: -2.3 mm/day within the model area). Model sensitivity to uncertainty in this parameter was investigated using scenario analysis, by adding or subtracting the standard deviation of the recharge, σ_R, to the recharge estimate, and calibrating these models. σ_R was estimated as $\sqrt{\left(\sigma_P{}^2 + \sigma_{ETa}{}^2\right)}$, where P is precipitation and ET_a is actual evapotranspiration. σ_P was estimated by comparing uncorrected precipitation estimates from Tropical Rainfall Measurement Mission (TRMM) (product 3B43) with precipitation data from 23 gauge stations within the study area. The estimated σ_P was 0.04 mm/day (=15 mm/year). An estimate of σ_{ETa} was obtained from data in Stisen et al. (2008). Our ET_a estimate was derived with similar methods as in Stisen et al. (2008), albeit with data from another remote sensor. Stisen et al. (2008)'s RMSE estimate (41.45 W/m^2 = 1.5 mm/day) is in the same order of magnitude as that obtained by most other authors, also cited in Stisen et al. (2008). The RMSE estimate was valid for daily estimates, and was re-calculated to the error of the yearly average ET_a by dividing it with the square root of the number of samples in a year ($\sqrt{365}$), yielding an σ_{ETa} of 0.08 mm/day (=29 mm/year) . The resulting estimate of σ_R was 0.09 mm/day. Spatial uncertainties on the recharge were not taken into account, as the spatial variation in the estimates of both ET_a and the precipitation is considered quite reliable. Moreover, synthetic modelling experiments indicate that the shape of groundwater catchments is influenced more by the uncertainty of the mean recharge than by the uncertainty of its spatial pattern (Hendricks Franssen et al., 2004).

To estimate the inflow from the Cretaceous area to the model domain (Models 3 and 4), surface water catchments of automatically delineated rivers were outlined based on topographic data using the software ILWIS 3.3 Academic (ITC, 2005). To a large extent the delineated rivers correspond to the structures connecting the Cretaceous area and the domain (Gondwe et al., submitted). The underlying assumption was that groundwater divides in the hilly area would correspond with surface water divides. It appears reasonable to assume that at least part of the recharge in the hilly area generates surface water flow, given the presence of a shallow low-permeability layer in this area, and the existence of swamps and ephemeral rivers (Gondwe et al., in review; submitted). Three main surface water catchments, consisting of sub-catchments connected by the rivers/structures, were obtained. They largely covered the Cretaceous part of the study area (Fig. 4). The surface water catchments termed 'North' and 'South' were used in the modelling. The surface water catchment 'Bacalar' appeared to dewater into the Río Hondo River on the boundary of the model domain, and was therefore not included. Average annual recharge of each 'North' and 'South' surface water catchment was calculated from the spatial recharge estimate. These values (in m^3/s) were then assigned as boundary inflow to the sections of the boundary where the structures of the 'North' and 'South' catchments intersected the boundary. In Conceptual Models 3 and 4, 100% of the calculated recharge was used as inflow (42.9 m^3/s and 57.1 m^3/s for 'North' and 'South', respectively). To investigate the sensitivity of the model to uncertainty in this parameter, the percentage of inflow was included as a calibration parameter in Conceptual Model 5. Since the resulting difference between Conceptual

Models 4 and 5 was minor, 50% of the calculated recharge was used as inflow in Conceptual Model 6, to study the influence of changing inflow on the model results.

The Preconditioned Conjugate Gradient solver (Hill, 1990) was used in the simulation for the saturated zone component. The overland flow was modelled using the diffusive wave approximation, with a Strickler/Manning law applied to the friction slopes, and the Successive Over-Relaxation solver of MIKE SHE. Manning's M=10 $m^{1/3}/s$ was applied to represent the friction losses due to micro-topography and the heavy vegetation of the Sian Ka'an wetlands.

2.3 Model calibration

The models were calibrated in steady state. Calibration was carried out using automatic inverse calibration. K-values (K_{matrix}, K_{struct}) were adjusted with the goal of minimizing the mean square error (MSE) between modelled and measured groundwater heads at 59 wells located within the model domain. Head data were a temporal average of the values presented in Gondwe et al. (in review); roughly two wet and two dry season measurements. Estimated uncertainty on the measured values was ± 4 cm based on average GPS error. The error due to time variation between head measurements was estimated to have its upper bound at ± 13 cm, but in reality to probably be much lower, because the temporal measurements have some correlation. Uniform uncertainty was assumed on all water level measurement points given that the same measurement method and same temporal sampling was applied to all. Therefore all points were weighted equally in the calibration. Structures and faults were assumed regionally connected (Fig. 5). Lindgren et al. (2005) assumed the same in their dual-continuum model of another karst region. The K_{struct} was not differentiated spatially. The literature (e.g. Liedl et al., 2003) indicates that conduits may become larger and/or have more branches downstream towards the outlet. Therefore some authors (e.g. Lindgren et al., 2005) assign different *K*-values along the course of the high permeability zones. Others (e.g. Kiraly, 2003) use a uniform approach as done here. A third *K*-value was assigned to the coastal boundary cells in all models (K_{coast}), controlling the coastal leakage. Finally, to take into account the possibility of extensive cave development only in the Pleistocene geology, Conceptual Model 7 was defined. It had a different coastal *K*-value at the Pleistocene geology (K_{coast_north}) than along the remainder of the coast, and otherwise resembled Conceptual Model 4 with structures and hilly inflow. Conceptual Model characteristics are summarized in Table 1.

Automated inverse calibration was carried out using the non-linear least squares fitting procedure 'nlinfit' in Matlab (version R2008b, The MathWorks), which uses the Gauss-Newton algorithm with Levenberg-Marquardt modifications. In certain cases the 'robust' fitting option was applied as it gave lower mean square error (MSE) (only used in the calibration of Conceptual Models 5 and 6). Heads in the entire model domain were constrained to be > 0 mamsl.

In order to ensure computational efficiency in the calibration a simplified overland flow representation was used. The head in the overland flow cell was set equal to the head in the underlying groundwater cell, and lateral flow in the overland compartment was neglected. Given the high friction in the SKBR overland flow compartment, this approximation is realistic. After model calibration, the overland flow component was enabled and models run again to generate results that included the quantification of overland flow. Due to limited field data, extensive model validation could not be carried out. Instead, the modelled fluxes were compared with literature values to accept or reject the different conceptual models.

Only Conceptual Models 4 and 7 were run in transient mode over a period of five years (2004–2008; the period for which estimates of both monthly precipitation and monthly ET_a were available). The available data was insufficient to calibrate a transient model independently, so *K*-values from the corresponding steady state model were used. Input was monthly recharge values from Gondwe et al. (in review). The specific yield (S_y) was adjusted by fitting a modelled transient hydrograph with a measured hydrograph at Dzula. Hilly inflow time series calculated from the recharge data were routed using a linear reservoir model. Time lag was adjusted by comparing with the Dzula hydrograph. A rough comparison with interferograms from Gondwe et al. (2010) was carried out to investigate the ability of the transient model to produce surface water level changes similar to those observed. For the sensor used in this study, a phase cycle (=”fringe”) of 0–2π corresponds to 3.9 cm relative water level change. Further details are given in Gondwe et al. (2010).

2.4 Stochastic catchment simulation

To delineate the catchment of Sian Ka’an, stochastic simulations were carried out with particle tracking. Similar approaches have been used by e.g. Vassolo et al. (1998), Stauffer et al. (2002; 2005) and Hendricks Franssen et al. (2004).

Following the inverse calibration, the resulting covariance matrix was used to determine the 95% confidence interval of the calibrated parameters and their cross-correlation. Due to very wide or undetermined 95% confidence intervals for K_{matrix} and K_{struct} when K_{coast} (and K_{coast_north}) was included in the inverse calibration, it was decided to fix K_{coast} (and K_{coast_north}) at the optimal value. The parameters K_{matrix} and K_{struct} were subsequently recalibrated and narrower 95% confidence intervals were obtained. These were used in Monte Carlo catchment simulations. Since K_{coast} varied by less than an order of magnitude in its 95% confidence interval, this approach was considered acceptable. A strong negative cross-correlation between K_{matrix} and K_{struct} existed in the models where both parameters were calibrated (e.g. Pearson's r was -0.88 (Conceptual Model 2), -0.92 (Conceptual Model 4), -0.86 (Conceptual Model 6)), except in Conceptual Model 7, where this correlation was positive (r = 0.96). These cross-correlations were incorporated into the Monte Carlo sampling. The Metropolis-Hastings algorithm (Hastings, 1970) of Matlab ('mhsample') was used. It is a Markov chain Monte Carlo method. The log-*K* values were sampled in the log-space, and subsequently transformed to their actual values. A multivariate normal distribution was used as probability density function for the log-*K* values, and random values were drawn using Cholesky decomposition and the Box-Muller transform.

For each equally likely set of *K*-values, the model was run, and particle tracking using MIKE SHE's random walk Particle Tracking module was applied. Since the effective porosity (φ_{eff}) is unknown, we first determined the steady state catchment, which is independent of φ_{eff}. This (worst case) greater envelope of the catchment was obtained by placing particles at the bottom of the model grid cells in the steady state models and tracking those that ultimately entered the official boundaries of Sian Ka'an. The combined area where the particles originated from corresponds to the inner and outer protection zones usually used within well protection strategies (e.g. Chave et al., 2006; Milanović, 2004). Probability maps of catchments were then calculated by stacking the results of the realizations. Also groundwater travel time zones are frequently used for groundwater protection and land use zonation, but these results depend strongly on the value of φ_{eff}. Following the recommendations of Worthington and Ford (2009), the travel time zones were delineated in different scenarios by adjusting φ_{eff} so that modelled velocities matched measured groundwater velocities in matrix and caves. Scenario 1 assumed a matrix velocity of $1 \cdot 10^{-5}$ m/s and, if the structures were differentiated, a structure (cave) velocity of 0.03 m/s. Maximum φ_{eff} was set to 0.3 (higher-end value measured by Gonzalez-Herrera, 1984), yielding velocities in the range of 10^{-5} m/s. Scenario 2 assumed a structure velocity of 0.03 m/s and also a matrix velocity of 0.03 m/s. The matrix velocity of 0.03 m/s is relevant if caves are assumed present in every single 1 km^2 matrix grid cell. This first-order approach of adjusting φ_{eff} values to obtain measured groundwater velocities can be useful to obtain an estimate of first breakthrough times for a water-borne pollution when using equivalent porous medium models. However, it is important to realize that this approach only simulates the fast flow through conduits and fractures. The slow extended release of contaminants from matrix, resulting from conduit-matrix exchange processes, cannot be estimated with this approach, and instead requires more refined transport simulation (Li et al, 2008; Geyer et al., 2007; Spiessl et al., 2007).

For the Conceptual Models 4, 6 and 7, 800 realizations yielded stable probability maps of the catchments. For Conceptual Model 3, only 500 realizations were needed.

3. Results

3.1 Results of Multiple Model Simulation; acceptance and rejection of conceptual models

Calibration results and key model outputs for the different conceptual models are shown in Table 1. For the models with a uniform coastal leakage, the MSE showed that including structures gave better fits (cp. Conceptual Model 1 and 2; 3 and 4/5/6). Including inflow from the Cretaceous area to the model domain improved model fits as well (cp. Model 1 and 3; 2 and 4). The 100% hilly inflow can apparently be estimated reliably with the surface water catchment method, as calibration of the hilly inflow (Model 5) resulted in almost the same value as Model 4 (105% instead of 100% and same MSE to the 3rd decimal). In these first 6 Conceptual Models, K_{struct} was always calibrated to be greater than K_{matrix} by 1–2 orders of magnitude. K_{struct} had the same order of magnitude as that used by Kiraly (2003), who used a similar equivalent porous medium modelling method, and determined K_{struct} to be ≥10 m/s. The calibrated value of K_{coast} was roughly one order of magnitude less than K_{matrix}. Scatter plots of measured vs. modelled heads are shown in Fig. 6. In Conceptual Model 1 the low heads (< 1 mamsl) were all modelled 0.5–1 m higher than measured (Fig. 6a). Spatially, these points were located from the northern part of the Sian Ka'an Biosphere Reserve up to the model boundary north of Tulum, in the area around the Holbox fracture zone. Conceptual Model 1 was rejected because of this large low-head discrepancy and the relatively large MSE. The remaining models showed the same overall shape of the scatter plots, which were not appreciably different from one another. Moreover, the MSE of the remaining models were similar. Conceptual Model 7 had the smallest MSE. Conceptual

Model 3 showed a similar, but less pronounced spatial bias of residuals in the northern part of the model area around the Holbox zone, as Model 1.

Clearly, the heads in the north near the Holbox zone were the reason why structures were assigned higher K than the matrix, in the models where structures were included. Conceptual Model 7 showed that when a different K at the coast was allowed in this northern area, coastal leakage was one order of magnitude larger in this area than in the remainder of the model area ($K_{coast\_north} >> K_{coast}$, Table 1). Because this changed leakage at the coast reduced the modelled heads around the Holbox zone to acceptable levels in Model 7, K_{struct} was not modelled to be appreciably different from K_{matrix} (also seen from their strong positive correlation). When including the overland flow component in the calibrated models, the MSE followed the same pattern as in the models without overland flow, and the MSE improved slightly, except in Models 2 and 6.

Where possible, the model results were compared with values from the literature to clarify whether all the remaining models could be considered plausible. The total discharge pr. km of coastline was seen to be rather constant in all models, approx. 0.2–0.4 m^3/s/km, except in Conceptual Model 2, which had a low value of 0.08 m^3/s/km. Estimates in the literature range from 0.27 m^3/s/km to 0.73 m^3/s/km (Table 2). In this light the low estimate of Conceptual Model 2 is clearly unrealistic. Therefore, this model was also rejected. The reason for the low coastal outflow in this model was that a large fraction of the total water input exited through the Holbox fracture zone instead (53.9 m^3/s compared to ~120 m^3/s recharge in this model).

The calculated maximum conduit flows were 3–18 m^3/s, when attributing all flow in structure cells to conduit flow, in Models 2, 4, 5 and 6. These values are not unrealistic judging from values reported in the literature (range: 1–17 m^3/s, Table 2). Literature values for overland flow are not available. However there was little difference between the different model estimates. A rough recalculation to average velocities, using simulated overland water depth and grid cell area, yielded max. overland flow velocities of 0.3 cm/s, and mean average velocities of 0.007 cm/s. The Shark River Slough of the Everglades also has low hydraulic gradients (3–4.7 cm/km, Bazante et al., 2006) and appears similar to Sian Ka'an's wetlands. Sian Ka'an's modelled overland flow velocities are in the same range as the velocities measured in Shark River Slough (average: 1–1.5 cm/s; range: 0.8–4 cm/s, Bazante et al., 2006). However, the model values represent average velocities for 1 km^2 grid cells, whereas actual velocities are highly determined by local cross-sections etc.

K_{coast} was calibrated to be in the order of 10^{-2} m/s – one order of magnitude less than K_{matrix} in Conceptual Model 3, 4 and 6. This was in agreement with divers' observations of possible coastal restriction to flow (at least near Tulum), and the same conclusion derived from the freshwater lens thickness > 0 m at the coast. However, the calculated Holbox outflow was very large in these models. In Conceptual Model 7 the calculated Holbox outflow seemed at a more reasonable level, although no field observations on Holbox outflow are available. Yet, in Model 7 K_{coast_north} was not sufficiently low to give the observed freshwater thickness at coast of at least 4.6 m, when using Dupuit-Ghyben-Herzberg computations. The remaining output parameters in Table 1 are not known in reality from other studies. Therefore, there were no reasons to discard the remaining models. Conceptual Models 3, 4, 6 and 7 were all deemed plausible and used in the further analysis. Of these, Models 4 and 7 had the best fits to measured heads.

Fig. 7a shows the modelled depth to groundwater plotted against the mean actual evapotranspiration (average of years 2004–2008) at each grid cell. Standard deviations are given as error bars. Also reference evapotranspiration, calculated with Hargreaves' equation (see Gondwe et al., in review) is shown (average of years 2004–2008). At sites with depth to groundwater between 0 and about 8 m below ground (mbg) evapotranspiration took place at potential rate (ET_a=ET_{ref}). At sites with depth to groundwater between 30 and 50 mbg, ET_a was constant, and hence did not depend on the depth to the groundwater. The vegetation was also equally dense and equally structured here (constant Vegetation Index (EVI from MODIS), Fig. 7b), and vegetation maps show uniform vegetation (INEGI, 1997). However, at sites with depth to groundwater between about 8–10 m and 30 m a decreasing ET_a-rate with increasing depth to groundwater could be observed. The relationship was linear (R^2=0.87). A decrease in ET_{ref} at these sites was clearly not part of the explanation – on the contrary, ET_{ref} was seen to increase in this interval. Differences in vegetation also did not appear to be the explanation, as EVI was rather constant here (Fig. 7b) and vegetation maps did not reveal any differences.

<u>3.2 Scenarios to assess impact of recharge and Holbox boundary uncertainty</u>

Scenario analyses (Table 3 and 4) were carried out on the two models giving the smallest MSE, namely Conceptual Model 4 and 7. The scenario analyses focused on two parameters: the Holbox fixed head boundary and the recharge. These parameters were kept fixed in the previous calibrations, but since these inputs are uncertain, the effect of these uncertainties needed to be assessed.

When varying the Holbox fixed head boundary by ± 4 cm, the model structure of Model 4 was robust (K_{struct} always >> K_{matrix}), whereas the model structure of Model 7 was not robust (K_{coast_north} became ≥ K_{matrix} whereas it was < K_{matrix} originally. K_{struct} became < K_{matrix} , whereas the two had been practically equal originally). Resulting outflows through the Holbox zone however remained at the same magnitudes as in the original models.

Also in the scenarios with changed recharge, the model structure of Model 7 was not robust (Table 4). The model structure of Model 4 remained robust in spite of the parameter change (K_{struct} > K_{matrix}). Outflow from the saturated zone was sensitive to a change in the recharge in both models, since this affected the water balance directly. The Holbox outflow was also very sensitive to changes in recharge. All Holbox outflows were reduced, either due to the change in calibrated K_{struct} (when recharge was increased) or due to reduced water input (recharge) to the model. In Model 4 maximum groundwater flow rates ('SZ max. flow') were sensitive to recharge changes, since flow rates were influenced by the resulting changes in K_{struct}.

3.3 Probability maps of catchments

The resulting probability maps for the steady state catchments from Conceptual Models 3, 4, 6 and 7 are seen in Fig. 8. The steady state catchments encompassed roughly the same area west of Sian Ka'an, and had the same east-west maximum extent. There were however also important differences, especially in the south-central part of the model area, where structures were prevalent. In Model 3, the shape of the steady state catchment was stable under parameter changes. The probability that a particular model cell was part of the steady-state catchment was either 0 or 1. In the other models the shape of the steady-state catchment was variable and probabilities ranged from 0 to 1. This was due to the different combinations of K_{struct} and K_{matrix} values in each realization. Conceptual Model 4 had the most extensive catchment area when considering all probabilities > 0. This steady state catchment and that of Model 6 were clearly influenced by the higher-permeable structures. Model 7's steady state catchment was influenced by the inflow from the hilly area, and thus bended slightly towards the south further inland. In Models 4, 6 and 7 the steady state catchments in reality also include an unknown part of the hilly area.

The estimated values of φ_{eff} ranged above or within the interval $1 \cdot 10^{-4}$ to $1 \cdot 10^{-3}$, which Worthington and Ford (2009) suggested to use in equivalent porous medium models for transport simulations that should imitate the rapid transport through caves. Only when the average matrix velocity of Model 4 was equal to 0.03 m/s, a lower φ_{eff} of $3 \cdot 10^{-5}$ was estimated. Zones of travel times to the boundary of Sian Ka'an are shown in Fig. 9, for different velocities and different scenarios. The 0–24 hr, 1–10 day and 11–50 day travel time zones correspond to the protection zones II and III of Milanović (2004) (zone III may extend to either 10 days or 50 days travel time). The 0.13–1 year, 2–10 year and 11–20 year protection zones are used by some countries as inner, middle and outer protection zones, but not specifically within karst (Chave et al., 2006).

3.4 Transient dynamics

The specific yield and the lag time of the hilly inflow was obtained from comparing measured and modelled heads at Dzula, and gave S_y= 0.4 and a lag time of about 3 months (Fig. 10). The lag time of 3 months corresponded well with a correlation between Sian Ka'an's flooding dynamics and a 3-months backward moving average of catchment precipitation (Gondwe et al., 2010).

Fits were satisfactory when comparing measured and modelled heads at all 59 wells at the four points in time where measurements were available. Median difference between measured and modelled heads was 3–14 cm for Model 4 and 1–8 cm for Model 7. Scatter plots showed no notable difference between the fits of the two models to measured heads at different times.

The modelled flooding dynamics showed most water in the Sian Ka'an wetlands in the months December–January, and least water in April to August, for both Model 4 and Model 7. This corresponds fairly well with radar-derived flooding results from August 2006 to February 2008. They showed max. flooding in December in normal years and min. flooding in May (Gondwe et al., 2010). The modelled flooding extent within SKBR (1750 to 1830 km^2) hardly varied in time. This is because the topographic distribution of values in the SRTM dataset does not reflect the actual bathymetry of the wetlands. Therefore the transient models could not be calibrated with the flooding extent time series of Gondwe et al. (2010). However, the modelled flooding extent was in the same range as that observed in the flooding maps of Gondwe et al. (2010) within SKBR's boundary (mean: 1730 km^2; min.: 1110 km^2; max.: 2090 km^2).

Lack of bathymetric data, lack of micro-topographic data, and the large grid-size used in the numerical models hampered comparison of the model results with measured water level changes from interferograms in Gondwe et al. (2010). However, overall the numerical models tended to have the same overall fringe directions as the observed interferograms, which indicates that the overall pattern of water level changes resembled reality fairly well. The simulated fringe directions in the Chunyaché slough, the Tigritos slough and the Santa Rosa slough were close to those observed (Fig. 11b and c). The observed north-south fringe direction in the Espíritu slough was not captured in the numerical models, but was likely due to micro-topographic effects (Gondwe et al., 2010), which were not captured by the topographic data used in the model. Like the observed interferograms, the modelled interferograms generally had few fringes (up to e.g. 5); thus the modelled relative surface water level changes were rather small, as they are in reality (Gondwe et al., 2010). Between the two Conceptual Models there were differences in timing of interferogram changes, but it was not possible to clearly distinguish whether one model was superior to the other. An example of a modelled and an observed interferogram from the same time period is shown in Fig. 11a and b.

4. Discussion

4.1 The impact of conceptual model uncertainty on management decision making

The steady state catchments (Fig. 8) show that the conceptual model uncertainty affects the extent of the steady state catchment. The nature of the structures determines whether the south-central area of the model domain and Cretaceous area contribute water to SKBR. In these areas agricultural activities are presently expanding, which will possibly lead to increased use of pesticides and fertilizers.

Given the limited field data availability, it is impossible to decide between the different conceptual models However, methods exist for combining the results from multiple conceptual models: Pooling (linear combination of the results with equal weights assigned to each model, Block et al., 2009 and references herein), linear regression weighting (linear combination of results, weights of each model determined from regression coefficient of observed vs. modelled conditions for each model, Block et al., 2009 and references herein), and Bayesian model averaging (e.g. Neuman, 2003; Rojas et al., 2008; 2009; Li and Tsai, 2009). For transient models the ‘hierarchical mixture of experts’ framework (Marshall et al., 2006) and kernel density estimators (Block et al., 2009) may be used to let the weight of each model in a linear combination vary in time. Moreover, non-linear weighting of conceptual models by means of artificial neural networks has been applied (Xiong et al., 2001). Combining different conceptual models typically provides more robust results than using one single conceptual model (e.g. Georgakakos et al., 2004; Rojas et al., 2008; Block et al., 2009). Combinations may however be sensitive to the assumptions used in the analysis. For instance Rojas et al. (2009) showed that Bayesian averaging methods rely not only on the posterior probabilities of each model (i.e. the weights used) but also on the prior model probabilities, i.e. the assumed probability distributions of the model input parameters.

The travel time zones in Fig. 9 show the significant influence of the choice of conceptual model, as well as φ_{eff}, on management decisions. Here, the influence of the structures on the areas that need to be protected in some way is even clearer than in the steady state catchments for Model 4 and 6. The various φ_{eff} chosen yield a very large difference in the extent of the protection zones for the models. Because it is impossible and economically unfeasible in practice to provide a high degree of aquifer protection to the whole steady state catchment, the φ_{eff} and/or actual groundwater travel times must be determined more accurately to be able to carry out efficient groundwater protection.

4.2 Discussion of the most robust modelling results

Results from all of the accepted conceptual models showed that groundwater outflow through the coastline within SKBR's boundary is 68–90 m^3/s. The groundwater that passes through Sian Ka'an is therefore a significant contribution to the marine environment, which hosts one of the most productive coral reef systems in the world, but which is also sensitive to changes in water quality (TNC, 2008; Lang et al., 1998). Therefore, it is clear that if the groundwater that flows into Sian Ka'an is protected, also a high water quality for the marine environment outside Sian Ka'an is ensured.

The overland flow within Sian Ka'an's wetlands equals about 4–12% of the total outflow from the model domain – within Sian Ka'an's boundary 7–16% of the outflow. In absolute numbers overland flow is on the order of 7–13 m^3/s. The overland flow is thus non-negligible, and constitutes an important part of the total water resource. However, groundwater flow within Sian Ka'an is much larger than the overland flow. This has to be taken into account when designing water flow and water quality monitoring networks for SKBR.

The hydrological models also show that the Sian Ka'an wetlands only exist due to recharge from the catchment. The wetlands are indeed groundwater-fed. Recharge over Sian Ka'an itself only constitutes on average about 41 mio. m^3/year, whereas the total average outflow from Sian Ka'an according to the models is ~2700–2900 mio. m^3/year, of which ~280–540 mio. m^3/year exits via the wetlands (overland flow). The timing of the flooding peaks is also different from the timing of the rainfall maximum and further indicates that Sian Ka'an's wetland dynamics is controlled by the catchment.

Main overland outflows within Sian Ka'an took place at Bahía de la Ascensión and Bahía del Espíritu Santo. The average water depth in the wetlands varied 0.5 to 1 m in the transient model runs, with the maximum varying from 1.2 to 2.5 m. The real water depth may be somewhat different locally, because the model does not take local bathymetry into account. Given the amount of recharge and the high aquifer transmissivities, groundwater abstractions in the catchment are unlikely to have a detrimental effect on the wetlands. Only direct water abstractions from the wetlands themselves could affect the wetlands' water quantities negatively, because the freshwater lens is thinner in this near-coastal zone, and since wetland ecosystems depend on certain hydroperiods, flooding frequencies, flooding areas and flooding depths (Powell et al., 2008; Acreman and Dunbar, 2004).

From the recharge estimates and the modelling results the overall water balance of the model domain can be determined. Direct recharge via infiltration constitutes 17% ±3% of the mean annual precipitation in the model domain (recharge: 4400 mio. m^3/year ± 700 mio. m^3/year). Boundary inflows from the hilly area may be of similar magnitude. Water exits the domain through overland flow (4–12%) and groundwater flow (88–96%). The latter is distributed between coastal outflow to the sea, and groundwater outflow towards the north via the Holbox fracture zone. The distribution between these two groundwater sinks is presently uncertain. However, it appears relatively certain that there *is* some water flowing through the Holbox fracture zone from south to north on average. Groundwater flow through the Holbox is in agreement with the dye tracing results of Beddows and Hendrickson (2008).

The modelled flooding dynamics and the flooding dynamics from Gondwe et al. (2010) show that the months April to August are probably the most vulnerable times of the wetlands, since any water-borne pollutants may be less diluted at these times and low water amounts may create increased vulnerability to reduction in water quantity. The high flow periods (December–January) and the medium flow periods (in between) are however also important to maintain the natural cycle of the wetlands.

It is worth noting the dependence of ET_a on the depth to groundwater in areas where the groundwater is located 0–30 mbg. This finding has not previously been shown for the Yucatan Peninsula. The only study known to the authors, which investigates water source of the vegetation in the region, has not shown that trees rely on groundwater as a source of water (Querejeta et al., 2007). However, the correlation between ET_a and depth to groundwater seen in Fig. 7 indicates that uptake of groundwater by trees and plants in the model domain does seem to have some importance in the areas where groundwater is <30 m from the surface. The relation between ET_a and depth to groundwater appears to be represented by a segmented line (Banta, 2000; Luo et al. 2009). In another karstic aquifer, yet not tropical, this has also been observed – roots could reach as deep as 25 mbg, and the deep roots were found specially optimized for deep water uptake (Jackson et al., 1999; McElron et al., 2004; Pockman et al., 2008). The areas with groundwater ≤ 8 mbg seem to be groundwater-dependent ecosystems – they have full access to water enabling them to transpire at potential rate. These areas are shown in Fig. 12.

The discharge pr. km of coast was in all models estimated to be about 0.3–0.4 $m^3/s/km$, which fits well with other estimates. The discharge along the coast near Tulum may or may not be higher than this (~1 $m^3/s/km$). The K_{coast} calibrated as < K_{matrix} (except, perhaps, around Tulum) shows that indeed there appears to be restriction to outflow at the coast. A freshwater lens thickness > 0 m at the coast in the whole model domain results from this. For local management purposes this is important to note. The extensive hotel construction taking place along the coast at Riviera Maya, and proposed for the Costa Maya, should ensure that this coastal restriction to outflow is maintained. The coastal freshwater resources are already limited. On a local (plot) scale they may be further reduced if the coastal restriction to outflow is breached, and since hotels often abstract water from their own plot (Beddows, 2002), they should have an interest in maintaining the fresh water lens as thick as possible near the coast.

The K_{matrix} calibrated in the models appears realistic. It is in the same order of magnitude as that estimated from geophysical measurements of depth to the halocline in Gondwe et al. (in review) (estimated to be 0.6 m/s when recharge constitutes ~400 mm/year, as in the case where 100% inflow from the hilly area is present).

5. Conclusions

Through automatic calibration and stochastic modelling, probability maps of the steady state catchment for the groundwater-dependent Sian Ka'an wetlands have been calculated. The use of different conceptual models shows that the conceptual model structure will have a huge impact on management decisions for karst aquifers. The same applies for the effective porosity, as it determines the extent of protection zones derived from groundwater travel times. Multiple Model Simulation is a useful way to examine the effect of conceptual uncertainty. Furthermore, through this method and scenarios that vary uncertain model input parameters, directions for further research can be obtained, as these methods reveal the most sensitive concepts and parameters for a management perspective. It is important to further investigate the properties of the structures – specifically whether they conduct water flow more easily than the surrounding matrix. It should also be determined whether coastal leakage is larger near Tulum than elsewhere in the model domain. Tracer testing could be carried out in the catchment to better determine φ_{eff} and the extent of the travel time zones. Inflow from the Cretaceous area may be important. The surface water catchments (Fig. 4) may be an acceptable first-order approach to determine where the water in the hilly area comes from. However, further studies of the hilly area's hydrogeology are warranted.

The spatial outputs from the hydrological models enable land use zonation based on aquifer protection concepts, and enable aquifer vulnerability mapping. Vulnerability mapping is applicable for well-field and ecosystem protection and management, but can also be valuable for guiding urban and tourism development plans in the area. The water balance insights from the hydrological modelling shows the importance of both the overland flows and the groundwater flows within Sian Ka'an, both for Sian Ka'an's ecosystems and for the marine environment, which is the final recipient of the outflows. The hydrological modelling indicates that groundwater may exit the model domain to the north through the Holbox fracture zone. This is important in order to understand the peninsular-scale hydrologic relation between regions.

6. Acknowledgements

We gratefully acknowledge financial support from the WWF Verdensnaturfonden/Aase & Ejnar Danielsens Fond 2006 and 2007, the COWIfoundation, Amigos de Sian Ka'an and the Technical University of Denmark.

7. References

Acreman, M., Dunbar, M.J., 2004. Defining environmental river flow requirements – a review. Hydrol. and Earth Syst. Sci. 8 (5), 861–876.

Arfib, B., de Marsily, G., 2004. Modeling the salinity of an inland coastal brackish karstic spring with a conduit-matrix model. Water Resour. Res. 40 (11), W115061–W1150610.

ASK, 2003. Tratamiento de Aguas Residuales. Report prepared by Amigos de Sian Ka'an A. C. (ASK). Available on the cd-rom of the workshop: Construyendo las Bases Para la Conservación del Agua y su Biodiversidad Asociada en la Península de Yucatan". 10 y 11 de noviembre 2003, Cancún Quintana Roo, Organizado por Amigos de Sian Ka'an, The Nature Conservancy y la Comisión de Áreas Naturales Protegidas.

Atkinson, T.C., 1977. Diffuse flow and conduit flow in limestone terrain in the Mendip Hills, Somerset (Great Britain). J. Hydrol. 35, 93–110.

Back, W., Hanshaw, B.B., Pyle, T.E., Plummer, L.N., Weidie, A.E., 1979. Geochemical significance of groundwater discharge and carbonate solution to the formation of Caleta Xel Ha, Quintana Roo, Mexico. Water Resour. Res. 15 (6), 1521–1535.

Banta, E.R., 2000. MODFLOW-2000. The U.S. Geological Survey modular ground-water model – documentation of packages for simulating evapotranspiration with a segmented function (ETS1) and drains with return flow (DRT1). U.S. Geol. Surv. Open-File Rep. 00-466. 127 pp.

Bauer, S., Liedl, R., Sauter, M., 2003. Modeling of karst aquifer genesis: influence of exchange flow. Water Resour. Res. 39 (10), SBH61–SBH612.

Bazante ,J., Jacobi, G., Solo-Gabriele, T., Reed, D., Mitchell-Bruker, S., Childers, D.L., Leonard, L., Ross, M., 2006. Hydrologic measurements and implications for tree island formation within Everglades National Park. J. Hydrol. 329, 606–619. doi: 10.1016/j.jhydrol.2006.03.011.

Beddows, P.A., 2003. Cave hydrology of the Caribbean Yucatan coast. Assoc. for Mex. Cave Stud.. Bull. 11. Austin, TX, USA.

Beddows, P.A., 2002. Where does the sewage go? The karst groundwater system of Municipalidad Solidaridad, Quintana Roo. Assoc. for Mex. Cave Stud. Activities Newsl. 25, 47–52.

Beddows, P.A., 2004. Groundwater hydrology of a coastal conduit carbonate aquifer: Caribbean coast of the Yucatán Peninsula, México. PhD thesis. Sch. of Geogr. Sci.. Univ. of Bristol, UK.

Beddows, P.A., Smart, P.L., Smith, S. L., Whitaker, F.F., 2005. Potential for inland dispersal of injection well effluent in coastal carbonate aquifers: evidence from Caribbean Yucatan coast. Proc. 2005 Natl. Cave and Karst Manage. Symp., Albany, NY, USA.

Beddows, P.A., Smart, P.L., Whitaker, F.F., Smith, S.L., 2007. Decoupled fresh-saline groundwater circulation of a coastal carbonate aquifer: Spatial patterns of temperature and specific electrical conductivity. J. Hydrol. 346, 18–32.

Beddows, P.A., Hendrickson, M.R., 2008. When the survey is not enough: temperature, salinity, and dye tracing reveal flow paths. In: Elliot, W.R., (Ed.). Proc. 2007 Natl. Cave and Karst Manage. Symp., St. Louis, Mo., USA. 198–203.

Birk, S., Liedl, R., Sauter, M., Teutsch, G., 2003. Hydraulic boundary conditions as a controlling factor in karst genesis: a numerical modeling study on artesian conduit development in gypsum. Water Resour. Res. 39 (1), SBH21–SBH214.

Block, P., Souza Filho, F.A., Sun, L., Kwon, H.-H., 2009. A streamflow forecasting framework using multiple climate and hydrological models. J. Am. Water Res. Assoc. 45 (4), 828–843. doi: 10.111/j.1752-1688.2009.00327.x.

Charvet, G., 2009. Exploration, modeling and management of groundwater resources in Northern Quintana Roo, Mexico. Master thesis. Dept. of Environ. Eng., Tech. Univ. of Den., Kgs. Lyngby, Den.

Chave, P., Howard, G., Schijven, J., Appleyard, S., Fladerer, F., Schimon, W., 2006. Groundwater protection zones. Chapter 17 in: Schmoll, O., Howard, J., Chilton, J., Chorus, I. (Eds.). Protecting groundwater for health - Managing the quality of drinking-water. WHO. IWA Publ. 465–492. ISBN 92-4-154668-9.

Cheng, J.M, Chen, C.X., 2005. An integrated linear/non-linear flow model fort he conduit-fissure-pore media in the karst triple void aquifer system. Environ. Geol., 47, 163–174. doi: 10.1007/s00254-004-1128-7.

Durlofsky, L.J., 1992. Representation of grid block permeability in course scale models of randomly heterogeneous porous media. Water Resour. Res. 28 (7), 1791–1800.

Eamus, D., Froend, R., 2006. Groundwater-dependent ecosystems: the where, what and why of GDEs. Aust. J. of Bot. 54, 91–96.

Escolero, O.A., Marín, L.E., Steinich, B., Pacheco, J., 2000. Delimitation of a hydrogeological reserve for a city within a karstic aquifer: the Merida, Yucatan example. Landsc. and Urban Plan. 51, 53–62.

Fideicomiso para la Promoción Turística de la Rivera Maya, 2004. Estadísticas de Riviera Maya.

Georgakakos, K., Seo, D.-J., Gupta, H., Shaake, J., Butts, M.B., 2004. Towards the characterization of streamflow simulation uncertainty through multimodel ensembles. J. Hydrol. 298, 222–241. doi: 10.1016/j.jhydrol.204.03.037.

Geyer, T., Birk, S., Licha, T., Liedl, R., Sauter, M., 2007. Multitracer test approach to characterize reactive transport in karst aquifers. Ground Water 45 (1), 36–45. doi: 10.1111/j.1745-6584.2006.00261.x.

Gondwe, B.R.N., Hong, S.-H., Wdowinski, S., Bauer-Gottwein, P., 2010. Hydrologic dynamics of the ground-water-dependent Sian Ka'an wetlands, Mexico, derived from InSAR and SAR data. Wetl. (in press).

Gondwe, B.R.N, Lerer, S., Stisen, S., Marín, L., Rebolledo-Vieyra, M., Merediz-Alonso, G., Bauer-Gottwein, P. (in review). Hydrogeology of the south-eastern Yucatan Peninsula: New insights from water level measurements, geochemistry, geophysics and remote sensing. Submitted to J. Hydrol..

Gondwe, B.R.N., Ottowitz, D., Supper, R., Merediz Alonzo, G., Bauer-Gottwein, P., (submitted). Exploring regional-scale preferential flow paths in the karst aquifer of southern Quinana Roo, Mexico. Submitted to J. Hydrol..

Gonzalez-Herrera, R.A., 1984. Correlacion de muestras de roca en pozos de la ciudad de Merida. Civil engineering thesis. Facultad de Ingeneria, Universidad de Yucatan, Merida, Yucatan, Mexico. 129 pp.

Graham, D.N., Butts, M.B., 2006. Flexible integrated watershed modeling with MIKE SHE. Chapter 10 in Singh, V. P, Frevert, D.K. (Eds.). Watershed models. CRC Press. 245–269. ISBN 0-8493-3609-0.

Hanshaw, B.B., Back, W.,1980. Chemical mass-wasting of the northern Yucatan Peninsula by groundwater dissolution. Geol., 8, 222-224.

Hastings, W.K., 1970. Monte Carlo sampling methods using Markov chains and their applications. Biometrika 57 (1), 97–109.

Hendricks Franssen. H.-J., Stauffer, F., Kinzelbach, W., 2004. Joint estimation of transmissivities adn recharges – application: stochastic characterization of well capture zones. J. Hydrol. 294, 87–102. doi: 10.1016/j.jhydrol.2003.10.021.

Hill, M.C.,1990. Preconditioned Conjugate-Gradient 2 (PCG2), a computer program for solving ground-water flow equations. U.S. Geol. Surv. Water-Res. Investig. Report 90-4048. Second Printing, 2003.

Højberg, A.L., Refsgaard, J.C., 2005. Model uncertainty – parameter uncertainty versus conceptual models. Water Sci. and Technol. 52 (6), 177–186.

INEGI, 1997. Carta de uso de suelo y vegatación (vegetation map). Recursos electónicos. Escala 1:250,000. Instituto Nacional de Estadística Geogrfía e Informática (INEGI). Shape file.

ITC, 2005. ILWIS 3.3 Academic. International Institute for Geo-Information Science and Earth Observation (ITC). Software for remote sensing and GIS.

Jackson, R.B., Moore, L.A., Hoffmann, W.A., Pockman, W.T., Linder, C.R., 1999. Ecosystem rooting depth determined with caves and DNA. Proc. of the Natl. Acad. of Sci. USA 96, 11387–11392.

Kenkmann, T., Schönian, F., 2006. Ries and Chicxulub: Impact craters on Earth provide insights for Martian ejecta blankets. Meteorics and Planet. Sci. 41 (10), 1587–1603.

Kilroy. G., Coxon, C., Ryan, J., O'Connor, A., Daly, D., 2005. Groundwater and wetland management in the Shannon river basin (Ireland). Environ. Sci. & Policy 8, 219–225.

Kiraly, L., 2003. Karstification and groundwater flow. Speleogenesis and Evolut. of Karst Aquifers 1 (3). 26 pp.

Knochenmus, L.A., Robinson, J.L., 1996. Descriptions of anisotropy and heterogeneity and their effect on ground-water flow and areas of contribution to public supply wells in a karst carbonate aquifer system. U.S. Geol. Surv. Water-Supply Pap. 2475. 46 pp. ISBN 0-607-86216-5.

Kovacs, A., Perrochet, P., Király, L., Jeannin, P.-Y., 2005. A quantitative method for the characterisation of karst aquifers base don spring hydrograph analysis. J. Hydrol. 303, 152–164. doi: 10.1016/j.jhydrol.2004.08.023.

Krause, S., Heathwaite, A.L., Miller, F., Hulme, P., Crowe, A., 2007. Groundwater-dependent wetlands in the UK and Ireland: controls, functioning and assessing the likelihood of damage from human activities. Water Resour. Manage. 21, 2015–2025. doi: 10.1007/s11269-007-9192-x.

Krekeler, M.P.S., Probst, P., Samsonov, M., Tselepis, C.M., Bates, W., Kearns, L.E., Barry Maynard, J., 2007. Investigations of subsurface flow constructed wetlands and associated geomaterial resources in the Akumal and Reforma regions, Quintana Roo, Mexico. Environ. Geol. 53, 709–726. doi: 10.1007/s00254-007-0684-z.

Lang, J., Alcolado, P., Carricart-Ganivet, J.P., Chiappone, M., Curran, A., Dustan, P., Gaudian, G., Geraldes, F., Gittings, S., Smith, R., Tunnell, W., Wiener, J., 1998. Status of coral reefs in the northern areas of the wider Caribbean. Chapter 8 in Wilkinson, C., (Ed.). Status of coral reefs of the world: 1998. Aust. Inst. of Mar. Sci. Townsv., Aust.

Larocque, M., Banton, O., Ackerer, P., Razack, M., 1999. Determining karst transmissivities with inverse modeling and an equivalent porous media. Ground Water 37 (6), 897–903.

Larocque, M., Banton, O., Razack, M., 2000. Transient-state history matching of a karst aquifer ground water flow model. Ground Water 38 (6), 939–946.

Li, G., Loper, D. E., Kung, R., 2008. Contaminant sequestration in karstic aquifers: Experiments and quantfication. Wat. Resour. Res. 44, W02429, doi: 10.1029/2006WR005797.

Li, X., Tsai, F. T.-C., 2009. Bayesian model averaging for groundwater head prediction and uncertainty analysis using multimodel and multimethod. Water Resour. Res. 45, W09403. doi: 10.1029/2008WR007488.

Liedl, R., Sauter, M., Hückinghaus, D., Clemens, T., Teutsch, G., 2003. Simulation of the development of karst aquifers using a coupled continuum pipe flow model. Water Resour. Res. 39 (3), SBH61-SBH611.

Lindgren, R.J., Dutton, A.R., Hovorka, S.D., Worthington, S.R.H., Painter, S., 2005. Conceptualization and simulation of the Edwards Aquifer, San Antonio Region, Texas. In: Kuniansky, E. (Ed.). Sci. Investig. Rep. 2005-5160, 48–57.

Lopez-Ramos, E., 1975. Geological summary of the Yucatan Peninsula. Chap. 7. In: Nairn, A.E.M., Stehli, F.G. (Eds.) The ocean basins and margins. Vol. 3 The Gulf of Mexico and the Caribbean. Plenum Press, NY, USA.

Luo, Y.F., Peng, S.Z., Khan, S., Cui, Y.L., Wang, Y., Feng, Y.H., 2009. A comparative study of groundwater evapotranspiration functions. In: Anderssen, R.S., Braddock, R.D., Newham, L.T.H.(Eds.). Proc. from the 18th World IMACS Congress and MODSIM09 International Congress on Modelling and Simulation. Cairns, Australia, 13–17 July 2009.

Marín, L.E., Steinich, B., Pacheco, J. Escolero, O.A., 2000. Hydrogeology of a contaminated sole-source karst aquifer, Mérida, Yucatán, Mexico. Geofís. Int. 49 (4), 359–365.

Marshall, L., Sharma, A., Nott, D., 2006. Modeling the catchment via mixtures: Issues of model specification and validation. Water Resour. Res. 42, W11409. doi: 10.1029/2005WR004613.

Martin, J.B., Screaton, E.J., 2001. Exchange of matrix and conduit water with examples from the Floridan aquifer. In : Kuniansky, E. (Ed.). Water-Resources Investigations Report 01-4011, U.S. Geological Survey. 38–44

Mazzotti, F.J., Fling, H.E., Merediz, G., Lazcano, M., Lasch, C., Barnes, T., 2005. Conceptual ecological model of the Sian Ka'an Biosphere Reserve, Quintana Roo, Mexico. Wetl. 25 (4), 980–997.

McElrone, A.J., Pockman, W.T., Martínez-Vilalta, J., Jackson, R. B., 2004. Variation in xylem structure and function in stems and roots of trees to 20 m depth. New Phytologist 163, 507–517

Milanović, P.T., 2004, Water resources engineering in karst. CRC Press, Florida, USA. 312 pp. ISBN 1-56670-671-8.

Miller, T.E., 1996. Geologic and hydrologic controls on karst and cave development in Belize. J. of Cave and Karst Stud. 58 (2), 100–120.

Moore, Y.H., Stoessell, R.K., Easley, D.H., 1992. Fresh-water/sea-water relationship within a ground-water flow system, northeastern coast of the Yucatan Peninsula. Ground Water 30 (3), 343–350.

Morales Barbosa, J.J., 1992. Los humedales, un mundo olvidado. Series: Sian Ka'an, Introducción a los Ecosistemas de la Península de Yucatan. Amigos de Sian Ka'an A. C. Impresos MARCA, Mérida, Yucatán, Mexico.

Münch, Z., Conrad, J., 2007. Remote sensing and GIS based determination of groundwater dependent ecosystems in the Western Cape, South Africa. Hydrogeol. J. 15, 19–28. doi: 10.1007/s10040-006-0125-1.

Neuman, S.P., 2003. Maximum likelihood Bayesian averaging of uncertain model predictions. Stoch. Environ. Res. and Risk Assess. 17, 291–305. doi:10.1007/s00477-003-0151-7.

Neuman, S.P., Wierenga, P.J., 2003. A comprehensive strategy of hydrogeologic modeling and uncertainty analysis for nuclear facilities and sites. Univ. of Ariz., Rep. NUREG/CR-6805.

Neuman, B.R., Rahbek, M.L., 2007. Modeling the groundwater catchment of the Sian Ka'an Reserve, Quintana Roo. Assoc. for Mex. Cave Stud.. Bull. 18. Austin, TX, USA.

Pacheco, J., Marín, L., Cabrera, A., Steinich, B., Escolero, O., 2001. Nitrate temporal and spatial Patterns in 12 water-supply wells, Yucatan, Mexico. Environ. Geology 40 (6), 708–715.

Perry, E., Velazquez-Oliman, G., Marin, L., 2002. The hydrogeochemistry of the karst aquifer system of the northern Yucatan Peninsula, Mexico. Int. Geol. Rev. 44, 191–221.

Perry, E., Paytan, A., Pedersen, B., Velazquez-Oliman, G., 2009. Groundwater geochemistry of the Yucatan Peninsula, Mexico: constraints on stratigraphy and hydrogeology. J. Hydrol. 367 (1–2), 27–40. doi: 10.1016/j.jhydrol.2008.12.026.

Peterson, E.W., Wicks, C.M., 2005. Fluid and solute transport from a conduit to the matrix in a carbonate aquifer system. Mathematical Geology 37 (8), 851–867. doi: 10.1007/s11004-005-9211-5.

Peterson, E.W., Wicks, C.M., 2006. Asessing the importance of conduit geometry and physical parameters in karst systems using the storm water management model (SWMM). J. Hydrol. 329, 294–305. doi: 10.1016/j.jhydrol.2006.02.017.

Pockman, W.T., McElrone, A.J., Bleby, T.M., Jackson, R.B., 2008. The structure and function of roots of woody species on the Edwards Plateau, Texas, USA, Eos Trans. AGU, 89(23), Jt. Assem. Suppl., Abstract H34A-02.

Pope, K.O., Dahlin, B. H., 1989. Ancient Maya wetland agriculture: new insights from ecological and remote sensing research. J. of Field Archeol. 16 (1), 87–106.

Pope, K.O., Ocampo, A.C., Fischer, A.G., Vega, F.J., Ames, D.E., King Jr., D.T., Fouke, B.W., Wachtman, R.J., Kletetschka, G., 2005. Chicxulub impact ejecta deposits in southern Quintana Roo, México, and central Belize. p. 171–190. In: Kenkmann, T., Hörz, F., Deutsch, A. (Eds.) Large meteorite impacts III. Geol. Soc. Am. Spec. Pap. 384.

Powell, S.J., Letcher, R.A., Croke, B.F.W., 2008. Modelling floodplain inundation for environmental flows: Gwydir wetlands, Australia. Ecol. Modelling 211, 350–362.

Querejeta, J.I., Estrada-Medina, H., Allen, M.F,. Jiménez-Osornio, J.J., 2007. Water resource partitioning among trees growing on shallow karst soils in a seasonally dry tropical climate. Oecologia 152, 26–36.

Refsgaard, J.C., Storm, B., 1995. MIKE SHE. In: Singh, V.P. (Ed.). Computer models in watershed hydrology. Water Resour. Publ., Colo., USA, 809–846.

Refsgaard, J.C., van der Sluijs, J.P., Brown, J., van der Keur, P., 2006. A framework for dealing with uncertainty due to model structure error. Adv. in Water Resour. 29, 1586–1597.

Refsgaard, J. C., van der Sluijs, J.P., Højberg, A.L., Vanrolleghem, P.A., 2007. Environ. Modelling & Softw. 22, 1543–1556. doi: 10.1016/j.envsoft.22007.02.004.

Rojas, R., Feyen, L., Dassargues, A., 2008. Conceptual model uncertainty in groundwater modeling: Combining generalized likelihood uncertainty estimation and Bayesian model averaging. Water Resour. Res. 44, W12418. doi: 10.1029/2008WR006908.

Rojas, R., Feyen, L., Dassargues, A., 2009. Sensitivity analysis of prior model probabilities and the value of prior knowledge in the assessment of conceptual model uncertainty in groundwater modelling. Hydrol. Process. 23, 1131–1146. doi: 10.1002/hyp.7231.

Rosencrantz, E., 1990. Structure and tectonics of the Yucatan Basin, Caribbean Sea, as determined from seismic reflection studies. Tectonics 9 (5), 1037–1059.

Sánchez-Sánchez, O., Islebe, G.A., 2002. Tropical forest communities in southeastern Mexico. Plant Ecol. 158, 183–200.

Scanlon, B.R., Mace, R.E., Barrett, M.E., Smith, B., 2003. Can we simulate regional groundwater flow in a karst system using equivalent porous media models? Case study, Barton Springs Edwards Aquifer, USA. J. Hydrol. 276, 137–158. doi: 10.1016/S0022-1694(03)00064-7.

Schönian, F., Stöffler, D., Kenkmann, T., Wittmann, A., 2004. The fluidized Chicxulub ejecta blanket, Mexico: Implications for Mars. Poster, 35th Annu. Lunar and Planet. Sci. Conf., Leag. City, TX, USA.

Schönian,F., Tagle, R., Stöffler, D., Kenkmann, T., 2005. Geology of southern Quintana Roo (Mexico) and the Chicxulub ejecta blanket. Abstract #2389. 36th Annu. Lunar and Planet. Sci. Conf., Leag. City, TX, USA.

SGM, 2007. Carta geológica de México. Escala 1:2,000,000. 6a edición. Servicio Geológico Mexicano (SGM).

Smart, P.L., Beddows, P.A., Coke, J., Doerr, S., Smith, S., Whitaker, F.F., 2006. Cave development on the Caribbean coast of the Yucatan Peninsula, Quintana Roo, Mexico. In: Harmon, R.S., Wicks, C. (Eds.) Perspectives on karst geomorphology, hydrology and geochemistry – A tribute volume to Derek C. Ford and William B. White. Geol. Soc. Am.. Spec. Pap. 404, 105–128.

Southworth. C.S., 1985. Applications of remote-sensing data, eastern Yucatan. p. 12–19. In: Ward, W.C., Weidie, A.E., Back, W. (Eds.) Geology and hydrogeology of the Yucatan and Quaternary geology of northeastern Yucatan Peninsula. New Orleans Geol. Soc. Publ., New Orleans, LA, USA.

Spiessl, S.M., Prommer, H., Licha, T., Sauter, M., Zheng, C., 2007. A process-based reactive hybrid transport model for coupled discrete conduit-continuum systems. J. Hydrol. 347, 23–34.

Stauffer, F., Attinger, S., Zimmermann, S., Kinzelbach, W., 2002. Uncertainty estimation of well catchments in heterogeneous aquifers. Water Resour. Res. 38 (11), 1238. doi: 10.1029/2001WR000819.

Stauffer, F., Guadagnini, A., Butler, A., Hendricks Franssen, H.-J., Van de Wiel, N., Bakr, M., Riva, M., Guadagnini, L., 2005. Delineation of source protection zones using statistical methods. Water Resour. Manage. 19, 163–185. doi: 10.1007/s11269-005-3482-7.

Stisen, S., Sandholt, I., Nørgaard, A., Fensholt, R., Høegh Jensen, K., 2008. Combining the triangle method with thermal intertia to estimate regional evapotranspiration – Applied to MSG-SEVIRI data in the Senegal River basin. Remote Sens. Environ. 112, 1242–1255.

Supper, R., Motschka, K., Ahl, A., Bauer-Gottwein, P., Gondwe, B., Merediz Alonso, G., Römer, A., Ottowitz, D., Kinzelbach, W., 2009. Spatial mapping of submerged cave systems by means of airborne electromagnetics: an emerging technology to support protection of endangered karst aquifers. Near Surf. Geophys. 7 (5), 613–627. doi: 10.3997/1873-0604.2009008.

Teutsch, G., Sauter, M., 1991. Groundwater modeling in karst terranes: Scale effects, data acquisition and field validation. Proc. 3rd conf. on hydrogeology, ecology, monitoring and management of groundwater in karst terranes. Nashv., Tenn., USA. Natl. Ground Water Assoc., Dublin, Ohio, USA, 17–34.

The MathWorks. The software Matlab, version R2008b.

Thomas, C., 1999. Aspects hydrogéologiques du Yucatan (Mexique). Karstologia 34 (2), 9–22.

TNC, 2008. Sian Ka'an Biosphere Reserve. Published on the website Parks in Peril by The Nature Concervancy (TNC). Accessed on URL: http://www.parksinperil.org/wherewework/mexico/protectedarea/siankaan.html November 2009.

Urrutia-Fucugauchi, J., Chavez-Aguirre, J.M., Pérez-Cruz, L., De la Rosa, J.L., 2008. Impact ejecta and carbonate sequence in the eastern sector of the Chicxulub crater. C. R. Geosci. 340, 801–810.

USGS. 2006. Shuttle Radar Topography Mission, 3 Arc Second, Finished 2.0. U.S. Geol. Surv. Glob. Land Cover Facil., Univ. of Maryland, College Park, Md. February 2000.

Vacher, H.L., 1988. Dupuit-Ghyben-Herzberg analysis of strip-island lenses. Geol. Soc. Am. Bull. 100 (4), 580–591.

Vassolo, S., Kinzelbach, W., Schäfer, W., 1998. Determination of a well head protection zone by stochastic inverse modelling. J. Hydrol. 206, 268–280.

Weidie, A.E., 1985. Geology of Yucatan Platform. p. 1–12. In: Ward, W.C., Weidie, A.E., Back, W. (Eds.) Geology and hydrogeology of the Yucatan and Quaternary geology of northeastern Yucatan Peninsula. New Orleans Geol. Soc. Publ., New Orleans, LA, USA.

White, W.B., 1999. Conceptual models for karstic aquifers. In: Palmer, A.N., Palmer, M.V., Sasowsky, I.D. (Eds.). Karst modeling. Spec. Publ. 5, The Karst Waters Institute, Charles Town, West Virginia, USA, 11–16.

Worthington, S.R.H., 2003. A comprehensive strategy for understanding flow in carbonate aquifer. Speleogenesis and Evol. of Karst Aquifers 1 (1), 1–8.

Worthington, S.R.H., Ford, D.C., 2009. Self-organized permeability in carbonate aquifers. Ground Water 47 (3), 326–336. doi: 10.1111/j.1745-6584.2009.00551.x.

Xiong, L., Shamseldin, A.Y., O'Connor, K.M., 2001. A non-linear combination of the forecasts of rainfall-runoff models by the first-order Takagi-Sugeno fuzzy system. J. Hydrol. 245, 196–217.

Figure captions

Fig. 1 Geology of the Yucatan Peninsula, modified from SGM (2007). Oldest sediments dated as Cretaceous instead of Paleocene, based on Schönian (2005) and Lopez-Ramos (1975) (Ichaiche Formation). Topography from SRTM (USGS, 2006) overlain as grey-scaled transparent. Study area outlined with thick grey polygon, model domain outlined as thick black polygon. Coordinates are UTM zone 16N, WGS84 datum and ellipsoid

Fig. 2 The different conceptual models used in the Multiple Model Simulation

Fig. 3 Measured depth to halocline vs. the modelled depth to halocline, estimated using the Dupuit-Ghyben-Herzberg relation and modelled groundwater heads

Fig. 4 a) Automatically delineated surface water catchments in the hilly area; b) The overall catchments used to estimate inflow through the boundary from the hilly Cretaceous area. Structures and faults from Gondwe et al. (submitted; 2010)

Fig. 5 Distribution of *K*-values in the models, and location of boundaries

Fig. 6 Measured vs. modelled heads for Conceptual Models 1–4, 6 and 7

Fig. 7 Actual (ET_a) and reference (ET_{ref}) evapotranspiration, as well as Enhanced Vegetation Index from MODIS (EVI), plotted against modelled depth to groundwater

Fig. 8 Probability (Prob.) of a cell belonging to Sian Ka'an's steady state catchment, for Conceptual Models 3, 4, 6 and 7

Fig. 9 Modelled travel time zones for different conceptual models and different values of φ_{eff}, adjusted to give the indicated modelled water travel times (v)

Fig. 10 Measured and modelled Dzula hydrograph, with different values of S_y and lag times for the hilly inflow

Fig. 11 Observed (a) and modelled (b) interferogram for Oct–Dec 2007, and observed interferogram examples from other dates showing characteristic fringes of the interferograms which are also found in the modelled interferogram (c-e). Modelled example was generated by Conceptual Model 4. Legend shows relative water level increase or decrease. c) Chunyaché slough, Jun-Aug 2007; d) Tigritos and Santa Rosa slough Jun-Aug 2007; e) Espíritu slough, Nov-Dec 2006

Fig. 12 Modelled depth to groundwater below topographic surface. Areas with groundwater $\leq$ 8 mbg are likely to be groundwater-dependent ecosystems (see text). Areas with groundwater 8–30 mbg may be partially groundwater dependent (see text). White areas have overland water.

Figures

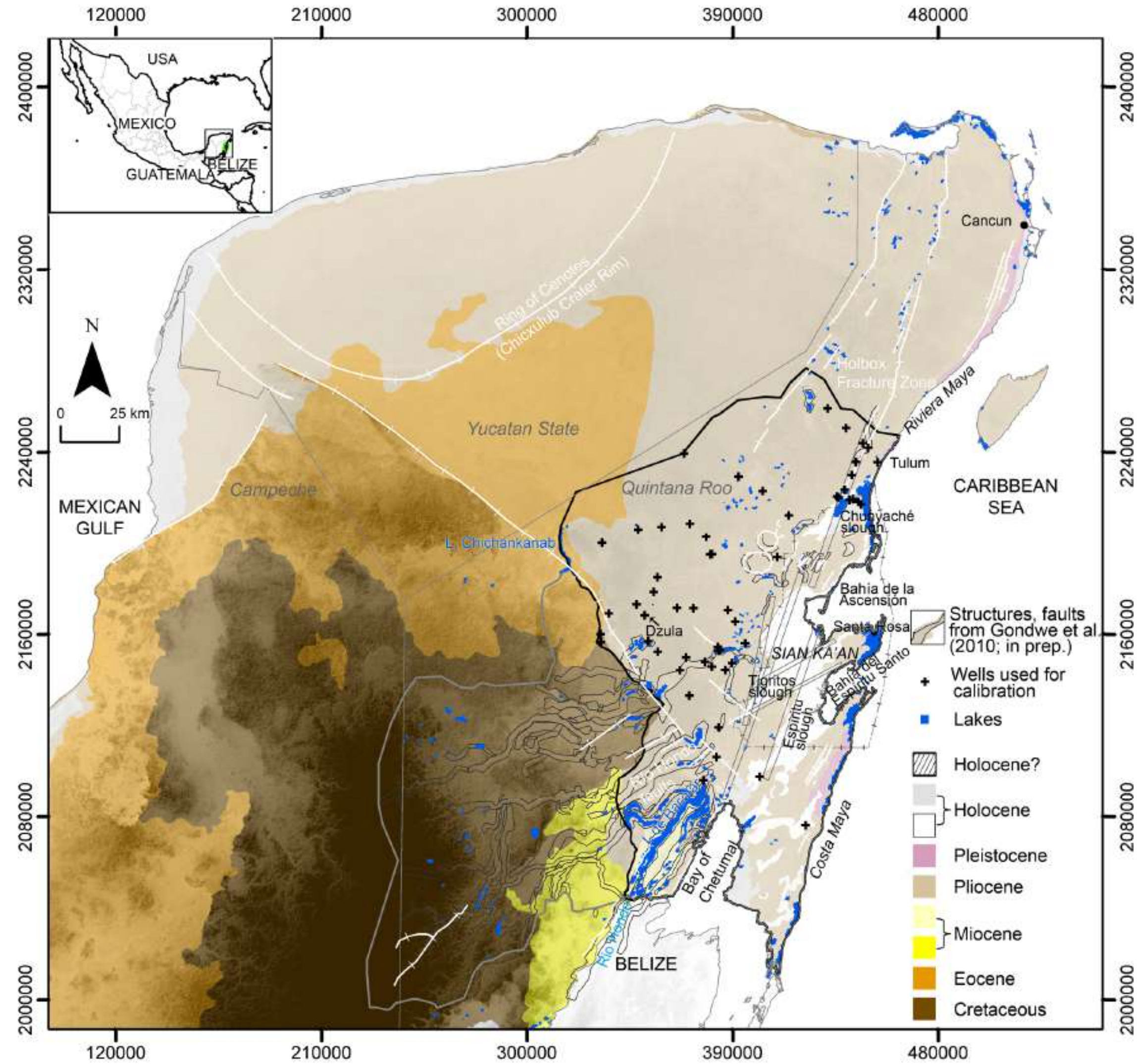

Fig. 1

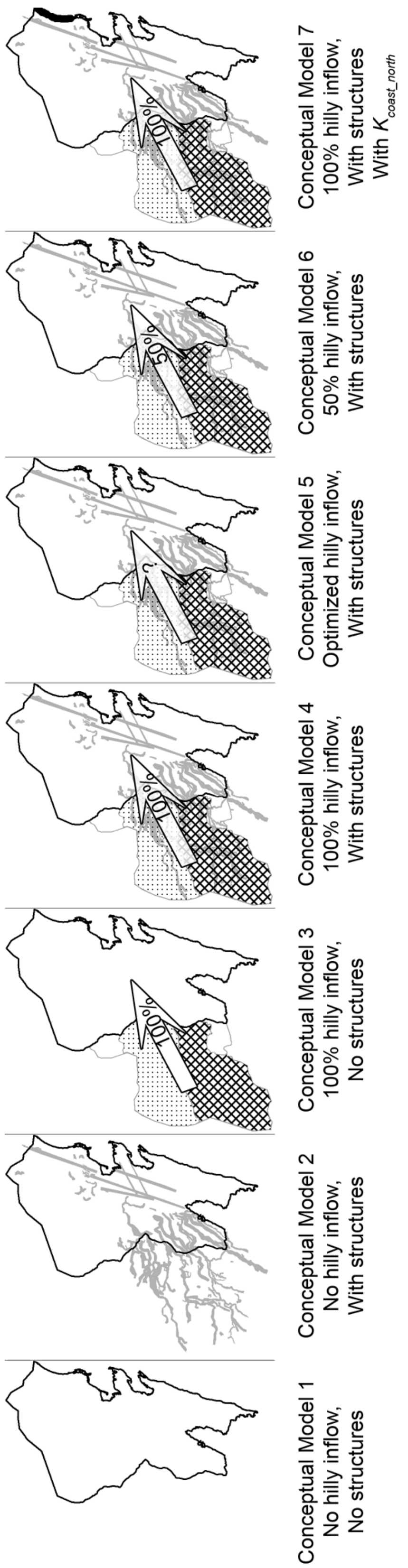

Fig. 2 (rotated 90 degrees)

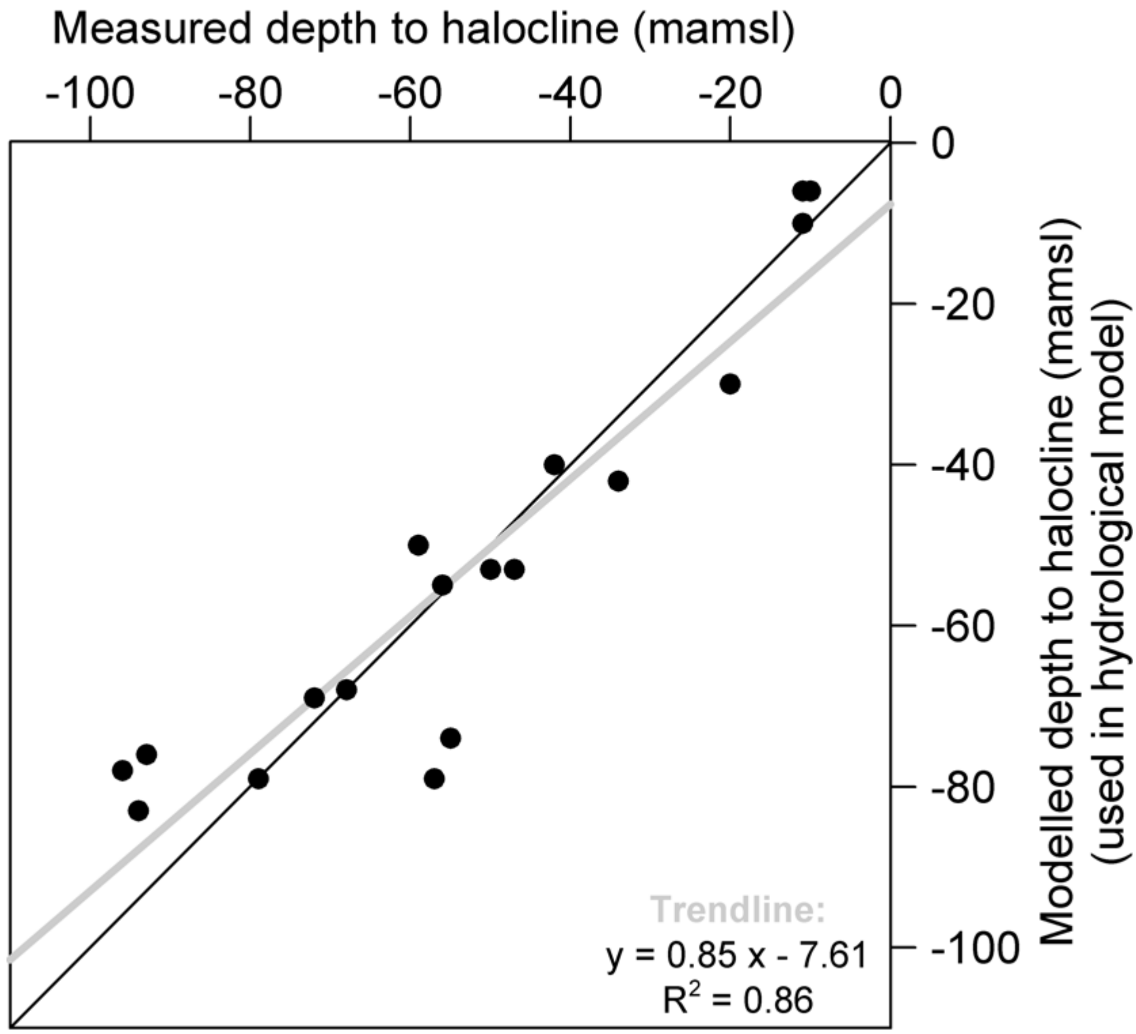

Measured depth to halocline (mamsl)
-100
-80
-60
-40
-20
0
Modelled depth to halocline (mamsl)
(used in hydrological model)
0
-20
-40
-60
-80
-100
Trendline:
y = 0.85 x - 7.61
R^2 = 0.86

Fig. 3

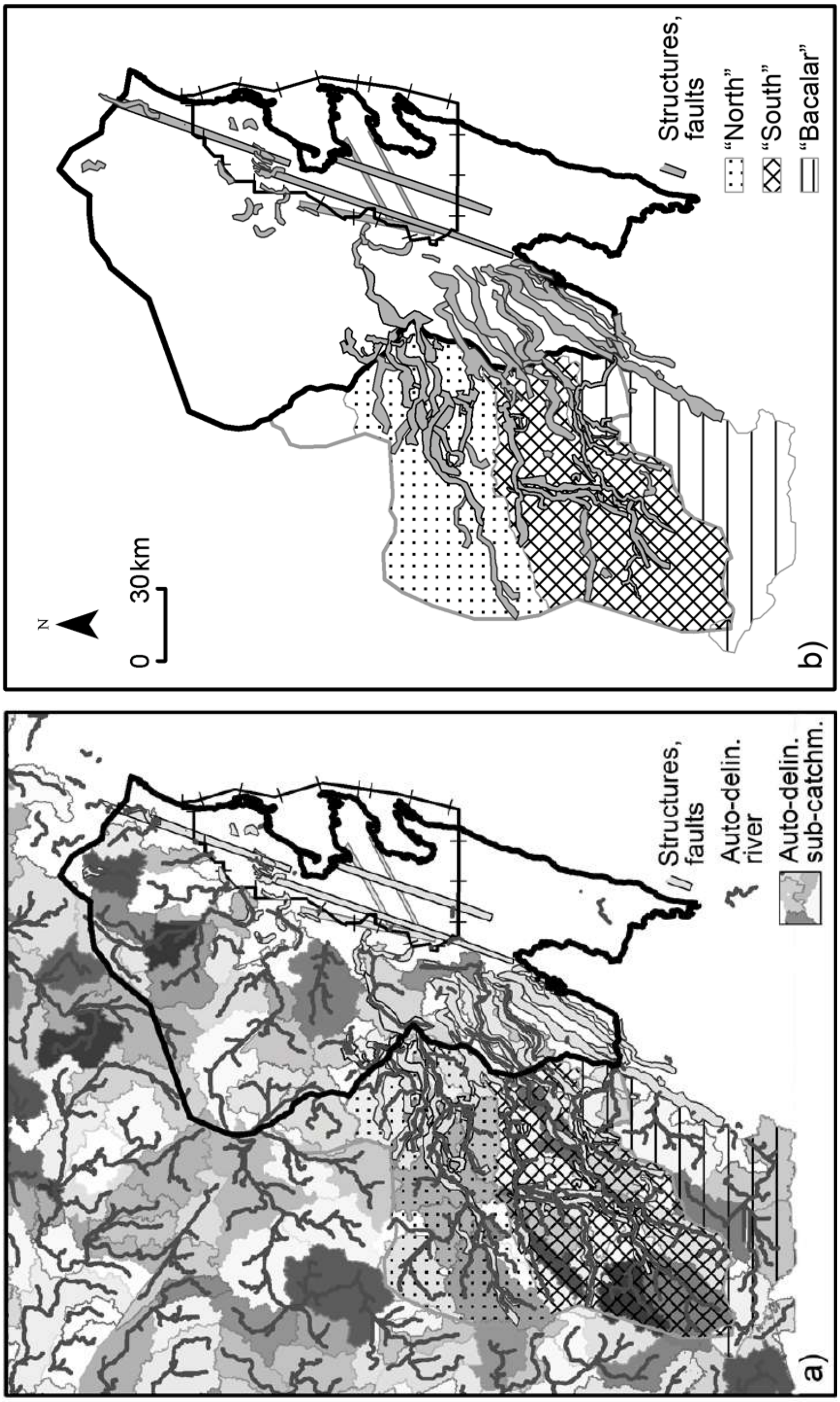

Fig. 4 (rotated 90 degrees)

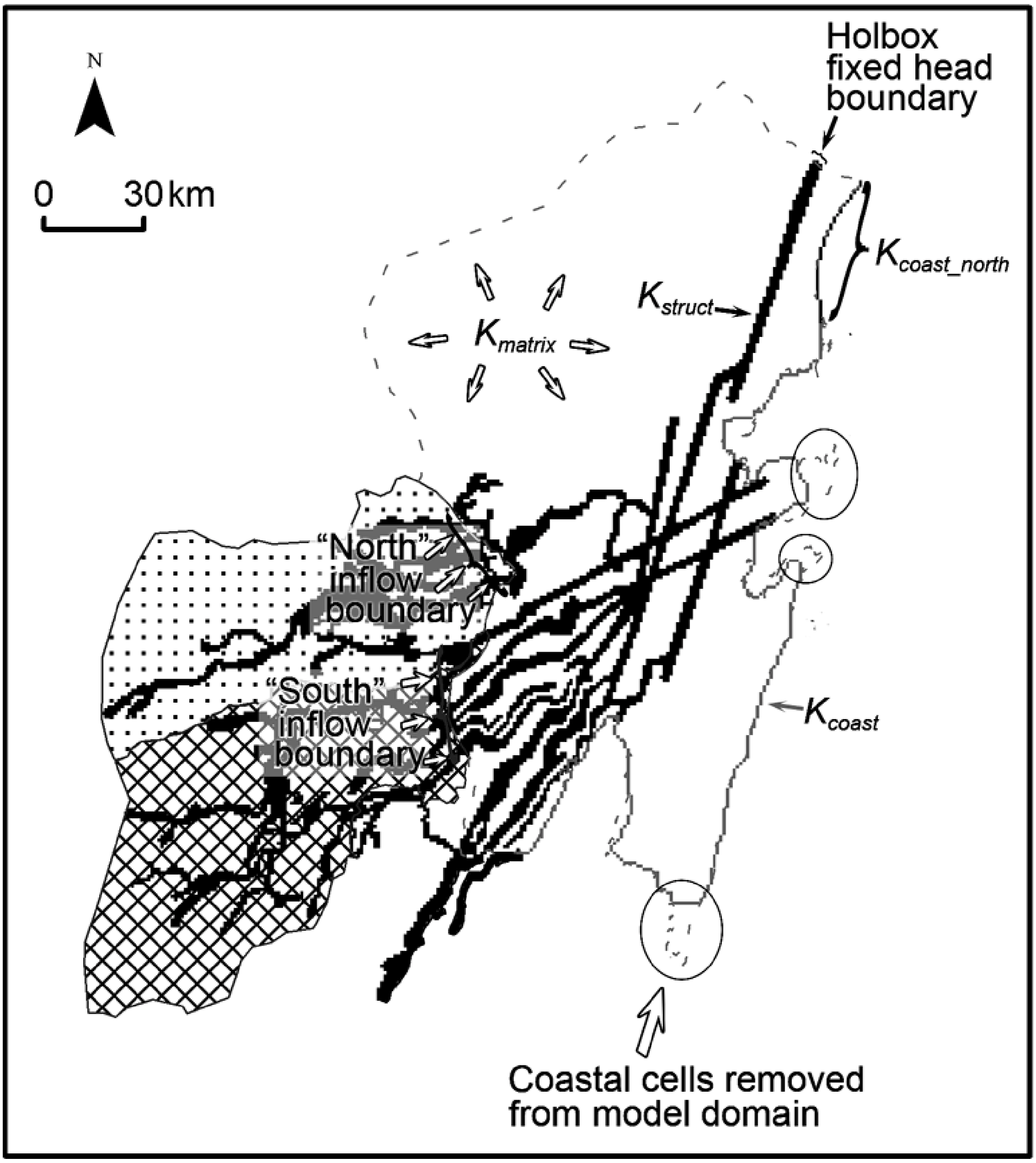
N
0
30 km
Holbox fixed head boundary
K_{coast_north}
K_{struct}
K_{matrix}
"North" inflow boundary
"South" inflow boundary
K_{coast}
Coastal cells removed from model domain

Fig. 5

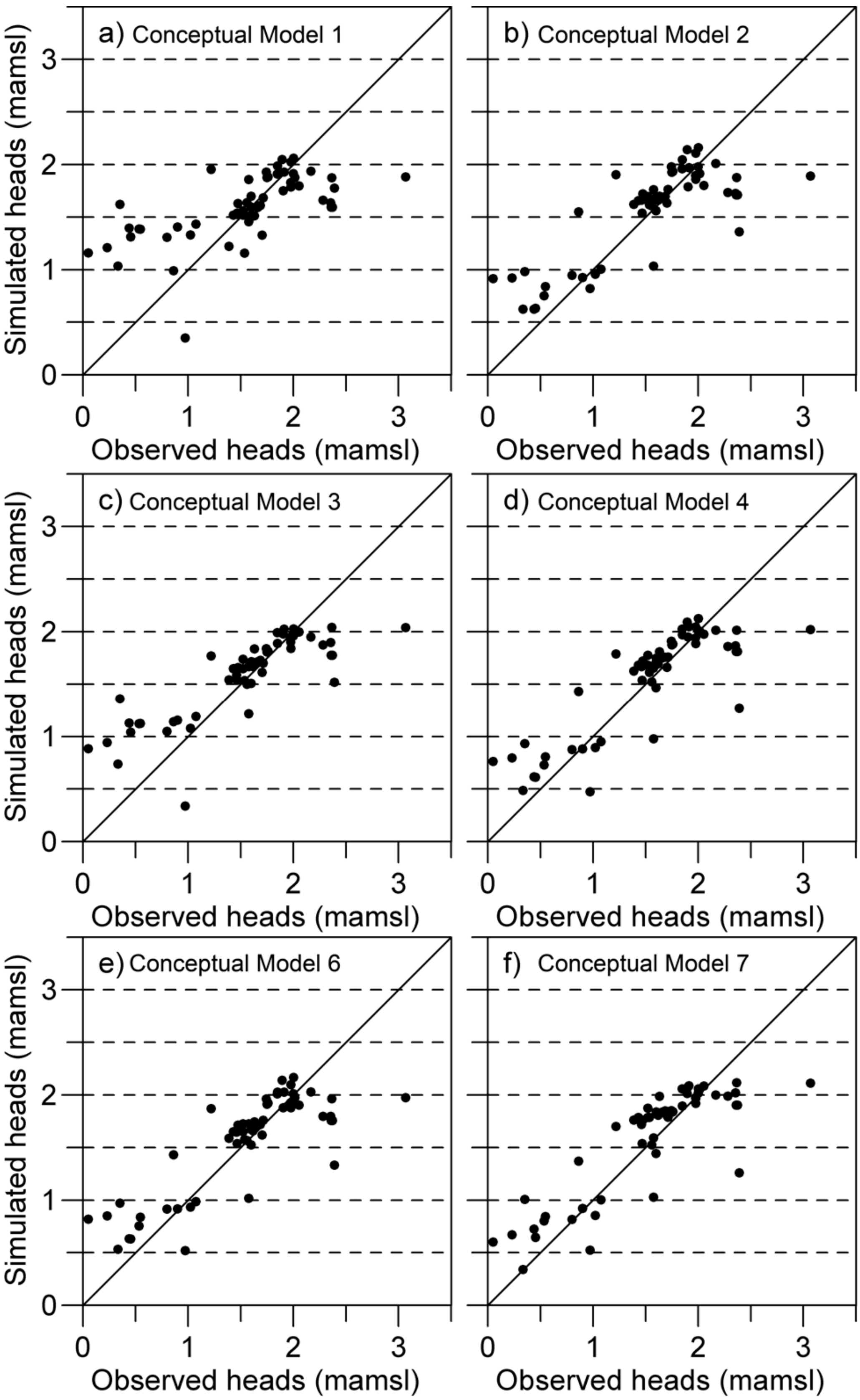
a) Conceptual Model 1
b) Conceptual Model 2
c) Conceptual Model 3
d) Conceptual Model 4
e) Conceptual Model 6
f) Conceptual Model 7
Simulated heads (mamsl)
Observed heads (mamsl)
0
1
2
3

Fig. 6

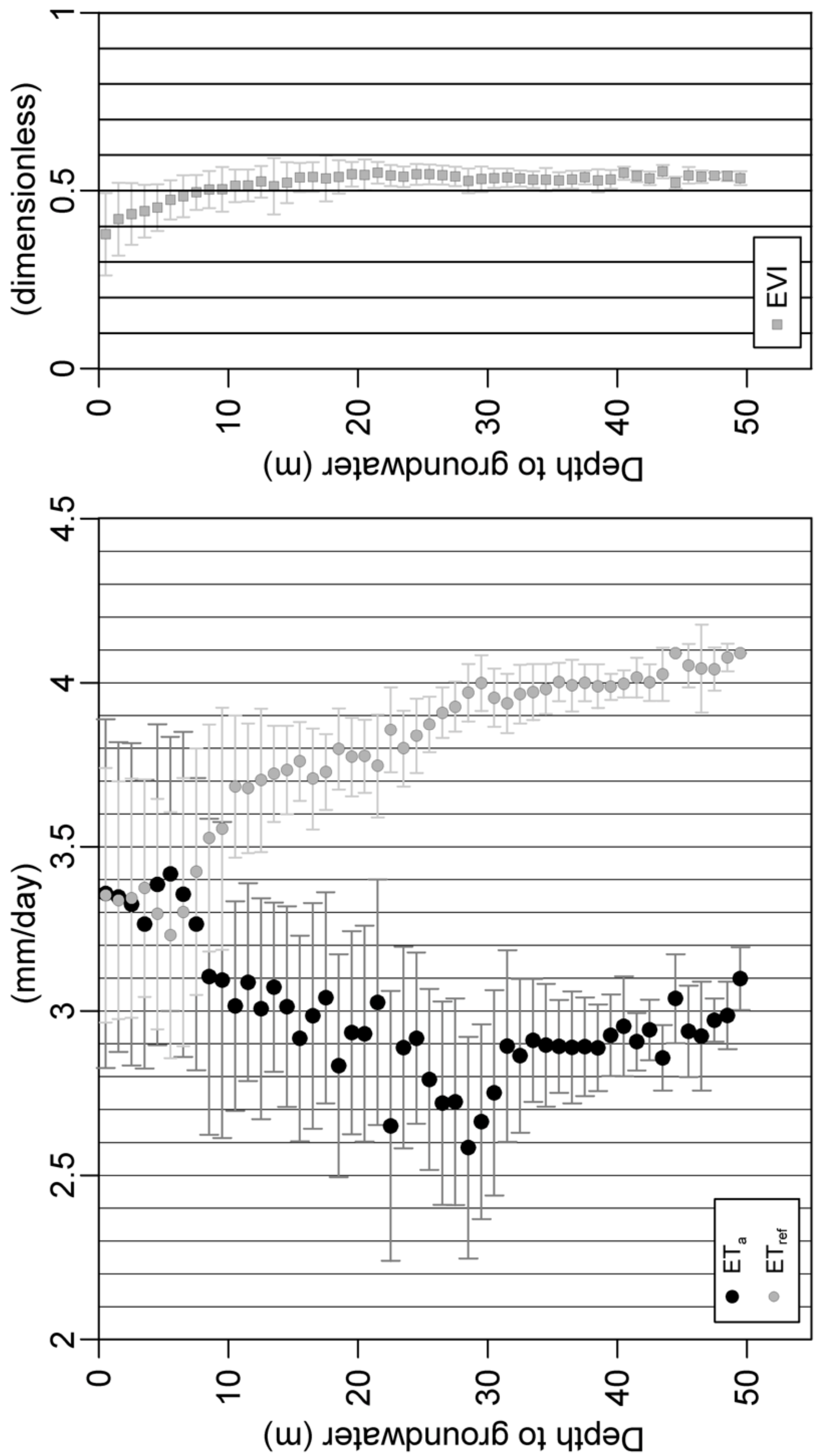

Fig. 7 (rotated 90 degrees)

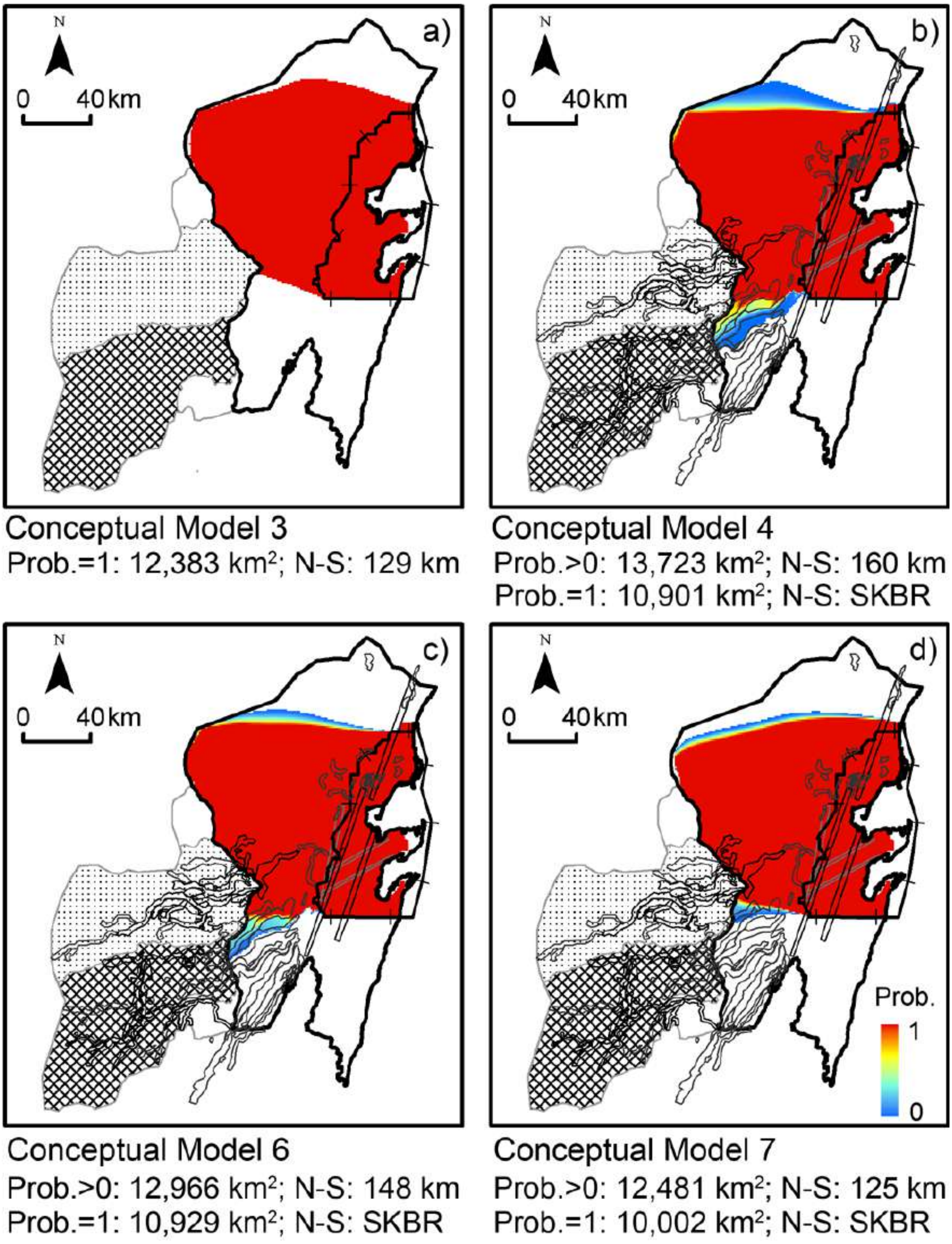
N
0 40 km
a)
Conceptual Model 3
Prob.=1: 12,383 km²; N-S: 129 km
N
0 40 km
b)
Conceptual Model 4
Prob.>0: 13,723 km²; N-S: 160 km
Prob.=1: 10,901 km²; N-S: SKBR
N
0 40 km
c)
Conceptual Model 6
Prob.>0: 12,966 km²; N-S: 148 km
Prob.=1: 10,929 km²; N-S: SKBR
N
0 40 km
d)
Prob.
1
0
Conceptual Model 7
Prob.>0: 12,481 km²; N-S: 125 km
Prob.=1: 10,002 km²; N-S: SKBR

Fig. 8

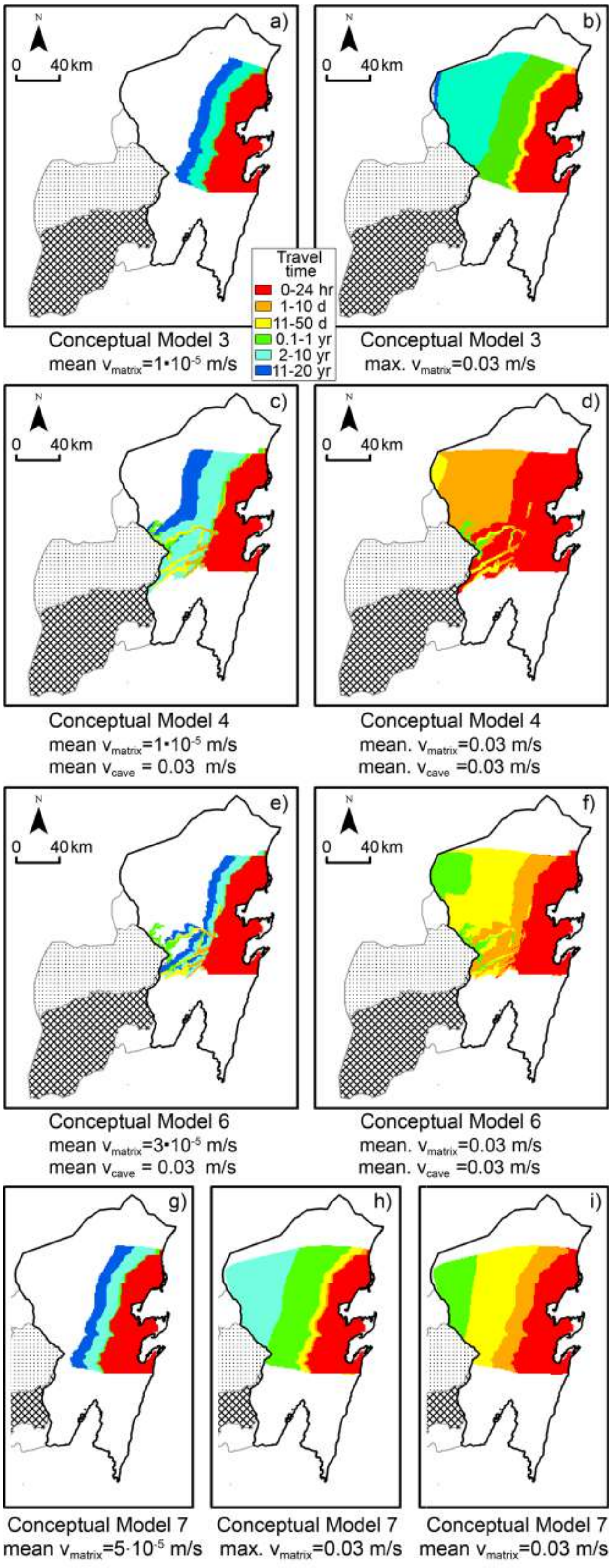
N
0 40 km
a)
b)
c)
d)
e)
f)
g)
h)
i)
Travel time
0-24 hr
1-10 d
11-50 d
0.1-1 yr
2-10 yr
11-20 yr
Conceptual Model 3
mean $v_{matrix}=1\cdot10^{-5}$ m/s
Conceptual Model 3
max. $v_{matrix}=0.03$ m/s
Conceptual Model 4
mean $v_{matrix}=1\cdot10^{-5}$ m/s
mean v_{cave} = 0.03 m/s
Conceptual Model 4
mean. $v_{matrix}=0.03$ m/s
mean. v_{cave} =0.03 m/s
Conceptual Model 6
mean $v_{matrix}=3\cdot10^{-5}$ m/s
mean v_{cave} = 0.03 m/s
Conceptual Model 6
mean. $v_{matrix}=0.03$ m/s
mean. v_{cave} =0.03 m/s
Conceptual Model 7
mean $v_{matrix}=5\cdot10^{-5}$ m/s
Conceptual Model 7
max. $v_{matrix}=0.03$ m/s
Conceptual Model 7
mean $v_{matrix}=0.03$ m/s

Fig. 9

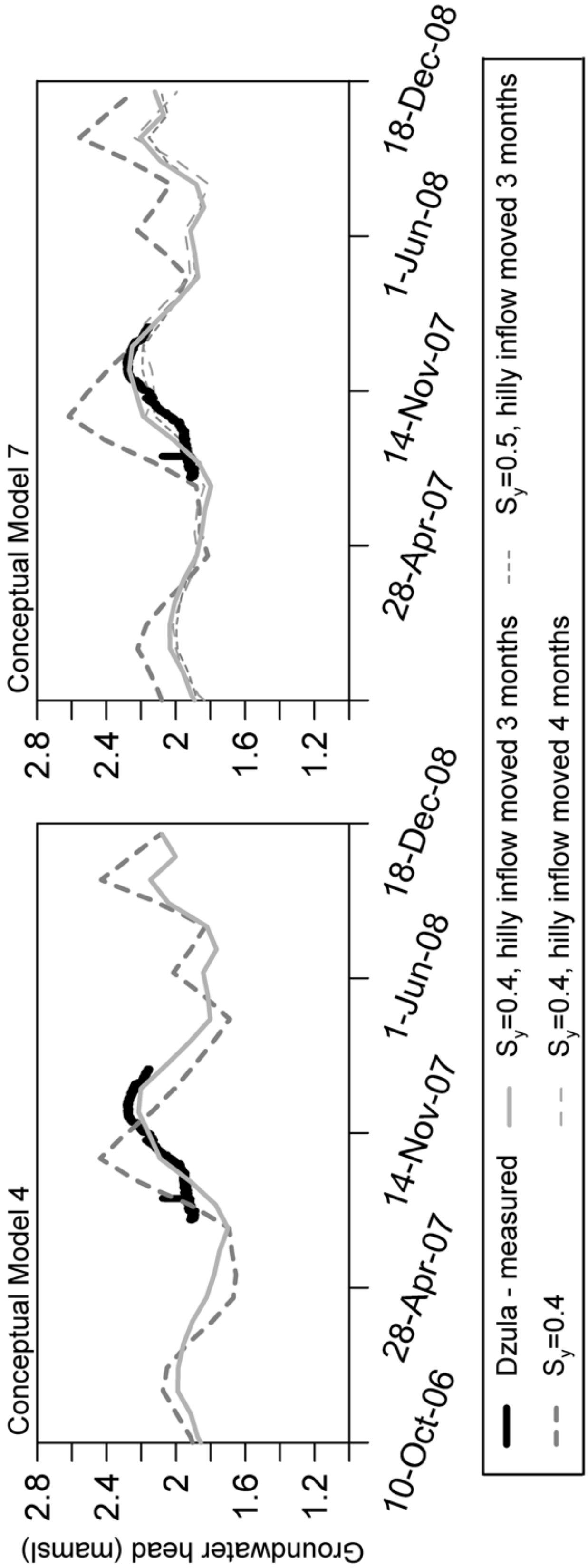

Fig. 10 (rotated 90 degrees)

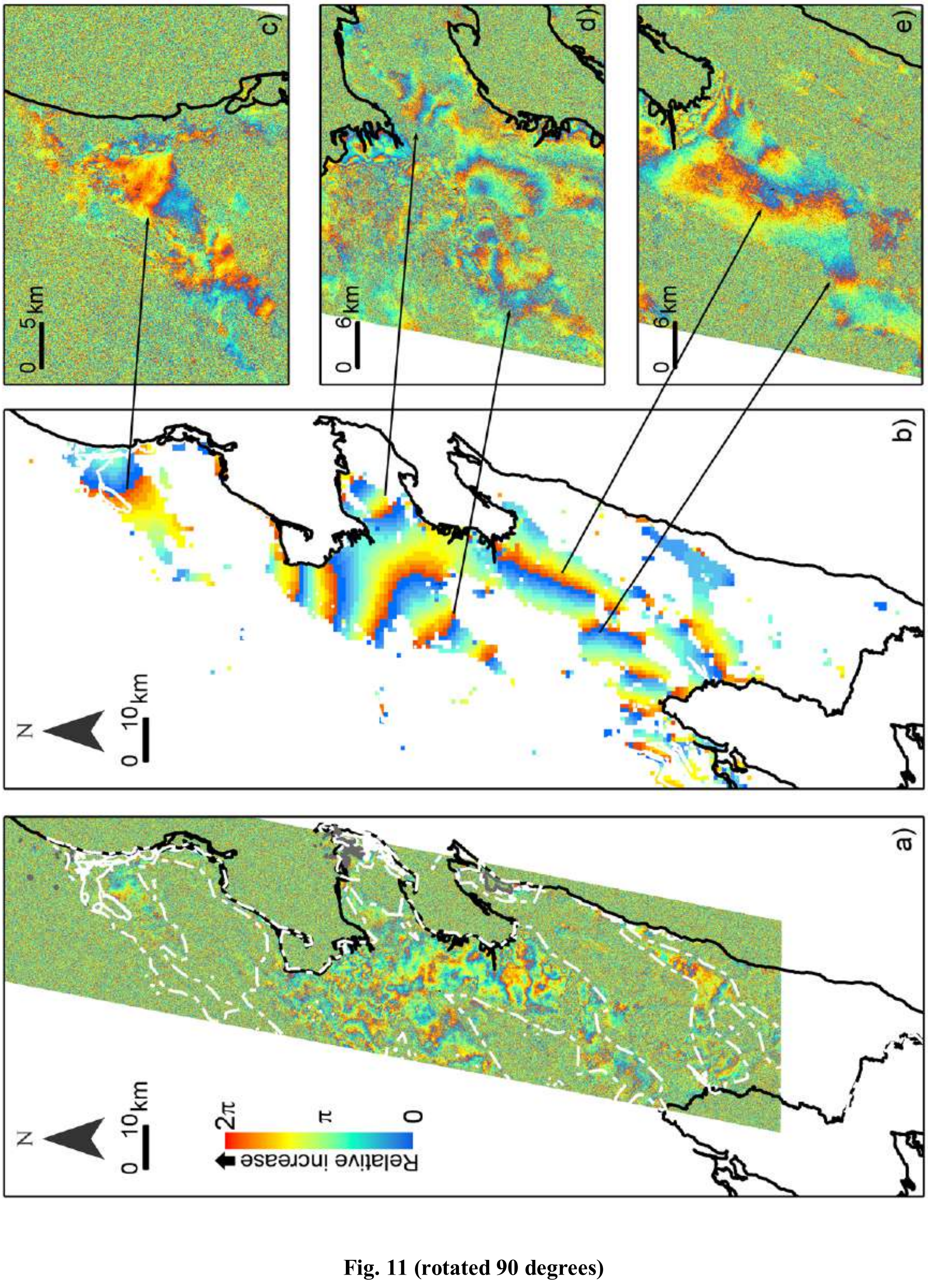

Fig. 11 (rotated 90 degrees)

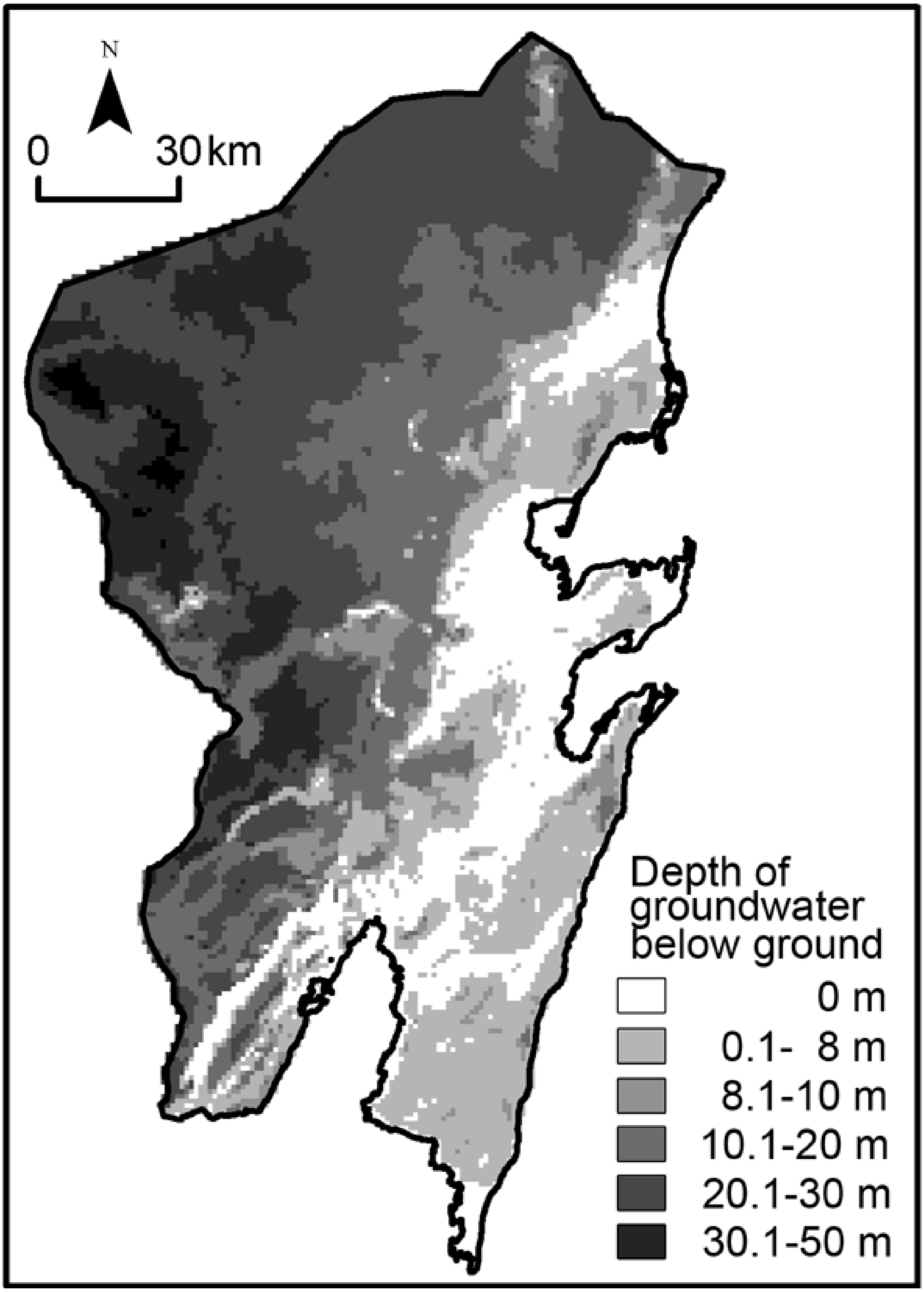
N
0
30 km
Depth of groundwater below ground
0 m
0.1- 8 m
8.1-10 m
10.1-20 m
20.1-30 m
30.1-50 m

Fig. 12

Tables

Table 1 Calibration results and selected model outputs for the conceptual models investigated. MSE= mean square error; OL: overland flow; SZ: saturated zone flow; SKBR: Sian Ka'an Biosphere Reserve; structs.: structures and faults, diff.: different. The two models giving the smallest MSE are marked in bold

Conceptual Model:	1 No hilly inflow, no structures	2 No hilly inflow, with structures	3 100% hilly inflow, no structures	**4 100% hilly inflow, with structures**	5 Hilly inflow optimized, with structures	6 50% hilly inflow, with structsures	**7 K_{coast_north} and 100% hilly inflow, with structures**
MSE [m^2]	0.2381	0.1393	0.1422	**0.1163**	0.1162	0.1245	**0.1086**
K_{coast} [m/s]	0.048	0.011	0.110	**0.059**	0.065	0.038	**0.060**
$K_{coast\ north}$ [m/s]	-	-	-	-	-	-	**0.440**
K_{matrix} [m/s]	0.71 [0.61; 0.83]	0.49 [0.31; 0.78]	0.94 [0.93; 0.95]	**0.61 [0.38; 0.97]**	0.66	0.52 [0.32;0.85]	**0.95 [0.36;2.59]**
$K_{structs}$ [m/s]	-	26.86 [16.40; 43.98]	-	**18.79 [5.13; 68.84]**	15.75	17.29 [6.87; 43.51]	**1.03 [0.26;4.16]**
Calibrated (optimized) inflow	-	-	-	-	105.3%	-	**-**
MSE with OL [m^2]	0.2208	0.1647	0.1336	**0.1160**	-	0.1809	**0.1047**
$\frac{OL\_Outflow\_al\_domain}{SZ\_Outflow\_all\_domain}$ [% and OL outflow in m^3/s]	11.7% ($12.5\ m^3/s$)	42.4% ($19.4\ m^3/s$)	5.7% ($11.9\ m^3/s$)	**10.3% ($16.7\ m^3/s$)**	-	16.8% ($24.6\ m^3/s$)	**7.8% ($15.0\ m^3/s$)**
$\frac{SZ\_Outflow\_SKBR}{SZ\_Outflow\_all\_domain}$ [% and SKBR SZ outflow in m^3/s]	49.5 % ($52.7\ m^3/s$)	47.4% ($21.7\ m^3/s$)	42.9% ($89.5\ m^3/s$)	**47.0% ($76.2\ m^3/s$)**	-	46.5% ($68.1\ m^3/s$)	**42.9% ($82.9\ m^3/s$)**
$\frac{OL\_Outflow\_SKBR}{SZ+OL\_Outflow\_all\_dom}$ [%]	9.2%	29.6%	4.2%	**7.3%**		11.7%	**5.2%**
Within SKBR only: $\frac{OL\_Outflow}{SZ\_Outflow}$ [% and SKBR OL in m^3/s]	18.5% ($9.8\ m^3/s$)	62.4% ($13.6\ m^3/s$)	9.8% ($8.7\ m^3/s$)	**15.5% ($11.8\ m^3/s$)**	-	25.2% ($17.1\ m^3/s$)	**12.2% ($10.1\ m^3/s$)**
Holbox outflow	0	54%	0	**21%**	-	26%	**6%**

[% of total groundwater outflow from domain and in m^3/s]	0	(53.9 m^3/s)	0	**42.1 m^3/s**		51.2 m^3/s	**12.5 m^3/s**
Total discharge pr. km coast [$m^3/s/km$]	0.20	0.08	0.38	**0.30**	-	0.27	**0.35 (0.95 at the northern coast with diff. *K*)**
SZ max. flow [m^3/s] x-dir y-dir	-0.6; 0.9 -1 ; 0.6	-4 ; 13 -12; 17	-1; 2 -2; 1	**-3; 18** **-16; 15**	-	-3; 18 -16; 16	**-1; 3** **-2; 2**
OL max. flow [m^3/s] x-dir y-dir	-0.1; 0.2 -0.2; 0.2	-0.2; 0.3 -0.3; 0.3	-0.2; 0.2 -0.2; 0.2	**-0.2; 0.3** **-0.3; 0.3**	-	-0.3; 0.4 -0.4; 0.3	**-0.2; 0.2** **-0.3; 0.2**

Table 2 Available literature values for model outputs

Parameter	Value	Reference and comments
Total discharge pr. km coast	0.27 $m^3/s/km$ 0.38 $m^3/s/km$ 0.73 $m^3/s/km$	Hanshaw and Back (1980), NW Yucatan Thomas (1999), based on total freshwater conduit outflow Beddows (2004), "crude assumption" from "19 known outflows/80 km of 1 m^3/s each" (i.e. 0.24 $m^3/s/km$) + (her guesstimate to represent further outflow from matrix) 0.5 $m^3/s/km$
SZ max. flow	<u>At cave outlets (submarine springs):</u> 2.43 m^3/s 1.9 m^3/s 5 m^3/s to 9 m^3/s 1.1 m^3/s 2.96 m^3/s 2.7 m^3/s	<u>At cave outlets (submarine springs):</u> Back et al. (1979) (measured at Xel Ha) Thomas (1999) (measured at Xel Ha) Beddows (2004) (measured at Xel Ha) Thomas (1999) (measured at Casa Cenote and Abejas) Beddows (2004) (measured at Casa Cenote) Thomas (1999) (measured at Xpu-Ha)

	5.1 m^3/s 17 m^3/s <u>Inside caves:</u> 0.8 m^3/s to 1.5 m^3/s 1 m^3/s to 13 m^3/s	Thomas (1999) (measured at Chuchuen, north of model area) Thomas (1999) (measured at Conil, outlet at north Holbox fracture zone) <u>Inside caves:</u> Beddows (2003) (estimated from measured dye tracing velocities and conduit dimensions at Nohoch Nah Chich) Neuman and Rahbek (2007) (estimated from pers. comm.. with cave divers)
Groundwater flow velocity	<u>At/near cave outlets:</u> 0.012 m/s 0.055 m/s 0.3 m/s 1 m/s <u>Inside caves:</u> 0.001 m/s 0.006 m/s 0.030 m/s 0.009 m/s 0.075 m/s 0.023 m/s 0.014 m/s <u>In matrix:</u> 2.1e-4 m/s 4.6e-7 m/s	<u>At cave outlets:</u> Moore et al. (1992) (measured) Beddows (2004) (measured, Casa Cenote, average value) Beddows (2004) (measured, Casa Cenote and Xel Ha, maximum values) Estimate from divers' scooter, Sistema Manatee (cave diver Le Maillot, pers. comm. in Neuman and Rahbek, 2007) <u>Inside caves:</u> Moore et al. (1992) (measured) Beddows (2003) (from dye tracing, lowest for dye peak) Beddows (2003) (from dye tracing, largest for dye peak) Beddows (2003) (from dye tracing, lowest for dye front) Beddows (2003) (from dye tracing, largest for dye front) Beddows (2004) (from dye tracing, average value Heaven's Gate) Beddows (2004) (from dye tracing, average value River Run/Ponderosa) <u>In matrix:</u> Moore et al. (1992) (measured in a borehole several km from coast; considered upper range velocity estimate) Neuman and Rahbek (2007) (estimate from numerical conduit-matrix modelling, considered lower range velocity estimate)

Table 3 Results of sensitivity analysis to changes in the Holbox fixed head boundary for Conceptual Models 4 and 7

Model	+ σ_{Holbox_bound} (Model 4)	- σ_{Holbox_bound} (Model 4)	+ σ_{Holbox_bound} (Model 7)	- σ_{Holbox_bound} (Model 7)
MSE [m^2]	0.1179	0.1149	0.1027	0.1015
K_{coast} [m/s]	0.058	0.061	0.083	0.091
$K_{coast,\ north}$ [m/s]	-	-	1.87	0.92
K_{matrix} [m/s]	0.61	0.63	0.96	0.86
$K_{structs}$ [m/s]	20.59	14.93	0.62	0.79
MSE with OL [m^2]	0.1180	0.1141	0.1068	0.1032
Holbox outflow [m^3/s]	42.5 m^3/s (change: +0.4 m^3/s or +1%)	39.3 m^3/s (change: -2.7 m^3/s or -7%)	8.9 m^3/s (change: -3.6 m^3/s or -29%)	10.7 m^3/s (change: -1.7 m^3/s or -14%)

Table 4 Results of recharge sensitivity analysis for Conceptual Models 4 and 7

Model:	+ σ_R (Model 4)	- σ_R (Model 4)	+ σ_R (Model 7)	- σ_R (Model 7)
MSE [m^2]	0.1136	0.1213	0.1008	0.1043
K_{coast} [m/s]	0.10	0.05	0.14	0.06
$K_{coast,\ north}$ [m/s]	-	-	1.38	0.92
K_{matrix} [m/s]	0.71	0.65	1.04	0.81
$K_{structs}$ [m/s]	5.31	12.63	0.44	1.11
MSE with OL [m^2]	0.1115	0.1126	0.1033	0.1077
$\frac{OL\_Outflow\_al\_domain}{SZ\_Outflow\_all\_domain}$ [% and OL outflow in m^3/s]	6.5% (13.6 m^3/s)	12.4% (18.0 m^3/s)	4.2% (9.4 m^3/s)	7.5% (13.3 m^3/s)
$\frac{SZ\_Outflow\_SKBR}{SZ\_Outflow\_all\_domain}$ [% and SKBR SZ outflow in m^3/s]	44.8% (92.1 m^3/s)	46.2% (67.4 m^3/s)	44.7% (99.5 m^3/s)	42.7% (75.1 m^3/s)
$\frac{OL\_Outflow\_SKBR}{SZ+OL\_Outflow\_all\_don}$ [%]	4.6%	8.6%	3.1%	5.1%
Within SKBR only: $\frac{OL\_Outflow}{SZ\_Outflow}$ [% and SKBR OL in m^3/s]	10.3% (9.5 m^3/s)	8.6% (12.5 m^3/s)	6.9% (6.8 m^3/s)	11.9% (8.9 m^3/s)
Holbox outflow [m^3/s]	23.9 (change: -18 m^3/s; -43%)	35.3 (change: -7 m^3/s; -16%)	10.5 (change: -2 m^3/s; -16%)	9.6 (change: -3 m^3/s; -23%)
Total discharge pr. km coast [$m^3/s/km$]	0.38	0.27	0.41 (at north coast: 1.03)	0.32 (at north coast: 0.85)
SZ max. flow [m^3/s] x-dir y-dir	-1.3; 7.2 -4.5; 6.1	-1.9; 12.3 -9.6; 10.3	-1.0; 4.1 -2.5; 2.4	-0.9; 2.4 -1.8; 1.3
OL max. flow [m^3/s] x-dir y-dir	-0.2; 0.2 -0.2; 0.2	-0.3; 0.3 -0.3; 0.3	-0.2; 0.2 -0.2; 0.1	-0.2; 0.2 -0.3; -0.2

VI

Technical Note

Maps and coordinates of field data points.

Appendix VI – Technical Note

This appendix contains maps and coordinates of the field measurements that have been carried out during the PhD research. All coordinates are UTM, zone 16, WGS84 datum and ellipsoid. The actual data may be obtained from Amigos de Sian Ka'an (afregoso@amigosdesiankaan.org; gmerediz@amigosdesiankaan.org) or Peter Bauer-Gottwein (pbg@env.dtu.dk) in electronic format. Inventory of the data available electronically is given in Section A6.7.

A6.1 Groundwater head measurement points

Places where groundwater heads and surface water levels have been measured.
Points believed to represent perched aquifers are marked with "P".
Points outside the study area, and surface water levels are separated in the table.
Water level recorded by automatic data loggers indicated with time span covered.

Elevations of reference points at wells, usually marked with painted crosses, are given in meters above mean sea level in the table. The water level data may be found in the electronic data material in the folder WaterLevels. In the sub-folders WaterLevels\Bibi and WaterLevels\Chiara Word-documents with photos and detailed descriptions/maps of each water level measurement site may be found.

Water level measurements in July 2007 were carried out by Chiara Fratini, whereas those in Nov-Dec 2008 were carried out by Amigos de Sian Ka'an. Those in April 2009, north of the study area, were carried out by Guillaume Charvet. Reading of surface water levels within Sian Ka'an ("SKBR") were carried out by CONANP and the author. Data loggers were installed at 4 sites, indicated in the table with time span covered. Automatic water level and temperature recording was carried out every 30 minutes within these time intervals.

Location	Northing	Easting		Collect dates 2007	Collect dates 2008 (or 2009 if noted	Elevation of reference point at well (mamsl)
Macario Gomez	2250445	439830		25-Feb, 15-Apr, 29-Jul	03-Feb, 18-Dec	16.60
Chankah Veracruz 1	2155872	395708		27-Feb, 01-Jul, 24-Jul	18-Feb, 03-Nov	7.30
Chankah Veracruz 2	2155958	395627		27-Feb, 01-Jul, 24-Jul	18-Feb, 03-Nov	7.33
Uhmay 1	2147337	389903		27-Feb, 10-Apr, 01-Jul	18-Feb, 03-Nov	6.57
Uhmay 2	2147279	389963		27-Feb, 01-Jul,	18-Feb,	6.77
Xpichil	2178418	355574		28-Feb, 30-Jun	19-Feb, 20-Dec	25.25
Chunhuas	2171192	373083		01-Mar, 10-Apr, 30-Jun, 24-Jul	19-Feb, 20-Dec	15.86
San Andres	2145706	381136		01-Mar, 14-Apr, 01-Jul	18-Feb, 19-Dec	7.93
Muyil	2220482	435844		02-Mar, 12-Apr, 29-Jun	04-Nov	7.77
Polyuc	2169003	336095		05-Mar, 22-Mar, 16-Apr, 30-Jun, 24-Jul	20-Dec	16.33
Nuevo Israel	2128279	336941	P	06-Mar, 16-Mar, 16-Apr, 02-Jul	20-Feb, 03-Nov	24.33
Las Panteras	2116966	343026		06-Mar, 16-Mar, 16-Apr, 02-Jul	20-Feb, 03-Nov	23.49
Los Divorciados	2110462	347284		06-Mar, 16-Mar, 16-Apr, 02-Jul	20-Feb, 03-Nov	31.93
Nuevo San Antonio	2170399	388132		07-Mar, 17-Mar, 30-Jun	17-Feb, 21-Dec	7.62
Señor	2194844	381145		07-Mar, 17-Mar, 30-Jun	17-Feb, 21-Dec	20.20
Tuzik	2202466	378648		07-Mar, 17-Mar,	17-Feb, 21-Dec	19.59

				30-Jun		
San Jose Segundo	2208588	371582		07-Mar, 17-Mar, 30-Jun	17-Feb, 21-Dec	22.63
Andres Quinta Roo	2119220	384115		08-Mar, 14-Apr, 01-Jul, 25-Jul	04-Feb, 03-Nov	12.72
Noh-Bec	2117429	377037	P	08-Mar, 14-Apr, 01-Jul	21-Feb, 03-Nov	7.74
Polinkin	2120586	377220	P	08-Mar, 14-Apr, 01-Jul	21-Feb, 03-Nov	10.80
Petcacab (Data logger: 14 Apr 2007 – 24 Jul 2007)	2133152	371317		08-Mar, 14-Apr, 01-Jul, 24-Jul		22.09
X-hacil 1	2144330	387057		09-Mar, 17-Mar, 14-Apr, 01-Jul	18-Feb, 19-Dec	7.67
X-hacil 2	2144310	386970		09-Mar, 17-Mar, 14-Apr, 01-Jul	18-Feb, 19-Dec	9.22
Noh-Cah 1	2147914	378136		09-Mar, 14-Apr, 01-Jul	18-Feb, 19-Dec	8.91
Noh-Cah2	2147818	378219		09-Mar, 14-Apr, 01-Jul	18-Feb, 19-Dec	7.13
Mixtequilla	2144148	367151		09-Mar, 19-Apr, 01-Jul, 24-Jul	18-Feb, 19-Dec	16.70
Santa Maria Poniente	2142013	352118	P	09-Mar, 01-Jul	18-Feb, 03-Nov	12.45
Limones	2106297	383198		10-Mar, 16-Mar, 16-Apr, 01-Jul, 25-Jul	20-Feb, 03-Nov	7.70
Chacchoben	2105314	376815	P	10-Mar, 16-Mar, 16-Apr, 01-Jul, 25-Jul	20-Feb, 03-Nov	14.11
Rancho La Herradurra	2100867	370950	P	10-Mar, 16-Mar, 16-Apr, 01-Jul	20-Feb, 03-Nov	7.86
Rancho La Herradurra	2100978	371005	P	10-Mar, 16-Mar, 16-Apr, 01-Jul	20-Feb, 03-Nov	8.36
Pedro A. Santos	2096201	377441		10-Mar,	20-Feb,	9.21

				02-Jul	03-Nov	
Tepich	2239246	368971		19-Mar, 29-Jun	17-Feb, 21-Dec	24.47
Francisco I. Madero	2229157	392735		19-Mar, 29-Jun	17-Feb, 21-Dec	16.35
Chumpon	2212198	414787		20-Mar, 29-Jun	17-Feb, 22-Dec	8.88
Chunya	2222926	403359		20-Mar, 29-Jun,	17-Feb,	15.05
San Luis	2172925	348144		22-Mar, 16-Apr, 30-Jun, 24-Jul	19-Feb, 20-Dec	25.50
Presidente Juarez (Data logger: 16 Apr 2007 – 25 Aug 2008)	2136769	335923	P	22-Mar, 16-Apr, 01-Jul, 24-Jul	20-Feb, 03-Nov	26.66
Betania	2171336	365858		22-Mar, 16-Apr, 30-Jun,	19-Feb, 20-Dec	15.57
Tres Reyes	2193589	409785		28-Mar, 14-Apr,	28-Feb, 22-Dec	7.26
Felipe Carrillo Puerto	2165409	391327		29-Mar, 14-Apr, 01-Jul	18-Feb, 21-Dec	9.71
San Francisco Ake	2207122	359071		30-Mar, 30-Jun	19-Feb, 20-Dec	23.62
Dzoyola	2205977	348808		30-Mar, 30-Jun	19-Feb,	17.66
Javier Rojo Gomez	2199865	333110		30-Mar, 30-Jun	19-Feb, 20-Dec	26.04
Santa Isabel	2153153	384697		31-Mar, 19-Apr, 01-Jul	18-Feb, 19-Dec	10.17
Laguna Ocom	2152742	384075		31-Mar, 19-Apr, 01-Jul	18-Feb, 03-Nov	3.22
Chunkakah	2154329	383716		31-Mar,	18-Feb, 03-Nov	10.87
Reforma	2079163	335824	P	03-Apr,	23-Feb, 02-Nov	29.65
Altos de Sevilla	2085154	324046	P	03-Apr, 02-Jul	22-Feb, 02-Nov	72.28
Morocoy (Data logger: 25 Feb 2008 – 28 Apr 2008)	2059112	306809	P	04-Apr	12-Feb, 31-Oct	69.01
Rio Escondido	2084621	313615	P	05-Apr 02-Jul	11-Feb, 30-Oct	59.68
Otillo Montaño	2105810	309561		05-Apr, 02-Jul	22-Feb, 02-Nov	50.11
Dzulá (Data logger: 24 Jul 2007 – 06 Feb 2008)	2168142	351695		07-Apr, 30-Jun, 24-Jul	05-Feb, 19-Dec	20.61
Laguna Kaná	2156930	353304		07-Apr, 01-Jul,	18-Feb, 19-Dec	23.53

				24-Jul		
Yoactun	2152193	357352		07-Apr, 01-Jul, 24-Jul	18-Feb, 19-Dec	23.49
Tulum federal plot	2235499	453592		08-Apr, 16-Apr, 29-Jun	03-Feb, 04-Nov	3.24
Holbox depression	2241759	449387		13-Apr, 16-Apr, 29-Jun	03-Feb, 01-Nov	1.00
Manuel Antonio May	2259019	431705		17-Apr,	03-Feb, 18-Dec	20.16
Centro Nocturno	2243783	447206		18-Apr, 29-Jun	03-Feb, 18-Dec	6.47
Cenote Azul	2062180	350879	P	03-Jul	23-Feb, 02-Nov	16.80
Santa Elena	2045599	352682	P	05-Jul	23-Feb	2.23
Calderitas	2052206	367799	P	05-Jul	23-Feb	9.11
Ucum Qroo	2046815	339502	P	05-Jul	23-Feb, 31-Oct	23.97
El Cedral	2069074	291758	P	07-Jul	01-Nov	88.14
Francisco Villa	2042999	304163	P	07-Jul	23-Feb, 02-Nov	85.80
Nicholas Bravo	2042066	296126	P	07-Jul	24-Feb, 31-Oct	102.89
Felipe Anjeles	2010502	259888	P	10-Jul	01-Nov	209.45
La Lucha	2025628	268554	P	10-Jul	24-Feb, 01-Nov	181.39
Veinte de Noviembre	2041729	256347	P	11-Jul	26-Feb, 02-Nov	202.90
Richardo Payro	2026620	241515	P	11-Jul	26-Feb, 01-Nov	262.39
El Once	2000876	237966	P	12-Jul	01-Nov	265.75
Narciso Mendoza pozo	2017596	240428	P	12-Jul	26-Feb, 01-Nov	245.64
Bel Ha	2094686	255190	P	13-Jul	27-Feb, 01-Nov	137.59
José Maria Morelos	2184891	320643		22-Jul	19-Feb	20.76
Nuevo Becar chico	2073045	279704	P	09-Jul	02-Nov	95.42
Xkan-Ha	2114278	253374	P	13-Jul	01-Nov	126.59
Ucum Campeche	2129315	254671	P	15-Jul	27-Feb, 01-Nov	106.00
Chanchen	2125415	262064	P	15-Jul	27-Feb, 01-Nov	150.31
Xmejia	2128053	250212	P	15-Jul	27-Feb, 01-Nov	4.98
Chunhuhub	2156398	332620		23-Jul		26.28
X-pichil_deep (logging site)	2184785	357307			06-Feb	26.38
Las Panteras_deep (logging site)	2113715	341417			07-Feb	21.90
Nuevo Israel_deep (logging site)	2126121	333379			08-Feb	26.36
Presidente Juarez_deep (logging site)	2134993	331399			08-Feb	27.83

Reforma_deep (logging site)	2076459	335318			11-Feb, 02-Nov	20.82
Chankah_Derrepente_deep (logging site)	2149759	369928			14-Feb	17.43
Señor_deep (logging site)	2194778	380402			14-Feb	19.65
Chunhuhub_deep (logging site)	2159949	332456			15-Feb	28.72
Emiliano_Zapata_deep (logging site)	2124021	341666			15-Feb	21.16
Nuevo_Becar_deep (logging site)	2049273	278016			16-Feb	125.22
La_Lucha_deep (logging site)	2022253	265349			26-Feb	194.43
Surface water bodies						
Laguna La Union	2235654	444141		18-Apr		0.96
Muyil lagoon	2219946	436454		26-Feb, 21-Mar, 18-Apr, 30-Jun, 17-Jul		1.91
SKBR Ruina X-lapak	2219026	441366		21-Mar, 06-Apr, 19-Apr, 30-Jun, 17-Jul		1.84
SKBR Boater stop	2219366	442750		21-Mar, 10-Apr		2.22
SKBR Place C	2217047	446296		21-Mar, 30-Jun, 17-Jul		0.85
SKBR Termite	2218158	445132		21-Mar, 30-Jun, 17-Jul		1.07
Laguna Nopalita	2223456	439192		13-Apr, 18-Apr, 01-Jul		1.38
Laguna Kaan Luum	2229886	442298		12-Apr, 18-Apr, 01-Jul		1.03
Laguna Chichankanab	2198918	314612	P	22-Jul		4.98
Zoh Laguna	2056997	244807	P	11-Jul		257.73
Uaymil_Vertice_7	2097806	402104			21-Feb	0.86
Uaymil_Vertice_9	2076134	422143			21-Feb	2.40
Points outside the study area						
La Union	1981106	300777	P	06-Jul		12.63
Tòmas Garrido	1996078	281219	P	08-Jul		48.04
Tres Garantias	2012759	290296	P	08-Jul		146.37
OjoDeAgua	1986995	263863	P	09-Jul		76.06

Conhuas	2052115	191369	P	09-Jul		152.35
Costitucion	2062674	168168	P	10-Jul		82.35
Hopelchen_Petch_Base	2185555	201617	P	14-Jul		93.58
Pakchèn	2161784	206915	P	14-Jul		147.48
Dzibalchèn_Base	2153764	213062	P	16-Jul		161.82
Chencoh	2150063	205250	P	16-Jul		170.69
Kancabchèn	2136764	223131	P	17-Jul		156.66
Chiunchintok	2142793	228841	P	17-Jul		132.46
Ich-Ek_Base	2184542	189028	P	17-Jul		77.77
RamonCorona_Rancho_Base	2155271	237352	P	17-Jul		137.01
Iturbide	2167100	227166	P	18-Jul		119.51
Campeo Aleman	2192356	143845	P	18-Jul		13.57
Bolonchel Cahuich	2152922	163275	P	18-Jul		29.66
Uayamòn	2176953	141188	P	19-Jul		27.01
Tikinmul_Base	2189048	162233	P	19-Jul		25.40
Nohyaxche	2172106	162406	P	19-Jul		25.15
Crucero Oxa	2184313	177315	P	20-Jul		66.08
Kambul	2210879	302598	P	20-Jul		35.70
Carolina	2169035	284412	P	20-Jul		75.50
Leona Vicario	2320772	478779			06-Apr09	6.73
Cenote 7 bocas	2308483	495449			07-Apr09	5.40
Ranch de la dama y del caballero	2331652	490632			08-Apr09	9.18
Ranch la calandaria	2340314	490705			08-Apr09	9.11
El Delicios	2305327	476760			13-Apr09	12.30
Agua Azul	2306394	466128			13-Apr09	5.77
La granja	2300076	465719			14-Apr09	9.90
Victoria	2299043	470952			14-Apr09	10.58
Valladolid nueva	2316004	466370			14-Apr09	4.74
Chulutan	2274535	399668			15-Apr09	22.43
Felipe Carillo	2266554	409477			15-Apr09	19.76
Xalau	2286396	395166			15-Apr09	22.85
Santa Rosa	2266410	385745			16-Apr09	23.89
Chamul	2253724	388798			16-Apr09	23.92
San Juan	2257791	424286			16-Apr09	8.22
Camp. Hidalgo	2277620	430337			16-Apr09	22.76
Rancho el viejo	2349313	511993			20-Apr09	9.07
Solferino	2362074	455808			21-Apr09	10.44
San Eusebio	2366413	465038			21-Apr09	10.14
San Angel	2348368	454935			22-Apr09	7.82
Rancho san Juan	2346085	464437			22-Apr09	8.34
El Tintal	2310580	451711			23-Apr09	7.37
Nuevo Xcan	2307877	437487			23-Apr09	21.75
Kantanulikin	2325483	448345			23-Apr09	8.30
Esperanza	2319133	458937			23-Apr09	13.70
Aguakan Pozo 1B	2329198	496554			25-Apr09	10.44
Aguakan Pozo 3B	2328700	497195			25-Apr09	9.90
Aguakan Pozo 12	2323209	494420			25-Apr09	9.65
Aguakan Pozo 23a	2319761	488966			25-Apr09	9.24
Aguakan Pozo 23b	2319761	488966			25-Apr09	9.11

Aguakan vallarta	2306924	495710			25-Apr09	5.95
Pabalan	2293272	413680			26-Apr09	21.15
Estrella	2301048	423250			26-Apr09	21.02
Cenote el eden	2342432	483312			28-Apr09	5.12

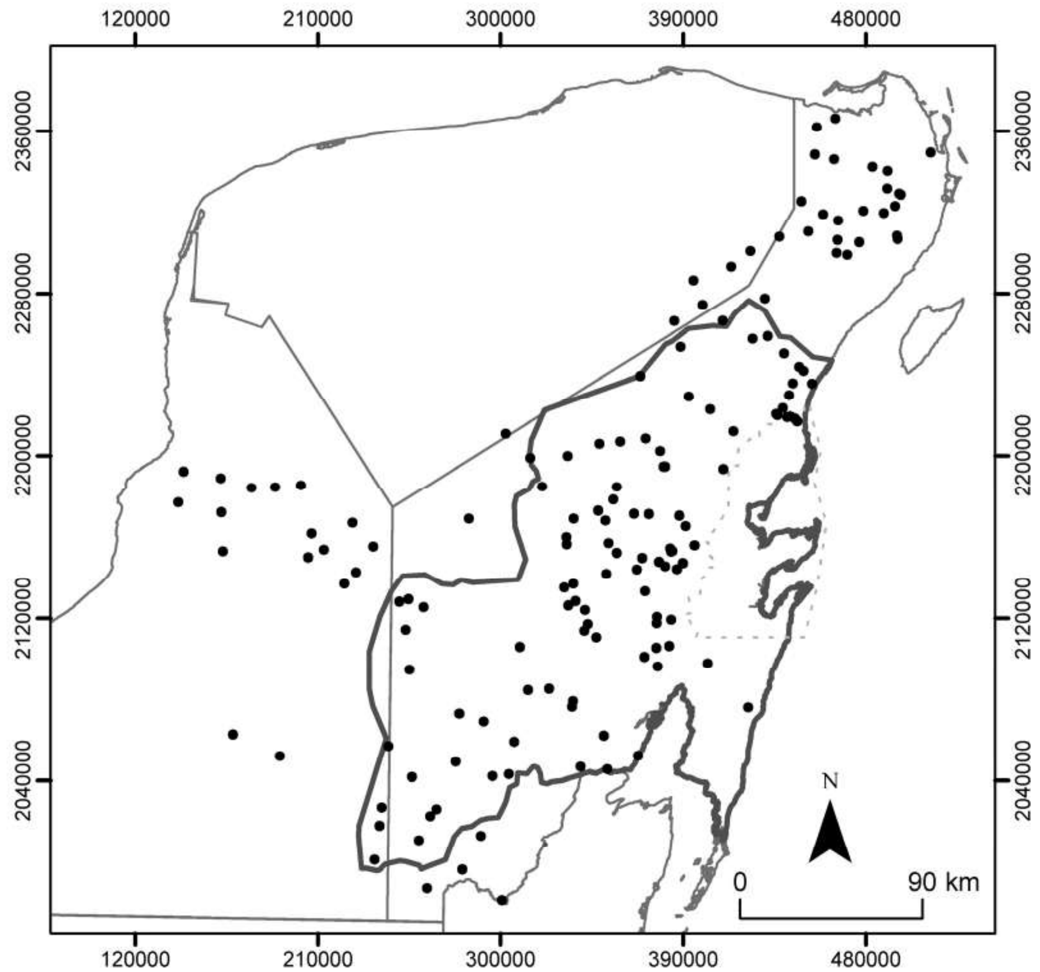

Fig. A6.1. Water level measurement points.

A6.2 GPS benchmarks

Elevations of GPS benchmarks at open spaces nearby the water level measurement sites. Benchmarks were also marked with paint in the field.

GPS measurements corresponding to the perched water level measurements from July 2007 were carried out by Chiara Fratini. GPS measurements corresponding to the sites north of the study area from April 2009 were carried out by Guillaume Charvet.

Location	Northing	Easting	Elevation of reference point at GPS benchmark (mamsl)
ASK Carillo	2165530.29	390614.04	18.10
Mariposa Tulum	2234528.53	450885.37	13.62
Bacalar	2066338.77	353465.20	16.26
Macario Gomez	2250444.93	439830.85	15.60
Chankah Veracruz	2155881.31	395648.41	5.63
Uhmay	2147267.76	389907.27	6.12
Xpichil	2178333.25	355594.37	22.41
Chunhuas	2171164.15	373073.24	15.15
San Andres	2145720.73	381162.60	6.41
Muyil	2220482.08	435844.86	5.37
Polyuc	2168998.47	336024.84	14.68
Nuevo Israel	2128291.53	336771.99	21.29
Las Panteras	2117135.32	342986.19	20.35
Los Divorciados	2110174.40	347023.06	33.05
Nuevo San Antonio	2170437.07	388121.87	8.73
Señor	2194780.54	381113.85	19.34
Tuzik	2202505.07	378621.66	19.78
San Jose Segundo	2208598.48	371608.71	21.59
Andres Quinta Roo	2117077.76	383997.46	11.52
Noh-Bec	2117476.24	376964.63	4.68
Polinkin	2120566.75	377073.88	9.75
Petcacab	2133133.23	371400.53	21.33
X-hacil	2144306.96	387020.57	6.67
Noh-Cah	2147856.05	378171.51	7.12
Mixtequilla	2144084.87	367154.46	16.22
Santa Maria Poniente	2142063.22	352205.85	10.16
Limones	2106314.48	383197.73	6.89
Chacchoben	2105304.48	376731.14	13.45
Rancho La Herradurra	2100902.04	370952.32	7.59
Pedro A. Santos	2096160.16	377380.88	9.49
Tepich	2239242.09	368945.63	23.24

Francisco I. Madero	2229167.16	392719.34	15.17
Chumpon	2212246.30	414667.54	7.88
Chunya	2222912.10	403573.57	15.09
San Luis	2172964.62	348141.79	23.99
Presidente Juarez	2136595.03	335842.68	25.32
Betania	2171390.35	365810.84	15.36
Tres Reyes	2193552.54	409797.62	7.38
Felipe Carrillo Puerto	2165592.82	391296.77	10.04
San Francisco Ake	2207264.17	358959.28	21.87
Dzoyola	2206336.47	348832.46	18.04
Javier Rojo Gomez	2199827.73	333162.24	24.94
Santa Isabel	2153126.65	384701.91	10.24
Laguna Ocom	2152767.76	384101.77	4.05
Chunkakah	2154335.99	383715.72	9.63
Reforma	2079186.16	335775.30	27.80
Altos de Sevilla	2085087.41	323979.22	69.18
Morocoy	2059103.01	306805.26	68.24
Rio Escondido	2084666.29	313658.13	58.83
Otillo Montaño	2105809.66	309560.73	49.36
Dzulá	2168249.80	351524.17	20.53
Laguna Kaná	2156931.26	353333.49	21.59
Yoactun	2152343.10	357358.85	22.00
Tulum federal plot	2235499.04	453583.19	2.57
Manuel Antonio May	2259023.39	431717.53	20.07
Centro Nocturno	2243802.33	447261.59	7.29
Cenote Azul	2062235.67	350866.27	16.08
Santa Elena	2045548.47	352714.16	1.66
Calderitas	2052211.91	367836.72	7.14
Ucum Qroo	2046782.50	339593.64	23.84
El Cedral	2069073.85	291758.09	88.98
Francisco Villa	2042999.44	304163.03	84.59
Nicholas Bravo	2042065.54	296126.16	105.19
Felipe Anjeles	2010501.92	259888.19	209.17
La Lucha	2025627.67	268553.63	179.86
Veinte de Noviembre	2041728.64	256347.09	200.39
Richardo Payro	2026620.46	241514.81	261.92
El Once	2000875.76	237965.56	266.27
Narciso Mendoza pozo	2017582.93	240426.60	241.89
Bel Ha	2094685.80	255190.06	138.05
José Maria Morelos	2184891.30	320642.61	23.35
Nuevo Becar chico	2072982.79	279730.84	96.73
Xkan-Ha	2114277.59	253373.51	129.42
Ucum Campeche	2129306.88	254665.22	105.29
Chanchen	2125429.25	262056.85	152.59
Xmejia	2127963.46	250245.68	3.86
Chunhuhub	2169034.74	284412.31	26.32
Surface water bodies			
Laguna Chichankanab	2198902.82	314565.40	3.86
Zoh Laguna	2056997.13	244806.72	259.80

Points outside the study area			
La Union	1981105.86	300777.24	10.66
Tòmas Garrido	1996078.41	281219.07	45.44
Tres Garantias	2012758.95	290295.88	149.58
OjoDeAgua	1986994.67	263863.31	74.05
Conhuas	2052115.49	191369.12	152.26
Costitucion	2062674.06	168167.78	82.26
Hopelchen_Petch_Base	2185554.92	201617.30	96.23
Pakchèn	2161783.50	206914.97	146.84
Dzibalchèn_Base	2153763.90	213062.10	164.54
Chencoh	2150063.23	205250.40	170.05
Kancabchèn	2136764.21	223131.29	156.56
Chiunchintok	2142792.52	228840.88	133.74
Ich-Ek_Base	2184542.14	189027.59	80.43
RamonCorona_Rancho_Base	2155270.62	237351.87	136.91
Iturbide	2167099.69	227165.63	119.51
Campeo Aleman	2192356.27	143844.98	12.67
Bolonchel Cahuich	2152921.74	163274.91	29.66
Uayamòn	2176952.92	141188.39	26.05
Tikinmul_Base	2189048.41	162233.43	27.61
Nohyaxche	2172106.29	162406.47	25.57
Crucero Oxa	2184313.38	177314.61	65.56
Kambul	2210878.54	302598.11	33.66
Carolina	2169034.74	284412.31	75.50
Leona Vicario	2320772.24	478779.44	5.79
Cenote 7 bocas	2308483.14	495448.97	5.76
Ranch de la dama y del caballero	2331652.04	490631.67	8.57
Ranch la calandaria	2340314.42	490705.30	8.37
El Delicios	2305327.35	476759.76	12.63
Agua Azul	2306393.87	466128.45	7.49
La granja	2300076.25	465719.37	11.68
Victoria	2299043.26	470952.39	10.57
Valladolid nueva	2316004.20	466369.79	3.71
Chulutan	2274534.55	399667.96	21.52
Felipe Carillo	2266553.74	409477.04	18.82
Xalau	2286395.77	395166.00	22.09
Santa Rosa	2266410.09	385745.18	22.05
Chamul	2253724.10	388798.15	21.92
San Juan	2257791.35	424285.84	7.45
Camp. Hidalgo	2277620.23	430336.55	22.03
Rancho el viejo	2349312.85	511993.06	8.31
Solferino	2362073.88	455808.07	9.94
San Eusebio	2366412.60	465038.05	8.39
San Angel	2348367.64	454934.93	7.46
Rancho san Juan	2346084.72	464437.28	7.82
El Tintal	2310579.98	451710.84	7.77
Nuevo Xcan	2307877.00	437487.26	21.08

Kantanulikin	2325483.28	448344.63	7.28
Esperanza	2319133.44	458936.52	13.82
Aguakan Pozo 1B	2329198.31	496553.87	9.92
Aguakan Pozo 3B	2328699.75	497194.65	9.48
Aguakan Pozo 12	2323208.91	494419.99	9.24
Aguakan Pozo 23a	2319760.71	488965.79	8.55
Aguakan Pozo 23b	2319760.71	488965.79	8.55
Aguakan vallarta	2306924.30	495709.69	5.61
Pabalan	2293271.54	413680.46	20.08
Estrella	2301048.40	423250.28	20.45
Cenote el eden	2342431.99	483311.56	6.64

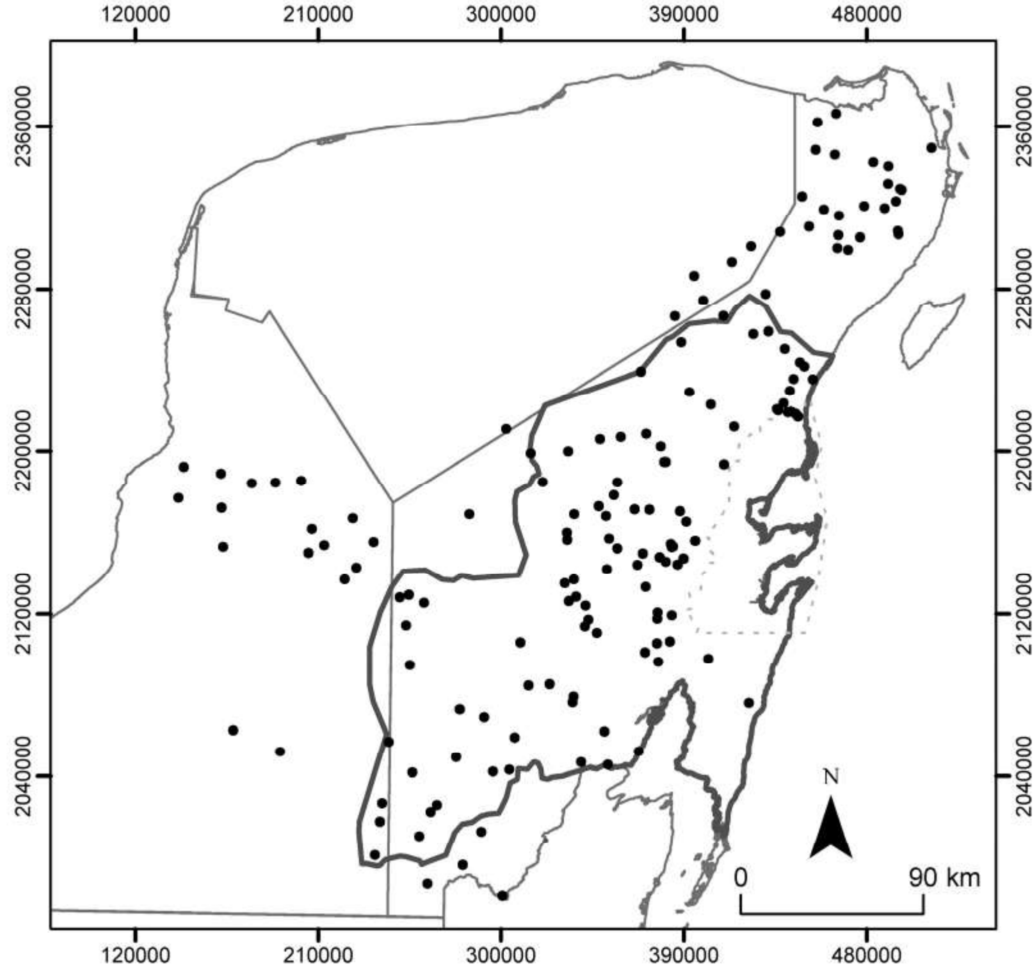

Fig. A6.2. GPS benchmarks.

A6.3 Water sampling sites

These data are also included as Electronic Supplement to Gondwe et al. (IV). The analysis run were: Ca^{2+}, Mg^{2+}, Sr^{2+}, K^{+}, Na^{+}, Ba^{2+}, SO_4^{2-}, Cl^{-}, NO_3^{-}, Br^{-}, HCO_3^{-}, $\delta^{18}O$.

Oxygen isotope analyses of water samples were kindly performed at Centre for Ice and Climate, Niels Bohr Institute, University of Copenhagen, Denmark. Sulfate and alkalinity analyses were kindly performed at CICY–CEA, Cancun, Mexico.

Location	Northing	Easting	Collect date
Groundwater			
Andres Quintana Roo	2119078	384045	24-Feb-08
Betania	2171991	364995	19-Feb-08
Caobas	2040402	278072	25-Feb-08
Dzula	2168188	351530	19-Feb-08
El Cedral	2069065	291628	23-Feb-08
Francisco Villa	2043887	305022	23-Feb-08
Las Panteras	2116954	343030	20-Feb-08
Limones	2103575	383133	20-Feb-08
Los Divorciados	2109676	346734	07-Feb-08
Mixtequilla	2144153	367118	18-Feb-08
Morocoy	2057464	308879	23-Feb-08
Naranjal Poniente	2141533	346663	18-Feb-08
Nicholas Bravo	2042505	296143	25-Feb-08
Noh Cah	2147855	378229	24-Feb-08
Nuevo Israel	2128250	337357	20-Feb-08
Otillo Montaño	2102587	307561	22-Feb-08
Pedro A. Santos	2096556	377217	20-Feb-08
Petcacab	2133494	371269	21-Feb-08
Polinkin	2120565	376854	21-Feb-08
Presidente Juarez	2137762	335917	20-Feb-08
Rancho Las Herraduras	2100867	370950	20-Feb-08
Reforma	2080887	334274	23-Feb-08
Rio Escondido	2088921	315400	22-Feb-08
San Luis	2172936	348052	19-Feb-08
Señor	2194275	380703	22-Feb-08
Ucum Q.Roo	2046238	339617	23-Feb-08
Xhacil	2144613	386587	18-Feb-08
Xkan-Ha	2114278	253374	27-Feb-08
Surface water			
Cenote Azul	2062367	350932	23-Feb-08
Narciso Mendoza	2017596	240428	26-Feb-08
Veinte de Noviembre	2041661	256369	26-Feb-08

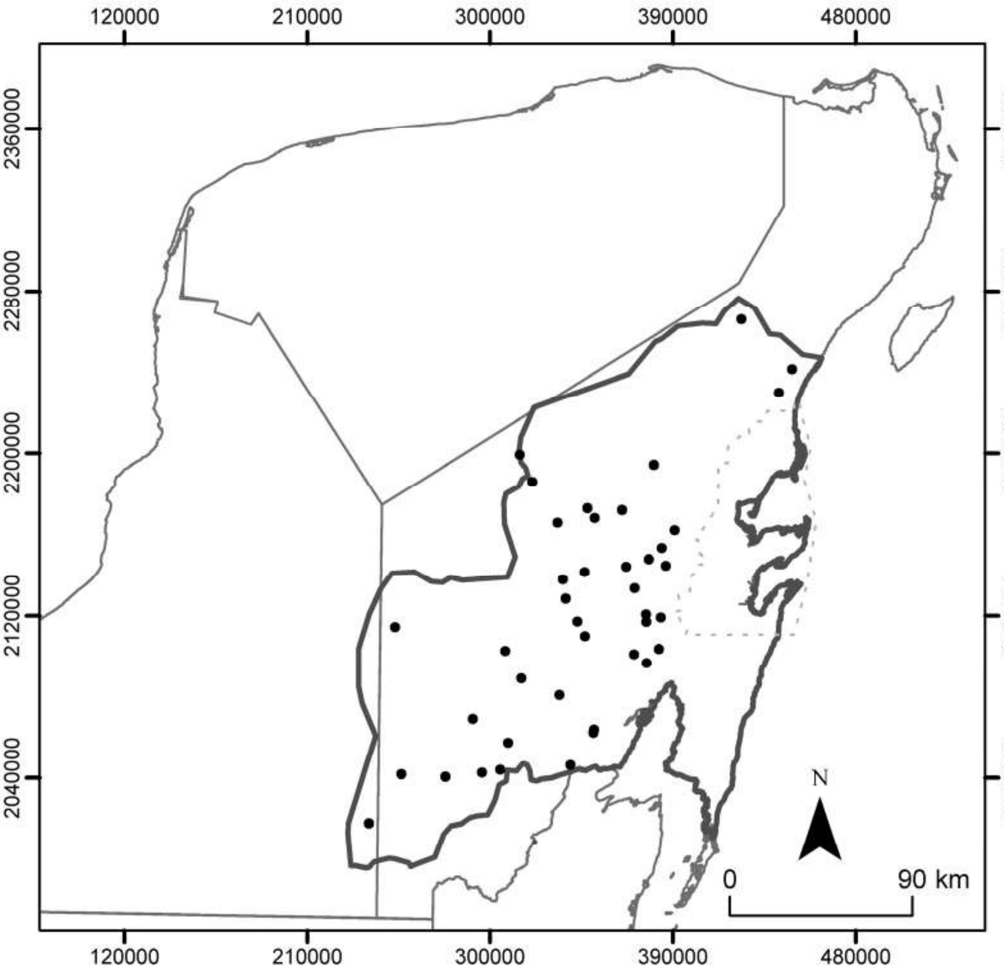

Fig. A6.3. Water sampling points.

A6.4 Time-domain EM measurements

Location	Northing	Easting	Collect date
Petcacab	2132856.48	371323.51	08-Mar-2007
Santa Maria Poniente	2142259.43	351003.55	09- Mar -2007
Chunhuas	2172005.95	373419.25	26- Mar -2007
Chunhuas	2172005.95	373419.25	28- Mar -2007
Uhmay	2146428.42	388542.65	29- Mar -2007
Andres Quintana Roo	2121908.04	383980.10	29-Mar-2007
Chumpon	2207223.85	420322.62	08-Apr-2007
Chumpon	2236617.00	454335.00	12- Apr -2007
Chumpon	2236231.20	454917.96	12- Apr -2007
Tulum airstrip	2237164.34	453513.25	12- Apr -2007
Muyil	2220496.25	435833.23	12- Apr -2007
Muyil	2220496.25	435833.23	15- Apr -2007
Macario Gomez	2250764.49	440307.24	15- Apr -2007
Centro Nocturno	2244101.04	447313.07	15- Apr -2007
Eden	2265885.56	473155.97	16- Apr -2007
Betania	2171406.39	365761.92	16- Apr -2007
Presidente Juarez	2136561.24	335946.37	16- Apr -2007
Manuel Antonio May	2258816.79	431917.09	17- Apr -2007
Tulum airstrip	2237164.34	453513.25	17- Apr -2007
Noh Cah	2147643.34	377737.96	19- Apr -2007
Mixtequilla	2143942.32	366940.15	19- Apr -2007
San Luis	2173347.12	348661.02	20- Apr -2007
Felipe Carrillo Puerto	2165534.72	386582.38	20- Apr -2007
Vigia Chico1	2173440.75	405328.02	22- Apr -2007
Vigia Chico2	2174981.54	407487.24	22- Apr -2007

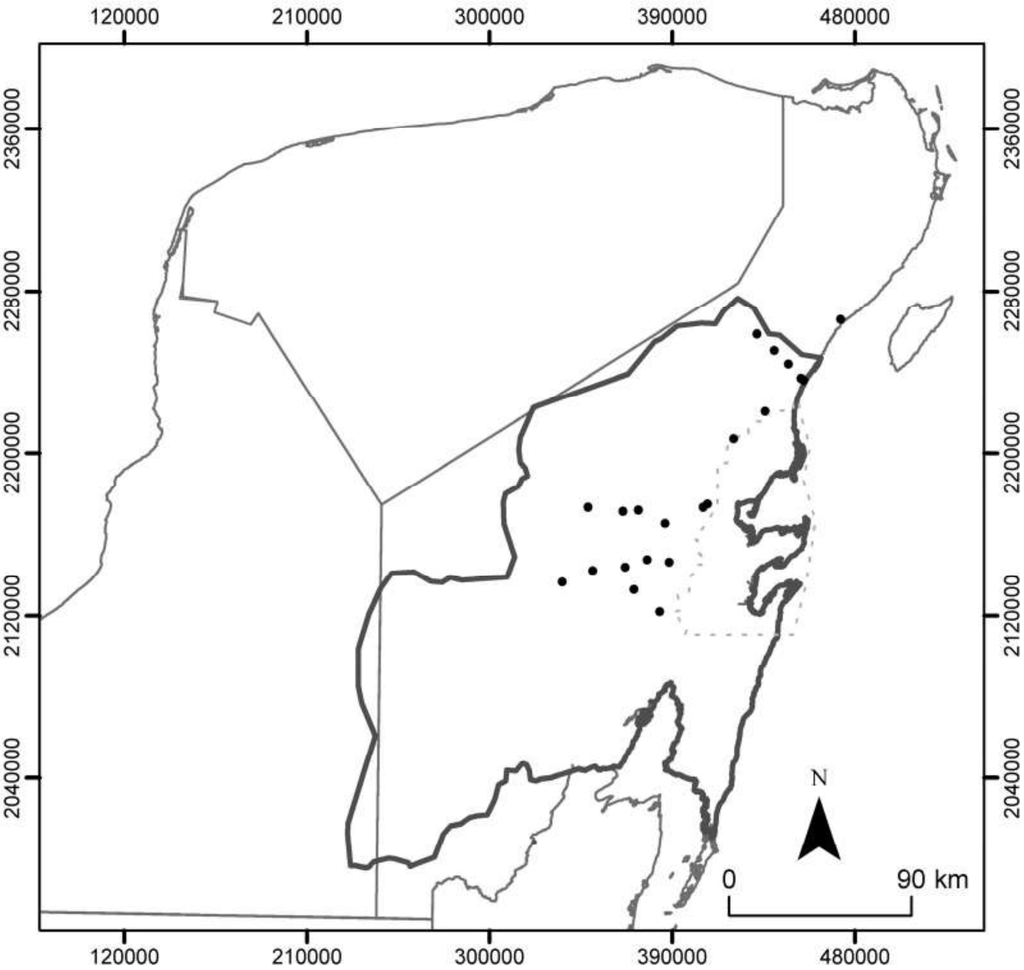

Fig. A6.4. Time-domain EM measurements.

A6.5 Borehole logging measurements

The following log types were carried out where possible: fluid temperature and fluid conductivity (F), natural gamma radiation (G), induction (I).

Location	Northing	Easting	Collect date	Type
Akumal 1	2261621	459155	31-Jan-08	F, G, I
Rancho Viejo	2244372	446092	31-Jan-08	F, G
Costa Maya km 30	2089897	409824	01-Feb-08	F, G, I
Costa Maya km 42	2081340	417453	01-Feb-08	F, I
X-pichil	2184785	357307	06-Feb-08	F, G, I
Felipe Carrillo Puerto	2165775	388591	07-Feb-08	F, G
Las Panteras	2113715	341417	07-Feb-08	F, G, I
Nuevo Israel	2126121	333379	08-Feb-08	F, G, I
Presidente Juarez	2134993	331399	08-Feb-08	F, G
Reforma	2076459	335318	11-Feb-08	F, G, I
Rio Escondido	2084621	313614	11-Feb-08	F, G, I
Morocoy	2059112	306809	12-Feb-08	F, G, I
Caobas	2041044	277498	12-Feb-08	G, I
Chankah Derepente	2144759	369928	14-Feb-08	F, G, I
Señor	2194778	380402	14-Feb-08	F, G, I
Chunhuhub	2159949	332456	15-Feb-08	F, G, I
Emiliano Zapata	2124021	341666	15-Feb-08	F, G, I
Nuevo Becar	2049273	278016	16-Feb-08	F, G, I

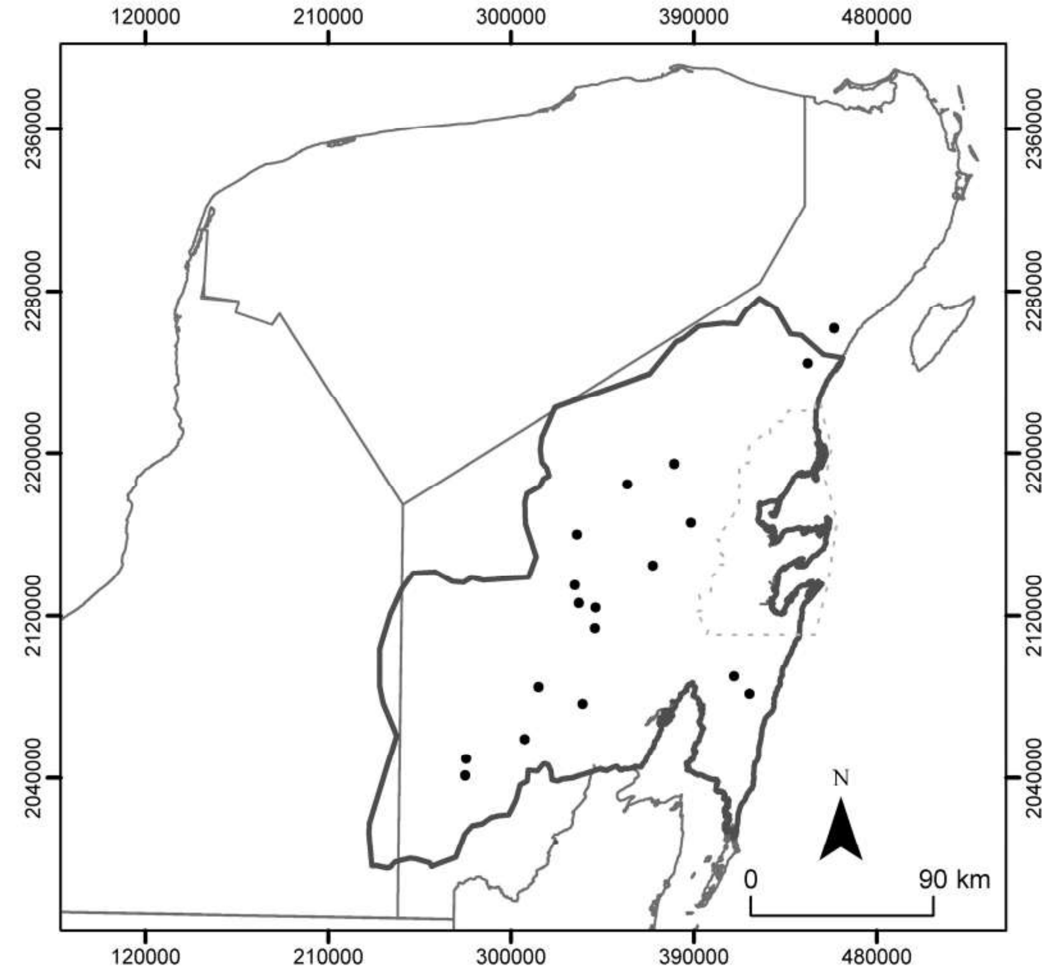

Fig. A6.5. Borehole logging measurements.

A6.6 Airborne EM transects

The locations of the airborne EM measurements are indicated on Fig. A6.6. The end points of the transects are given in the below table. The Holbox zone was flown with dense flight lines; 100 and 200 m line spacing. Across the inland structures, 5–6 parallel flight lines were flown, yielding transects ~1000 to 1500 m wide.

Location	Northing	Easting	Comment
Holbox zone	2243641	445969	Corner point 1 of area
	2239163	457019	Corner point 2 of area
	2235006	442700	Corner point 3 of area
	2231133	453395	Corner point 4 of area
Transect A	2137564	319720	
	2116502	340470	
Transect B	2101159	334463	
	2086877	353699	
Transect C	2148103	364053	
	2140434	373304	
Transect D	2093644	310300	
	2084971	319087	
Transect E	2076581	322658	
	2067454	330991	

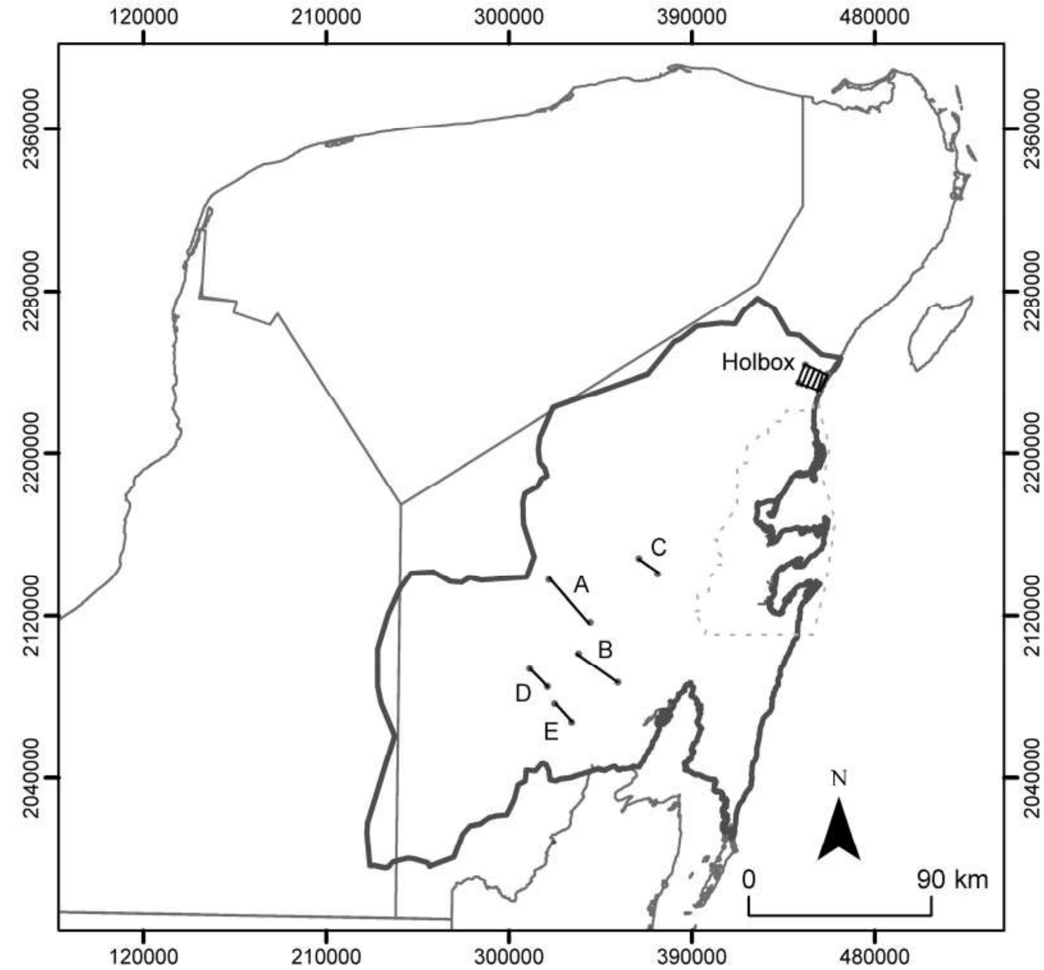

Fig. A6.6. Airborne EM measurements.

A6.7 Inventory of electronic data material

Inventory of electronic data material, available on DVD from the contact persons given in the beginning of this chapter. Folder names underlined and subfolders formatted with hanging indents. Brief descriptions also given. Airborne EM data is not given here; special permission to use these data must be obtained from Amigos de Sian Ka'an and Geological Survey of Austria.

<u>FIELD_DATA</u>

<u>WaterLevels</u>

Water level data, distributed in sub-folders according to the person who collected the data (Bibi, Chiara, Guillaume, ASK).

<u>GPSData</u>

GPS data, distributed in sub-folders according to the person who collected the data (Bibi, Chiara, Guillaume).

<u>WaterSamples</u>

Raw data in various files, including quality control data and methods used. Also all data collected in one spreadsheet given, as also presented in electronic supplement for Gondwe et al. IV.

<u>TDEM</u>

Raw TDEM data files and Excel-sheet with the processed data.

<u>Logging</u>

Raw logging data files as well as Excel-sheet and Word-document describing with the processed data

<u>REMOTE_SENSING_DATA</u>

<u>Bibi_ET</u>

TRMM monthly rainfall data covering the whole peninsula, 1999-2008, raw and adjusted according to the climate station data from CONAGUA. Excel sheet with the calculation of adjustment data also given.

All data used for producing the ET_a daily estimates for 2004-2008. I.e. ET_a calculated with the “triangle method” for cloud free pixels covering the whole peninsula, K_c, ET_{ref} (via Hargreaves, in folder PET), scripts for processing the data in ENVI-IDL. Method described in Gondwe et al. IV, Lerer (2008) and Stisen et al. (2008).

Structures

Shapefiles of structures outlined via visual inspection of satellite imagery. Used in the hydrological models.

Shapefiles of faults suggested in Gondwe et al. (I).

Landsat TriDecadal

Landsat TriDecadal imagery, used to outline the structures. See reference in Gondwe et al. IV for data source.

Landsat ETM+

Landsat imagery, used to outline the structures. See reference in Gondwe et al. IV for data source.

Interferograms

Georeferenced interferograms, subsets covering Sian Ka’an

Flooding_maps

Georeferenced_floodmaps

Landsat for flood verification The data used to compare classifications with. See Gondwe et al. (I) for data source.

An Excel-sheet with the no. of pixels in each flooding category is also given in this folder.

HYDROLOGICAL MODELLING

InputFiles

Input files used in hydrological models.

SteadyState_7ConceptModels

MIKE SHE files and result files for the 7 steady state models run. The results folders also include Excel-sheets comparing modelled and measured groundwater heads.

Examples also given of files used in particle tracking in separate particle tracking folder.

Transient_2ConceptModels

MIKE SHE files and result files for the 2 transient models run. Modelled interferograms and script for converting output to interferogram also given.

MonteCarloStackedResults

The stacked outputs of the MonteCarlo simulations.

ExampleMonteCarloScripts

Example of scripts used to generate the Monte Carlo simulations.

ExampleAutocalibrationScripts

Example of script used to autocalibrate the models using Matlab's nlinfit.

The Department of Environmental Engineering (DTU Environment) conducts science-based engineering research within four themes:
Water Resource Engineering, Urban Water Engineering,
Residual Resource Engineering and Environmental Chemistry & Microbiology.
Each theme hosts two to five research groups.

The department dates back to 1865, when Ludvig August Colding, the founder of the department, gave the first lecture on sanitary engineering as response to the cholera epidemics in Copenhagen in the late 1800s.

DTU Environment
Department of Environmental Engineering
Technical University of Denmark

Miljoevej, building 113
DK-2800 Kgs. Lyngby
Denmark

Phone: +45 4525 1600
Fax: +45 4593 2850
e-mail: reception@env.dtu.dk
www.env.dtu.dk

ISBN 978-87-91855-85-6